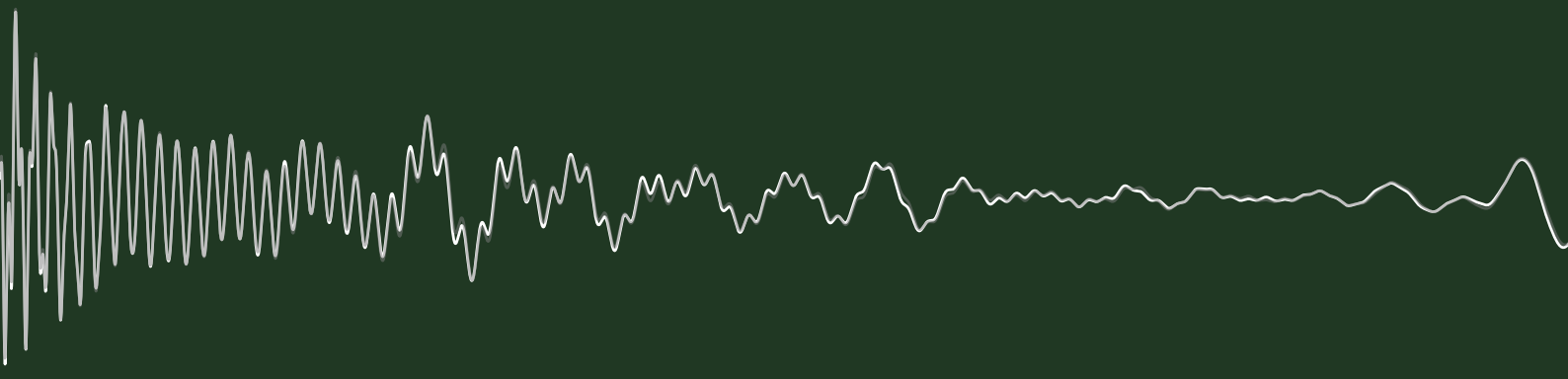
Estimating Ship Structural Response Using Sparse Sensor Measurements

Transient (Slamming) Effects

Andrew Gaard



TU Delft

Estimating Ship Structural Response Using Sparse Sensor Measurements

Transient (Slamming) Effects

by

Andrew Gaard

to obtain the degree of Master of Science
at the Delft University of Technology,
to be defended publicly on November 26, 2026 at 16:00.

Student number:	6148069	
Project duration:	November 12, 2025 through November 26, 2026	
Thesis committee:	Dr. Ir. J.H. den Besten	TU Delft, chair
	Dr. A. Grammatikopoulos	TU Delft
	Dr. Ir. P.R. Wellens	TU Delft
	Dr. N. Yue	TU Delft
	Ir. R.L.G. Slange	TU Delft
	Dr. Ir. G. Bufalari	Damen Naval
	R. van Dijke	Damen Naval

An electronic version of this thesis is available at `https://repository.tudelft.nl`.

TU Delft Delft University of Technology

DAMEN NAVAL

Summary

Slamming can accelerate fatigue damage accumulation in ship structures, but the developing cracks are not always easily detectable. Sparse sensor measurements can be used to estimate the structural response of ships, perform a fatigue assessment, and identify areas requiring preventive maintenance. To estimate irregular linear wave loading and response, measured strains are often multiplied by an inverted modal basis, resulting in a set of amplitude estimates that scales the external loading and structural response at all finite elements. The modal basis itself is commonly constructed as a set of particular solutions to the frequency domain equation of motion (distortion modes), but higher-order vibrations are excited by slamming loads and are best represented by the homogeneous solution (wet modes). To address global effects, this work proposes a method for estimating the global high-frequency loading and response by means of using wet modes, a truncated set of complex eigenvectors obtained using structural mass, stiffness, damping, and frequency-dependent radiation coefficients. To address local hydroelastic slamming effects, this work proposes a method for estimating the local high-frequency response by means of using dry modes, a truncated set of real eigenvectors obtained using structural mass and stiffness matrices of an orthotropically stiffened panel. The two methods are investigated using one-dimensional finite element models: a scale segmented barge and an orthotropically stiffened plate, which is represented by a beam. Results show that a truncated basis of wet modes accurately estimates high-frequency strains and pressures at unmeasured locations, while low-frequency rigid body motions introduce inestimable effects. The basis of distortion modes is found to introduce significant loading estimation error, despite estimating strains near the measured locations with relatively good accuracy. A truncated basis of dry modes accurately estimates the hydroelastic response of a panel at unmeasured locations. Three sensors and three modes are required in both cases, but separation of high- and low-frequency measurements by means of a discrete filter is required for accurate high-frequency estimates in the global model. Models are verified against analytical, numerical, and experimental results from literature.

Contents

1 Introduction **1**
- 1.1 Motivation . . . 1
- 1.2 Problem Statement . . . 2
- 1.3 Research Scope . . . 2
- 1.4 Objective . . . 3
- 1.5 Implications . . . 3
- 1.6 Outline . . . 4

I Literature Review **5**

2 Loading and Response of Structures in Waves **6**
- 2.1 An Overview of Ship Motions . . . 6
- 2.2 Steady-State . . . 7
  - 2.2.1 Exact Boundary Value Problem . . . 7
  - 2.2.2 Linearization . . . 9
  - 2.2.3 Forces . . . 10
  - 2.2.4 Equation of Motion . . . 11
- 2.3 Transient . . . 12
  - 2.3.1 Slamming . . . 12
  - 2.3.2 Whipping . . . 14
- 2.4 Numerical Methods . . . 14
  - 2.4.1 Boundary Element Method . . . 14
  - 2.4.2 Finite Element Method . . . 16
  - 2.4.3 Model Order Reduction . . . 17
- 2.5 Models . . . 19
- 2.6 Conclusions . . . 21

3 Fatigue in Welded Joints **22**
- 3.1 Assessment Concepts . . . 22
  - 3.1.1 Nominal Stress . . . 22
  - 3.1.2 Hot Spot Structural Stress . . . 23
  - 3.1.3 Effective Notch Stress . . . 23
  - 3.1.4 Total Stress . . . 24
- 3.2 Resistance . . . 24
- 3.3 Damage Accumulation Models . . . 25
- 3.4 Conclusions . . . 26

4 Loading and Response Estimation Using Sparse Sensor Measurements **27**
- 4.1 Objective . . . 27
- 4.2 Methods . . . 28
  - 4.2.1 Method of Least Squares . . . 28
  - 4.2.2 Ritz Vectors . . . 32
  - 4.2.3 Inverse Finite Element Method . . . 32
  - 4.2.4 Kalman Filters . . . 33

4.2.5 Transmissibility . . . 34
4.2.6 Slamming Identification, Localization, and Signal Decomposition . . . 37
4.3 Conclusions . . . 37

5 Research Overview **38**
5.1 Research Gap . . . 38
5.2 Hypotheses and Research Question . . . 38
5.3 Modeling Plan . . . 39

II Modeling **40**

6 Global Model: Segmented Barge **41**
6.1 Loading and Response . . . 42
6.1.1 Model Setup . . . 42
6.1.2 Steady State . . . 44
6.1.3 Transient . . . 48
6.1.4 Verification . . . 49
6.2 Stress and Pressure Estimation . . . 54
6.2.1 Modal Bases . . . 54
6.2.2 Number and Position of Strain Gauges . . . 56
6.2.3 Filtering . . . 57
6.2.4 Error Metrics . . . 57

7 Local Model: Stiffened Panel **59**
7.1 Loading and Response . . . 59
7.1.1 Model Parameters . . . 59
7.1.2 Slamming Model . . . 59
7.1.3 Analytical Euler-Bernoulli Beam Model . . . 60
7.1.4 Quasi-Static Response . . . 60
7.1.5 Hydroelastic Response . . . 60
7.2 Stress Estimation . . . 64
7.2.1 Modal Basis . . . 65
7.2.2 Number and Position of Strain Gauges . . . 65
7.2.3 Noise . . . 65
7.2.4 Filtering . . . 65
7.2.5 Error Metrics . . . 65

III Results **66**

8 Global Results: Segmented Barge **67**
8.1 Regular Wave . . . 68
8.2 Irregular Waves . . . 72
8.3 Impulse Load . . . 76
8.4 Regular Wave with Impulse Load . . . 81
8.5 Irregular Waves with Impulse Load . . . 86

9 Local Results: Stiffened Panel **91**
9.1 Plate Impact with Wave . . . 91
9.2 Falling Wedge Impact . . . 93

IV Judgment and Future Work **95**

Bibliography **100**

Chapter 1

Introduction

1.1 Motivation

Fatigue is often a governing limit state in ship and offshore structures. Therefore, the understanding of fatigue and the phenomena by which damage accumulates is essential for design and maintenance. In ship and offshore structures, fatigue damage accrues through wave-induced cyclic stress, which can be assessed in either the frequency or time domains. Depending on the structural configuration and operating conditions, a quasi-static (one-way) or hydroelastic (two-way) model can be used to determine the loading and response at both global and local levels. A fatigue assessment is then performed by means of substituting far-field stresses into one of various stress concepts at the structural detail level. Finally, damage is quantified by adopting an accumulation model.

For many ship and offshore structures, a quasi-static approach is sufficient for assessing fatigue damage and performing preventive maintenance if the sea state is well-approximated by a superposition of linear waves and far-field stress state transfer functions, consisting of a Response Amplitude Operator (RAO) and phase information, are known. For this approach to be valid, the global ship motions must be relatively small. However, for vessels that operate in heavier seas, are relatively flexible, have slamming-prone hull shapes, or operate at high speeds, nonlinear loading and response must be considered. In particular, local transient loading and response (slamming) can increase excitation of higher-order structural modes, which may accelerate fatigue damage accumulation. For example, Tuitman [1] showed that slamming-induced whipping reduced the predicted fatigue lifetime of two ultra-large container ships by about 40%, and increased the ultimate bending moment by about 20%. Pferdekamper and Bekker [2] concluded that slamming and whipping contributed up to 69% of the total fatigue damage in a polar class vessel, with an average of 37.4%. An additional study found that following seas causes transom slamming in the same polar-class vessel when stationary, leading to 46.3 times more damage than in head seas [3]. At the local level Hascoët and Jacques [4] found, using a non-dimensional orthrotropically stiffened wedge, that slamming-induced fatigue damage can lead to a non-conservative design, with up to a 5x safety factor error. The influence of slamming on fatigue damage cannot be neglected in both the design and maintenance of ships, but the computational effort required to accurately simulate slamming-induced fatigue damage is exceptionally high.

Cracks that develop in ship and offshore structures are not always easily detectable, and repairing cracks by welding can be a costly procedure, depending on the location. To assess the remaining operational life of a vessel and perform predictive maintenance on developing cracks (detectable or not), new research has been dedicated to Structural Health Monitoring (SHM). In a SHM system, sensors such as strain gauges and accelerometers are used to estimate the far-field stress at unmeasured fatigue-sensitive locations, perform a damage assessment, and identify areas requiring preventive maintenance in real-time. By using measurements as opposed to simulations, the accumulated fatigue damage can be estimated with improved confidence.

Numerous methods have been developed to process data from SHM sensors. To estimate fatigue damage in ship and offshore structures, two main categories of SHM methods are found in literature: the method of least squares and state-space estimation. For ship structures, the method of least squares is often used. One form is known as the conversion matrix method, although a very similar mathematical foundation can be found in other literature, particularly on fixed offshore structures. Currently, many maritime companies and research

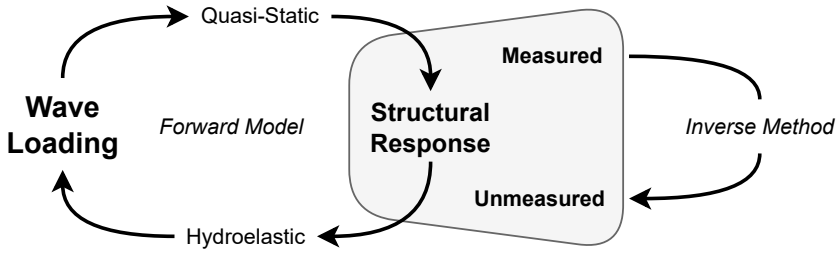


Figure 1.1: A conceptual schematic illustrating the differences between one-way (quasi-static) and two-way (hydroelastic) loading and response in forward modeling, and the objective of inverse methods.

organizations use the conversion matrix method as it has enjoyed the benefit of validation (measurement) campaigns on sailing ships [5] and can be implemented with linear seakeeping software. However, the effects of slamming and whipping on its accuracy at fatigue-sensitive structural details are largely unknown. The second category, state-space estimation, tends to focus on control theory and force estimates, although recent literature on fixed offshore structures highlights fatigue damage accumulation as a viable application.

Regardless of the method chosen, five key challenges exist for the estimation of fatigue damage accumulation in ship and offshore structures due to combined steady-state and transient loading using sparse sensor measurements:

1. Wave loading is characterized by time-variant spatial distribution and amplitude: many estimation methods assume a fixed spatial distribution.
2. Response to slamming is both local and global: sensors may not accurately capture both.
3. The inverse problem is ill-posed and ill-conditioned: the solution is not unique, and errors can amplify due to sensor noise and model uncertainty.
4. An accurate discretized (finite element) model of the structure is large: forward or inverse solutions may take longer than real-time.
5. Quasi-static and hydroelastic responses of structures depend on cyclic wave loads: the equation of motion becomes frequency-dependent.

1.2 Problem Statement

Recognizing the importance of both steady-state and transient loading and response on fatigue damage accumulation in ship and offshore structures and the five key challenges outlined in Section 1.1, the following problem statement is formulated:

PROBLEM STATEMENT Current model-based inverse methods, as used in the assessment of fatigue damage accumulation in ship and offshore structures, do not explicitly address the coupled effects of steady-state (rigid body, springing) and transient (slamming, whipping) loading and response on far-field stress error at unmeasured locations using sparse sensor measurements.

The current model-based inverse methods mentioned in the problem statement will be reviewed thoroughly in Chapter 4.

1.3 Research Scope

This research focuses on the inverse method used to estimate fatigue damage accumulation based on sparse sensor measurements. As such, novel literature on the loading and response of structures in waves and fatigue in welded joints is not considered. To arrive at a reasonable and attainable objective, the scope of this research is limited[1] to: ships constructed of welded (steel or aluminum) slender elements (plates, beams,

[1]The following aspects are explicitly *not* considered in this research: multi-body interaction; ships sailing in close proximity to fixed features or in channels; suspended masses or joints; sloshing, ice, shock, blast, thermal, cargo, ballast, vehicle, and

rods, and shells), built to nominal dimensions, and installed with strain gauges and accelerometers; external hydrodynamic and hydrostatic loads; linear elastic material; incompressible, inviscid, irrotational, and homogeneous external fluid; deep water; time-domain calculations. To limit modeling effort to a reasonable amount, multiaxial fatigue and torsion are not considered.

1.4 Objective

The problem statement outlined in Section 1.2 is reformulated into an objective which guides the literature review and the resulting research hypotheses and questions.

RESEARCH OBJECTIVE Numerically verify a practical and computationally efficient time-domain inverse method which accurately estimates far-field stress states at fatigue-sensitive structural details for a ship structure instrumented with sparse sensor measurements and subjected to combined steady-state and transient (slamming) wave loads.

In the research objective, the inverse method novelty is left unspecified, because it is possible that current methods can accurately account for transient (slamming) effects in the far-field stress response estimation. Novel methods will be further explored in the hypotheses and research question (Section 5.2). The method should be sufficiently practical for implementation with modest (preferably open-source) boundary and finite element software. The objective will be considered reached if preventive maintenance decisions can be made based on the estimated fatigue damage accumulation with high, quantifiable confidence: in other words, if the far-field stress error is negligible relative to the uncertainty introduced by the fatigue assessment itself.

1.5 Implications

Practical The lifetime of ship structures can be significantly reduced by fatigue damage, which is accelerated by springing, slamming, and whipping. When performed at the proper moment, preventive maintenance can extend the life of structures. Therefore, the quantification of error in inverse methods is important for their practical use in informing decisions regarding the maintenance of vessels. This research aims to quantify and minimize the error such that estimates of accumulated fatigue damage are useful and trustworthy. Practically, a successful implementation of this research would lead to reduced inspection frequency and improved efficacy of preventive maintenance, which would increase time in operation and extend the sailing life of ships.

Scientific While inverse methods have been extensively covered in diverse fields such as technical medicine (electrocardiography and magnetic resonance imaging), the treatment of frequency-dependent structural problems with non-proportional damping is still an active area of research in offshore engineering, particularly for floating structures. Inverse methods based on the minimization of least-squared error and Kalman filters are quite advanced for fixed offshore structures, as the boundary conditions at the seabed allow for a well-defined load-based modal basis using Ritz vectors. However, this assumption cannot be made for floating offshore structures. In addition, the complexity of ships is generally higher than that of fixed offshore structures such as jacket and tower wind turbine foundations, and fatigue damage can accumulate at any fatigue sensitive location (e.g. a welded joint) within a complex structure. This research aims to address the frequency-dependence, non-proportional damping, and structural complexity inherent to ship structures through the use of thoroughly validated forward models that are clearly rooted in the governing (first-order) hydrostructural physics of a structure floating on a fluid half-space.

Societal Reliable ships are essential for the modern world. While the list of ship types that are prone to fatigue damage is quite extensive, a specific example (an icebreaker) is considered here which is particularly relevant for this research on the effects of slamming and whipping on estimating fatigue damage accumulation at welded joints. Icebreakers are critical for polar research, especially as global temperatures rise and

other non-hydrodynamic or hydrostatic loads; (macro-scale) material and geometric imperfections that would violate the linear elastic and nominal geometry assumptions; residual stresses, plasticity, and composite materials; cracked geometry; fluid-air mixtures and air entrapment; frequency-domain calculations.

increased activity is expected in polar regions. Icebreakers such as the S.A. Agulhas II are well-suited for such research, and play an important role in providing reliable access to remote cold regions and Antarctic stations. However, these vessels are particularly susceptible to high slamming and whipping load-induced fatigue damage due to their pronounced flared bow, which is used to crush ice. It is expected that predictive maintenance will be particularly important for such vessels when sailing to and from their home ports, which requires the crossing of heavy sea states in the southern oceans [3]. While the S.A. Agulhas II in particular is instrumented with a large number of strain gauges and accelerometers, the ship structure itself is quite complex and stiff. For this reason, it is difficult to accurate estimate fatigue damage accumulation far from locations where strain gauges are installed, especially with current methods. Indirectly, one goal of this research is to help extend the lifetime of vessels such as the S.A. Agulhas II and thus decrease the costs of critical polar research.

1.6 Outline

Part I — Literature Review

Three main topics are addressed in the context of estimating fatigue damage accumulation in ship and offshore structures. **Chapter 2** provides an overview of steady-state and transient (slamming) loading and response of structures in waves with a focus on computationally efficient forward models. **Chapter 3** reviews the fundamental principles of fatigue stress assessment concepts, resistance, and damage accumulation models with an emphasis on the propagation of uncertainty. These first two chapters provide the conceptual, physical, and mathematical framework for **Chapter 4**, which critically reviews foundational and state-of-the-art literature regarding inverse methods which can estimate far-field stress states in ship and offshore structures based on sparse sensor measurements. Finally, **Chapter 5** outlines the identified research gaps, hypotheses, and question. A brief modeling overview is provided, which explains how the research hypotheses and questions are evaluated using numerical models.

Part II — Modeling

Two models are created to answer the research question and hypotheses formulated in the literature review in Part II. **Chapter 6** outlines the implementation of a global model, which is constructed as a segmented barge subjected to incident, diffraction, radiation, and impulse loads. The method of estimating structural stress and external hydrostatic and hydrodynamic pressures is presented. **Chapter 7** outlines the implementation of a local model, which simulates an orthotropically stiffened panel strip subjected to quasi-static and hydroelastic loading. The method of stress estimation is similar to that outlined in **Chapter 6**; key differences are explained.

Part III — Results **Chapter 8** presents results for the global numerical model. Five loading and response scenarios are considered: a single impulse, a regular wave, irregular waves, and combinations of the single impulse with regular and irregular waves. The structural stress and pressures are estimated at various parts of the segmented barge and compared with the observed values to assess the estimate error. **Chapter 9** presents results for the local numerical model. Two configurations are considered: a wave impacting the orthotropically stiffened panel, and a wedge falling into still water with some specified velocity. Stress is estimated at the middle and ends of the panel for each configuration and compared with the observed values to assess the estimate error.

Part IV — Conclusion The research question and hypotheses are addressed using the global and local modeling results. Outcomes from the literature review, modeling, and results are discussed. Future work and practical implementation steps for the modeling methods used in this thesis are mentioned.

Part I

Literature Review

Chapter 2

Loading and Response of Structures in Waves

A significant contribution to fatigue damage in ship and offshore structures comes from waves, which introduce cyclic and transient loading. In literature on ship structures, three definitions are often used to categorize wave loading and structural response: slamming and whipping (transient), and springing (steady-state). A slam is an impulsive load that acts locally and can contribute to significant high-frequency fatigue damage at structural details close to the location of impact. Whipping is the global transient response to a slam and contributes to lower high-frequency fatigue damage throughout the entire structure. Springing is the global steady-state response to waves in the fluid environment, and contributes to low-frequency fatigue damage throughout the entire structure.

In this chapter, the three kinds of loading and response are addressed by first defining the types of motions (quasi-static and elastic) that govern the global and local responses of ship structures (Section 2.1). In Section 2.2, the exact boundary value problem is formulated and linearized, leading to the equations of motion for global steady-state (springing) loading and response in the frequency domain. Section 2.3 focuses on transient loading and response, which is first addressed at the local level with a review of various slamming models and the conclusions derived from both experiments and numerical methods. The equations of motion typically used for the transient global whipping response are presented thereafter as a modification of the steady-state frequency domain equation of motion. Section 2.4 covers the Boundary Element Method (BEM) and the Finite Element Method (FEM), which are essential numerical methods for determining the stresses at structural details based on a linearized first-order equation of motion. Section 2.5 reviews three coupled forward modeling methods, in which slamming, springing, and whipping are modeled using combined or implicit approaches. The relevant conclusions made from the application of these coupled methods are summarized with respect to the estimate of fatigue damage accumulation. Conclusions follow in Section 2.6.

As explained in Section 1.3, the literature review for loading and response of structures in waves is limited to thoroughly verified and validated methods. It will be shown in the following sections that the complexity and computational cost of more accurate seakeeping methods, or those that take into account higher-order terms in the boundary value problem, become increasingly restricted to time-domain forward models and thus less useful for efficient inverse methods based on measured strain time series. However, recently developed software, namely PanshipNL from the Maritime Research Institute of the Netherlands (MARIN) has shown to provide useful time-domain seakeeping results for combined springing, slamming, and whipping effects, and is thus a valuable tool for verification of an inverse model. However, linearization of the free surface is still used in this method, which will be outlined in Section 2.2.2.

2.1 An Overview of Ship Motions

At rest (in static equilibrium), the forces of gravity acting on a ship are balanced by normal hydrostatic forces on the hull surface. A constant stress distribution is present throughout the ship structure, which for slender ships is typically well-approximated as a distributed bending moment about the y axis. This is often referred to as a *still-water bending moment*. A ship in motion tends to oscillate as a rigid body in six degrees

of freedom: surge, sway, heave, roll, pitch, and yaw. While the rigid-body assumption can be useful for seakeeping calculations, the forces associated with rigid-body motion induce a stress state in the hull, and the effect of resulting deformations on the fluid motion is negligible. This description reflects a rigid-body, or quasi-static one-way coupling, approach to seakeeping calculations. A similar effect is observed locally due to slamming loads: for low impact velocities, in which the wetting time is long relative to the first natural period, water pressure acting on the hull results in quasi-static panel deformation.

In the past 50 years, it has become widely accepted that ships are also flexible, and that the resulting deformation can significantly influence the fluid motion, and vice-versa: a hydroelastic, or two-way coupling, effect is observed [6]. In relatively flexible ships such as an ultra-large container ship, the hydroelastic response can dominate the rigid-body motions when the frequency of excitation is close to that of a resonant hydroelastic mode. Similarly, at the local level, two-way fluid-structure interaction is observed during slam events if the wetting time is short relative to the first natural period: the panel will tend to vibrate, which results in radiated pressure waves in the surrounding fluid. Furthermore, the response to impulsive loads can propagate as global vibrations, a whipping response.

The description of ship motions as a superposition of rigid-body motions and elastic deformation is known as the *generalized modes* method, and is often credited to the seminal works of Bishop and Price [6] and Newman [7]. The method of generalized modes is particularly well-suited for linear seakeeping models as the rigid-body and flexible modes can be readily substituted into the body boundary condition, which will be explained in Section 2.2.1. The inclusion of elastic modes is also relevant for higher-frequency oscillations (whipping) resulting from impulsive (slamming) loads. The concept of quasi-static and hydro-elastic deformation at the local level due to slamming is often credited to Faltinsen [8].

In summary, the motions of floating ship and offshore structures can generally be decomposed into rigid-body (quasi-static) and flexible (hydro-elastic) modes. The total stress state at any point in time results from the superposition of quasi-static, hydroelastic, and still-water equilibrium stress states.

2.2 Steady-State

In this section, the exact boundary value problem is first formulated and then linearized to show how the global equation of motion is derived for a deformable floating body.

2.2.1 Exact Boundary Value Problem

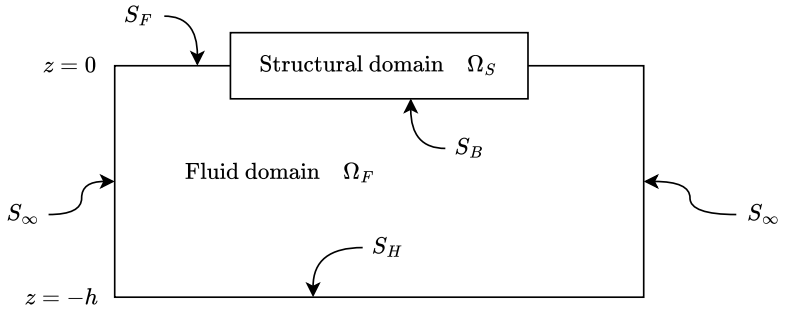


Figure 2.1: The simplified boundary value problem represented in two dimensions. Shown is the fluid free surface S_F, the boundary far from the moving body (to enforce uniqueness in the solution) S_∞, the body boundary S_B, the seabed S_H, the structural domain Ω_S, and the fluid Ω_F.

The fluid is assumed to be incompressible, irrotational, and inviscid. Surface tension is assumed negligible. A velocity potential Φ is required that satisfies these assumptions and whose gradient returns the velocity vector $\mathbf{v}(\mathbf{x},\ t) = \nabla\Phi$ at a point in space $\mathbf{x} = [x,\ y,\ z]$. The boundary value problem is formulated by a field equation in the fluid domain, kinematic and dynamic boundary conditions at the free surface S_F, and a kinematic boundary condition at the fluid-structure interface S_B. Conservation of mass requires that the divergence of $\mathbf{v}$ is zero for an incompressible fluid. The resulting field equation is simply the Laplacian of the velocity potential:

$$\nabla \cdot \mathbf{v} = \nabla^2 \Phi = 0 \quad \text{in the fluid domain} \quad \Omega_F \tag{2.1}$$

The fluid is irrotational when the vorticity vector is zero: $\boldsymbol{\omega} = \nabla \times \mathbf{v} = 0$, which is satisfied through the Cauchy-Riemann relations for a complex velocity potential Φ and corresponding stream function Ψ. A particle at the free surface is assumed to remain at the free surface. Mathematically, this is expressed as $z = \zeta(x, y, t)$ where $\zeta(x, y, t)$ is the wave elevation. Applying the material derivative to the difference $z - \zeta(x, y, t)$ and rewriting results in the kinematic free-surface boundary condition.

$$\zeta_t + \Phi_x \zeta_x + \Phi_y \zeta_y = \Phi_z \quad \text{on the exact free surface} \quad S_F \tag{2.2}$$

The fluid pressure follows from Bernoulli's equation, in which p_a is the atmospheric pressure, z_0 corresponds to the mean free surface, and Φ_t is the first time derivative of the velocity potential Φ:

$$p = -\rho \left(\Phi_t + \frac{1}{2} \left(\nabla \Phi \cdot \nabla \Phi \right) + g z_0 \right) + p_a \tag{2.3}$$

The dynamic boundary condition $p = p_a$ at the free surface takes the form

$$\Phi_t + \frac{1}{2} \left(\nabla \Phi \cdot \nabla \Phi \right) + g z_0 = 0 \quad \text{on} \quad z_0 = \zeta \tag{2.4}$$

which leads to an explicit equation for the free surface elevation as a function of the velocity potential and its first time derivative:

$$\zeta = -\frac{1}{g} \left(\Phi_t + \frac{1}{2} \left(\nabla \Phi \cdot \nabla \Phi \right) \right) \quad \text{on the exact free surface} \quad S_F \tag{2.5}$$

Taking the spatial derivative and substituting (2.5) into (2.2) results in a combined free surface condition for an unknown elevation $\zeta(\mathbf{x_0}, t)$:

$$\Phi_{tt} + 2 \nabla \Phi \cdot \nabla \Phi_t + \frac{1}{2} \nabla \Phi \cdot \nabla \left(\nabla \Phi \cdot \nabla \Phi \right) + g \Phi_{z0} = 0 \quad \text{on} \quad z_0 = \zeta \quad (S_F) \tag{2.6}$$

Two initial conditions are required because (2.6) is second order in time:

$$\Phi = \Phi_t = 0 \quad \text{for} \quad z_0 = 0, \; t < t_0 \tag{2.7}$$

t_0 is an arbitrary starting time. The body boundary condition is then established by setting the normal component of the fluid ($\nabla \Phi$) and body ($\mathbf{u}_t = [u_t, v_t, w_t]$) velocities equal at the body boundary S_B for an outward-facing normal vector $\mathbf{n}$ at point $\mathbf{x}$:

$$\nabla \Phi \cdot \mathbf{n} = \mathbf{v} \cdot \mathbf{n} = \mathbf{u}_t \cdot \mathbf{n} \quad \text{on} \quad S_B \tag{2.8}$$

The body velocity can include forward motion U. The far-field boundary condition on S_∞ imposes vanishing waves far away from the floating body:

$$\Phi, \; \Phi_t \to 0 \quad \text{as} \quad |\mathbf{x}| \to \infty \tag{2.9}$$

The boundary value problem has now been formulated using the field equation (2.1) in the fluid domain Ω_F, a combined free-surface boundary condition (2.6) on S_F, a body boundary condition (2.8) on the fluid-structure interface S_B, two initial conditions (2.7), and two far-field boundary conditions (2.9) on S_∞.

2.2.2 Linearization

The boundary value problem as derived in Section 2.2.1 cannot be readily solved for the velocity potential Φ. Linearization of the free surface condition, body boundary conditions, and the Bernoulli equation is performed to obtain a tractable problem. To do this, perturbation expansions are used. Assume the free surface has small slope, and that expansion of the potential and free-surface elevation in terms of a small parameter ϵ is justified [9]:

$$\phi(\mathbf{x},t) = \epsilon\phi^{(1)} + \epsilon^2\phi^{(2)} + \epsilon^3\phi^{(3)} + \mathcal{O}\left(\epsilon^3\right) \tag{2.10}$$

$$\zeta(x,y,t) = \zeta^{(0)} + \epsilon\zeta^{(1)} + \epsilon^2\zeta^{(2)} + \mathcal{O}\left(\epsilon^3\right) \tag{2.11}$$

To linearize the body boundary condition, the displacement $\mathbf{u}$ and normal vector $\mathbf{n}$ are expanded. Small motions are assumed, so oscillations of the body relative to the earth-fixed reference frame are of the first order ϵ^1. $\mathbf{R}^{(1)}$ is the first-order rotation matrix.

$$\mathbf{n} = \mathbf{n}^{(0)} + \epsilon\mathbf{n}^{(1)} = \mathbf{n}^{(0)} + \epsilon\mathbf{R}^{(1)}\mathbf{n}^{(0)} \tag{2.12}$$

$$\mathbf{u} = \epsilon\left(\mathbf{u}^{(1)} + \mathbf{R}^{(1)}\mathbf{n}^{(0)}\right) \tag{2.13}$$

The body boundary condition can then be expressed as:

$$\left(\epsilon\nabla\Phi^{(1)} + \epsilon^2\nabla\Phi^{(2)}\right)\cdot\left(\mathbf{n}^{(0)} + \epsilon\mathbf{n}^{(1)}\right) = \left(\epsilon\mathbf{u}_t^{(1)}\right)\cdot\left(\mathbf{n}^{(0)} + \epsilon\mathbf{n}^{(1)}\right) \tag{2.14}$$

To avoid evaluating the velocity potential at the instantaneous (accelerating) surface, a Taylor expansion is applied about the mean position, leading to the linearized first-order body boundary condition:

$$\nabla\Phi^{(1)}\cdot\mathbf{n}^{(0)} = \mathbf{u}_t^{(1)}\cdot\mathbf{n}^{(0)} \quad \text{on} \quad S_0 \tag{2.15}$$

By substituting expansions (2.10) and (2.11) into the field equation, boundary conditions, and initial conditions, a set of linear problems for each order of ϵ is obtained.

$$\nabla^2\Phi^{(1)} = 0, \quad \nabla^2\Phi^{(2)} = 0 \quad \text{in} \quad \Omega_F \tag{2.16}$$

The zero-order term (ϵ^0) in the dynamic free-surface boundary condition implies that the mean elevation is zero for all time:

$$g\zeta^{(0)} = 0 \quad \text{on} \quad S_F \tag{2.17}$$

The first (ϵ^1) and second (ϵ^2) order terms of the dynamic free-surface boundary condition are:

$$g\zeta^{(1)} + \Phi_t^{(1)} = 0 \qquad g\zeta^{(2)} + \frac{1}{2}\left(\nabla\Phi^{(1)}\cdot\nabla\Phi^{(1)}\right) + \Phi_t^{(2)} = 0 \tag{2.18}$$

Similarly, the first (ϵ^1) and second (ϵ^2) order terms of the kinematic free-surface boundary condition are:

$$g\Phi_z^{(1)} + \Phi_{tt}^{(1)} = 0 \qquad 2\nabla\Phi^{(1)}\cdot\nabla\Phi_t^{(1)} + g\Phi_z^{(2)} + \Phi_{tt}^{(2)} = 0 \tag{2.19}$$

The two first-order free surface conditions can be combined to obtain:

$$\Phi_{tt}^{(1)} + \Phi_z^{(1)} = 0 \quad \text{on} \quad S_F \qquad \Phi_n^{(1)} = \mathbf{u}_t^{(1)} \quad \text{on} \quad S_B \qquad \Phi^{(1)},\ \Phi_t^{(1)} \to 0 \quad \text{as} \quad |\mathbf{x}| \to \infty \tag{2.20}$$

The first-order linearized boundary value problem allows for decomposition of the velocity potential into a steady problem ($\overline{\Phi}$) for a constant forward speed U and a radiation-diffraction problem, which includes the potential due to an oscillating body in calm water Φ_R[1], the incident wave potential Φ_I, and the diffracted wave potential Φ_D in the ship-fixed reference frame:

$$\Phi = \overline{\Phi} + \sum_{k=1}^{N} \Phi_{Rk} + \Phi_I + \Phi_D \tag{2.21}$$

Only the incident, radiation, and diffraction potentials are considered. The pressure can be linearized by creating a perturbation expansion and substituting the three potentials into Bernoulli's equation:

$$\begin{aligned} p &= p^{(0)} + \epsilon p^{(1)} \quad + \epsilon^2 p^{(2)} + \mathcal{O}\left(\epsilon^3\right) \\ &= \rho g z + \epsilon \rho \Phi_t^{(1)} + \epsilon^2 \rho \left(\Phi_t^{(2)} + \frac{1}{2} \left(\nabla \Phi^{(1)} \cdot \nabla \Phi^{(1)} \right) \right) \end{aligned} \tag{2.22}$$

2.2.3 Forces

The fluid forces and moments acting on the floating body can be evaluated by integrating the normal component of the pressure p over the fluid-structure interface S_B, which consists of a mean part S_0 and oscillating part S_δ. An outward-facing normal vector $\mathbf{n}$ is assumed. For brevity, only the force expressions are shown in this subsection.

$$\mathbf{f} = -\iint_{S_B} p \cdot \mathbf{n} \, dS \tag{2.23}$$

The expansions of pressure and the normal vector are substituted into Equation 2.23 as follows:

$$\mathbf{f} = -\iint_{S_B} \left(p^{(0)} + \epsilon p^{(1)} + \epsilon^2 p^{(2)} + \mathcal{O}\left(\epsilon^3\right) \right) \cdot \left(\mathbf{n}^{(0)} + \mathbf{n}^{(1)} \right) \, dS \tag{2.24}$$

Collecting coefficients of the polynomial in ϵ leads to zero, first, and second-order fluid forces:

$$\mathbf{f} = \mathbf{f}^{(0)} + \epsilon \mathbf{f}^{(1)} + \epsilon^2 \mathbf{f}^{(2)} + \mathcal{O}\left(\epsilon^3\right) \tag{2.25}$$

The zero order elemental force term can be physically interpreted as a hydrostatic force.

$$\mathbf{f}^{(0)} = -\iint_{S_0} p^{(0)} \cdot \mathbf{n}^{(0)} \, dS = -\iint_{S_0} \rho g z \cdot \mathbf{n}^{(0)} \, dS \tag{2.26}$$

The first order force contains three parts: rotation-induced translation forces, contributions over the constant wetted surface S_0, and a negligible contribution over the instantaneous wetted surface S_δ:

$$\begin{aligned} \mathbf{f}^{(1)} &= -\iint_{S_0} \left(p^{(0)} \cdot \mathbf{n}^{(1)} + p^{(1)} \cdot \mathbf{n}^{(0)} \right) \, dS - \iint_{S_\delta} \left(p^{(0)} \cdot \mathbf{n}^{(0)} \right) \, dS \\ &= -\iint_{S_0} \left(\rho g z \cdot \mathbf{R}^{(1)} \mathbf{n}^{(0)} \right) \, dS - \iint_{S_0} \left(\rho \Phi_t^{(1)} \cdot \mathbf{n}^{(0)} \right) \, dS \end{aligned} \tag{2.27}$$

Second order drift forces contribute to the mean, but they are considered negligible for the purposes of this analysis [10]. The hydrostatic restoring coefficient matrix $\mathbf{C}$ can be found by substituting the vertical displacement w_i for mode i and the first-order normal vector $\mathbf{n}_j^{(1)}$ for mode j into Equation 2.27.

[1] Subscript $_k$ indicates a mode number, for example pitch or heave.

$$\mathbf{C}_{ij} = \rho g \iint_{S_0} w_i \mathbf{n}_j^{(0)} + w_i \mathbf{R}_j^{(1)} \mathbf{n}_j^{(0)} \, dS = \rho g \iint_{S_0} w_i \left(\mathbf{n}_j^{(0)} + \mathbf{R}_j^{(1)} \mathbf{n}_j^{(0)} \right) \, dS \tag{2.28}$$

The velocity potential consists of incident, radiated, and diffracted parts. Radiation forces are proportional to acceleration and velocity. The components $\mathbf{A}_{ij}$ and $\mathbf{B}_{ij}$ form the added mass and damping matrices ($\mathbf{A}$, $\mathbf{B}$). Assume the velocity potential is complex and oscillating in time with frequency ω such that $\Phi = \phi e^{i\omega t}$ and the first time derivative $\Phi_t = i\omega\phi e^{i\omega t}$.

$$\omega^2 \mathbf{A}_{ij} - i\omega \mathbf{B}_{ij} = -i\omega\rho \iint_{S_0} \phi_{Rj} \mathbf{n}_i^{(0)} \, dS \tag{2.29}$$

The incident wave force $\mathbf{f}_I$ is obtained by substituting a first-order velocity potential (neglecting the body boundary condition) into Equation 2.27. The diffraction force $\mathbf{f}_D$ is found by applying the following boundary condition:

$$\nabla\Phi_I \cdot \mathbf{n} + \nabla\Phi_D \cdot \mathbf{n} = 0 \quad \text{on} \quad S_0 \tag{2.30}$$

The added mass, damping, incident wave force, and diffraction force are all frequency-dependent; rigid body modes are coupled through the hydrodynamic and hydrostatic matrices. Numerical methods used for determining the coefficient matrices corresponding to each force term will be presented in Section 2.4. For now, the structural stiffness matrix ($\mathbf{K}$) and gravity restoring coefficients ($\mathbf{G}$) are left undefined.

2.2.4 Equation of Motion

If linear loading and response is assumed, as it was in the previous section, ship motions can be efficiently modeled in the frequency domain, where regular wave loading can be characterized by a spectrum and the response at each frequency is obtained using the following equation of motion, where the vector $\boldsymbol{\xi}(\omega)$ consists of modal amplitudes:

$$\left(-\omega^2 \left(\mathbf{M} + \mathbf{A}(\omega)\right) + i\omega\mathbf{B}(\omega) + \mathbf{C} + \mathbf{G} + \mathbf{K}\right) \boldsymbol{\xi}(\omega) = \mathbf{f}_I(\omega) + \mathbf{f}_D(\omega) \tag{2.31}$$

The forces and moments are applied to the accelerating reference frame, which is assumed to move with small amplitudes such that an earth-fixed reference frame is appropriate. For vessels sailing with forward speed, second-order errors while arise due to the displaced hull surface and additional flow around the vessel. To correct for these errors, the forward speed must be included in the body boundary condition on S_B.

Non-linear loading is not included in this equation because of the first-order restriction after linearization and the assumption of pure harmonic motion. Furthermore, the radiation, incident wave, and diffraction forces are solved in the earth-fixed reference frame (assuming zero speed). The loading and response captured in this equation is considered dominant for most fatigue assessments. The cyclic deformation due to wave loading in these conditions is often called springing.

Practically, the use of a rotation matrix and the rigid body motions when transforming the displacement and normal vectors means that the fluid forces are solved in a different reference frame. For example, if a ship is heaving and pitching with relatively large amplitude, such that the motions are significant (but still sufficiently small as to be considered linear using the small-angle approximation), the fluid pressures will necessarily be different at other parts of the hull when compared with pressures obtained when the ship is in equilibrium. If the ship is moving with forward speed, there is some steady-state heave and pitch due to the free-stream velocity of the fluid. Including the rotation matrix accounts for these deflections.

In this literature review, no forward speed is assumed (although it is often necessary for slamming to occur), and that the motions are small about the equilibrium position such that the forces can be solved in the earth-fixed reference frame. Clearly, slamming-induced whipping will be affected by radiation forces differently if part of the hull is entirely out of the water. However, it is assumed that the deformation of the hull is similar enough such that a wet mode shape can accurately approximate this deflection even if large amplitude motions are present.

2.3 Transient

In this section, various slamming models are first reviewed with respect to their assumptions, governing equations, and applicability. Then, the transient (time-domain) equation of motion is formulated based on the concept of impulse response, in keeping with the linear assumptions made in 2.2.

2.3.1 Slamming

A slam is defined as an impulsive load acting on a structure by the surrounding fluid, and is typically characterized by a rapid change in pressure. On floating structures, slamming can occur anywhere the surrounding fluid impacts the hull with relatively high velocity and short wetting time. Usually, the wet deck and bow experience the highest slamming loads due to the small deadrise angle β and high relative velocities. This literature review is not intended to improve the accuracy of slamming pressure estimation, nor is it intended to be a comprehensive review of all 1D, 2D, and 3D slamming models existing in literature. However, the outcomes from some studies, particularly those that validate analytical or numerical models with empirical results, provide insights into the importance of various phenomena as they relate to the local and global response of a ship to slamming. In particular, PanshipNL, a software which is available for use in the verification of models in this thesis, does not use a dedicated slamming model, but rather incorporates higher-order terms from the body boundary condition on the instantaneous wetted surface. In this section, the theory behind this method will be substantiated in the context of 2D methods which provide basic insights into the phenomena of slamming and its role on fatigue damage accumulation.

von Karman The first slamming model is generally attributed to von Karman [11], and is a momentum-based approach that was originally intended to determine the maximum fluid pressure exerted on the floats of a seaplane. In this model, the free-surface remains flat during impact, and the wetted length of the wedge can be determined from the geometry. Contributions to pressure from the jet and spray regions are neglected. The force is found by taking the derivative of the momentum.

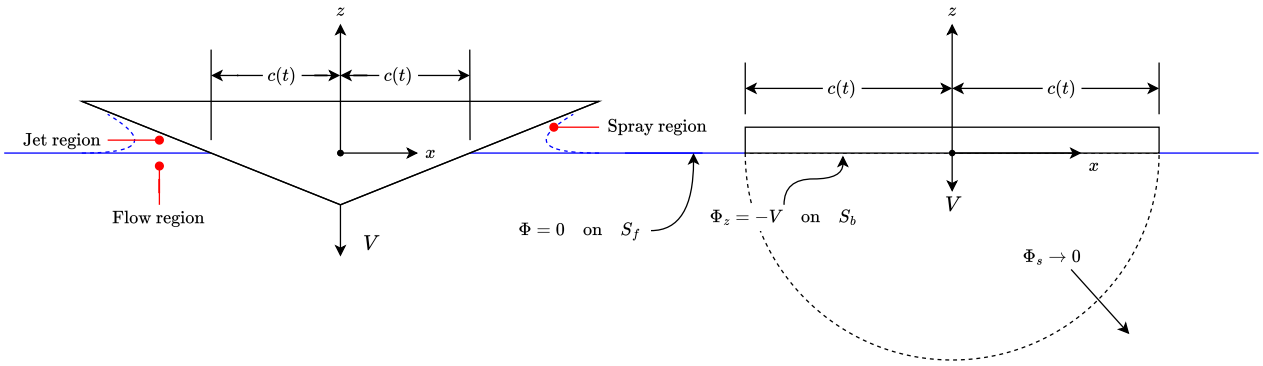


Figure 2.2: General slamming schematic for a 2D wedge with the associated boundary value problem for the Wagner model. Blunt 2D cross sections such as the wedge shown here can be roughly approximated by a flat plate with increasing width $c(t)$ corresponding to the wetted length of the 2D cross section.

Wagner Model Wagner [12] improved on the momentum-based approach of von Karman [11] by incorporating the jet region using a blunt-body approximation[2]. Wagner [12] assumed an incompressible, inviscid, and irrotational flow, satisfying Equation 2.1. The jet region is approximated using a submergence η, which can be related geometrically to the wetted length $c(t)$. The geometry is simplified to a flat plate of increasing width $(2c(t))$ using a Joukowski transformation, which yields a first-order boundary value problem, similar in form to that found in Section 2.2.2, for which the velocity potential Φ must be solved. Only the 2D domain is considered. Newman [13] provides an analytical solution as a function of the wetted length, Equation 2.32. The pressure acting on the flat plate can then be evaluated using Bernoulli's equation.

$$\Phi(x,z)|_{z=0} = -V\sqrt{c(t)^2 - x^2} + iVx; \quad \|x\| < c(t) \tag{2.32}$$

[2]For ships, a blunt body may be a flared bow with small deadrise angle β_d, radius R, or a flat plate.

Matched Asymptotic Expansions Cointe and Armand [14][3] improved on the model of Wagner [12] by evaluating pressure on the instantaneous wetted surface using a matched asymptotic expansion. To do this, the boundary conditions were linearized using perturbation expansions of non-dimensional parameters, and the boundary value problem was solved for both the inner (jet) and outer (flow) regions.

Generalized Wagner Model To address more complex geometries, particularly bodies with larger deadrise angles, Zhao and Faltinsen [16] evaluated the boundary value problem for the instantaneous wetted surface using linearized free-surface conditions, assuming the effect of gravity was negligible. The instantaneous free and wetted surfaces were estimated by Zhao and Faltinsen [16] using a discretization of the exact non-linear free surface elevation up to a point which was reasonably far from the body. Conservation of mass, energy, and momentum were checked. The velocity potential itself is solved using Green's second identity. No air pockets are allowed, so the range of validity for deadrise angles is limited to $4^\circ \leq \beta_d \leq 81^\circ$. Zhao and Faltinsen [16] note that for small deadrise angles, the approach of matched asymptotic expansions [14] provides a reasonable estimate of the pressures. In addition, flow separation was not addressed by Zhao and Faltinsen [16], and the jet region is truncated when solving the potential because as the jet becomes thin, its velocity increases and the resulting pressure will approach that of the atmosphere. In effect, the force contributing to the slamming problem is low. The potential function satisfying the boundary conditions and field equation is:

$$\phi(y_m, z_m) = \frac{1}{2\pi} \int_{S_\delta} \left[\nabla\phi(y_n, z_n) \cdot \mathbf{n}(y_n, z_n) \log r - \phi \nabla \log r \cdot \mathbf{n}(y_n, z_n) \right] \, dS \tag{2.33}$$

where $r = \sqrt{(y_m - y_n)^2 + (z_m - z_n)^2}$.

A second paper from Zhao [17] further developed the model from Zhao and Faltinsen [16] to handle bodies of arbitrary shape and flow separation. The same boundary value problem as in Zhao and Faltinsen [16] was used, but for geometries in which separation is likely (at knuckles or along convex surfaces), the thin jet region is reintroduced when the truncated free-surface boundary reaches such a point of separation. Again, gravity is neglected, which provides a reasonable result during initial impact, but affects the accuracy after flow separation [17].

Modified Logvinovich Model The Modified Logvinonvich Model (MLM) approaches wave-impact of a body by returning to the simplifying assumption first made by Wagner [12]: the geometry can be transformed into a flat plate, which simplifies the boundary value problem. Modifications are made to account for the non-uniform geometry. While this approach is quite fast because it uses the Wagner simplification, Tuitman [1] found that the MLM is not accurate enough for use in coupled seakeeping calculations because of the blunt-body assumption.

Hydroelasticity In the methods proposed by von Karman [11], Wagner [12], Cointe and Armand [14], Zhao and Faltinsen [16], and Zhao [17], the loading is quasi-static. Hydroelastic effects are not included, but were subsequently investigated by Faltinsen [18], Faltinsen et al. [19], Faltinsen [20] and Faltinsen [8]. For impacts in which the wetting time is small relative to the natural frequency of the first bending mode, hydroelasticity is important. In his PhD thesis, Bereznitski [21] endeavored to establish a more general criterion to determine the importance of hydroelasticity using 1D and 2D finite element models, coupling both the structural and fluid domains at their interface. Bereznitski [21] found that hydroelasticity is important for the analysis of slamming loads when the duration of impact divided by the first natural period of vibration is less than 2. Calculating the hydroelastic response using a Wagner model can be achieved in the time-domain using 4th-order Runge-Kutta integration of the state-space model which includes time-dependent modal added mass and damping coefficients. The local hydroelastic (orthotropically stiffened) plate response is typically dominated by the first and second local bending modes.

[3] Among others. Korobkin and Pukhnachov [15] provides a more thorough review of the literature on slamming models after von Karman [11] and Wagner [12]

2.3.2 Whipping

Whipping is broadly defined as the global transient response of a ship structure to some arbitrary impulsive load. In ships, slamming loads often dominate the whipping response. In literature, the slamming force $\mathbf{f}_S(t)$ is often included in the right hand side of the impulse equation of motion, and as a result, the same formulation can be used to capture both springing and whipping phenomena in the time domain. Since the global steady-state and transient responses can, in general, be evaluated in the time domain using the same equation of motion, this section will focus on illustrating the effects of slamming on the transient (whipping) motions and deformation in various ships. In the time domain, the equation of motion derived by Cummins [22] and Ogilvie T. [23] is commonly adopted, and takes into account the memory effect of radiation:

$$(\mathbf{M} + \mathbf{A}(\infty))\,\boldsymbol{\xi}_{tt}(t) + \mathbf{B}(\infty)\boldsymbol{\xi}_t(t) + (\mathbf{C} + \mathbf{K})\,\boldsymbol{\xi}(t) + \int_{-\infty}^{t} \mathbf{K}^{\mathbf{h}}(t-\tau)\boldsymbol{\xi}_t(\tau)\,d\tau = \mathbf{f}_I(t) + \mathbf{f}_D(t) + \mathbf{f}_S(t) \quad (2.34)$$

The convolution is performed on the matrix of impulse response functions using the frequency-dependent radiation potential which satisfies the linearized boundary value problem. The Fourier transform of the time-domain equation of motion is equivalent to the frequency-domain formulation. The benefit of Equation 2.34 is that transient forces such as those induced by slamming events can be readily substituted into the right hand side, provided the linearization steps performed in Section 2.2.2 are reasonably valid. For many large ships, the assumptions of small-amplitude motion are generally quite good, while the accuracy tends to break down in scale-model tests and for smaller vessels.

2.4 Numerical Methods

In order to arrive at the added mass and radiation potentials in the steady-state and transient equations of motion, the linearized boundary value problems as derived in Section 2.2 and 2.3 must be solved for the velocity potential Φ. The numerical procedure for doing this is known as the boundary element method, which is described in Section 2.4.1. Similarly, the hydroelastic response of a local structure to slamming loads requires a time-domain evaluation of the added mass and damping matrices. Ship structures are usually orthotropic and hierarchical. The ship response to loading can be approximated using the finite element method, which is explained briefly in Section 2.4.2. However, an accurate finite element model is typically large and can be computationally expensive. Therefore, modal reduction is often used. One common way to combine the finite and boundary element methods for ship structures is to use the method of generalized modes, which is covered by Section 2.4.3.

2.4.1 Boundary Element Method

To solve the boundary value problem for the radiation and diffraction potentials, the fluid-structure interface S_B is discretized. At each panel, a source is placed at its geometric center, the collocation point. First, the complex amplitude of the potential $\phi_j(x, y, z)$ with strength σ_j at a point (x, y, z) is considered for some mode j:

$$\phi_j = -\frac{\sigma_j}{4\pi r} \quad (2.35)$$

The complex potential Φ_j of a harmonic point source with frequency ω has the form:

$$\Phi_j = \mathrm{Re}\left[\phi_j e^{-i\omega t}\right] = \mathrm{Re}\left[-\frac{\sigma_j}{4\pi r} e^{-i\omega t}\right] \quad (2.36)$$

The complex potential at one panel is related to the source strength at the collocation point coordinates of another panel $\mathbf{x}_n$:

$$d\phi_j(\mathbf{x}_m) = -\frac{\sigma_j(\mathbf{x}_n)}{4\pi r} dS_0 \quad (2.37)$$

where r is the distance between point $\mathbf{x}_m$ and point $\mathbf{x}_n$. A Green's function can be found which satisfies the boundary conditions at $S(\infty)$, S_F, and S_0 [13][4].

$$\phi(\mathbf{x}_m) = \frac{1}{4\pi} \iint_{S_0} \sigma(\mathbf{x}_n)\, G(\mathbf{x}_m, \mathbf{x}_n)\; dS \tag{2.38}$$

By splitting the complex potential into radiation and diffraction components and applying the fluid-structure kinematic boundary condition at each panel, the source strengths σ_j can be found for every panel:

$$\begin{aligned} \nabla\Phi_I \cdot \mathbf{n} = -\nabla\Phi_D \cdot \mathbf{n} \implies \nabla\phi_I \cdot \mathbf{n} = -\nabla\phi_D \cdot \mathbf{n} \quad \text{(Diffraction)} \\ \nabla\Phi_R \cdot \mathbf{n} = \mathbf{u}_t \cdot \mathbf{n} \implies \nabla\phi_R \cdot \mathbf{n} = i\omega \mathbf{u} \cdot \mathbf{n} \quad \text{(Radiation)} \end{aligned} \tag{2.39}$$

The normal derivative of a complex potential ϕ at collocation point $\mathbf{x}_m$ is found by taking the normal derivative of the Green's function within the surface integral:

$$\nabla\phi(\mathbf{x}_m) \cdot \mathbf{n}(\mathbf{x}_m) = \frac{1}{4\pi} \iint_{S_0} \sigma(\mathbf{x}_n)\, \nabla G(\mathbf{x}_m, \mathbf{x}_n) \cdot \mathbf{n}(\mathbf{x}_n)\; dS \tag{2.40}$$

The equation above contains a singularity if $\mathbf{x}_m = \mathbf{x}_n$, which is apparent from the homogeneous solution of the Green's function in $\mathbb{R}^3$: $G = \dfrac{1}{r} = \dfrac{1}{\|\mathbf{x_m} - \mathbf{x_n}\|}$. To estimate the potential at this singularity, the limit as $r \to 0$ is evaluated on a half sphere S_r of radius r:

$$\begin{aligned} \nabla\phi(\mathbf{x}_m) \cdot \mathbf{n}^{(0)}(\mathbf{x}_m) &= \lim_{r\to 0} \left[\frac{1}{4\pi} \iint_{S_r} \sigma(\mathbf{x}_m)\, \nabla\left(\frac{1}{r}\right) \cdot \mathbf{n}(\mathbf{x}_m)\; dS_r \right] + \frac{1}{4\pi} \iint_{S_0} \sigma(\mathbf{x}_n)\, \nabla G(\mathbf{x}_m, \mathbf{x}_n) \cdot \mathbf{n}(\mathbf{x}_n)\; dS_B \\ &= -\frac{1}{2}\sigma(\mathbf{x}_m) + \frac{1}{4\pi} \iint_{S_0} \sigma(\mathbf{x}_n)\, \nabla G(\mathbf{x}_m, \mathbf{x}_n) \cdot \mathbf{n}(\mathbf{x}_n)\; dS_B \end{aligned} \tag{2.41}$$

The integral formulation can be rearranged as a system of linear equations with respect to the source strengths at panel j, which can be readily solved by inverting the matrix of coefficients.

$$\nabla\phi(\mathbf{x}_m) \cdot \mathbf{n}(\mathbf{x}_m) \approx -\frac{1}{2}\sigma(\mathbf{x}_n) + \frac{1}{4\pi} \sum_n \sigma(\mathbf{x}_n)\, \nabla G(\mathbf{x}_m, \mathbf{x}_n) \cdot \mathbf{n}(\mathbf{x}_n)\, S_n \tag{2.42}$$

$$\underbrace{\begin{bmatrix} -\frac{1}{2} & \cdots & A(\mathbf{x}_1, \mathbf{x}_n) \\ \vdots & \ddots & \vdots \\ A(\mathbf{x}_m, \mathbf{x}_1) & \cdots & -\frac{1}{2} \end{bmatrix}}_{\mathbf{A}} \begin{bmatrix} \sigma(\mathbf{x}_1) \\ \vdots \\ \sigma(\mathbf{x}_n) \end{bmatrix} = i\omega \begin{bmatrix} \mathbf{u}(\mathbf{x}_1) \cdot \mathbf{n}(\mathbf{x}_1) \\ \vdots \\ \mathbf{u}(\mathbf{x}_m) \cdot \mathbf{n}(\mathbf{x}_m) \end{bmatrix} \tag{2.43}$$

The matrix of coefficients $\mathbf{A}$ can be solved for both radiation and diffraction potentials.

$$\mathbf{A}_{mn} = \begin{cases} -\dfrac{1}{2} & \text{if} \quad \mathbf{x}_m = \mathbf{x}_n \\ \dfrac{1}{4\pi} \nabla G(\mathbf{x}_m, \mathbf{x}_n) \cdot \mathbf{n}(\mathbf{x}_n)\, S_n & \text{if} \quad \mathbf{x}_m \neq \mathbf{x}_n \end{cases} \tag{2.44}$$

Similarly, the body boundary condition for diffracted waves yields an equivalent set of homogeneous linear algebraic equations:

[4] Literature on efficient methods of computing the free-surface Green's function is abundant. Modeling steps will focus on the method provided by Newman [24] because it provides six-decimal accuracy throughout the full region of applicability, although other options are available [25, 26, 27, 28, 29, 30, 31, 32]

$$\begin{bmatrix} -\frac{1}{2} & \cdots & A(\mathbf{x}_1, \mathbf{x}_n) \\ \vdots & \ddots & \vdots \\ A(\mathbf{x}_m, \mathbf{x}_1) & \cdots & -\frac{1}{2} \end{bmatrix} \begin{bmatrix} \sigma(\mathbf{x}_1) \\ \vdots \\ \sigma(\mathbf{x}_n) \end{bmatrix} = \begin{bmatrix} -\nabla\phi_I(\mathbf{x}_1) \cdot \mathbf{n}(\mathbf{x_1}) \\ \vdots \\ -\nabla\phi_I(\mathbf{x}_m) \cdot \mathbf{n}(\mathbf{x}_m) \end{bmatrix} \tag{2.45}$$

The radiation and diffraction velocity potentials can be found for each collocation point by means of substituting the source strengths back into Equation 2.38 and evaluating the surface integral [33, 1].

$$\phi(\mathbf{x}_m) = \frac{1}{4\pi} \iint_{S_0} \sigma(\mathbf{x}_n) G(\mathbf{x}_m, \mathbf{x}_n) \, dS \approx \frac{1}{4\pi} \sum_n \sigma(\mathbf{x}_n) G(\mathbf{x}_m, \mathbf{x}_n) S_n \tag{2.46}$$

A known issue in this boundary element formulation is the presence of resonant fluid waves of the free surface which is bounded by S_0. The frequency of these resonant waves can be shifted to higher frequencies by means of introducing panels on the free surface itself. However, the Green's function contains a singularity when $\mathbf{x}_m$ or $\mathbf{x}_n$ is on the free surface. Malenica and Chen [34] proposes a downward shift of these lid panels by a small value, which depends on the surface-piercing structure's geometry, namely the overall length L and breadth B given a desired frequency range $\omega \in [0, \omega_{\max}]$:

$$z_{\max} \leq \frac{\tanh^{-1}\left(\frac{\pi g \sqrt{L^{-2} + B^{-2}}}{\omega_{\max}^2}\right)}{\pi\sqrt{L^{-2} + B^{-2}}} \tag{2.47}$$

The appropriate boundary condition on the bounded free surface S_F^* is:

$$-\frac{1}{2}\sigma(\mathbf{x}_m) + \int_{S_0 + S_F^*} \sigma(\mathbf{x}_n) \nabla G(\mathbf{x}_m, \mathbf{x}_n) \cdot \mathbf{n}(\mathbf{x}_n) \, dS = 0 \quad \text{for all} \quad \mathbf{x}_m \quad \text{on} \quad S_F^* \tag{2.48}$$

$$\begin{bmatrix} -\frac{1}{2} & \cdots & A(\mathbf{x}_1, \mathbf{x}_n) \\ \vdots & \ddots & \vdots \\ A(\mathbf{x}_m, \mathbf{x}_1) & \cdots & -\frac{1}{2} \end{bmatrix} \begin{bmatrix} \sigma(\mathbf{x}_1) \\ \vdots \\ \sigma(\mathbf{x}_n) \end{bmatrix} = \begin{bmatrix} \mathbf{0} \\ \vdots \\ \mathbf{0} \end{bmatrix} \tag{2.49}$$

The practical implementation of the boundary element method for an actual structure is outlined in the next section, which introduces the finite element method and its application in the current context.

Ship structures are often modeled using finite shell elements. A practical approach to implement the boundary element method and generalized modes involves using the exterior shell elements themselves for numerically solving the boundary value problem. Doing so avoids the geometric discrepancies introduced by different meshes, and simplifies the application of fluid pressures on the finite element model, since every exterior (wetted) shell corresponds to a collocation point, the pressure at which can be numerically evaluated using the procedure above. However, the number of wetted shell elements is typically quite large, justifying an approximation of the Green's function and its derivative. A comparison of methods [24, 29, 30, 25] shows that accuracy ranging from 3D to 6D (3 to 6 decimal places) can be achieved while significantly reducing computation time [31].

2.4.2 Finite Element Method

Ship and offshore structures are primarily constructed of slender elements such as rods, beams, plates, and shells. To model such structures numerically, the continuous structure is discretized into elements, which are connected by nodes. Displacements within the element and at each node are approximated using shape functions, which are defined for each element domain Ω_e. The goal of this method is to determine the weight of each shape function such that the summation of all shape functions results in a close approximation of the actual displacements [35, 36].

Consider an element on the discretized structure which is bounded by nodes. The displacement field within an element $\mathbf{u}$ can be calculated from the vector of nodal displacements $\mathbf{d}$ and a set of shape functions, which are organized as a matrix $\mathbf{N}$: $\mathbf{u} = \mathbf{N}\mathbf{d}$. The strain field $\boldsymbol{\epsilon}$ is obtained by differentiating the shape function matrix and multiplying the matrix of shape function derivatives with the nodal displacement vector. Here, a linear operator $\mathcal{L}$ is used. $\boldsymbol{\epsilon} = \mathbf{B}\mathbf{d} = \mathcal{L}\mathbf{B}\mathbf{d}$. Linear elasticity is assumed. The stress field is therefore related to the strains through an elasticity tensor $\mathcal{C}$ such that $\boldsymbol{\sigma} = \mathcal{C}\boldsymbol{\epsilon}$.

The elemental equation of motion can be obtained by invoking the stationarity principle $\delta\Pi = 0$ for a given functional Π for a set of state variables [36]. In this case, the functional Π is expressed as the total sum of kinetic and potential energy less the work applied:

$$\begin{aligned}\delta\Pi_e &= \delta T_e + \delta U_e - \delta W_e = 0 \\ &= \sum_{i=1}^{N} \left[\left(\frac{d}{dt} \frac{\partial T}{\partial \mathbf{d}_{i,t}} - \frac{\partial T}{\partial \mathbf{d}_i} \right) + \left(\frac{\partial U_e}{\partial \mathbf{d}_i} \right) - \mathbf{f_e} \right] \delta \mathbf{d}_i = 0\end{aligned} \tag{2.50}$$

The variational formula is based on Lagrange's equation of motion and the variation in kinetic co-energy, potential energy, and external work [37]. The term in brackets must vanish since an arbitrary displacement $\delta\mathbf{d}_i$ is used. The elemental mass $\mathbf{M_e}$ and stiffness $\mathbf{K_e}$ matrices relate the nodal displacement vector $\mathbf{d}$ to the kinetic T_e and potential U_e energy of each element Ω_e given a density ρ_e, which is defined for each element, and the elasticity tensor $\mathcal{C}$.

$$\begin{aligned} T_e &= \frac{1}{2} \int_{\Omega_e} \rho_e \mathbf{u}_t^T \mathbf{u}_t \, d\Omega = \frac{1}{2} \int_{\Omega_e} \rho_e \left(\mathbf{N}\mathbf{d}_t \right)^T \left(\mathbf{N}\mathbf{d}_t \right) \, d\Omega = \frac{1}{2} \mathbf{d}_t^T \mathbf{M_e} \mathbf{d}_t \\ \mathbf{M_e} &= \int_{\Omega_e} \mathbf{N}^T \rho_e \mathbf{N} \, d\Omega \quad \text{such that} \quad \frac{d}{dt} \frac{\partial T_e}{\partial \mathbf{d}_t} = \mathbf{M_e} \mathbf{d}_{tt} \end{aligned} \tag{2.51}$$

$$\begin{aligned} U_e &= \frac{1}{2} \int_{\Omega_e} \boldsymbol{\epsilon}^T \boldsymbol{\sigma} \, d\Omega = \frac{1}{2} \int_{\Omega_e} \left(\mathbf{B}\mathbf{d} \right)^T \left(\mathcal{C}\mathbf{B}\mathbf{d} \right) = \frac{1}{2} \mathbf{d}^T \mathbf{K_e} \mathbf{d} \\ \mathbf{K_e} &= \int_{\Omega_e} \mathbf{B}^T \mathcal{C} \mathbf{B} \, d\Omega \quad \text{such that} \quad \frac{\partial U_e}{\partial \mathbf{d}} = \mathbf{K_e} \mathbf{d} \end{aligned} \tag{2.52}$$

Elemental force vectors $\mathbf{f_e}$ are obtained by integrating the shape functions with the applied body $\mathbf{b}$ throughout the element domain Ω_e and traction $\mathbf{f}$ forces on the boundary Γ_e.

$$\mathbf{f_e} = \int_{\Omega_e} \mathbf{N}^T \mathbf{b} \, d\Omega + \int_{\Gamma_e} \mathbf{N}^T \mathbf{t} \, d\Gamma \tag{2.53}$$

2.4.3 Model Order Reduction

Solving the coupled hydroelastic problem using the boundary and finite element methods is exceedingly expensive, prohibitively so in the time domain. To obtain reasonable results in a shorter amount of time, model order reduction is required. The most common way to do this is with generalized modes, which are based on the dry natural modes of the finite element-based free vibration problem. Both the rigid-body and elastic modes are included. In this section, the concept of generalized modes will be introduced with the eigenvalue problem for an undamped finite element model. Then, the eigenvectors (modes) are substituted into the linearized (first order) boundary value problem to obtain the total velocity potential for each mode, which can be directly substituted into the linearized Bernoulli equation. A derivation of the modal added mass, damping, and hydrostatic matrices is presented afterwards. This section concludes with an overview of load-based modal order reduction techniques that can be used instead of the dry modes.

Dry Modes

Assume the equation of motion has been derived for a linear elastic finite element model with vector of time-dependent nodal displacements $\mathbf{u} = \mathbf{u}(t)$. The first approach seeks the solution to the linear free-vibration problem $\mathbf{M^s}\mathbf{u}_{tt} + \mathbf{K^s}\mathbf{u} = 0$ [35, 36]. The equation of motion can then be rewritten in the standard format for

eigenvalue problems: $\mathbf{Ah} = \lambda\mathbf{Ih}$ such that $\mathbf{M^{s}}^{-1}\mathbf{K^{s}u} = \omega^2\mathbf{Iu}$. The orthogonal eigenvectors $\mathbf{h}$ and associated eigenvalues $\lambda = \omega^2$ form the basis of the eigenvector matrix $\mathbf{H}$; the eigenvectors form the column space of $\mathbf{H}$. Then, the solution $\mathbf{u}$ can be rewritten in terms of a superposition of the modal shapes:

$$\mathbf{u} = \sum_{j=1}^{N} \mathbf{h}_j \xi_j = \mathbf{H}\boldsymbol{\xi} \tag{2.54}$$

where $\mathbf{h}_j$ are the columns (eigenvectors) of $\mathbf{H}$, and $\boldsymbol{\xi}$ is the vector of generalized modal coordinates. The eigenvectors are orthogonal, by definition. Modal mass and stiffness matrices are obtained using the matrix of eigenvectors:

$$\mathbf{M} = \mathbf{H}^T\mathbf{M^{s}H} \qquad \mathbf{K} = \mathbf{H}^T\mathbf{K^{s}H} \tag{2.55}$$

Generalized Modes

In the method of generalized modes, each mode shape $\mathbf{h}_j$ is substituted into the body boundary condition:

$$\nabla\Phi_{Rj} \cdot \mathbf{n} = \mathbf{h}_j \cdot \mathbf{n} \tag{2.56}$$

Incident wave and diffraction potential are solved using the same body boundary condition as in Section 2.2.2. Added mass and damping coefficients can be solved by means of substituting the radiation velocity potential into Equation 2.29 [7]. The generalized fluid force vector is given by Equation 2.57. Recall that only zero and first order forces are considered.

$$\begin{aligned} \mathbf{f^{s}} &= \sum_{\mathbf{e}} \left[-\iint_{\Omega_e} \mathbf{N_e}^T p \cdot \mathbf{n}\, d\Omega \right] \\ &= \sum_{\mathbf{e}} \left[-\iint_{\Omega_e} \mathbf{N_e}^T \rho g w \cdot \mathbf{R}^{(1)}\mathbf{n}^{(0)}\, d\Omega - \iint_{\Omega_e} \mathbf{N_e}^T \rho \Phi_t^{(1)} \cdot \mathbf{n}^{(0)}\, d\Omega \right] \end{aligned} \tag{2.57}$$

Coupled radiation coefficients are obtained by multiplying the assembled global force vector for mode j by the mode shape transpose $\mathbf{h}_i^T$, where $\mathbf{f}_{Rj}$ is the fluid force vector obtained using a radiation coefficient $\Phi_{Rj,t}$:

$$\omega^2\mathbf{A}_{ij} - i\omega\mathbf{B}_{ij} = \mathbf{h}_i^T\mathbf{f}_{Rj}^{\mathbf{s}} \tag{2.58}$$

Similarly, the hydrostatic restoring coefficients are obtained from the following equation, where $\mathbf{f}_{Cj}^{\mathbf{s}}$ is the hydrostatic restoring force vector obtained from the zero-order pressure term $\rho g w_j \cdot \mathbf{n}$:

$$\mathbf{C}_{ij} = \mathbf{h}_i^T\mathbf{f}_{Cj}^{\mathbf{s}} \tag{2.59}$$

Diffraction and incident wave potentials are multiplied by each mode shape transpose, but are only defined for the static structure. Here, the force vectors are obtained using the radiation and diffraction potentials Φ_I and Φ_D:

$$\mathbf{f}_I + \mathbf{f}_D = \mathbf{H}^T\mathbf{f}_I^{\mathbf{s}} + \mathbf{H}^T\mathbf{f}_D^{\mathbf{s}} \tag{2.60}$$

Some authors contend that gravity should be included in the matrix of restoring coefficients [38, 1, 39, 7]. Doing so would lead to gravity force coupling between modes due to rotations. One option involves the use of $\mathbf{R}^{(1)}$, the first-order rotation matrix:

$$\mathbf{f}_{Gj}^{\mathbf{s}} = \sum_{\mathbf{e}} \left[\left(\mathbf{R}_j^{(1)}\right)^T \iint_{\Omega_e} \rho_e g \mathbf{N_e}^T \mathbf{k}\, d\Omega \right] \tag{2.61}$$

The restoring coefficients due to gravity $\mathbf{G}_{ij}$ could then be expressed after assembly as:

$$\mathbf{G}_{ij} = \mathbf{h}_i^T \mathbf{f}_{Gj}^{\mathbf{s}} \tag{2.62}$$

Finally, the mass and stiffness matrices are reduced in order using the mode shape matrix $\mathbf{H}$ to obtain the final equation of motion:

$$(\mathbf{M} + \mathbf{A}(\infty))\,\boldsymbol{\xi}_{tt}(t) + \mathbf{B}(\infty)\boldsymbol{\xi}_t(t) + \int_{-\infty}^{t} \mathbf{K}^{\mathbf{h}}(t-\tau)\boldsymbol{\xi}_t(\tau)\,d\tau + (\mathbf{C} + \mathbf{G} + \mathbf{K})\,\boldsymbol{\xi}(t) = \mathbf{f}_I(t) + \mathbf{f}_D(t) + \mathbf{f}_S(t) \tag{2.63}$$

This equation can be expressed either in the frequency domain or as the impulse equation of motion[5]. Recall the assumptions of small-amplitude motions, linear first-order waves, zero-speed, and the substitution of eigenvectors into the boundary value problem to obtain the radiation, hydrostatic restoring, and coupled gravity coefficients. The procedure outlined in this section approximates the divergence and gradient terms in the hydrostatic restoring matrices [7, 42, 38] to the first order, meaning mode shapes that correspond to a reduced submerged volume could be coupled with heave motion (for example).

Load-Based Modes

While the superposition of a sufficient number of dry mode shapes can reproduce the nodal response obtained using a direct method, some structures can be more efficiently modeled using load-based modes, or Ritz vectors [35, 43, 44, 45, 46, 47]. Load-based mode shapes can improve the accuracy for a given number of mode shapes when a known load distribution dominates the response [48]. Instead of solving the free vibration problem, the nodal displacement vector $\mathbf{u}$ is first solved using the equation of static equilibrium given some applied force vector $\mathbf{f}$: $\mathbf{h} = \mathbf{K}^{-1}\mathbf{f}$. The resulting vector constitutes the first mode shape in the matrix $\mathbf{H}$. The other mode shapes are solved through an iterative procedure, which is omitted from this literature review for brevity (see Cook et al. [35] for further reading). For free-floating structures excited by spatially-varying wave loads and restrained by hydrostatic restoring forces, the solution of $\mathbf{h} = \mathbf{K}^{-1}\mathbf{f}$ poses a problem: uniqueness is not satisfied. While some authors have shown that imposing a small constant multiple of the mass matrix $\mathbf{M}$ can yield a reasonable estimate of the first Ritz vector, this is not necessarily a stable method [47, 46].

2.5 Models

Literature about models that couple steady-state (springing) and transient (slamming, whipping) loading and response in an efficient manner is limited. Three notable methods were found: a fully-coupled springing, slamming, and whipping formulation that takes into account large amplitude motions [49], van Walree et al. [50], and Malenica et al. [51]. The three approaches will be discussed in this section. Only the second method, from Van Walree et al. [52], is available for verification. Conclusions will be drawn from the numerical results from each method as they relate to inverse methods.

Fully Coupled Springing, Slamming, and Whipping (Tuitman) As was shown in Section 2.2.4, the linearized frequency domain equation of motion can be expressed using constant hydrostatic restoring and frequency-dependent added mass and damping coefficients, mass and stiffness matrices from the finite element model, and external (linear and non-linear) wave forces. The time-domain formulation can be obtained by performing a convolution of the modal velocity vector and the matrix of impulse response functions, which are derived from the frequency-dependent linear radiation damping coefficients. In both the frequency- and time-domain formulations, any modal basis can be used for model order reduction, but generalized modes (solutions of the finite element eigenvalue problem) are typically adopted. In Section 2.3.1, it was noted that no efficient computational model exists for determining 3D slamming loads. To develop an efficient model that couples springing, slamming, and whipping loading and response, Tuitman and Malenica [49] used a modified version of the impulse equation of motion to account for large-amplitude motions, and

[5] Equations of similar but equivalent form are found in literature [40, 41]

2D quasi-static slamming models (Generalized Wagner and Modified Logvinovich) in a fourth-order Runge-Kutta time stepping regime with kinematic constraints applied to the rigid-body motions. Hydrostatic and hydrodynamic loads are solved in the most convenient (unsteady, accelerating) body-fixed reference frame and translated to the steadily-translating coordinate system using Euler angles.

HOMER (Bureau Veritas) Malenica et al. [51] further developed the method developed by Tuitman and Malenica [49], but solves the hydrostatic and hydrodynamic forces in the steadily-translating reference frame using Equation 6.30 [22, 53]. The Generalized Wagner Model is adopted based on the recommendations outlined by Tuitman and Malenica [49]. The dry natural modes are substituted into the boundary value problem using the generalized modes approach. It is unclear from the literature how forward speed is taken into account; it is assumed that the fluid forces are solved in the steadily-translating reference frame based on a suitable transient Green function. Stresses at local structural details are solved for using a top-down approach, in which modal displacements from the coarse structural mesh are applied to a finer mesh locally; the details of this procedure are found in Sireta et al. [54] and Malenica et al. [39]. Modal convergence is achieved by separating the response into quasi-static and elastic components. The generalized modes framework [6, 42, 7] is suitable for any floating structure, and by extension, the method of Malenica et al. [51] is as well.

PanshipNL (MARIN) The third method that couples springing, slamming, and whipping loading and response adopts a different approach based on the work of Lin and Yue [55], a time-domain large-amplitude ship motion method. Instead of solving for the frequency-domain linear radiation added mass and damping coefficients as a means of formulating the impulse equation of motion, the exact body boundary condition is satisfied on the instantaneous wetted surface of the moving body while the free-surface boundary conditions are linearized. The problem is solved using a transient free-surface Green function on the submerged hull, which has an instantaneous wetted surface. In this way, slamming forces are implicitly captured, because the same body boundary condition is used in the Generalized Wagner method for a 2D impact problem. In particular, Van Walree et al. [52] explains that by integrating pressure over the instantaneous wetted panels in the Bernoulli equation, impulsive loads (slamming) is implicitly taken into account. Zhao and Faltinsen [16] and Van Walree et al. [52] apply the same free-surface boundary conditions and evaluate Bernoulli's equation the instantaneous wetted surface to the same order. Therefore, reasonable 3D quasi-static slamming load accuracy can be expected when the jet region is neglected. However, it is worth noting that the structural model used by Van Walree et al. [52] is lower-order: a 1D finite element model is adopted, which uses the ship sectional properties in a coupled beam model including bending, extension, and (warping) torsion [56][6]. The translated, rotated, and deformed finite element model is extrapolated to the hydrodynamic mesh based on the nodal displacements and velocities at each ship section. For this reason, it is impractical to directly evaluate structural stresses from the nodal results of the 1D finite element model. Instead, an application of the hydrodynamic pressures as solved using the transient Green's function and (extrapolated) nodal accelerations at each point in the 3D finite element model is suggested as a reasonable approximation of the response. Clearly, local hydroelastic effects cannot be accurately captured because the 1D finite element model does not take local geometry into account. In addition, some physics of slamming, such as the jet and spray regions, will not be captured because of the linearized free surface condition imposed. In other words, waves are assumed linear to the first order, only. The higher wave steepness inherent to higher-order terms that could possibly capture wave pile up due to slamming is not included. Furthermore, only incompressible, irrotational, and inviscid fluid is assumed. Compressible behavior due to air entrapment, wave-slap slamming, and green loading is omitted. Assessing the net result in terms of accuracy is difficult *a priori*, but it can be concluded that only global effects can be modeled here.

Summary While only the software from MARIN [52] is available for use in this thesis, it is worthwhile to compare the assumptions to those made by Tuitman [1] and Malenica et al. [51], both of whom couple generalized modes and 2D slamming models. Two points are important:

1. Generalized modes cannot capture local quasi-static and hydroelastic slamming effects unless an unreasonably higher number of mode shapes is included in the analysis. Deformation at other points in the hull may be inaccurate as a result.

[6]The (warping) torsion model has not been verified or validated by MARIN. For this reason, torsion will not be evaluated numerically in this thesis.

2. 2D slamming models can take into account hydroelasticity, but 3D effects are missing. Evaluating (rotated) slices of a flared bow allows for an improved estimate of the (quasi-static or hydroelastic) slamming loading and response, but the coupled model is still highly sensitive to global motions such as surge oscillations and forward velocity [1]. One benefit is that computational cost is significantly reduced, since the instantaneous wetted surface is not evaluated for each time step as done in Van Walree et al. [52].

Model testing is often considered for validating time domain hydroelastic programs. One challenge in the numerical approximation of scale models is that the linearized assumptions, especially for vessel motions and waves, are not necessarily valid at small scale, and significant errors can be observed [1]. Furthermore, local effects cannot be captured based on currently available methods; flexible models are under development, but scaling effects still pose a considerable challenge [57]. Due to the amount of time required to set up a physical scale model, and the challenges mentioned above, model testing will not be considered in the scope of this thesis project.

2.6 Conclusions

In this chapter, the loading and response of ship structures was briefly reviewed with an emphasis on computationally efficient forward models. The chapter began with the exact boundary value problem and linearization. The equations of motion for steady-state loading and response were presented in both the frequency and time domains based on Cummins [22] and Ogilvie [53]. The various hydrostatic and hydrodynamic components in the equation of motion were derived based on linearization of the boundary value problem. Transient effects were addressed in the following section by presenting the foundational slamming models used in literature and the assumptions that differentiate the various models. Global slamming-induced transient effects (whipping) were acknowledge by means of numerical and empirical examples from literature. The following section aimed to contextualize the boundary value problems and equations of motion in terms of efficient numerical models, namely the boundary and finite element methods. The left hand side of the impulse equation of motion was derived using these numerical methods. Finally, three relatively recent forward models that couple steady-state and transient effects for actual ships were summarized.

To bring the conclusions from this chapter into the context of estimating fatigue damage, some additional remarks are necessary. With regard to global loading, it is evident that limited forward models exist which properly couple springing, slamming, and whipping in both a computationally effective and accurate way, particularly for the slamming loads. To the author's knowledge, there is no forward model available, either in literature or implemented as software, which accurately captures both local and global hydroelastic loading and response using a 3D finite element model composed of 2D shell elements. As a result, this thesis must have split focuses: global hydroelastic effects can be modeled reasonably accurately using a forward model (PanshipNL from MARIN [52], for example), and local hydroelastic effects can be approximated using the Wagner (not generalized) model of plate-wave impact. The global effects are probably the most relevant for present problems related to preventive maintenance due to accumulated fatigue damage, but it is also important to understand how fatigue damage can be estimated locally at the location of high slamming pressures. Both global and local effects can be evaluated using the finite element method by estimating nodal forces and the response using a suitable modal decomposition.

Chapter 3

Fatigue in Welded Joints

The cyclic loading and response of ship and offshore structures in a fluid environment contributes to fatigue, a local, progressive, structural damage mechanism introducing fracture [58]. Four dimensions are often referenced to characterize fatigue physics: material, geometry, loading and response, and environment [59]. In this literature review, only the loading and response dimension is critically examined as a research subject. Fatigue resistance, stress assessment concepts, and damage accumulation models are not exhaustively reviewed, as the structural model is assumed to be linear elastic and the objective of this thesis is to develop an inverse estimation method, the output of which can be used by any combination of fatigue assessment concepts.

This chapter is outlined as follows: Section 3.1 describes four stress assessment concepts in increasing order of accuracy, complexity, and computational cost. Section 3.2 covers the basic principles of fatigue resistance, including cycle number classifications, the Wöhler (SN) curve, and linear and random fatigue limit models. In Section 3.3, linear and non-linear damage accumulation models are briefly reviewed.

3.1 Assessment Concepts

In a structural health monitoring system, the far-field stress components can be used as input to estimate damage accumulation in welded structural details. The fatigue assessment concepts, or damage criteria, can be classified based on the global and local geometry of the structural detail, whether the material is cracked or intact, the physical property considered (stress, strain, or energy), and the input type (point, line, or area / volume) [60]. In this section, the Nominal Stress Concept (NSC), Hot Spot Structural Stress Concept (HSSSC), Effective Notch Stress Concept (ENSC), and Total Stress Concept (TSC) are discussed. Particular emphasis is placed on the assumptions made with respect to material parameters, computational efficiency, and their applicability within a time-domain fatigue damage accumulation estimation framework. The accuracy (scatter) of each concept and its relevance for condition-based maintenance is also stressed.

3.1.1 Nominal Stress

The NSC is a global approach which uses the nominal stress range $S_n = \Delta\sigma_n$ as a basic point criterion (a linear intact geometry parameter) for Medium Cycle Fatigue (MCF) and High Cycle Fatigue (HCF) welded joint resistance. In the NSC, it is assumed that most of the structural detail's lifetime N is related to crack initiation, as opposed to crack growth. The shape and size of the specimen must be taken into account to select the appropriate SN curve. While an infinite number of theoretical geometries exist, NEN [61] and Hobbacher [62] limit the possible FATigue (FAT) classes to 80.

When estimating fatigue damage in a ship structure using sparse strain measurements, the NSC is attractive for its low computational efficiency and concept complexity. However, accuracy is sacrificed because S_n is a point criterion and size effects induced by the local stress gradient are not explicitly taken into account. If the structural detail does not closely match a FAT class description, corrections for the stress concentration must be determined. In addition, it can be difficult to define the criterion S_n in a complex structure because the local stress state can be multiaxial, and large gradients can exist close to the welded joint.

3.1.2 Hot Spot Structural Stress

While the NSC is a point-based criterion that does not include local stress gradient effects, the HSSSC includes local structural detail information by means of the equivalent equilibrium far-field stress distribution [63]. The HSSSC range $S_s = \Delta\sigma_h$ is a linear elastic intact geometry parameter assuming the major part of life time N is related to crack initiation rather than crack growth [59]. The HSSSC damage criterion S_s is related to S_n through the structural Stress Concentration Factor (SCF) K_s: $S_s = K_s S_n$ [64]. Engineering judgment is required to determine which of the four accepted approaches should be used to evaluate the SCF: linear or non-linear surface extrapolation, a sub-surface virtual node, or through-thickness linearization. Structural details can be classified as load-carrying or non-load-carrying, which reduces the number of required FAT classes to two. While there is no explicit rule that governs the applicability of a load-carrying or non-load-carrying approach, the extent to which a weld is load-carrying can be quantified using a finite element model through the parameter C_{bw}, which scales the structural stress to obtain the weld load-carrying bending component [65]:

$$\sigma_{bw}\left(\frac{r}{t_p}\right) = \sigma_s C_{bw}\left[2\left(\frac{r}{t_p}\right) - 1\right] \quad \text{for all} \quad \left(\frac{r}{t_p}\right) \quad \text{such that} \quad 0 \leq \left(\frac{r}{t_p}\right) \leq 1 \tag{3.1}$$

One critical limitation of using the HSSSC is that only weld toe fatigue damage is included [64]. Since cracks can initiate at either the weld toe or root in a ship structure, estimating fatigue damage accumulation at fatigue-sensitive details throughout the entire structure requires an additional stress concept. In addition, relative size effects are not explicitly included, and require a finite element model-based correction which introduces additional sources of error (mesh type and resolution).

3.1.3 Effective Notch Stress

The ENSC is a local intact geometry stress-based approach based on line criteria and, in contrast with the NSC and HSSSC, explicitly accounts for the structural detail size and shape. The ENSC assumes a small notch radius ($\rho \to 0$) and that the peak fatigue resistance criterion $S_{\max} = \Delta\sigma_{\max}$ would be too conservative, since a stress singularity is introduced by the notch. A presumed crack path is assumed. An effective notch stress estimate $S_e = \Delta\sigma_{\text{avg}}$ can be obtained by averaging along the presumed crack path over a micro- and meso-structural length ρ^*:

$$\sigma_{\text{avg}} = \frac{1}{\rho^*}\int_0^{\rho^*} \sigma_n\left(\frac{r}{t_p}\right) dr \tag{3.2}$$

To incorporate the notch stress gradient contribution, a presumed radius ρ^* is formulated, then artificially enlarged by a support factor s, which takes geometry and loading into account: $\rho_f = s\rho^*$. The effective notch radius is the sum $\rho_e = \rho + \rho_f$. The notch stress range is defined by the effective radius of the original geometry $S_e = \Delta\sigma_e = \Delta\sigma_{\text{avg}} = \delta\sigma_{\max}(\rho_e)$ [66, 67, 59]:

$$S_e = \Delta\sigma_e = 2\sigma_e = 2K_f\sigma_s \tag{3.3}$$

Since size and shape effects are explicitly included, only one fatigue resistance curve is needed. The International Institute of Welding specifies one reference radius ($\rho_r = 1$ mm) and a minimum base plate thickness ($t_p \geq 5$ mm) for both weld toe and root notches. The formulation of this distribution is semi-empirical, and takes into account both symmetric and non-symmetric welds. Because the weld geometry causes a local change in stiffness and shift in neutral axis, the weld itself is load-carrying and quantified by the parameter C_{bw}. It is assumed that the structural stress is modified by the local notch distribution through this parameter, and that the product $\sigma_s C_{bw}$ is a linear superposition of a normal force and bending moment-induced structural field stress components:

$$\sigma_s C_{bw} = \sigma_m C_{bm} + \sigma_b C_{bb} \tag{3.4}$$

The coefficients C_{bm}, C_{bb}, and C_{bw} can be determined using nodal forces and moments from a finite element solution, or by using parametric fitting functions [68]. Thus, the ENSC incorporates local information, but

at the cost of increased setup complexity. However, once the nodal forces and moments (or coefficients of the parametric fitting functions) are obtained, the application is efficient.

3.1.4 Total Stress

The TSC further improves on the ENSC by incorporating stress gradients over the full thickness; crack growth is controlled during both zone 1 crack initiation and zone 2 steady crack growth stages, but does not extend into zone 3 [60]. Cyclic loading and response turns the SCF K into a crack growth-driving force ΔK (a Stress Intensity Factor (SIF)). In this way, more fatigue strength similarity is obtained. The TSC comprises a total stress damage area-equivalent line criterion S_t. The benefit of such a method is that only one S-N curve is required, local dimensional variations are included, and size effects are explicitly taken into account.

3.2 Resistance

Fatigue damage is often classified by cycle number N: Low Cycle Fatigue (LCF) ($N = \mathcal{O}(10^1 \dots 10^4)$), MCF ($N = \mathcal{O}(10^4 \dots 10^6)$), HCF ($N = \mathcal{O}(10^6 \dots 10^7)$), and Very High Cycle Fatigue (VHCF) ($N = \mathcal{O}(10^7 \dots 10^9)$) [62, 59, 69]. Fatigue resistance is often represented by a Wöhler curve, which relates a constant-amplitude stress S to the number of cycles N [70] on a $\log - \log$ scale. In ship and offshore structures, the far-field response spectrum is predominantly linear elastic, meaning MCF and HCF is most important for design. Structural strain can be adopted if elastoplasticity is important, particularly in the case of LCF [59, 71]. A log-log linear $N(S)$ relationship is observed for MCF and HCF; a semi-empirical Basquin model is adopted [72]:

$$\log(N) = \log(C) - m\log(S) \tag{3.5}$$

In such a linear model, Variable Amplitude (VA) loading primarily affects the fatigue strength C, while a minimal effect is observed on the slope m. A bilinear Basquin formulation is used in guidelines [73], standards [61], and classification notes [69] if a finite slope is observed for both MCF and HCF regions [72]. A 5-parameter formulation could be adopted for a more gradual MCF-HCF transition.

$$\begin{aligned} \log(N) &= \log(C) - m\log(S) - \left[\left(\frac{m}{m_t}\right) - 1\right] \\ &= \log\left[1 + \exp\left(\log(S) - \log(S_t)\right)^{-m_t}\right] \end{aligned} \tag{3.6}$$

Random fatigue limit models also exist in literature for constant-amplitude loading to account for threshold stresses, below which no damage is accumulated [72]. Examples include the ordinary, bilinear, and generalized random fatigue limits. A more thorough explanation of the benefits and drawbacks to each approach can be found in the Master's thesis by Deul [74].

An infinite number of possible structural details exist in a welded structure [59]; therefore, a model which takes into account local details (for example, geometry near the weld and material properties) can help reduce the number of required fatigue resistance (SN) curves. The effective notch stress concept takes both local structural detail geometry and material parameters into account, which reduces the number of required SN curves to one.

SN curves can be obtained from a series of failure and run-out points from small, large, or full-scale fatigue tests. For example, a linear Basquin-type single-slope curve can be formed by obtaining the log-likelihood function L for a log-normal based lifetime distribution and maximizing the likelihood function with respect to the SN curve parameters C, m, and S (Equation 3.5). The strength scatter index is a measure of the inference or quality of the fatigue lifetime prediction, and is defined as $T = 1 : \left(\frac{S_{n,R10}}{S_{n,R90}}\right)$.

3.3 Damage Accumulation Models

The wave loading and response of ship and offshore structures leads to variable amplitude stress time series at structural details. In this section, conservative linear and non-linear damage accumulation models are presented with emphasis on the relevance for fatigue damage estimation.

The most commonly used linear fatigue damage accumulation model is based the Palmgren-Miner hypothesis that the number of applied loading cycles expressed as a percentage of the number to failure at a given stress level defines the proportion of useful life expended [75]. In this hypothesis, failure is defined as the initiation of a crack (consistent with the linear elastic assumption) which occurs when a maximum amount of work is performed on the structural detail. Furthermore, Miner [75] assumes a sinusoidal loading signal.

$$D = \sum_{i=1}^{n} \frac{n_i}{N(\sigma_i)} \leq 1 \tag{3.7}$$

where D is the linear accrued damage, n is the number of stress cycles, $N(\sigma_i)$ is the number of cycles until failure for a given stress level σ_i. Rainflow counting is one method of assessing the fatigue damage under variable-amplitude cyclic loading [76]. $N(\sigma_i)$ is related to the SN curve, where k and m are material-specific parameters.

$$N(\sigma_i) = \frac{k}{\sigma_i^m} \tag{3.8}$$

The algorithm proposed by Rychlik [76] partitions the temporal signal based on a discrete set of stress blocks, defined by a mean σ_m and range $\Delta\sigma$. A spectrum can be created for the number of cycles accumulated in each stress block: $n_i = n(\Delta\sigma_i)$. Often, a probability density function is fitted to the histogram; a Weibull distribution is typically used in this case [77]:

$$f(\Delta\sigma) = \frac{h}{q}\left(\frac{\Delta\sigma}{q}\right)^{h-1} \exp\left[-\left(\frac{\Delta\sigma}{q}\right)^{h}\right], \quad \Delta\sigma \geq 0 \tag{3.9}$$

Provided the continuous function $f(\Delta\sigma)$, the damage D can be estimated by evaluating the integral:

$$D = \int_0^{\infty} \frac{n \cdot f(\Delta\sigma)}{N(\Delta\sigma))}\, d\Delta\sigma \tag{3.10}$$

The creation of a histogram discards the effect of mean values, which is known to affect the fatigue life. Incorporating the mean stress effect thus improves the estimate. To this end, Walker's mean stress model incorporates the mean σ_m, range $\Delta\sigma$, and ratio $R = \sigma_{\min}/\sigma_{\max}$ using a material-dependent parameter $\gamma \in [0.3, 1]$[1] [78]:

$$\Delta\sigma_{\mathrm{e}} = \Delta\sigma^{\gamma}\sigma_{\max}^{(1-\gamma)} = \frac{\Delta\sigma}{(1-R)^{1-\gamma}} \tag{3.11}$$

In a stress time series, the ratio R varies for each cycle. The integral can be evaluated using the gamma function Γ:

$$D = \frac{f_0 T}{C}\left(8m_0\right)^{m/2}\Gamma\left(1+\frac{m}{2}\right) \tag{3.12}$$

The effective stress range can then be substituted into Equation 3.10.

[1] Recent studies show that for Mode-I loading, the material dependent parameter γ is closer to 0.9 [68, 72]

3.4 Conclusions

In this chapter, fatigue resistance, assessment concepts, and damage accumulation models have been reviewed with a particular emphasis on applicability in a time-domain fatigue damage accumulation estimation framework. Since the combination of steady-state (springing) and transient (slamming, whipping) loading introduces a variable-amplitude stress time series with a possible non-zero mean shift and high stress range amplitudes, previous authors have concluded that the ENSC combined with a mean-stress corrected variable-amplitude loading damage accumulation model provides a sufficient balance between scatter, generality, and computational efficiency.

Based on the number of required SN curves and scatter indices of the NSC, HSSSC, ENSC, and TSC [72], it is clear that a TSC-based fatigue assessment would be the logical choice for a damage estimation framework. However, the complexity inherent to the TSC, namely that attributed to estimating zone 3 crack growth, renders the concept too complex for estimating fatigue damage accumulation in all sensitive hot spots in a ship structure. Therefore, the ENSC is a suitable alternative, especially considering the relatively small increase in scatter according to the fatigue resistance curves provided by Qin et al. [72], a conclusion also reached by Deul [74] in her MSc thesis. Of course, as explained in the introduction to Chapter 3, by estimating the time series of far-field stress components such as $\sigma_m(t)$ and $\sigma_b(t)$, any assessment concept can be applied. In the context of estimating remaining fatigue life, a suitable approach could be to use a concept with lower complexity until the remaining fatigue life approaches the $S_{n,R10}$ lower bound, then switch to a more advanced concept. In this way, higher computational cost could be reduced to only the most fatigue-sensitive structural details.

Chapter 4

Loading and Response Estimation Using Sparse Sensor Measurements

4.1 Objective

Recalling the problem statement (Section 1.2) of this literature review, a minimization of the error between estimated D^e and observed D^o damage at fatigue-sensitive structural details is desired. The error minimization can be expressed mathematically as an objective function of the parameter x which controls the estimate[1].

$$f(x) = \min\left(\|D^o - D^e\|\right) \tag{4.1}$$

As explained in Section 3.3, fatigue damage accumulation due to variable-amplitude loading can be quantified using a time series of the far-field membrane and bending stresses, a suitable fatigue assessment concept, and a fatigue strength parameter which takes into account the mean stress effect. In a structural health monitoring system, strain gauges and accelerometers are typically installed in locations which are sensitive to global responses; for example, a long based strain gauge may be installed amidships to estimate the first vertical bending moment [5, 79]. Additionally, local loading and response can be estimated using local sensors, such as shear strain gauges for estimating ice loads [80]. The number of sensors installed on ship and offshore structures is typically small (less than 10); in other words, the sensors are sparse relative to the structure size and complexity. To accurately estimate fatigue damage provided sparse sensor measurements, the first objective should be the minimization of error between the actual and estimated far-field stresses, as they control the fatigue damage estimate. By setting this objective, the inverse estimation method and damage assessment concepts are decoupled. Mathematically, the minimization of far-field membrane, bending, and shear[2] stress errors can be expressed as an multi-objective function.

$$f = \min\left(e_{\sigma_m},\ e_{\sigma_b},\ e_{\sigma_v},\ \ldots\right) = \min\left(\|\sigma_m^{\mathrm{e}} - \sigma_m^{\mathrm{m}}\|,\ \|\sigma_b^{\mathrm{e}} - \sigma_b^{\mathrm{m}}\|,\ \|\sigma_v^{\mathrm{e}} - \sigma_v^{\mathrm{m}}\|,\ \ldots\right) \tag{4.2}$$

In most literature on estimating fatigue damage accumulation, minimizing the objective function is achieved in one of two ways:

1. By minimizing the least-squared error;
2. By estimating the (loading and) response in discrete time using a state-space model

This chapter will address these two common approaches and the various flavors that distinguish notable papers from each other. The third section will address other approaches related to fatigue damage estimation that share similar objectives, methods, or relevant findings, but do not explicitly minimize the main objective function as outlined in this literature review. Finally, conclusions are made regarding the assumptions, range

[1] In this section, measured, estimated, and observed scalars will be denoted by the superscripts $^{\mathrm{m}}$, $^{\mathrm{e}}$, and $^{\mathrm{o}}$, respectively. Measured, estimated, and observed vectors will use an equivalent bold superscript: $^{\mathbf{m}}$, $^{\mathbf{e}}$, and $^{\mathbf{o}}$. A measured quantity

[2] For multiaxial fatigue, other components may be relevant.

of applicability, computational cost, accuracy, and complexity of the reviewed approaches. Opportunities for the synthesis of various methods will be further explained in the final chapter of this literature review, as they are hypothetical and unproven.

4.2 Methods

In this section, various methods will be reviewed. All minimize squared error in some way, but the approaches differ significantly.

4.2.1 Method of Least Squares

Minimizing the far-field stress error can be achieved in a number of ways. In a ship, the entire structure accumulates fatigue damage, which implies the error must be minimized for the far-field stress near any fatigue-sensitive structural detail. The method of least squares attempts to minimize the distance between estimated and observed stress at measured points. To illustrate this concept geometrically, consider the strain amplitude at two arbitrary points on the structure as vectors lying on orthogonal axes. The amplitude of each strain scales a unit vector along each axis. Summing the scaled unit vectors yields a resultant vector, with an endpoint corresponding to the strain state. Again, only two points are considered for now.

Consider another set of strains, measured at other points on the structure. To estimate the fatigue damage at the two points considered earlier, the amplitudes which scale the unit vectors along both axes must be found. Assume the estimate has some error. In this graphical representation, the error appears as a distance between the observed and estimated points: $\|\boldsymbol{\epsilon}^{\mathbf{e}} - \boldsymbol{\epsilon}^{\mathbf{m}}\|^2$. Reducing the estimate error is equivalent to minimizing this distance.

As an illustrative problem, consider a set of strain measurements for a beam modeled with one-dimensional finite elements. The vector of strain measurements $\boldsymbol{\epsilon}$ are related to the displacement vector $\mathbf{u}$ through the matrix of strain-displacement relations $\mathbf{B}_{\boldsymbol{\epsilon}}$ such that $\boldsymbol{\epsilon} = \mathbf{B}_{\boldsymbol{\epsilon}}\mathbf{u}$, where $\boldsymbol{\epsilon} = \begin{bmatrix}\epsilon_1, & \epsilon_2, & \ldots, & \epsilon_M\end{bmatrix}^T$ and $\mathbf{B}_{\boldsymbol{\epsilon}}$ is constructed to evaluate strain at points on select isoparametric elements, which correspond to the measured or estimated locations. Suppose a reduced-order model with matrix of basis vectors $\mathbf{H}$ is used such that $\mathbf{u} = \mathbf{H}\boldsymbol{\xi}$. The strain-modal amplitude relationship can then be expressed as:

$$\boldsymbol{\epsilon} = \mathbf{B}_{\boldsymbol{\epsilon}}\mathbf{H}\boldsymbol{\xi} \tag{4.3}$$

The estimated strains are calculated using the strain-displacement relationship matrix $\mathbf{B}_{\boldsymbol{\epsilon}}$, eigenvectors $\mathbf{H}$, and estimated modal amplitudes $\boldsymbol{\xi}^{\mathbf{e}}$, which can be calculated by minimizing the objective function:

$$\boldsymbol{\xi}^{\mathbf{e}} = \min\|\mathbf{B}_{\boldsymbol{\epsilon}}^{\mathbf{m}}\mathbf{H}\boldsymbol{\xi} - \boldsymbol{\epsilon}^{\mathbf{m}}\|^2 \tag{4.4}$$

If the matrix $\mathbf{B}_{\boldsymbol{\epsilon}}\mathbf{H}$ is ill-posed and ill-conditioned, which is often the case when using sparse measurements, Tikhonov regularization can be added to the objective function. By introducing a small positive scalar which modulates the estimate norm $\|\boldsymbol{\xi}^{\mathrm{e}}\|^2$, the effect of small singular values is reduced:

$$\boldsymbol{\xi}^{\mathbf{e}} = \min\|\mathbf{B}_{\boldsymbol{\epsilon}}^{\mathbf{m}}\mathbf{H}\boldsymbol{\xi} - \boldsymbol{\epsilon}^{\mathbf{m}}\|^2 + \lambda\|\boldsymbol{\xi}\|^2 \tag{4.5}$$

By differentiating the objective function and setting the derivative equal to 0, a linear equation is obtained with respect to the vectors $\boldsymbol{\xi}$ and $\boldsymbol{\epsilon}^{\mathbf{m}}$:

$$0 = \frac{d}{d\boldsymbol{\xi}}\left(\|\mathbf{B}_{\boldsymbol{\epsilon}}^{\mathbf{m}}\mathbf{H}\boldsymbol{\xi} - \boldsymbol{\epsilon}^{\mathbf{m}}\|^2 + \lambda\|\boldsymbol{\xi}\|^2\right) = 2\left(\mathbf{B}_{\boldsymbol{\epsilon}}^{\mathbf{m}}\mathbf{H}\boldsymbol{\xi} - \boldsymbol{\epsilon}^{\mathbf{m}}\right)^T\mathbf{B}_{\boldsymbol{\epsilon}}^{\mathbf{m}}\mathbf{H} + 2\lambda\boldsymbol{\xi}^T \tag{4.6}$$

Rearranging and substituting $\mathbf{A}$ for $\mathbf{B}_{\boldsymbol{\epsilon}}^{\mathbf{m}}\mathbf{H}$ yields:

$$\left(\mathbf{A}^T\mathbf{A} + \lambda\mathbf{I}\right)\boldsymbol{\xi} = \mathbf{A}^T\boldsymbol{\epsilon}^{\mathbf{m}} \tag{4.7}$$

The modal amplitude can then be estimated:

$$\boldsymbol{\xi}^{\mathbf{e}} = \left(\mathbf{A}^T\mathbf{A} + \lambda\mathbf{I}\right)^{-1}\mathbf{A}^T\boldsymbol{\epsilon}^{\mathbf{m}} \tag{4.8}$$

Note that the linear operator acting on the measured strains is precisely that of the Moore-Penrose pseudoinverse of the matrix: $\mathbf{A}^+ = \left(\mathbf{A}^T\mathbf{A} + \lambda\mathbf{I}\right)^{-1}\mathbf{A}^T$. It has thus been shown that the Moore-Penrose pseudoinverse minimizes the weighted least-squares error of the objective function, which can include the regularization parameter λ for the purpose of limiting the influence of small singular values on the estimated quantity. λ is usually selected by the user, and when set to 0 the problem simplifies to a basic least-squares estimation. One method of selecting the value of λ uses the error norm $\|\mathbf{B}^{\mathbf{m}}_{\boldsymbol{\epsilon}}\mathbf{H}\boldsymbol{\xi}^{\mathbf{e}} - \boldsymbol{\epsilon}^{\mathbf{m}}\|$ and the estimate norm $\|\boldsymbol{\xi}^{\mathbf{e}}\|$. Plotting the two quantities against each other and varying the regularization parameter λ results in a so-called L-curve. Many systems have a well-defined corner which corresponds to the global minimum of the objective function which includes the regularization parameter. Various methods of identifying this point exist in literature, but a generally well-accepted method is by finding the point of maximum curvature along the L-curve [81, 82]. In the geometric argument, regularization attempts to scale the basis vectors such that their amplitudes are more equivalent. If the modal basis is chosen in a way that represents the physical problem reasonably well, such a constraint enforces an estimate of modal amplitudes based on the physics at hand. However, if a modal basis is chosen arbitrarily, regularization attempts to force good accuracy at the measured locations through the scaling of non-physical modes. Extremely high error can be enforced at other locations on the structure in this way, or the modal amplitudes can be forced to zero. The balance is found using the L-curve[3].

Until now, only the modal amplitude has been estimated. Using the same modal basis and the matrix of strain-displacement relationships for the desired estimated points in the finite element model, the strains can be estimated[4]:

$$\boldsymbol{\epsilon}^{\mathbf{e}} = \mathbf{B}^{\mathbf{e}}_{\boldsymbol{\epsilon}}\mathbf{H}\left(\mathbf{B}^{\mathbf{m}}_{\boldsymbol{\epsilon}}\mathbf{H}\right)^{+}\boldsymbol{\epsilon}^{\mathbf{m}} \tag{4.9}$$

Only three aspects of the equation above can be controlled for the purposes of estimating fatigue damage accumulation in ship structures:

1. The number and position of strain gauges ($\boldsymbol{\epsilon}^{\mathbf{m}}$);
2. The locations where far-field stress estimates are required ($\boldsymbol{\epsilon}^{\mathbf{e}}$);
3. The modal basis $\mathbf{H}$.

First, controlling aspect 1 is not realistic for sailing ships; it is only controllable in the design phase of the hull structure monitoring system. Second, the location of fatigue-sensitive locations can be assessed during the structural design phase, but fatigue-sensitive details can be overlooked. Inspection or processing of hull structure monitoring data can help identify such details. If an existing sailing vessel is to be evaluated by an inverse method, only the third aspect, the modal basis, can be controlled. It is precisely this basis of vectors, in combination with the regularization parameter λ, which can be selected to improve the far-field stress estimation for assessing damage accumulation in fatigue-sensitive structural details. Three conditions limit the accuracy of strain estimation in ship and offshore structures:

[3] A recent paper published by Van Zijl et al. [83] examined the limitations of estimating modal hydrostatic and hydrodynamic force components acting on a floating flexible cylinder using Tikhonov-regularized inversion in the frequency domain. Van Zijl et al. [83] found that while regularization can indeed smooth the modal amplitude estimates, as explained above, it does not allow for the accurate estimate of modal forces outside of the modal basis, which is exactly where Tikhonov regularization is intended to be applied. Similar conclusions were obtained by the author of this thesis in an independent study of a static, fixed-fixed Euler-Bernoulli beam constructed using finite elements. The response induced by a point load, a simple and easily verifiable analytical case, is well-approximated if the number of dry mode shapes is equal to or less than the number of sensors. Tikhonov regularization tended to smooth the results, but the response estimates were always worse than those obtained using a truncated modal basis with a fewer number of modes than sensors. The regularization parameter was evaluated by rotating the L-curve (solution and residual norms) by 45°and finding the minimum. This method is both robust and novel, but does not contribute to the findings in this thesis for the same reasons mentioned in Van Zijl et al. [83].

[4] $\mathbf{B}^{\mathbf{m}}_{\boldsymbol{\epsilon}}$ and $\mathbf{B}^{\mathbf{e}}_{\boldsymbol{\epsilon}}$ are the strain-displacement relationship matrices for the measured and estimated points, respectively. These matrices depend on the type of finite element involved (e.g. beam, shell, rod, etc.) and the locations at which the strains in vectors $\boldsymbol{\epsilon}^{\mathbf{m}}$ and $\boldsymbol{\epsilon}^{\mathbf{e}}$ are evaluated. In practice, both matrices implicitly include a selection matrix to retrieve the nodal displacements associated with the elements in which the strains are to be evaluated.

1. A limited number of sensors are installed on ship and offshore structures.
2. The number of mode shapes required to accurately model the global ship structural response often exceeds the number of sensors; local responses are not reasonably modeled with mode shapes of the entire ship finite element model.
3. Data obtained using strain gauges and accelerometers is often corrupted by noise.

Combining conditions 1. and 2. leads to an ill-posed problem. Consider a slender structure, a beam, on which four strain gauges are installed. If an accurate response requires five modes of a reduced-order model, the strain gauge readings will reflect all five modes, but the estimate of modal amplitudes will be skewed by the fifth mode because of the nontrivial null space. The resulting estimation error can be large, especially if the strain gauges are installed close to a node. The error due to the ill-posed nature of the pseudoinverse $(\mathbf{B}_{\boldsymbol{\epsilon}}^{\mathbf{m}}\mathbf{H})^{+}$ can be reduced if modes required for an accurate response are equal to or less than the number of installed sensors. If this is not possible, reducing the number of required modes will help reduce the error. Improvements in the estimate with regards to the ill-posed nature of the problem can thus be addressed by the selection of an optimal modal basis $\mathbf{H}$. Suppose M modes are required to accurately model the response of the beam, and N strain gauges are used to estimate the response such that the product $\mathbf{B}_{\boldsymbol{\epsilon}}^{\mathbf{m}}\mathbf{H}$ has shape $M \times N$ and rank $r \leq M$ and $r \leq N$. To estimate the strain in other parts of the structure, the modal amplitudes must be estimated using the measured strains:

$$\boldsymbol{\xi}^{\mathbf{e}} = \left(\mathbf{B}_{\boldsymbol{\epsilon}}^{\mathbf{m}}\mathbf{H}\right)^{-1} \boldsymbol{\epsilon}^{\mathbf{m}} \tag{4.10}$$

If $N = M$, the matrix $\mathbf{B}_{\boldsymbol{\epsilon}}^{\mathbf{m}}\mathbf{H}$ is invertible because the matrix has full rank $r = N = M$. However, the matrix is not invertible if $N \neq M$. The pseudoinverse can be used to estimate the modal amplitudes $\boldsymbol{\xi}^{\mathbf{e}}$ by minimizing the square of the modal amplitude error. From a linear algebra perspective, an optimal modal basis $\mathbf{H}$ is one for which the column space of $\mathbf{B}_{\boldsymbol{\epsilon}}^{\mathbf{e}}\mathbf{H}\left(\mathbf{B}_{\boldsymbol{\epsilon}}^{\mathbf{m}}\mathbf{H}\right)^{+}$ spans all possible response vectors $\boldsymbol{\epsilon}$. Similarly, it is the non-trivial null space of the matrix $\mathbf{B}_{\boldsymbol{\epsilon}}^{\mathbf{m}}\mathbf{H}$ which makes the direct inversion difficult. Returning to the graphical interpretation: for a two-measurement strain vector, a suitable modal basis would be the unit vector corresponding to the measured strain vector: only one modal amplitude estimate is required.

Adding condition 3 introduces ill-conditioning. Consider again a slender structure with four strain gauges. If the combined environmental and measurement noise is large relative to the signal, estimated strain error at other points along the beam will become large. While filtering of the time series through an appropriate low-pass filter will certainly help, decreasing the cutoff frequency and increasing the number of poles in the filter will have an effect on the frequency content on significant components of the strain time series. To reduce the effect of filtering on significant components of the time series, regularization can be included in the objective function, which dampens the effect of high-frequency noise on the estimated modal amplitudes (ill-conditioning).

Distortion (Load-Based) Modes

Bigot et al. [84] addresses the ill-posed nature of the problem (see Section 2.4.3) by adopting a load-based set of modal basis; in Bigot et al. [84] and citing papers, the product $\mathbf{B}_{\boldsymbol{\epsilon}}^{\mathbf{e}}\mathbf{H}\left(\mathbf{B}_{\boldsymbol{\epsilon}}^{\mathbf{m}}\mathbf{H}\right)^{+}$ is referred to as a "conversion matrix" and takes the symbol $\mathbf{M}$. In Bigot et al. [84] the modal basis is formed by first evaluating the stationary (steady-state) response of a vessel to predefined, relevant sea states by solving for the linear radiation, diffraction, and incident wave forces. The nodal displacements of the finite element model can be solved by balancing the model with nodal accelerations (applied to each node of the finite element model), gravity, and the external pressures (interpolated from the hydrodynamic to finite element mesh). The resulting nodal displacement vector is one possible distortion mode. However, sea states are selected without knowing in advance which resulting modes will span the response subspace. To arrive at a suitable modal basis $\mathbf{H}$, the vector of nodal displacements that best represent to the first vertical bending moment is selected as the first "distortion" mode. The remaining columns are filled by subsequent modes based on their orthogonality with the first mode. Bigot et al. [84] argues that such an approach is required for an accurate estimate at (fatigue sensitive) structural details as the dry modal basis is slowly convergent with respect to strain, an argument substantiated by Malenica et al. [39], Malenica et al. [51], and Tuitman and Malenica [49]. However, the reference values presented by Bigot et al. [84] are calculated using *dry*

flexible generalized modes; convergence issues are addressed by decomposing the response into quasi-static and dynamic parts.

The conclusions of Bigot et al. [85], Bigot et al. [84], and Malenica et al. [39] are thus somewhat conflicting. The forward model implemented in Malenica et al. [51] is well-validated for a range of deformable structures by performing modal decomposing on the impulse equation of motion [53, 22] using a set of dry generalized modes, yet Bigot et al. [85] shows that modal convergence is not achieved until over 25 modes.

There is some confusion in literature about the type of response that is required: quasi-static or hydroelastic. For example, Andoniu et al. [86] applied the method of Bigot et al. [84] on a floating production, storage, and offloading vessel in a quasi-static way, but mentions springing and whipping, the latter of which is dominated by hydroelastic radiation. Confusion can arise from the software used. While HOMER [51] is capable of hydroelastic analysis using generalized modes, Andoniu et al. [86] only applied hydrodynamic pressure to a finite element model after solving the linear radiation-diffraction problem. Andoniu et al. [86] uses standard deviation as a measure of accuracy, which does not take into account the variable stress cycles which define fatigue loading.

By estimating the amplitudes of distortion modes using sparse strain measurements, external fluid pressures are also implicitly estimated. As a counterexample: using a dry modal basis implicitly assumes that no fluid pressure is acting on the ship structure. When using distortion modes, the hydrostatic and hydrodynamic pressures due to rigid body motions and free vibration are assumed to be well-defined by a superposition of pressures exerted on the ship structure by waves with certain heights, lengths, phases, and headings. Distortion modes thus conflate structural response and fluid pressure loading. Literature on distortion modes focuses heavily on estimating only the structural response, plausibly because strain is more accessible than pressure as a measurable extrinsic property. The accuracy of hydrostatic and hydrodynamic pressure estimates which affect the local response have not been reviewed in literature, a remarkable omission given the role of fluid pressure on the structural response of the hull and fatigue damage caused by such stresses.

Wet Modes

In the previous section, distortion modes were considered as a candidate for the modal basis $\mathbf{H}$. However, as the impulse response function formulation from shows, radiation forces contribute significantly to the equation of motion, especially in the absence of incident and diffraction forces [22, 53]. To incorporate the contributions of forces from the surrounding fluid into the eigenvalue problem associated with damped vibration due to an impulse response, wet mode shapes can be calculated. Assuming a linear response, ship structures are generally underdamped systems. Radiation forces contribute to the response, and because the damping coefficients are non-proportional, the resulting eigenvalues and eigenvectors are complex and frequency-dependent [49]. Assuming a dry generalized mode has been used to solve for the added mass and damping coefficients, the damped eigenvalue problem can be solved in state-space form:

$$\begin{bmatrix} \mathbf{0} & \mathbf{I} \\ -\left(\mathbf{M}+\mathbf{A}(\omega)\right)^{-1}\left(\mathbf{C}+\mathbf{G}+\mathbf{K}\right) & -\left(\mathbf{M}+\mathbf{A}(\omega)\right)^{-1}\mathbf{B}(\omega) \end{bmatrix} \begin{bmatrix} \boldsymbol{\xi} \\ \lambda\boldsymbol{\xi} \end{bmatrix} = \lambda \begin{bmatrix} \boldsymbol{\xi} \\ \lambda\boldsymbol{\xi} \end{bmatrix} \tag{4.11}$$

By iterating this process using the preceding (wet) eigenvector as input for the generalized mode boundary value problem, the true wet mode shapes can be obtained. The series is considered converged when the natural frequency residual between iterations is less than a specific threshold value $|\boldsymbol{\omega_N} - \boldsymbol{\omega_{N-1}}| \leq \epsilon_\omega$.

This procedure results in one wet mode shape, and must be repeated for the others. In general, solving the hydrodynamic boundary value problem becomes increasingly more expensive as the frequency ω increases. For this reason, added mass and damping coefficients can be extrapolated [49].

Recall that this procedure applies for both rigid-body and flexible mode: radiation forces contribute to the stress state in both a quasi-static and hydroelastic way, and the rigid-body modes are no longer rigid but quasi-static. Obtaining wet mode shapes is therefore one way to determine the modal basis for both quasi-static and hydroelastic responses. To obtain a modal equation of motion, a range of frequencies can be substituted into the first-order pressure term using the set of wet generalized modes. Hydrostatic restoring, added mass, and damping coefficients for each combination of mode shape and velocity potential populate the matrices $\mathbf{C}$, $\mathbf{A}(\omega)$, and $\mathbf{B}(\omega)$, respectively.

4.2.2 Ritz Vectors

Recent literature, namely Augustyn et al. [87], investigated the use of modal decomposition and Ritz vectors for the strain estimate of a bottom-founded offshore structure. The work builds on that of Henkel et al. [88]. One limitation in the research of [88] was that the modal decomposition method did not capture both local brace modes and "wave-governed modes" well. The method of [87] uses a vector of mode shapes (a combination of load-based modes and eigenvectors) to approximate the response given measured strain information. The key feature in this paper is the use of the expansion matrix, which contains a *mixture* of both static and dynamic modes. Augustyn et al. [87] also partitions modes based on the measured and estimated responses. Interestingly, no mention is made about the orthogonality of the static and dynamic modes used in the analysis. Estimates of wave loads were calculated using a fifth-order Stokes wave theory and the Morison equation. Skafte et al. [89] also uses Ritz vectors to assess the quasi-static response to wave loads.

One major limitation of the use of load-based mode shapes, particularly Ritz vectors, is the quasi-static nature of the equilibrium problem. For fixed structures such as wind turbines and towers, the application is straightforward because the equilibrium response is unique; however, for a free body, such as a ship or aircraft, there is no unique solution to the equilibrium problem for a given applied load; dynamic effects are always present.

4.2.3 Inverse Finite Element Method

The inverse Finite Element Analysis (iFEM) method is founded on the work of Tessler [90]. In contrast with the Finite Element Method (FEM), which (for structural problems) computes nodal displacements u^e and strains ϵ^e given a boundary value problem, the inverse method seeks the nodal displacement u^e given some measured strains ϵ^e using the matrix of shape function derivatives for membrane $\mathbf{B_m}$, bending $\mathbf{B_b}$, and shear $\mathbf{B_v}$ strain components. The inverse finite element method was originally intended for shape-sensing of slender plates and shells, but through dimensional simplifications 1D-elements such as beams can also be readily evaluated.

In Tessler [90], the nodal displacement vector $\mathbf{u}$ is obtained by finding an minimum of the least squares functional $f_\lambda(u)$ taking into account membrane $\boldsymbol{\epsilon_m}$, bending $\boldsymbol{\epsilon_b}$, and shear $\boldsymbol{\epsilon_v}$ strain components:

$$f_\lambda(\mathbf{u}) = \|\boldsymbol{\epsilon_m}(\mathbf{u}) - \boldsymbol{\epsilon_m^*}\|^2 + \|\boldsymbol{\epsilon_b}(\mathbf{u}) - \boldsymbol{\epsilon_b^*}\|^2 + \lambda\|\boldsymbol{\epsilon_v}(\mathbf{u}) - \boldsymbol{\epsilon_v^*}\|^2 \qquad \mathbf{u^e} = \min\left(f_\lambda(\mathbf{u})\right) \tag{4.12}$$

By setting the first variation of the error functional $f_\lambda(\mathbf{u})$ equal to zero with respect to the displacement (kinematic) variables and integrating by parts, Euler equations are obtained with a set of consistent boundary conditions. The nodal displacement vector is solved in equilibrium:

$$\frac{\partial f_\lambda(\mathbf{u})}{\partial \mathbf{u}} = \mathbf{K}\mathbf{u} - \mathbf{f} = 0 \tag{4.13}$$

Not all nodal strains can be directly measured by strain gauges, which is why Tessler [90] makes a distinction between measured and unmeasured norms. An extrapolation method is required to obtain the boundary conditions given a set of sparse strain measurements, which is referred to in Tessler [90] as Smoothing Element Analysis (SEA). While the inverse finite element method inherently requires a set of kinematic boundary conditions which, for a floating structure, do not exist globally, the inverse finite element method has been applied to sections of ship structures. However, inverse finite element method requires a very large number of sensors to obtain reasonable results, and an equilibrium problem must be solved. As a result, most applications in literature focus on partially fixed structures [91, 92, 93, 94, 95, 96, 97, 98, 99, 100, 101]. For example, 21×10^3 virtual strain rosettes were applied to a chemical tanker section in Kefal and Oterkus [98] to obtain a reasonable response. In Kefal et al. [99], 2.26% of the *elements* were instrumented on a bulk carrier section, and 327 out of 15×10^3 elements were instrumented in Kefal and Oterkus [97] on a Panamax container ship section. While example in literature show good dynamic results for simple beam tests [95], there is limited evidence that inverse finite element method is a suitable for use with sparse sensor measurements on a shell structure.

4.2.4 Kalman Filters

An alternative approach to minimizing the least-squared error is adaptive filtering, a broad class of algorithms which are numerically similar to low-pass filters. The most well-known is the Kalman filter [102], which is based on the state-state representation of a linear but not necessarily stationary [102] system. The Kalman filter is also designed as a least-squared minimizing algorithm. However, the minimization is performed while including noise in the system through Bayesian filtering. One strong advantage of the Kalman filter is that model uncertainty is taken into account in a probabilistic (Bayesian) sense. The Kalman filter begins with a discrete-time equation for the measured strain ϵ_k^m based on the product of a gain term a_k, the actual or observed strain ϵ_k^o, and a noise term n_k. The objective is to minimize the squared error, or the difference between estimated and observed quantities. The error is thus a function of the parameter which controls the estimate, which is exactly the conclusion made at the beginning of this section. The expected value E of the error function is minimized.

$$f(x) = \min E\left(\|\epsilon_k^o - \epsilon_k^e\|^2\right) \tag{4.14}$$

In literature on Kalman filtering in the context of fatigue damage accumulation estimation, the following discrete-time model is commonly adopted:

$$\mathbf{x}_{k+1} = \mathbf{A}\mathbf{x} + \mathbf{B}\mathbf{p}_k + \mathbf{w}_k \qquad \mathbf{d}_k = \mathbf{G}\mathbf{x}_k + \mathbf{J}\mathbf{p}_k + \mathbf{v}_k \tag{4.15}$$

where $\mathbf{x}_k$ is the state such that $\mathbf{x}_k = [\mathbf{u}_k,\ \mathbf{u}_{t,k}]$, $\mathbf{d}_k$ is the output, and $\mathbf{p}_k$ is the unknown input representing loads [103]. Process noise is captured by the vector $\mathbf{w}_k$ and measurement noise by $\mathbf{v}_k$. The subscript $_k$ denotes a sample at time $t = t_k$. The linear model enters through a state-space formulation. Some authors decompose the force vector into space- and time-varying components $\mathbf{S}(t)$ and $\mathbf{p}(t)$, where $\mathbf{S}$ is a matrix corresponding to nodal locations which depends on time and $\mathbf{p}(t)$ is the time-dependent amplitude for each nodal force [104, 105]:

$$\mathbf{M}\mathbf{u}_{tt} + \mathbf{D}\mathbf{u}_t + \mathbf{K}\mathbf{u} = \mathbf{f}(t) = \mathbf{S}(t)\mathbf{p}(t) \tag{4.16}$$

In the formulation above, $\mathbf{D}$ is structural, or Rayleigh, damping [35, 36]. The state-space formulation is defined by the following continuous (with subscript $_\mathbf{c}$) and discrete-time matrices:

$$\begin{aligned} \mathbf{A} &= \exp \mathbf{A_c}\Delta t; \quad \mathbf{B} = (\mathbf{A} - \mathbf{I})\,{\mathbf{A_c}}^{-1}\mathbf{B_c} \\ \mathbf{A_c} &= \begin{bmatrix} \mathbf{0} & \mathbf{I} \\ -\mathbf{M}^{-1}\mathbf{K} & -\mathbf{M}^{-1}\mathbf{D} \end{bmatrix}; \quad \mathbf{B_c} = \begin{bmatrix} \mathbf{0} \\ \mathbf{M}^{-1}\mathbf{S_p} \end{bmatrix} \end{aligned} \tag{4.17}$$

The observation equation is described by the matrices $\mathbf{G}$ and $\mathbf{J}$. In the context of structural finite element analysis, some authors use selection matrices $\mathbf{S_d}$, $\mathbf{S_v}$, and $\mathbf{S_a}$ to specify the locations of measurements:

$$\mathbf{G_c} = \left[\mathbf{S_d} - \mathbf{S_a}\mathbf{M}^{-1}\mathbf{K},\ \mathbf{S_v} - \mathbf{S_a}\mathbf{M}^{-1}\mathbf{D}\right]; \quad \mathbf{J_c} = \left[\mathbf{S_a}\mathbf{M}^{-1}\mathbf{S}\right] \tag{4.18}$$

Since strains ϵ are related to displacements $\mathbf{u}$ in a finite element model such that $\boldsymbol{\epsilon} = \mathbf{B}_{\boldsymbol{\epsilon}}\mathbf{u}$, the strains can be obtained using the observation equation. A subscript $\boldsymbol{\epsilon}$ is added to differentiate the stress-strain relations $\mathbf{B}_{\boldsymbol{\epsilon}}$ from matrix $\mathbf{B}$ in the state-space formulation above.

$$\boldsymbol{\epsilon}_k = \mathbf{B}_{\boldsymbol{\epsilon}k}\mathbf{u}_k = \mathbf{B}_{\boldsymbol{\epsilon}k}\mathbf{S_d}\mathbf{x}_k \tag{4.19}$$

The noise vectors $\mathbf{w}_k$ and $\mathbf{v}_k$ must be defined. To do this, a zero-mean, white-noise (Gaussian) assumption is often made based on known covariance matrices $\mathbf{Q} = \mathrm{E}\left(\mathbf{w}_k\mathbf{w}_l^T\right) \geq \mathbf{0}$, $\mathbf{R} = \mathrm{E}\left(\mathbf{v}_k\mathbf{v}_l^T\right) > \mathbf{0}$. For joint state-space estimation, a method introduced by Lourens et al. [106], an additional noise vector $\boldsymbol{\eta}_k$ is added to the load estimate $\mathbf{p}_{k+1} = \mathbf{p}_k + \boldsymbol{\eta}_k$, with covariance matrix $\mathbf{Q^p} = \mathrm{E}\left(\boldsymbol{\eta}_k\boldsymbol{\eta}_k^T\right)$.

It is clear from the formulations introduced to estimate motions, strains, and loads based on sparse sensor measurements, a few key challenges exist: the load distribution $\mathbf{S}(t)$ must be known to formulate the state-space model; covariance matrices for the process, measurement, and noise must be known to perform the estimate; initial conditions are required because of the discrete time-stepping procedure; the model is of high dimension because the nodal displacement vector $\mathbf{u}$ depends on the finite element model; a linear stationary (Gaussian) assumption is often implicitly made in the state-space model and covariance matrices. The mathematical complexity involved in addressing these challenges tends to increase as accuracy improves. Nonetheless, the Kalman filter has been applied for the purposes of estimating fatigue damage in offshore structures, particularly those with fixed boundary conditions at the seabed. Key challenges are addressed in different ways: for example, Caglio et al. [107] incorporates so-called Physics-Informed Latent force models to describe the spatial distribution of wave loads on an offshore tower structure. Model order reduction using dry mode shapes (the eigenvectors obtained by solving $\mathbf{M}^{-1}\mathbf{K}\mathbf{h} = \lambda\mathbf{h}$) is typically employed. The continuous state-space model can then be rewritten in terms of the new mode shape matrix $\mathbf{H}$ consisting of eigenvectors $\mathbf{h}_i$, eigenvalues λ_i, and modal amplitude state vector $\boldsymbol{\Xi} = [\boldsymbol{\xi},\ \boldsymbol{\xi}_t]^T$:

$$\mathbf{x} = \begin{bmatrix} \mathbf{H} & \mathbf{0} \\ \mathbf{0} & \mathbf{H} \end{bmatrix} \begin{bmatrix} \boldsymbol{\xi} \\ \boldsymbol{\xi}_t \end{bmatrix} \qquad \boldsymbol{\Xi}_t(t) = \mathbf{A_c}\boldsymbol{\Xi}(t) + \mathbf{B_c}\mathbf{p}(t) \qquad \mathbf{d}(t) = \mathbf{G_c}\boldsymbol{\xi}(t) + \mathbf{J_c}\mathbf{p}(t) \tag{4.20}$$

The continuous-time matrices can be obtained by assuming the decomposed mass and stiffness matrices in the equation of motion are diagonal. The discrete-time model is then obtained using a sampling rate of $1/\Delta t$, where $\mathbf{x}_k = \mathbf{x}(k\Delta t)$ or $\boldsymbol{\xi}_k = \boldsymbol{\xi}\,(k\Delta t)$, $\mathbf{p}_k = \mathbf{p}\,(k\Delta t)$, and $\mathbf{d}_k = \mathbf{d}\,(k\Delta t)$.

As in the method of least squares, the modal basis used for the decomposition affects estimate accuracy. Furthermore, introducing a model basis only reduces the order; force vectors and covariance matrices must be estimated without knowing the actual time-varying spatial distribution or amplitude of the force. A Gaussian assumption may not necessarily be valid for transient loads [108]. In the thesis of Vigsø [109], a Kalman filter was applied to a fixed offshore structure to estimate wave forces. The spatial distribution was fixed, derived from wave gauges and supported by wave theory. Even with a specified spatial distribution, the method was incapable of distinguishing between a point and distributed line load. Additionally, the thesis first uses measurements to perform system identification, which is not always possible for a ship or offshore structure. It is thus a common challenge among [109], [107], and [108] that the time-varying spatial distribution of the load must be determined with reasonable accuracy to obtain an accurate estimate of the force. Lourens and Fallais [108] illustrates this effect on accuracy concisely with a fixed-free Euler-Bernoulli 1D finite element model. Lourens and Fallais [108] showed that the Kalman filter estimates displacement, velocity, and acceleration very well if the model is known exactly. However, uncertainty in the loading leads to significant error. Spatially-varying steady-state and non-linear transient wave loads are expected to further complicate the estimation.

Furthermore, the state-space model is frequency-dependent if added mass and damping forces are included in the continuous-time matrices $\mathbf{A_c}$, $\mathbf{B_c}$, $\mathbf{G_c}$, and $\mathbf{J_c}$. In addition, the number of sensors relative to the modal content of the response affects estimate accuracy, as found by Lourens et al. [106].

4.2.5 Transmissibility

Recent literature has focused on the use of transmissibility, or the correlation of two (or multiple) frequency response functions, to estimate the response of a structure based on a limited number of measured sensors. The transmissibility concept is based on the work of [110] and [111]. An applied load $\mathbf{f_a}(t)$ and the resulting structural response $\mathbf{x}(t)$ can be represented by performing a convolution on the force and frequency response function $h(t)$, a scalar value. Applying the Fourier transform results in the frequency-domain relationship[5]:

[5]To maintain consistency with literature, the variable naming in this section has been largely preserved. One key distinction is made regarding the matrix $\mathbf{H}$: in this subsection on transmissibility, $\mathbf{H}$ is a frequency-dependent matrix which contains frequency response functions for pairs of physical values in a structure, such as strains, accelerations, forces, or displacements. It is not to be confused with the modal basis $\mathbf{H}$ which is used in the sections on model order reduction or the method of least squares. One reason for the use of variables $\mathbf{X}$ and $\mathbf{Y}$ is that different physical values can be used as inputs and outputs in the method of transmissibility, so prescribing consistency with strain or acceleration symbols in this literature review would be misleading.

$$x_j(t) = \int_0^t f_j(\tau) h_{ja}(t-\tau)\, dt \rightarrow X_j(\omega) = H_j(\omega) F_a(\omega) \tag{4.21}$$

The scalar transfer function between known and unknown responses can be formed by taking the ratio of known and unknown frequency response functions. The term (ω) is omitted for brevity:

$$T_{aku} = \frac{X_u}{U_k} = \frac{H_{ua} F_a}{H_{ka} F_a} = \frac{H_{ua}}{H_{ka}} \tag{4.22}$$

It has been shown by Maia et al. [110] and Ribeiro et al. [111] that the relationship between known and unknown responses can be determined without load information, provided the matrices of frequency response functions are known:

$$\mathbf{T_{aku}} = \mathbf{H_{ua}} \mathbf{H_{ka}}^{+} \quad \text{such that} \quad \mathbf{X_u} = \mathbf{T_{aku}} \mathbf{X_k} \tag{4.23}$$

Again, all matrices in the equation above are frequency-dependent. Linear system theory allows for reconstruction of the unknown (estimated) time series using the discrete Fourier transform: $x(t) = \mathcal{F}^{-1}\left(\mathcal{F}\left(x(t)\right)\right)$. In the context of a finite element model and far-field stress estimation, the stress-strain relationship $\mathbf{B_\epsilon}$ is multiplied by the estimated response to return the nodal strain estimate. Transmissibility has been used by a number of authors: De Klerk and Ossipov [112] and de Klerk [113] use the concept of transmissibility in the context of automotive noise propagation. Moi et al. [114] applied the same concept for use in a knuckle boom crane. In the context of ship and offshore structures, Gebrezgabir et al. [115] investigated slamming loads using a set of strain gauges on a sailing wave-piercing catamaran, and showed excellent reconstruction of strain signals during slamming events, based on a short time series of measured data. In Gebrezgabir et al. [115], it is clear that the matrix $\mathbf{T_{aku}}$ must be defined based on actual measurements, which limits the applicability for estimating strain at unmeasured locations. However, transmissibility could easily be used for reconstructing signals from a faulty sensor and thus complement another approach such as the method of least-squares or Kalman filtering. The PhD thesis of Alsalah [116] includes the use of transmissibility for detecting and locating slams on a wave-piercing catamaran and provides important insights on the propagation of structural waves due to slamming loads. Indeed, Alsalah [116] concludes that the strain time series at measured locations close to the position of peak pressure on the hull showed an earlier response than those measured far away from the site of impact. This finding is consistent with the conclusions made in Chapter 2 about global and local hydroelastic responses. Most recently, Durandt and Bekker [117] and Durandt and Bekker [118] used strain and acceleration-based transmissibility matrices for predicting strain on the S.A. Agulhas II, a polar class research vessel. Jagite et al. [119] claims a novel approach by using linear seakeeping software to construct the matrix $\mathbf{T_{aku}}$, but the requirement of condition-dependence conflicts with the conclusions made by Gebrezgabir et al. [115], who stated that the influence of vessel speed and heading has a negligible effect on the resulting error. A set of virtual sensors was used to verify the approach, using a Bureau Veritas software HOMER [51]. This paper builds on the work of Sireta et al. [120], which uses the concept of transmissibility to determine the relation between responses at various locations in the frequency domain. Jagite et al. [119] obtains the transmissibility matrix in the frequency domain: given a stress response Response Amplitude Operator (RAO) for a virtual sensor i and physical sensor j $\sigma_i(\omega, \beta)$ and $\sigma_j(\omega, \beta)$, the transmissibility can be determined using the following relationship:

$$\mathbf{H}_{ij}(\omega, \beta) = \frac{\int_{-\pi/2}^{\pi/2} \left[|\sigma_i(\omega, \beta)|^2 S(\omega) f(\alpha) \right] \, d\alpha}{\int_{-\pi/2}^{\pi/2} \left[|\sigma_j(\omega, \beta)|^2 S(\omega) f(\alpha) \right] \, d\alpha} = \frac{\int_{-\pi/2}^{\pi/2} \left[|\sigma_i(\omega, \beta)|^2 f(\alpha) \right] \, d\alpha}{\int_{-\pi/2}^{\pi/2} \left[|\sigma_j(\omega, \beta)|^2 f(\alpha) \right] \, d\alpha} \tag{4.24}$$

where ω is the wave frequency, β is the relative wave direction, $f(\alpha)$ is the directional distribution of wave energy, and $S(\omega)$ is the unidirectional wave energy spectrum. The spectrum components can be canceled out in the equation above. Thus, the ratio between the stress-responses spectra is the ratio of the square of the RAOs; they only depend on the wave direction. In the time domain, Jagite et al. [119] provides a formulation identical to that found in De Klerk and Ossipov [112] and Durandt and Bekker [118]. The

variance and covariance matrices for input-input $\mathbf{R}_{XX}$ and input-output $\mathbf{R}_{XY}$ can be obtained using the matrices $\mathbf{X}_{(H_s,T_p,\beta,\gamma,\alpha)}$ and $\mathbf{Y}_{(H_s,T_p,\beta,\gamma,\alpha)}$, which are calculated based on the responses at input and output sensors for a given set of environmental conditions. In this formulation, γ is the peak enhancement factor and α is the wave spectral directional width. Matrices $\mathbf{X}$ and $\mathbf{Y}$ are formed by performing a discrete Fourier transform on each signal (m outputs, n inputs) for a set of r measurement blocks.

$$\underbrace{\begin{bmatrix} H_{11} & \cdots & H_{1n} \\ \vdots & \ddots & \vdots \\ H_{m1} & \cdots & H_{mn} \end{bmatrix}}_{\mathbf{H}(\omega)} \underbrace{\begin{bmatrix} x_{11} & \cdots & x_{1r} \\ \vdots & \ddots & \vdots \\ x_{n1} & \cdots & x_{nr} \end{bmatrix}}_{\mathbf{X}(\omega)} = \underbrace{\begin{bmatrix} y_{11} & \cdots & y_{1r} \\ \vdots & \ddots & \vdots \\ y_{m1} & \cdots & y_{mr} \end{bmatrix}}_{\mathbf{Y}(\omega)} \tag{4.25}$$

$$\mathbf{R}_{XX} = [\overline{\mathbf{x}_i \mathbf{x}_j}]_{t\to\infty} = \frac{1}{n_t}\mathbf{X}^T\mathbf{X}; \quad \mathbf{R}_{XY} = [\overline{\mathbf{x}_i \mathbf{y}_j}]_{t\to\infty} = \frac{1}{n_t}\mathbf{X}^T\mathbf{Y} \tag{4.26}$$

where n_t represents the number of time steps for matrices $\mathbf{X}$ and $\mathbf{Y}$. The estimated response vector $\mathbf{y^e}$ can then be evaluated using the covariance matrices and the vector of measured responses $\mathbf{x^m}$:

$$\mathbf{y}^{\mathbf{e}}_{(H_s,T_p,\beta,\gamma,\alpha)} = \left(\mathbf{R}_{XX}^{-1}\mathbf{R}_{XY}\right)\mathbf{x}^{\mathbf{m}}_{(H_s,T_p,\beta,\gamma,\alpha)} \tag{4.27}$$

It can be easily shown that the basis $\mathbf{H}$ is based on the least-squares operation of matrix $\mathbf{X}$, which is used by [115]:

$$\mathbf{y^e}(\omega) = \left(\mathbf{R}_{XX}^{-1}\mathbf{R}_{XY}\right)\mathbf{X} = \left(\left(\mathbf{X}^T\mathbf{X}\right)^{-1}\mathbf{X}^T\mathbf{Y}\right)\mathbf{x^m} = \left(\mathbf{X}^{+}\mathbf{Y}\right)\mathbf{x^m} = \mathbf{H}\mathbf{x^m}(\omega) \tag{4.28}$$

The time series $\mathbf{y^e}(t)$ can be recovered using the inverse discrete Fourier transform $\mathcal{F}^{-1}\left(\mathbf{y^e}(\omega)\right)$, although the mean value may not be accurately captured, which affects the fatigue assessment accuracy. The fundamental difference between transmissibility and the method of least squares based on a known modal basis is the inclusion of measured responses in the modal basis itself, as is apparent in Equation 4.28: the matrix $\mathbf{Y}$ is included in the calculation of $\mathbf{H}$. The practical implication is that numerous frequency- or time-domain analyses must be performed using a representative hydrostructural model. In addition, the relationships between measured and output values are only known at discrete points, which must be selected prior to formulation of the matrix $\mathbf{H}$. If the fatigue-sensitive locations are not known, the size of matrix $\mathbf{H}$ can become quite large for a ship, which significantly reduces computational efficiency compared to a modal basis which corresponds to the motions of a ship (heave, pitch, bending, torsion, etc). Implied in the time-domain approach is an assumption that the modal basis $\mathbf{H}$ changes based on the sea state, vessel speed, and heading. Therefore, the ship must also be used as a wave buoy, or the sea state must be identified based on historical data. The covariance matrices $\mathbf{R_{XX}}$ and $\mathbf{R_{XY}}$ can also be computed using the stress Response Amplitude Operators, but this approach also requires the sea state and heading. The effects of slamming on the accuracy using such a linear model have not been explored by [119].

Durandt and Bekker [118] compared strain gauge signals from a sailing vessel and noted that the matrix $\mathbf{H}$ provides a good estimate up to the two-node bending natural frequency for a polar-class vessel. One added complication of using the concept of transmissibility for virtual or physical sensors is that the transfer functions that relate responses to each other must be determined using the principles of stochastic subspace identification, which uses so-called Block Hankel matrices [121, 122, 123]. In other words, multiple non-overlapping time series of $\mathbf{X}$ and $\mathbf{Y}$ from must be recorded and correlated to arrive at the transmissibility matrix $\mathbf{H}$. Such an approach lends itself well to estimating the modal properties of the linear system, since the state-space representation can be linked to the Kalman filter [109, 124, 125, 126]. However, the length of time must be decided on to construct the Block Hankel matrix, which affects the relationships. Note that the methods of transmissibility, operational modal analysis, and stochastic subspace identification are usually applied for empirical measurements; while using a forward seakeeping model sounds like a promising approach, significant computational time is required to build a sufficient set of training data. Furthermore, local hydroelastic effects cannot be captured by today's seakeeping software when combined with whipping and springing effects.

4.2.6 Slamming Identification, Localization, and Signal Decomposition

In the literature review on estimating strains due to slamming loads, many papers were obtained regarding the identification (in time) and localization (in space) of slamming loads provided sparse strain or acceleration measurements. Some authors used wavelet transforms to decompose the measurement signals into quasi-static and dynamic parts [127, 116], which assisted in the identification and localization. This method could potentially be an inverse equivalent to the decomposition used by Malenica et al. [39] and Tuitman [1] in forward time domain seakeeping models. Alsalah et al. [127], Alsalah [116], Amin et al. [128], Dessi [129], Kim et al. [130], Bekker et al. [131], and Du et al. [132] used various forms of the wavelet transform to separate high-frequency responses, and generally agreed that wavelets provided a better mathematical framework for transient signals (such as those obtained during slamming-induced whipping events) than short-time discrete Fourier transforms [133] or the typically used discrete Fast Fourier Transform. Another category of literature focused on the identification of slamming impacts, although in the present context these results are not particularly useful, as the stress range is more important for estimating fatigue damage [134, 135, 136]. Other authors focused on reconstructing the slamming force itself, but this literature focused mainly on segmented backbone models [137, 138, 139, 140].

4.3 Conclusions

In this chapter, an objective function was formulated based on the error between estimated and observed fatigue damage. The far-field stresses, as shown in Chapter 3, govern this error, so the function was reformulated in terms of the far-field stress. An assumption of linear elasticity allows the substitution of strain for stress in this objective function. The method of least squares was briefly reviewed as a preface to methods found in literature. Geometric and physical arguments motivated the method of least squares, and Tikhonov regularization was introduced as one, albeit flawed, means of minimizing error. The modal basis $\mathbf{H}$ was found to be the most important variable in the equation relating measured and estimated strains. Recognizing this importance, two load-based approaches (distortion modes and Ritz vectors) were highlighted. Then, Kalman filters were shown to minimize the error using a state-space representation. Transmissibility was discussed as one promising method of estimating strains due to transient slamming loads. Finally, literature on slam identification, localization, and signal decomposition was mentioned.

Among the methods presented, only the method of least squares (including the use of distortion modes and Ritz vectors as the modal basis), Kalman filters, and the concept of transmissibility provide a reasonable framework for estimating far-field stresses based on sparse sensor measurements. Of these, the method of least squares is applied most often to floating ship and offshore structures. In addition, the modal basis used in the method of least squares also applies to forward models based on the generalized modes framework. For these reasons, the method of least squares is deemed most suitable for the estimation of far-field stresses in ship structures. The modal basis itself can be modified to improve the estimate.

Chapter 5

Research Overview

5.1 Research Gap

Research gaps for both global and local loading and response have been identified based on the literature.

Global: While a variety of inverse load and response estimation methods exist for ship and offshore structures, no papers have been found which explicitly estimate combined steady-state (springing) and transient (slamming, whipping) load-induced fatigue damage accumulation in ship structures using sparse sensor measurements. Furthermore, estimation error attributed to the number and type of sensors, column space of the reduced order modal basis, and spectral content of the loading and response has not been quantified for combined steady-state and transient load-induced fatigue damage accumulation. As a result, it is unclear from the literature whether implementation of an existing inverse response estimation method on an instrumented slamming-prone vessel would provide reliable information for the inspection and maintenance of fatigue-sensitive structural details.

Local: While sufficient attention has been given to the estimation of steady-state load-induced fatigue damage accumulation in ship structures using sparse sensors which capture the global response, a distinct gap is present in the literature regarding local effects. Modern ships, especially icebreakers, are sometimes instrumented with sensors (usually shear strain gauges) on slamming- and ice load-prone stiffened panels. However, the use of such sensors has not been investigated as a means of estimating local slamming loads or the high-frequency fatigue damage accumulation at nearby structural details.

5.2 Hypotheses and Research Question

The main hypotheses of this literature review can be stated as follows:

> **HYPOTHESIS 1** The quasi-static and elastic wet mode shapes of a ship structure, obtained from linear radiation and hydrostatic restoring forces in a generalized modes framework, form a suitable modal basis for estimating global steady-state (springing) and transient (slamming, whipping) far-field stresses with the method of least squares.

Central to Hypothesis 1 is the assumption that in stiff floating ship and offshore structures, steady-state wave loading tends to induce low-frequency rigid-body motion and a quasi-static stress response, while transient (slamming) loading contributes significantly to elastic (bending, torsion) motions and a dynamic stress response. Hypothesis 1 implicitly asserts that the spatial distribution of pressure for both quasi-static (rigid-body) and elastic (flexible) loading is well-approximated by pressures applied during the iterative procedure used to obtain wet mode shapes. Such a hypothesis may not hold for fixed offshore structures, where wave loading does not induce a rigid body response[1]

[1] Refer to Section 2.4.3 and literature (e.g. Augustyn et al. [87]) for comparison. A mixed modal basis is found to be suitable for some structures such as fixed offshore wind turbine towers.

HYPOTHESIS 2 The dry mode shapes of an orthotropically stiffened panel, obtained from a undamped finite element model, form a suitable modal basis for estimating local quasi-static and hydroelastic transient (slamming) far-field stresses with the method of least squares.

Hypothesis 2 recognizes that the local[2] hydrostructural vibrations during and after slamming events are generally of a low order, meaning reasonable convergence in the structural response is achieved with the first few dry mode shapes. The use of dry modes also has a practical motivation: accurate modeling of 3D quasi-static and hydroelastic slamming events is an active field of research, and is computationally expensive. In addition, a wet or load-based mode would be accurate only during the phase in which the structure is wetted, while the free (dry) vibration following impact is important for fatigue.

A research question based on identified gaps in scientific knowledge is proposed:

RESEARCH QUESTION How can steady-state and transient wave loading-induced fatigue damage accumulation be accurately estimated in a linear elastic ship structure using sparse strain measurements?

5.3 Modeling Plan

To answer the primary research question, numerical models will be used. Validation using a scale model is not considered due to time constraints. The numerical modeling steps are outlined below; the global model tests Hypothesis 1, and the local model tests Hypothesis 2.

Global Model: Segmented Barge A 1D structural finite element model (a barge) coupled with a 3D hydrodynamic boundary element model using generalized modes provides a very efficient numerical framework for assessing the far-field stress error using different inverse methods while still being reasonably representative of a real ship. The current conversion matrix approach can be implemented by solving the linear radiation-diffraction problem for a discrete number of head wave frequencies and phases. Distortion modes can be obtained quasi-statically using generalized modes. It is expected that the conversion matrix approach will lead to increased error when the model is subjected to broad-band (slamming-representative) loading. Steady-state response will be simulated using the frequency-domain radiation-diffraction solution for a wave distribution. Transient response will be simulated using a decay test (similar to that performed by Tuitman et al. [141] on a physical model) and a wave impact (an impulse response applied to the bow node).

Local Model: Stiffened Panel A 1D finite element model of a orthotropically stiffened panel based on Euler-Bernoulli beam elements with fixed boundary conditions can provide an efficient numerical framework for assessing the far-field stress error using the method of least squares. Such a model would show that the local transient effects, which are difficult to measure using global sensors, could be accurately estimated using local strain gauges. As a preliminary model, a Wagner formulation will be used. Both quasi-static and hydroelastic effects will be modeled by varying the impact velocity of a wedge with low deadrise angle.

[2] At the plate-strip, plate-stiffener, and stiffener-frame levels of an orthotropically stiffened panel, for example.

Part II

Modeling

Chapter 6

Global Model: Segmented Barge

The first aim of this thesis is to assess methods of accurately estimating the far-field stress state at any point in a stiff, free-floating ship structure based on sparse strain measurements. To facilitate an efficient investigation into the effect of various input parameters on the estimated loading and response, a scale segmented barge is modeled. In Chapter 6, the modeling steps used to evaluate and estimate the loading and response of the barge are presented; key steps are shown in Figure 6.1. Section 6.1 explains the numerical methods used to approximate the loading and response[1] of the structure in regular and irregular waves given significant wave height H_s and period T_p. The impulse load model is also specified. Section 6.2 reviews the modal bases used to estimate the loading and response, the number and positioning of strain gauges, the low- and high-pass filters used to separate the measured responses, and the error metrics used to quantify the quality of the estimates. Throughout this chapter, important modeling steps are verified or validated against numerical, analytical, or experimental results published in literature. Discrepancies are highlighted as they affect the model's suitability for answering the global research question and accepting or rejecting the hypothesis.

The segmented barge is modeled using one-dimensional isoparametric Euler-Bernoulli finite elements with constant cross-sectional linear density, bending stiffness, and structural damping. Each submerged surface is discretized using a structured, quadrilateral mesh; each panel in the mesh is represented by a collocation point and unit normal vector. Loading and response analyses are conducted in both the frequency and time domains using the method of generalized modes, where the real eigenvectors obtained from the free-vibration eigenvalue problem are used as the modal basis. Radiation and diffraction potentials are solved at each collocation point using the boundary element method. Irregular frequencies are suppressed using lid panels, and high-frequency radiation potentials are extrapolated using an exponential decay function and the Kramers-Kronig relations. The frequency-domain analysis includes loading due to hydrostatic pressure and incident, diffracted, and radiated waves. A fourth-order Runge-Kutta method is used to solve a free decay problem. Results are compared with those from literature.

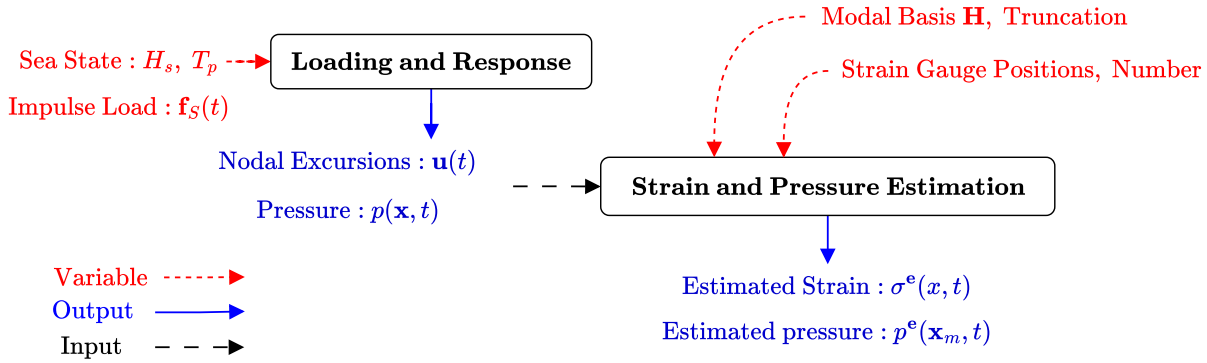
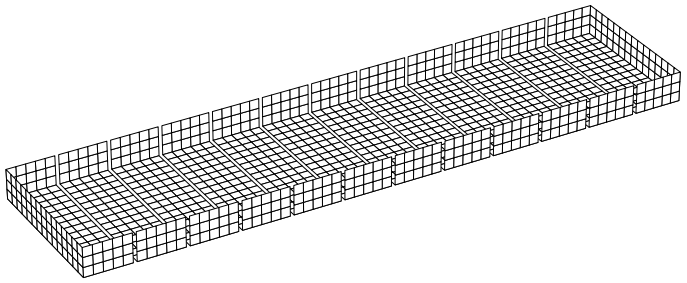
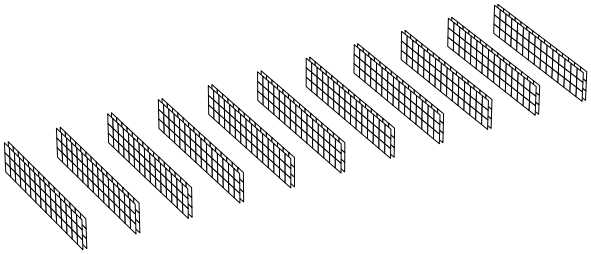


Figure 6.1: Outline of the global modeling workflow, including variables, inputs, and outputs.

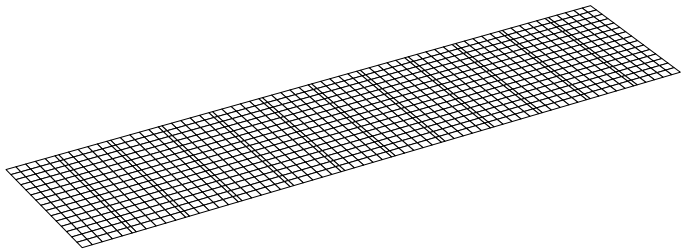
[1] Outputs are stored as vectors of nodal excursions $\mathbf{u}(t)$ and pressures $p(\mathbf{x})$.



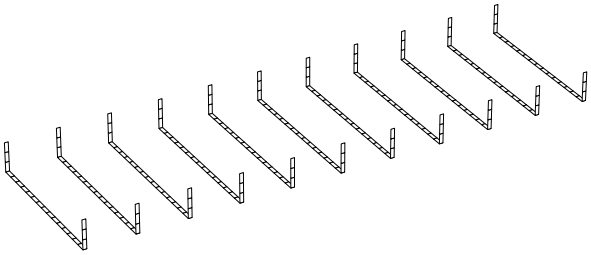
(a) External: hydrostatic, incident, radiation, diffraction



(b) Internal: hydrostatic, incident



(c) Lid: radiation, diffraction



(d) Gap: radiation, diffraction

Figure 6.2: Deconstructed hydrodynamic mesh of a 12-segmented barge showing external, internal, lid, and gap panels. The types of pressures solved for each panel type are indicated.

6.1 Loading and Response

6.1.1 Model Setup

Coordinate System The segmented barge is constructed in a Cartesian coordinate system with axes x, y, and z corresponding to forward (surge) u, lateral (sway) v, and vertical (heave) w displacements and roll ϕ, pitch θ, and yaw ψ rotations; positive rotation follows the right hand rule. The global origin is located at the intersection of the mean waterline plane and the beam midpoint.

Geometry The barge consists of 12 floaters, each with a length of 19 cm, width of 60 cm, and height of 25 cm. The draft is 12 cm. The two steel strips are flat plates with cross-sectional dimensions 50 mm $\times$ 15 mm (Configuration 1), with the exception of the segmented model used for verification, which defines the plate thickness as 4 mm (Configuration 2). The earth-fixed reference frame origin is coincident with the mean waterline and the beam midpoint. A body-fixed reference frame origin is defined by the intersecting neutral axis and midpoint plane.

Structural Properties A steel density of 7850 kg/m^3 is assumed. The draft and geometry provided in literature is used with this assumption to calculate the density and mass of the floaters. The geometric center of each floater is used as the axis of rotation for determining the moment of inertia. A rigid connection between each floater and the two beams is assumed. The elastic modulus E is set such that the analytical wet natural frequencies for the barge with a backbone thickness of 4 mm match those as listed in Malenica et al. [38].

Hydrodynamic Mesh The submerged part of each floater is discretized to obtain a uniform, structured hydrodynamic mesh of quadrilateral panels. To maintain consistency with published results from literature, mesh refinement near sharp edges is not performed [141, 38][2]. Each panel at index n is defined by a collocation point with coordinates $\mathbf{x}_n = \begin{bmatrix} x_n & y_n & z_n \end{bmatrix}$, normal vector $\mathbf{n}_n = \begin{bmatrix} n_x & n_y & n_z \end{bmatrix}$, and area S_n. Four types of

[2]Refining the mesh near sharp edges improves the accuracy of numerical radiation and diffraction potential estimates.

panels are defined: exterior, interior, gap, and lid. Incident and hydrostatic pressures are solved on the exterior and interior panels, while radiation and diffraction pressures are only evaluated on external surfaces. Irregular frequencies are suppressed in the radiation and diffraction problems by prescribing $\nabla\phi \cdot \mathbf{n} = \mathbf{0}$ on the lid and gap panels and appending these boundary conditions to the system of linear equations. To evaluate whether the hydrodynamic mesh is sufficient to properly enforce diffraction and radiation boundary conditions, the Nyquist frequency is used as a criterion. The wavelength λ [m] at wave frequency ω [rad/s] can be approximated using the deep water dispersion relation: $\lambda = 2\pi/k = 2\pi g/\omega^2$. The Nyquist frequency ω_N is set equal to the incoming wave frequency ω. To avoid aliasing, the sampling frequency must be double the Nyquist frequency: $\omega_s \geq 2\omega_N = 2\omega$. To obtain the maximum allowable panel length, the sampling frequency is converted back to wavelength: $k_s = \omega_s^2/g = 4\omega^2/g = 4/\lambda$.

$$\text{Panel length} \leq \frac{2\pi}{k_s} = \frac{2\pi g}{\omega_s^2} = \frac{\pi g}{2\omega^2} = \frac{\lambda}{4} \tag{6.1}$$

Based on this criterion, the maximum allowable panel length in any direction is one-fourth of the wavelength λ at frequency ω. Incident, radiation, and diffraction potentials are only evaluated up to frequencies at which this criterion is satisfied. Computational constraints limit the maximum frequency to 20 rad/s and the panel length to 2 cm.

Finite Element Model A 12-node Euler-Bernoulli beam model with constant cross-sectional density and stiffness is implemented using isoparametric elements. Elemental mass and stiffness matrices ($\mathbf{M_e}$, $\mathbf{K_e}$) are obtained using density $(\rho A)_e$ and bending stiffness $(EI)_e$ based on the cross section of the combined backbones. The curvature-displacement matrix $\mathbf{B}$ is the second derivative of the shape function matrix: $\mathbf{B} = \mathbf{N}_{xx}$. The strain-displacement matrix $\mathbf{B_\epsilon}$ also includes the distance from the neutral axis (in this application, half of the beam thickness) and selects the nodal indices based on the coordinate x. The work per unit length results in the elemental force vector $\mathbf{q_e}$ based on a distributed force per unit length q.

$$\mathbf{M_e} = \int_{\Omega_e} \mathbf{N}^T (\rho A)_e \, \mathbf{N} \, d\Omega \qquad \mathbf{K_e} = \int_{\Omega_e} \mathbf{B}^T (EI)_e \, \mathbf{B} \, d\Omega \qquad \mathbf{q_e} = \int_{\Omega_e} \mathbf{N}^T q \, d\Omega \tag{6.2}$$

The shape functions themselves N_i are continuously differentiable to the order used in the formulation of elemental matrices. For an Euler-Bernoulli beam, only the second derivatives are required. Taking the derivative with respect to x for each shape function implies that every element has a different shape function. Isoparametric mapping fixes this issue by assigning one uniform set of shape functions for an element with dimension $\xi \in (-1,\ 1)$ instead of x, whose bounds vary per element. A cubic Hermite polynomial is continuously differentiable to the second order: $N_i(\xi) = A + B\xi + C\xi^2 + D\xi^3$. To find the coefficients, $N_i(\xi)$ is set to 1 or 0 depending on the degree of freedom. The Jacobian J relates ξ and x coordinates: $J \rightarrow J = \partial\xi/\partial x$. For an Euler-Bernoulli beam, the Jacobian is simply half the length of the element. Integration is performed numerically using two-point Gauss quadrature, which is exact for a cubic Hermite polynomial. Global mass and stiffness matrices ($\mathbf{M}$, $\mathbf{K}$) are assembled using element-node connectivity. The rigid body motions of each floater are described by the generalized nodal displacement vector $\mathbf{u}$, which consists of vertical and rotational displacements w, and $\theta = -w_x$.

Modal Analysis The eigenvalues (natural frequencies) ω_n^2 and eigenvectors $\mathbf{h}_j$ are solved from the eigenvalue problem $\mathbf{M^{s}}^{-1}\mathbf{K^s}\mathbf{h}_j = \lambda\omega^2\mathbf{h}_j$ such that $\mathbf{H} = \begin{bmatrix}\mathbf{h}_1 & \mathbf{h}_2 & \dots & \mathbf{h}_N\end{bmatrix}$, where N is the number of modes used in the analysis. The mass and moment of inertia of each segment are added to the diagonal of the structural mass matrix. Modal mass $\mathbf{M}$ and stiffness $\mathbf{K}$ are found using the following equation:

$$\mathbf{M} = \mathbf{H}^T\mathbf{M^s}\mathbf{H} \qquad \mathbf{K} = \mathbf{H}^T\mathbf{K^s}\mathbf{H} \tag{6.3}$$

Structural Damping Damping of a finite element model is often prescribed in modal space. For example, Rayleigh damping is obtained as a linear combination of the mass and stiffness matrices. However, to obtain a balanced nodal finite element model, the total external and internal (inertial) forces must be equivalent, which cannot be obtained directly using modal quantities. For this reason, distributed damping is approximated as follows: $(c_d)_e = \beta\,(EI)_e \quad \text{where} \quad \beta = 2\zeta/\omega$. The elemental structural damping matrix $\mathbf{D_e}$ is obtained

by integration over the isoparametric elements. The full structural damping matrix $\mathbf{D^s}$ is assembled using element-node connectivity.

$$\mathbf{D_e} = \int_{\Omega_e} \mathbf{N}^T \left(c_d\right)_e \mathbf{N}\, d\Omega \qquad \mathbf{D^s} = \sum_{\mathbf{e}} \mathbf{D_e} \qquad \mathbf{D} = \mathbf{H}^T \mathbf{D^s} \mathbf{H} \tag{6.4}$$

6.1.2 Steady State

The equation of motion for the steady-state problem in the time domain is as follows:

$$\left(\mathbf{M} + \mathbf{A}(\infty)\right) \boldsymbol{\xi}_{tt} + \left(\mathbf{B}(\infty) + \mathbf{D}\right) \boldsymbol{\xi}_t + \left(\mathbf{C} + \mathbf{G} + \mathbf{K}\right) \boldsymbol{\xi} + \underbrace{\int_0^t \mathbf{K^h}(t-\tau) \boldsymbol{\xi}_t(\tau)\, d\tau}_{\mathbf{f}_K(t)} = \mathbf{f}_I(t) + \mathbf{f}_D(t) \tag{6.5}$$

The equation of motion is implemented in discrete time by converting the analytical form into a series of two linear equations for each time step t^n. A fourth-order Runge-Kutta method is implemented for solving the modal amplitudes $\boldsymbol{\xi}(t^{n+1})$.

$$\begin{bmatrix} \mathbf{0} & \mathbf{I} \\ -\left(\mathbf{M} + \mathbf{A}(\infty)\right)^{-1} \left(\mathbf{C} + \mathbf{G} + \mathbf{K}\right) & -\left(\mathbf{M} + \mathbf{A}(\infty)\right)^{-1} \left(\mathbf{B}(\infty) + \mathbf{D}\right) \end{bmatrix} \begin{bmatrix} \boldsymbol{\xi}(t^{n+1}) \\ \boldsymbol{\xi}_t(t^{n+1}) \end{bmatrix} = \begin{bmatrix} \mathbf{0} \\ \left(\mathbf{M} + \mathbf{A}(\infty)\right)^{-1} \left(-\mathbf{f}_K(t^n) + \mathbf{f}_I(t^n) + \mathbf{f}_D(t^n)\right) \end{bmatrix} \tag{6.6}$$

The remainder of this section outlines the procedure for calculating the added mass, damping, hydrostatic, and gravity coefficients, as well as the impulse response functions $\mathbf{K^h}$ and incident and diffraction forces. The time step is 0.005 seconds. The total duration of the simulation is 200 seconds. Convolution is only performed for 10 seconds, as the modal impulse response functions decay to zero within 5 seconds; an additional 5 seconds are kept as buffer. 8 generalized modes are included in the analysis.

Incident and Diffraction Pressures The complex incident potential ϕ_I at coordinate $\mathbf{x}_m = [x_m,\ y_m,\ z_m]$ in deep water is expressed as a function of the acceleration of gravity g, wave frequency ω, wave number k, and wave heading μ. For a ship traveling in the $+x$ direction, head waves have a heading of $\mu = 180\,\text{deg}$.

$$\phi_I\left(\mathbf{x}_m\right) = \frac{g}{\omega^2} e^{kz_m} e^{-ik(x_m \cos\mu + y_m \sin\mu)} \tag{6.7}$$

The diffraction potential ϕ_D at the same point $\mathbf{x}_m$ satisfies the following relation:

$$\nabla\phi_D\left(\mathbf{x}_m\right) \cdot \mathbf{n}_m = -\nabla\phi_I\left(\mathbf{x}_m\right) \cdot \mathbf{n}_m \tag{6.8}$$

The incident pressures are solved for external and internal surfaces of each segment, while diffraction pressures are only solved on external surfaces. Irregular frequencies are suppressed by amending homogeneous boundary conditions on the lid and gap panels to the system of linear equations which define the diffraction problem:

$$\nabla\phi_D\left(\mathbf{x}_m\right) \cdot \mathbf{n}_m = \mathbf{0} \quad \text{for all lid, gap panels} \tag{6.9}$$

Incident and diffraction pressures are solved using the linearized Bernoulli's equation and integrated over the surface of each floater to obtain nodal finite element forces and moments, which are assembled as generalized force vectors $\mathbf{f_I^s}(\omega)$ and $\mathbf{f_D^s}(\omega)$, respectively. Modal incident $\mathbf{f}_I(\omega)$ and diffraction $\mathbf{f}_D(\omega)$ forces are solved for each mode i:

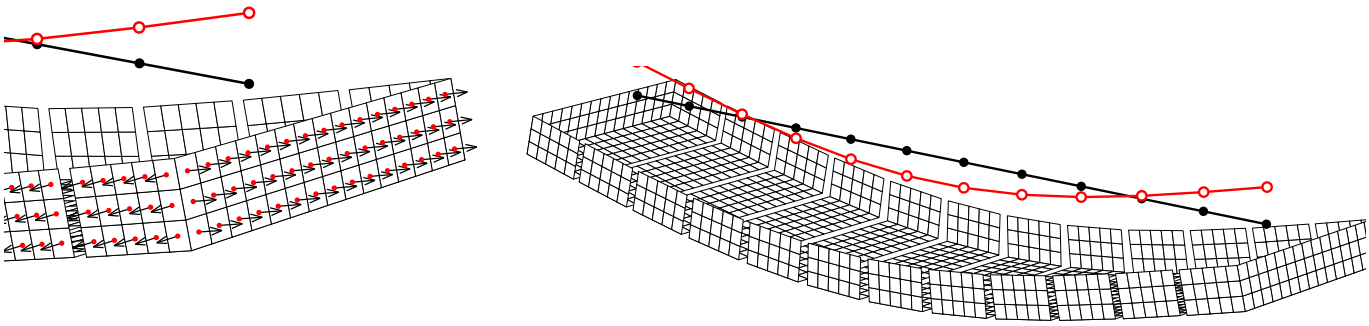
$$\mathbf{f}_I(\omega) = \mathbf{h}_i^T \mathbf{f_I^s}(\omega) \qquad \mathbf{f}_D(\omega) = \mathbf{h}_i^T \mathbf{f_D^s}(\omega) \tag{6.10}$$

Boundary Element Method Implementation The boundary element method was initially implemented using the expressions provided in Newman [24]. The evaluation of this Green's function and its normal derivative is rather slow, but very accurate. To accelerate simulations, the FORTRAN routines developed for NEMOH and implemented in the open source Python software Capytaine are used [142, 143]. Both methods are compared against analytical solutions for a surging and heaving sphere. All results obtained for the segmented barge use Capytaine for the evaluation of the Green's function and its normal derivative [142, 143].

Projection onto Collocation Points The elemental displacements and rotations $\mathbf{d}_{\mathbf{e}j}$ of each finite element eigenvector $\mathbf{h}_j$ are projected onto the collocation points and normal vectors to obtain modal added mass, damping, and hydrostatic restoring coefficients. Each eigenvector is multiplied by a small scalar to enforce hydrostatic and gravity linearity numerically. To project nodal displacement onto the collocation points, the first order rotation matrix $\mathbf{R}^{(1)}(\theta)$ is used [144].

$$\mathbf{R}^{(1)}(\theta) = \begin{bmatrix} \cos\theta & 0 & \sin\theta \\ 0 & 1 & 0 \\ -\sin\theta & 0 & \cos\theta \end{bmatrix} \approx \begin{bmatrix} 1 & 0 & \theta \\ 0 & 1 & 0 \\ -\theta & 0 & 1 \end{bmatrix} \tag{6.11}$$

The first order displacements and rotations at each collocation point are evaluated using the vector of generalized nodal displacements for each mode $\mathbf{h}_j$. Since the connection point of each segment is coincident with the x-coordinate of each finite element node, the displacement and rotation of each segment origin reduces to the nodal displacement and rotation.



(a) Displaced collocation points and rotated vectors.

(b) Displaced and rotated hydrodynamic mesh panels.

Figure 6.3: Projection of the first vertical bending mode on the hydrodynamic mesh panels, collocation points, and normal vectors. The finite element nodes and elements are shown along with the displaced nodes. Only exterior panels are shown.

Radiation Pressure and Modal Coefficients The complex radiation potentials are solved numerically using the projected mode shapes $\mathbf{h}_j$ and the boundary element method.

$$\nabla\phi_{Rj}(\mathbf{x}_m) \cdot \mathbf{n}_m = i\omega \mathbf{h}_j \cdot \mathbf{n}_m \tag{6.12}$$

Radiation pressures are solved using the linearized Bernoulli's equation and integrated over the surface of each floater to obtain nodal finite element forces and moments $\mathbf{f}^{\mathbf{s}}_{Rj}(\omega)$. Modal added mass $\mathbf{A}_{ij}$ and damping coefficients $\mathbf{B}_{ij}$ are solved for each combination of modes i and j.

$$\omega^2 \mathbf{A}_{ij}(\omega) - i\omega \mathbf{B}_{ij}(\omega) = \mathbf{h}_i^T \mathbf{f}^{\mathbf{s}}_{Rj}(\omega) \tag{6.13}$$

The added mass at infinite frequency is critical for the accuracy of a time domain simulation using the impulse equation of motion. The infinite frequency Green's function simplifies enormously because the wave number K is proportional to the square of frequency; only the limit $\left(R^2 - Z^2\right)^{-1/2}$ remains.

Gravity Forces and Restoring Coefficients The force of gravity constitutes a first-order restoring moment due to nodal rotations. Restoring coefficients are obtained by multiplying each finite element force vector by a generalized mode $\mathbf{h}_i$. Linearization is imposed numerically by means of perturbing the model from equilibrium by a small amplitude $\delta\boldsymbol{\xi}_j$.

$$\mathbf{G}_{ij}\delta\boldsymbol{\xi}_j = \mathbf{h}_i^T \delta\mathbf{f}_{Gj}^{\mathbf{s}} \tag{6.14}$$

Hydrostatic Pressure and Modal Coefficients The sum of zeroth and first order hydrostatic pressures are solved for each collocation point $\mathbf{x}_m$ using the vertical displacements w associated with each mode j. Linearization is imposed numerically by scaling each eigenvector $\mathbf{h}_j$ by a small amplitude $\delta\boldsymbol{\xi}_j$ such that $\delta\mathbf{h}_j = \mathbf{h}_j\delta\boldsymbol{\xi}_j$. Hydrostatic restoring coefficients are solved for each combination of modes i and j by projecting small nodal perturbations onto the hydrodynamic mesh and integrating the resulting change in hydrostatic pressures over the wetted panels:

$$\mathbf{C}_{ij}\delta\boldsymbol{\xi}_j = \mathbf{h}_i^T \delta\mathbf{f}_{Cj}^{\mathbf{s}} \tag{6.15}$$

Interpolation and Extrapolation of Damping Coefficients Damping coefficients can only be calculated for a limited, discrete set of frequencies due to computational constraints [1]. The maximum frequency $\omega_{\max}$ is limited by the associated minimum wavelength $\lambda_{\min}$ which, in this thesis, is set using the Nyquist frequency criterion. The damping coefficients are interpolated on an array of monotonically increasing frequencies and extrapolated by fitting a polynomial to the tail of the discrete, calculated damping values. The damping coefficients above $\omega_{\max}$ can be estimated using an exponential decay law with coefficients satisfying the following expressions:

$$\mathbf{B}_{ij}(\omega)\big|_{\omega>\omega_{\max}} = a_{ij}e^{b_{ij}\omega} \qquad a_{ij}e^{b_{ij}\omega_{\max}} = \mathbf{B}_{ij}(\omega)\big|_{\omega=\omega_{\max}} \qquad b_{ij}a_{ij}e^{b_{ij}\omega_{\max}} = \left.\frac{\partial\mathbf{B}_{ij}(\omega)}{\partial\omega}\right|_{\omega=\omega_{\max}} \tag{6.16}$$

The discrete modal damping coefficients for frequencies below $\omega_{\max}$ may result in over- or underestimates of the partial derivative if only two points are used. To obtain a more reliable slope estimate, a polynomial is fitted to the calculated damping coefficients such that:

$$\mathbf{B}_{ij}(\omega)\big|_{\omega\leq\omega_{\max}} \approx c_0 + c_1\omega + \ldots + c_n\omega^n \qquad \left.\frac{\partial\mathbf{B}_{ij}(\omega)}{\partial\omega}\right|_{\omega=\omega_{\max}} \approx c_1 + \ldots + nc_n\omega_{\max}^{n-1} \tag{6.17}$$

Solving for the coefficients a_{ij} and b_{ij} results in the following expressions:

$$a_{ij} = \frac{\mathbf{B}_{ij}(\omega_{\max})}{e^{b_{ij}\omega_{\max}}} \qquad b_{ij} = \frac{1}{\mathbf{B}_{ij}(\omega_{\max})}\left.\frac{\partial\mathbf{B}_{ij}(\omega)}{\partial\omega}\right|_{\omega=\omega_{\max}} \tag{6.18}$$

The coefficient b_{ij} should be strictly negative, as the damping coefficient tends to 0 as $\omega \to \infty$. The extrapolation procedure outlined above is illustrated using the damping coefficients of a heaving and surging half-sphere. The extrapolated added mass coefficients are also estimated using the Kramer-Kronig relations. As a result, an estimate of the infinite added mass is obtained.

To evaluate the pressures acting on the hull surface due to higher-order vibrations, the same procedure is done for every collocation point on the hull. Nodal (structural, denoted $^{\mathbf{s}}$) radiation force vectors $\mathbf{f}_{nj}^{\mathbf{s}}(\omega)$ have been solved for every collocation point n and mode j for a discrete set of frequencies ω, as the first step of solving for the modal damping coefficients. Recall that this vector is complex valued, and that the real and imaginary parts are used to obtain the coupled modal added mass and damping coefficients, respectively.

Impulse Response Functions The real radiation force can be evaluating in the time domain through convolution of the modal velocity and impulse response functions $\mathbf{K}^{\mathbf{h}}_{ij}(t)$.

$$\mathbf{K}^{\mathbf{h}}_{ij}(t) = \frac{2}{\pi}\int_0^{\infty} \left(\mathbf{B}_{ij}\left(\omega\right) - \mathbf{B}_{ij}(\infty)\right)\cos\left(\omega t\right) d\omega \approx \frac{2}{\pi}\sum_{k=1}^{N} \left(\mathbf{B}_{ij}\left(\omega_k\right) - \mathbf{B}_{ij}(\omega_N)\right)\cos\left(\omega_k t\right)\Delta\omega_k \tag{6.19}$$

$$\mathbf{K}^{\mathbf{h}}_{ij}(t) = \frac{2}{\pi}\int_0^{t_0} \left(\mathbf{B}_{ij}\left(\omega\right) - \mathbf{B}_{ij}(\infty)\right)\cos\left(\omega t\right) d\omega \approx \frac{2}{\pi}\sum_{k=1}^{N} \left(\mathbf{B}_{ij}\left(\omega_k\right) - \mathbf{B}_{ij}(\omega_N)\right)\cos\left(\omega_k t\right)\Delta\omega_k \tag{6.20}$$

The width of each frequency bin $\Delta\omega_k$ is set such that the damping functions do not repeat within the time interval $[t, t_0]$. The following criteria is used: $\Delta\omega_k \leq 2\pi/t_0$. Repeating damping functions would introduce erroneous radiation forces long after the initial motion becomes numerically insignificant. The impulse response functions are also evaluated for every finite element radiation damping vector and for pressures at selected collocation points.

Evaluation of Zero-Frequency Radiation Coefficients Added mass and damping coefficients cannot be calculated when the frequency is 0. To extrapolate between $\omega = 0$ and the first calculated frequency, the limit of Equations 6.21 and 6.22 as $\omega \to 0$ is taken. The zero-frequency damping values are only used for verification of the implementation, since they must be equal to zero.

$$\mathbf{A}_{ij}(0) \approx \mathbf{A}_{ij}(\infty) - \lim_{\omega\to 0}\left(\frac{1}{\omega}\sum_n \mathbf{K}^{\mathbf{h}}_{ij}(t_n)\sin\left(\omega t_n\right)\Delta t\right) = \mathbf{A}_{ij}(\infty) - \sum_n \mathbf{K}^{\mathbf{h}}_{ij}(t_n) t_n \Delta t \tag{6.21}$$

$$\mathbf{B}_{ij}(0) \approx \mathbf{B}_{ij}(\infty) + \lim_{\omega\to 0}\left(\sum_n \mathbf{K}^{\mathbf{h}}_{ij}(t_n)\cos\left(\omega t_n\right)\Delta t\right) = \mathbf{B}_{ij}(\infty) + \sum_n \mathbf{K}^{\mathbf{h}}_{ij}(t_n)\Delta t \tag{6.22}$$

Extrapolation of Added Mass Coefficients: Kramers-Kronig Relations Added mass coefficients are extrapolated using the damping functions and the infinite added mass values by means of the Kramers-Kronig relations. The highest frequency is dictated by the Nyquist frequency corresponding to the uniform time step. Extrapolation up to this frequency is required not only for the calculation of wet mode shapes, but also to ensure that the coefficients are estimated at the frequencies obtained using a fast Fourier transform of the modal amplitudes. This is required for estimating radiation pressures in the time domain.

$$\begin{aligned} \mathbf{A}(\omega) &= \mathbf{A}(\infty) - \frac{1}{\omega}\int_0^{\infty} \mathbf{K}^{\mathbf{h}}(t)\sin\left(\omega t\right) dt & \mathbf{B}(\omega) &= \mathbf{B}(\infty) + \int_0^{\infty} \mathbf{K}^{\mathbf{h}}(t)\cos\left(\omega t\right) dt \\ &\approx \mathbf{A}(\infty) - \frac{1}{\omega}\sum_n \mathbf{K}^{\mathbf{h}}(t_n)\sin\left(\omega t_n\right)\Delta t & &\approx \mathbf{B}(\infty) + \sum_n \mathbf{K}^{\mathbf{h}}(t_n)\cos\left(\omega t_n\right)\Delta t \end{aligned} \tag{6.23}$$

Sea States Various spectra exist for defining irregular linear sea states that satisfy the first order boundary value problem outlined in Chapter 2, Section 2.2.2. In this thesis, the Pierson-Moskowitz spectrum is used for generating frequency and time domain irregular wave profiles, and is defined using significant wave height H_s and mean zero-crossing period T_p [33]. Wave elevations are calculated for each frequency ω using the associated spectral values $S(\omega)$ and bin width $\Delta\omega$ [1]: $\zeta_a(\omega) = \sqrt{2S(\omega)\Delta\omega}$. The maximum frequency bin width $\Delta\omega$ is set to avoid repeating the signal within time period t: $\Delta\omega \leq 2\pi/t$. The wave amplitude as a function of time $\zeta_a(t)$ is calculated using the inverse Fourier transform of the spectral values $\zeta_a(\omega)$: $\zeta_a(t) = \mathcal{F}^{-1}\left(\zeta_a(\omega)e^{i\epsilon}\right)$. Random phases ϵ are introduced to make the sea state irregular. Similarly, forces due to incident and diffraction pressures are solved for each time step at every collocation point $\mathbf{x}_m$ using the inverse Fourier transform of the frequency domain solution. The same random phases ϵ are included: $\mathbf{f}(\mathbf{x}_m, t) = \mathcal{F}^{-1}\left(\mathbf{f}(\mathbf{x}_m, \omega)\zeta_a(\omega)e^{i\epsilon}\right)$. The incident and diffraction forces are smoothly scaled from 0% to 100% of their prescribed amplitudes over a time period of 10 seconds to numerically enforce periodicity in the time domain, which is important for evaluating radiation pressures using the Fourier transform. In this model, a significant wave height of $H_s = 96$ [mm] and a mean zero-crossing period of $T_p = 1.6$ [s] are used,

in alignment with one of the test cases outlined in Tuitman [1]. A regular wave is formed using only one spectral component; in this case, the wave height is the significant wave height and the wave frequency is the inverse of the mean zero-crossing period.

Structural Response Loading of the finite element model consists of external pressures and internal inertial forces. The nodal displacements, in principle, can be found by multiplying the internal and external forces by the inverted structural stiffness matrix $\mathbf{K^s}$. However, ship structures are free-floating: the structural stiffness matrix is singular and, when inverted, will result in rigid body nodal amplitude which is many orders of magnitude higher than the internal and external forces. No strain is induced by rigid body modes, so an alternative formulation is introduced for the purposes of evaluating the structural response, since rigid body motions have already been solved using either the modal frequency or time domain equations of motion.

Consider a force displaced by some small nodal excursion vector $\delta\mathbf{u}$. The internal and external virtual work must be equivalent: $\delta\mathbf{u}^T\left(\mathbf{K^s}\mathbf{u}-\mathbf{f}\right)=0$. Let the small arbitrary nodal excursion consist of both rigid body and elastic components: $\left(\delta\mathbf{u}_R^T+\delta\mathbf{u}_E^T\right)\left(\mathbf{K^s}\left(\mathbf{u}_E+\mathbf{u}_R\right)-\mathbf{f}\right)=0$. By definition, the rigid body response does not contribute to strain: $\delta\mathbf{u}_R^T\mathbf{K^s}=\mathbf{0}$. Further, a balanced model results in net zero rigid body forces: virtual rigid body work is zero: $\delta\mathbf{u}_R^T\mathbf{f}_R=\mathbf{0}$. Only the elastic nodal displacement remains: $\delta\mathbf{u}_E^T\left(\mathbf{K^s}\mathbf{u}_E-\mathbf{f}\right)=0$. Numerically, the elastic nodal displacements $\mathbf{u}_E$ can be found by minimizing the expression within brackets, since an arbitrary nodal excursion $\delta\mathbf{u}$ is used: $\mathbf{u}_E=\min\|\mathbf{K^s}\mathbf{u}_E-\mathbf{f}\|^2$. This form is equivalent to that used when estimating modal amplitudes from measured strains. Taking the derivative as done earlier results in the following equation:

$$\mathbf{u}_E=\left(\mathbf{K^s}^T\mathbf{K^s}\right)^{-1}\mathbf{K^s}^T\mathbf{f}=\mathbf{K^s}^+\mathbf{f} \tag{6.24}$$

The elastic structural response $\mathbf{u}_E$ is solved in the time domain by first calculating the radiation forces. Added mass and damping coefficients are only available in the frequency domain; to obtain the time domain radiation force, the Fourier transform is used. The time domain modal amplitudes are flipped about the time axes and the complex conjugate of the radiation force vector is placed on the negative time axis. The inverse Fourier transform is then applied to the product of these two complex frequency domain arrays. The frequency and time domain forces are found to be equivalent. The same procedure is applied to obtain radiation pressures in the time domain.

$$\mathbf{u}(t)=\mathbf{K^s}^+\left(\mathbf{M^s}\mathbf{H}\boldsymbol{\xi}_{tt}(t)-i\omega\mathbf{D^s}\mathbf{H}\boldsymbol{\xi}_t(t)-\mathbf{f}_C^{\mathbf{s}}\mathbf{H}\boldsymbol{\xi}(t)+\mathbf{f}_R^{\mathbf{s}}(t)++\mathbf{f}_I^{\mathbf{s}}(t)+\mathbf{f}_D^{\mathbf{s}}(t)\right) \tag{6.25}$$

$$\mathbf{f}_R^{\mathbf{s}}(t)\approx\mathrm{Re}\left[\mathcal{F}^{-1}\left(\mathbf{f}_R^{\mathbf{s}}(\omega)\mathcal{F}\left(\boldsymbol{\xi}(t)\right)\right)\right] \tag{6.26}$$

6.1.3 Transient

The equation of motion for transient analysis is identical to that of the steady state formulation except for the addition of a modal impulse load $\mathbf{f}_S(t)$.

$$\left(\mathbf{M}+\mathbf{A}(\infty)\right)\boldsymbol{\xi}_{tt}+\left(\mathbf{B}(\infty)+\mathbf{D}\right)\boldsymbol{\xi}_t+\left(\mathbf{C}+\mathbf{G}+\mathbf{K}\right)\boldsymbol{\xi}+\underbrace{\int_0^t\mathbf{K^h}(t-\tau)\boldsymbol{\xi}_t(\tau)\,d\tau}_{\mathbf{f}_K(t)}=\mathbf{f}_I(t)+\mathbf{f}_D(t)+\mathbf{f}_S(t) \tag{6.27}$$

$$\begin{bmatrix}\mathbf{0} & \mathbf{I}\\ -\left(\mathbf{M}+\mathbf{A}(\infty)\right)^{-1}\left(\mathbf{C}+\mathbf{G}+\mathbf{K}\right) & -\left(\mathbf{M}+\mathbf{A}(\infty)\right)^{-1}\left(\mathbf{B}(\infty)+\mathbf{D}\right)\end{bmatrix}\begin{bmatrix}\boldsymbol{\xi}(t^{n+1})\\ \boldsymbol{\xi}_t(t^{n+1})\end{bmatrix}$$
$$=\begin{bmatrix}\mathbf{0}\\ \left(\mathbf{M}+\mathbf{A}(\infty)\right)^{-1}\left(-\mathbf{f}_K(t^n)+\mathbf{f}_I(t^n)+\mathbf{f}_D(t^n)+\mathbf{f}_S(t^n)\right)\end{bmatrix} \tag{6.28}$$

The segmented barge as implemented lacks slamming-prone geometry. To evaluate the effects of such an impulse on the loading and response, a vertical force with amplitude $f_S=200$ [N] is applied to the bow

node as a boxcar function starting at time $t_0 = 59$ [s] with duration $\Delta t_S = 0.1$ [s] and smoothed using a Hann window. The modal force components are obtained by multiplying the finite element force vector by the matrix of eigenvectors $\mathbf{H}$.

$$\mathbf{f}_S(t) = \mathbf{H}^T \mathbf{f}_S^{\mathbf{s}}(t) \tag{6.29}$$

6.1.4 Verification

The methods outlined in Sections 6.1.2 and 6.1.3 are verified using three models: a vertical wall, for verifying the calculation of incident and diffraction potentials using the boundary element method; a heaving and surging half sphere, for verifying the calculation of radiation potentials and the time domain solver for a single degree of freedom system; and a flexible segmented barge (Configuration 2), for verifying the hydrostructural model in the frequency and time domains. While some discrepancies are noted between values from literature and those obtained using the current method, especially for the segmented barge RAO, reasonable agreement is observed across all models.

Vertical Wall

The implementation of incident and diffracted potentials is verified against analytical solutions for the wave pressure exerted on a fixed wall in the $y - z$ plane due to head waves ($\mu = 180\,\text{deg}$). A wall of width $B = 200$ meters and draft $T = 50$ meters is discretized using 101×50 quadrilateral panels. An incoming wave frequency of $\omega = 1$ radians per second is considered. Under the deep water assumption, the force decays to less than 1% of its maximum free-surface value above the selected draft of the wall, $B = 50$ meters. The resulting pressures are plotted along the vertical axis z. The wall is not infinite; waves diffract around the edges, leading to a periodic imaginary component and reduced forces near the edges, at $y = -B/2$ and $y = B/2$. The numerical result converges to the analytical solution, indicating that method used for evaluating potential source strengths at each collocation point is sufficiently accurate.

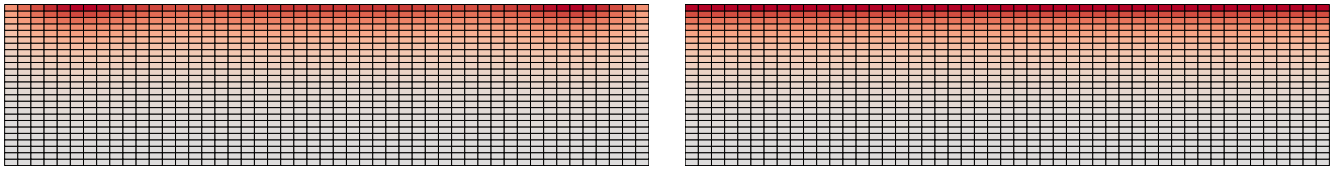


Figure 6.4: Normalized real component of diffraction (left) and incident (right) pressures acting on a semi-infinite wall. Periodic fluctuations are observed in the diffraction pressure due to edge effects. The structured, uniform, quadrilateral mesh is superimposed on the plot.

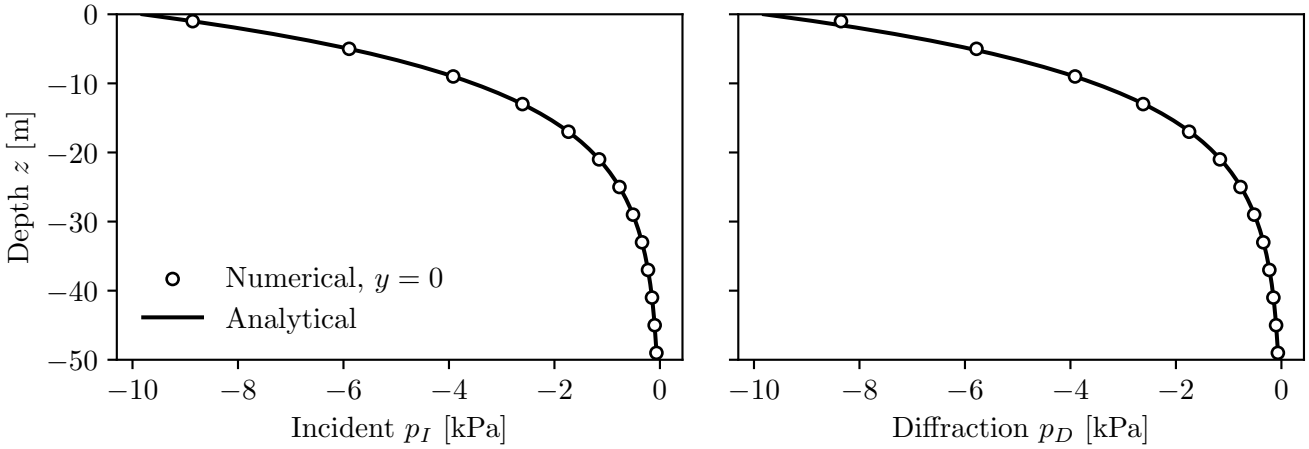


Figure 6.5: Numerical and analytical solutions of incident and diffracted wave pressures acting on a wall in the $y - z$ plane at $x = 0$ and $y = 0$.

Half Sphere in Surge and Heave

To verify the numerical methods used to evaluate radiation potentials at discrete points on the segmented barge, a half-sphere is discretized using quadrilateral panels, as shown in Figure 6.6. The calculated added mass and damping coefficients for surge and heave modes are compared with analytical and numerical results from literature in Figure 6.7. Damping coefficients are then extrapolated using the exponential decay function and plotted in Figure 6.8. The Kramers-Kronig relations are used to extrapolate added mass to high frequencies using the damping coefficients; the results are plotted in Figure 6.10. A (heave) free decay simulation is performed to verify implementation of the historical damping force; the vertical displacement is compared to experimental and numerical results in Figure 6.11.

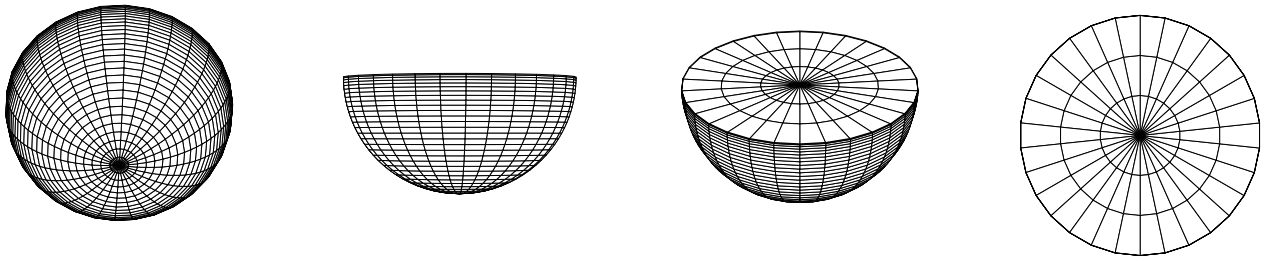


Figure 6.6: Hydrodynamic mesh of a half-sphere. Submerged and lid panels are shown at four roll angles about the x-axis. Quadrilateral elements are scaled near the equator to improve accuracy of the surge coefficients. Lid panels are shown in the top (right-hand) view.

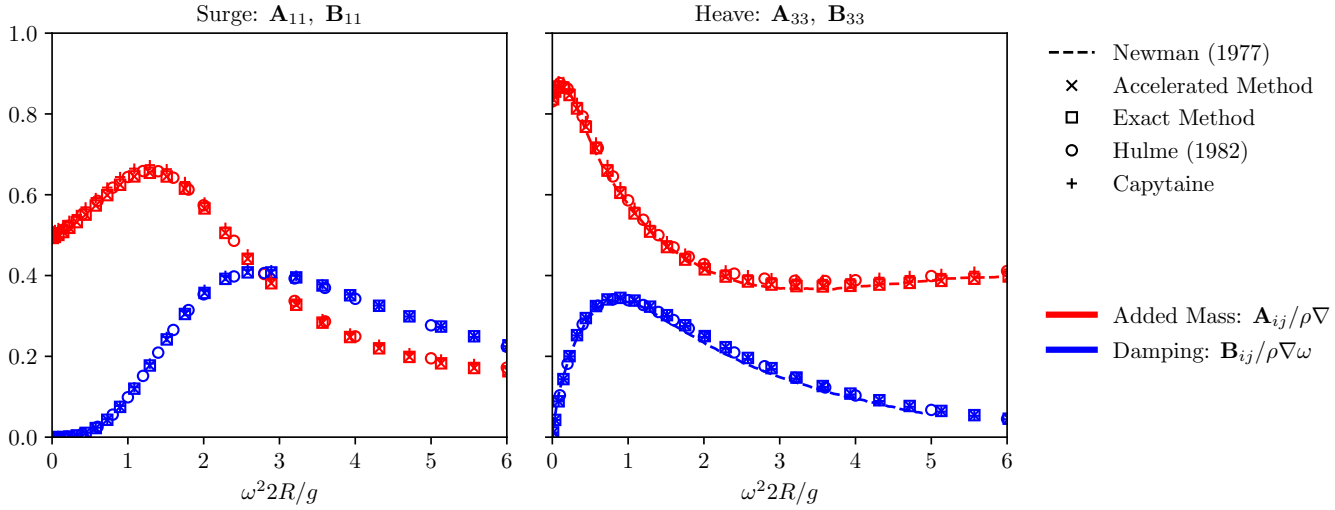


Figure 6.7: Non-dimensional added mass and damping coefficients for a half-sphere of diameter D in heave and surge; analytical and numerical examples from literature [145, 13] and an open-source boundary element method software [142, 143] are compared with the present exact (derived) and accelerated (using Capytaine's FORTRAN routine) values.

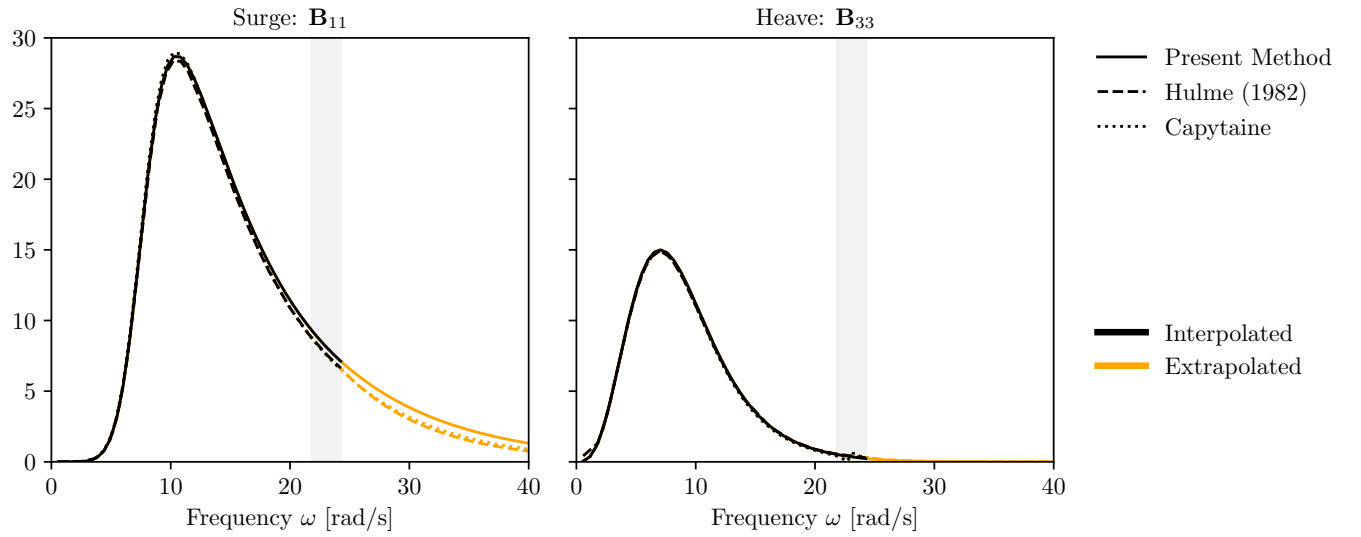


Figure 6.8: Interpolated and extrapolated damping coefficients for a half-sphere. The range of values used for evaluating the polynomial coefficients is highlighted in gray.

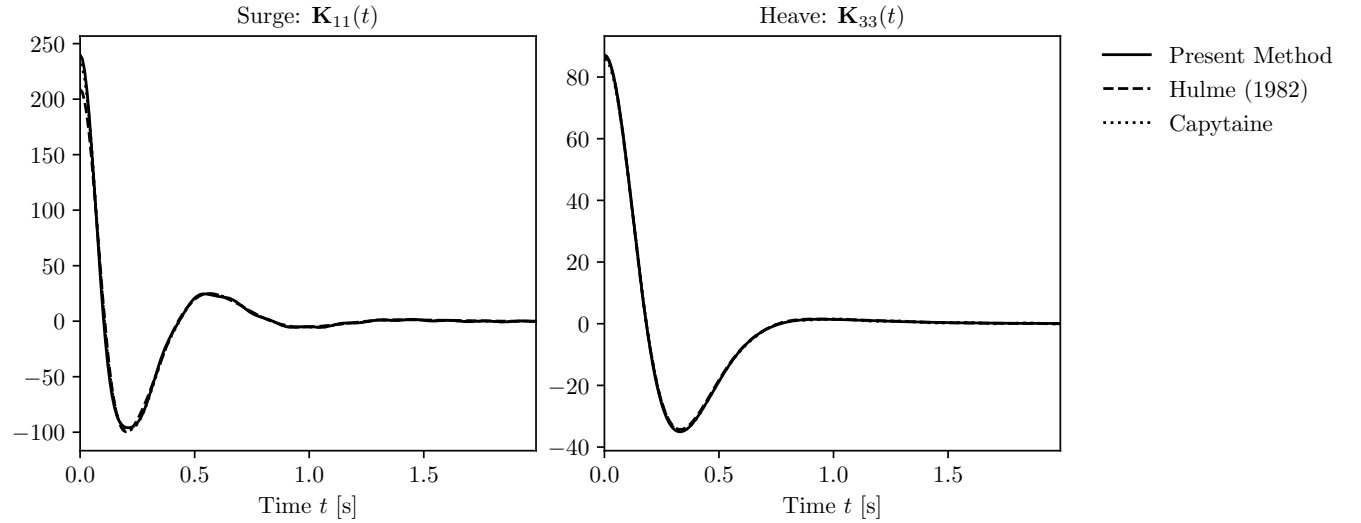


Figure 6.9: Damping functions $\mathbf{K}_{ij}(t)$ plotted for surge and heave of a half-sphere. Comparison is made between the present (accelerated) method, analytical values [145], and numerical results from Capytaine [142].

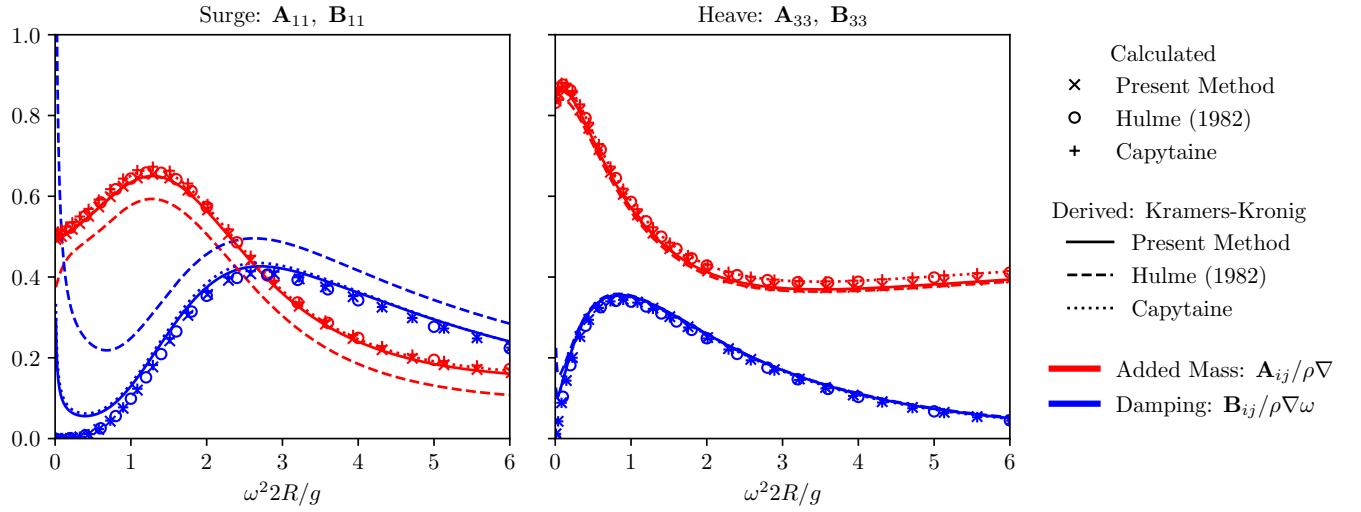


Figure 6.10: Non-dimensional added mass and damping coefficients for a half-sphere in surge and heave derived from interpolated and extrapolated damping coefficients by means of the Kramers-Kronig relations.

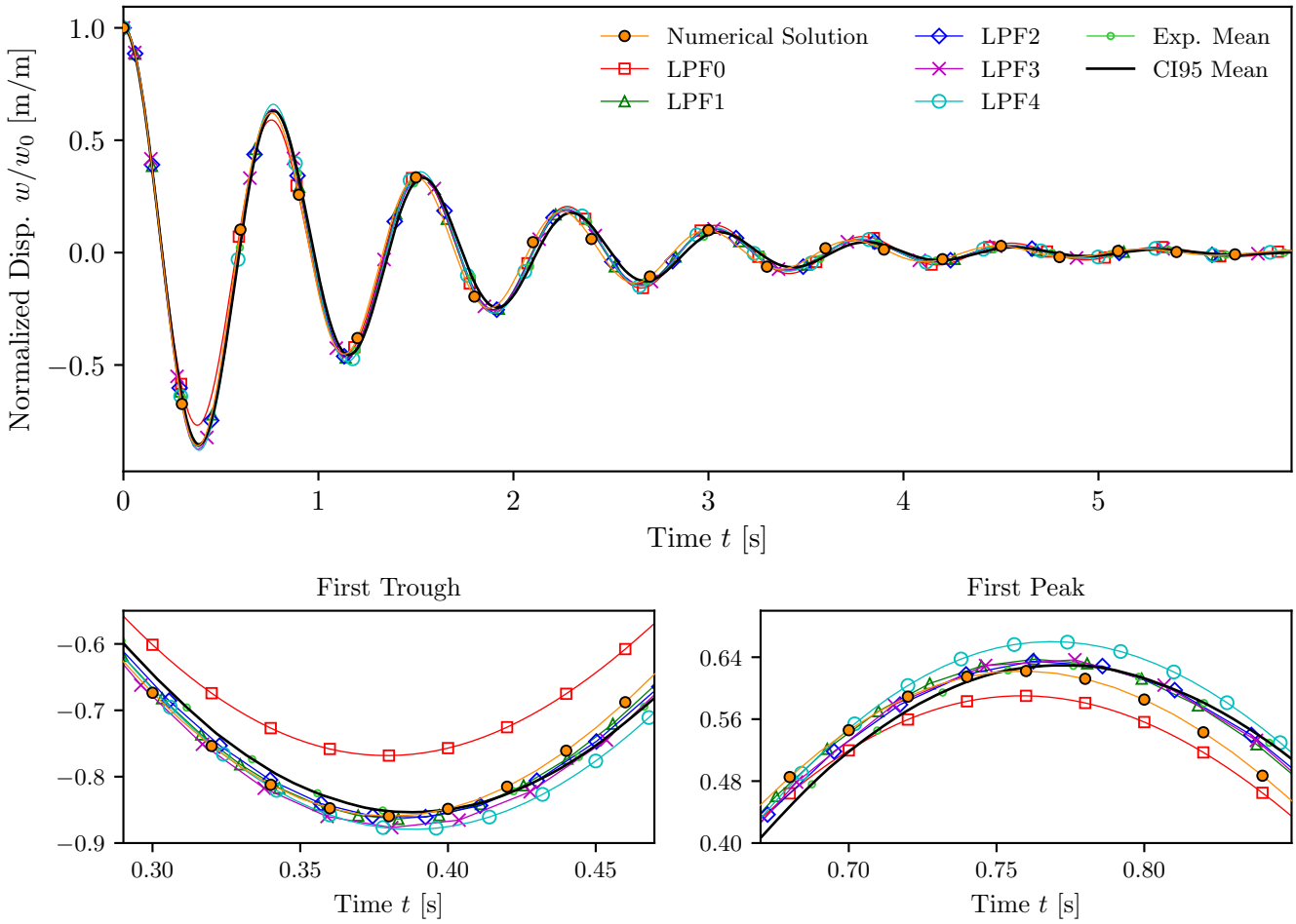


Figure 6.11: Free decay of a half-sphere, normalized to the initial heave position. Results from the implementation in this thesis are superimposed on analytical, numerical, and experimental results from literature [146]; model names in the legend correspond exactly with those from literature. The first trough and peak are highlighted to illustrate accuracy in the time domain.

Flexible Segmented Barge

To verify the hydrostructural model, the methods outlined in this section and verified for a single degree of freedom system, a heaving half sphere, are extended to the flexible segmented barge (Configuration 2, backbone thickness of 4 mm). A free decay test, RAO evaluation, and wet modal analysis are performed. The equation of motion for the free decay test is as follows:

$$(\mathbf{M}+\mathbf{A}(\infty))\,\boldsymbol{\xi}_{tt}+\mathbf{B}(\infty)\boldsymbol{\xi}_t+(\mathbf{C}+\mathbf{G}+\mathbf{K})\,\boldsymbol{\xi}+\underbrace{\int_0^t \mathbf{K}^{\mathbf{h}}(t-\tau)\boldsymbol{\xi}_t(\tau)\,d\tau}_{\mathbf{f}_K(t)}=0 \tag{6.30}$$

The equation of motion is then expressed in state-space form and substituted into a fourth-order Runge-Kutta solver with uniform time stepping.

$$\begin{bmatrix}\mathbf{0} & \mathbf{I}\\ -(\mathbf{M}+\mathbf{A}(\infty))^{-1}(\mathbf{C}+\mathbf{G}+\mathbf{K}) & -(\mathbf{M}+\mathbf{A}(\infty))^{-1}\mathbf{B}(\infty)\end{bmatrix}\begin{bmatrix}\boldsymbol{\xi}(t^{n+1})\\ \boldsymbol{\xi}_t(t^{n+1})\end{bmatrix}=\begin{bmatrix}\mathbf{0}\\ -(\mathbf{M}+\mathbf{A}(\infty))^{-1}\mathbf{f}_K(t^n)\end{bmatrix} \tag{6.31}$$

The modal initial conditions $\boldsymbol{\xi}_0$ are estimated using the method of least squares, which is consistent with Malenica et al. [38]:

$$\boldsymbol{\xi}_0=(\mathbf{C}+\mathbf{G}+\mathbf{K})^{-1}\mathbf{H}^T\mathbf{f}_0 \tag{6.32}$$

The amplitude of force vector $\mathbf{f}_0$ is set such that the vertical displacement at the bow mode is reasonably close to that shown in literature. To avoid fitting Rayleigh damping coefficients to match a model which used an entirely different damping method, the free decay response obtained from the undamped model is emphasized for validation. The frequency at which the segments decay matches experimental and numerical values, as do the first three extrema. Variations are observed after $t = 2.5$ seconds, which is expected given the nonlinear aspects of the model from literature. What is perhaps more surprising is the extent to which the first three extrema match those from the nonlinear undamped model. The initial displacement guarantees nonlinearity, but the amplitudes of each extrema are nearly the same.

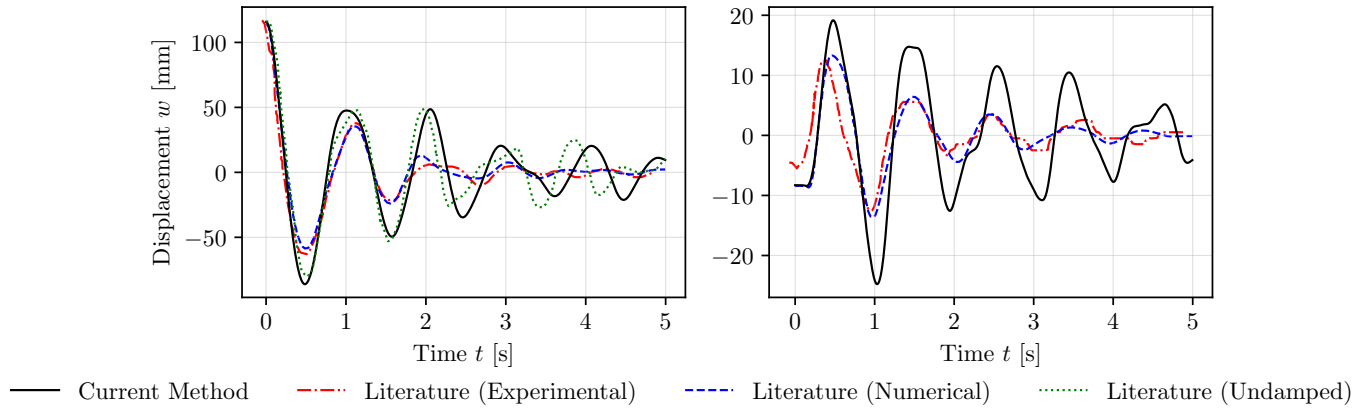


Figure 6.12: A comparison of the free decay response of the first floater of the segmented barge (Configuration 2) displaying numerical and experimental results from literature and the current method. No damping is included in the results of the current method. Left: bow floater. Right: 7th floater from bow.

The frequency domain calculations are compared with those from literature by means of the vertical displacement RAO at the first (bow) floater. Note that the RAO from literature is evaluated using spectral methods from a time domain simulation; irregular waves were used. Nonlinear effects are therefore included in the RAO values from literature. The low frequency response is well-matched, but discrepancies are observed both in amplitude and peak position starting from $\omega = 5.5$ rad/s.

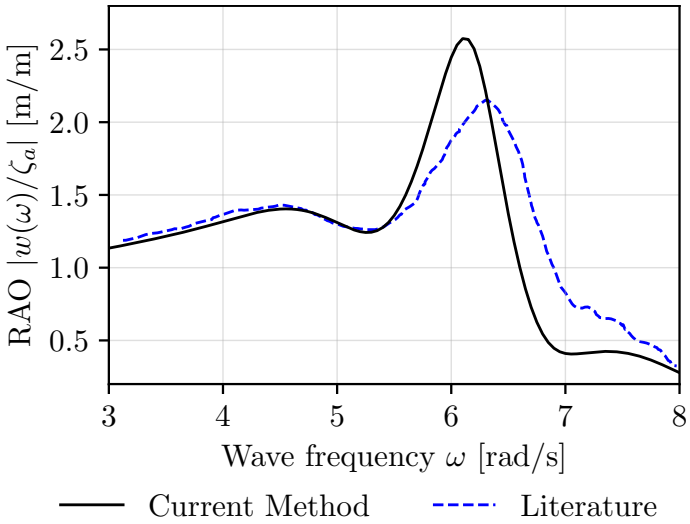


Figure 6.13: Response Amplitude Operators (RAO) for the first floater of the segmented barge in head seas. The current method is compared with the multi-body approach from Tuitman [1], without damping.

The third method of verification is the comparison of wet natural frequencies from literature. The first three modes are very close to those obtained by Tuitman [1], while the 2nd vertical bending moment differs from the analytical and numerical values from literature. This difference could be explained by the mass properties of the segments, which are not available in literature. Mass properties in this thesis are calculated based on the geometry and basic hydrostatics. The elastic modulus of the backbone is tuned such that the analytical wet natural frequencies match those presented in Malenica et al. [38].

Mode	Analytical	Numerical (Malenica)	Numerical (Tuitman)	Current Method
Heave	5.50	5.50	5.45	5.47
Pitch	5.50	5.71	5.68	5.66
1st VBM	6.17	6.45	6.27	6.26
2nd VBM	9.43	9.56	9.68	9.17

Table 6.1: Wet natural frequencies (radians per second) of the flexible segmented barge (Configuration 2), compared with values from literature.

6.2 Stress and Pressure Estimation

The frequency and time domain analyses result in nodal displacements and rotations of the finite element model and incident, diffraction, radiation, and hydrostatic pressures at each collocation point. The frequency domain results are used to construct modal bases for estimating structural stresses and external pressures in the time domain. Strain gauges are positioned based on the structural response associated with each mode shape, and Gaussian noise is introduced to simulate measurement noise. A method of identifying the optimal Tikhonov regularization parameter is introduced and evaluated using a static test case. The following subsection illustrates how filtering is used to separate the quasi-static and dynamic responses for the purposes of estimating modal amplitudes. Finally, the equations used for calculating hydrostatic and hydrodynamic pressures based on the modal time domain solution are presented.

6.2.1 Modal Bases

Wet Modes

To determine the complex radiation pressures associated with each wet mode, the modal amplitudes are first solved for each frequency ω by decomposing the homogeneous equation of motion into a linear system, as shown in Equation (6.34). The wet natural frequencies for stiff ships cannot be calculated directly; to approximate the added mass and damping coefficients at high frequencies, the interpolation, extrapolation, and Kramers-Kronig procedure outlined in the previous section is used.

$$\left(\lambda^2 \left(\mathbf{M} + \mathbf{A}(\omega)\right) + \lambda \left(\mathbf{B}(\omega) + \mathbf{D}\right) + \mathbf{C} + \mathbf{G} + \mathbf{K}\right) \boldsymbol{\xi} = \mathbf{0} \tag{6.33}$$

$$\begin{bmatrix} \mathbf{0} & \mathbf{I} \\ -\left(\mathbf{M} + \mathbf{A}(\omega)\right)^{-1} \left(\mathbf{C} + \mathbf{G} + \mathbf{K}\right) & -\left(\mathbf{M} + \mathbf{A}(\omega)\right)^{-1} \left(\mathbf{B}(\omega) + \mathbf{D}\right) \end{bmatrix} \begin{bmatrix} \boldsymbol{\xi} \\ \lambda\boldsymbol{\xi} \end{bmatrix} = \lambda \begin{bmatrix} \boldsymbol{\xi} \\ \lambda\boldsymbol{\xi} \end{bmatrix} \tag{6.34}$$

Solving the eigenvalue problem for each frequency results in a series of complex eigenvalues $\boldsymbol{\lambda}(\omega)$ and eigenvectors $\boldsymbol{\xi}(\omega)$. The imaginary part of each eigenvalue corresponds to the frequency at which the associated eigenvector oscillates. The wet natural frequencies are found by identifying the minimum differences between the input frequency ω and the imaginary part of the eigenvalues corresponding to each mode.

$$\omega_j = \arg\min \left(\| \omega - \mathrm{Im}\left(\lambda_j\right) \| \right) \tag{6.35}$$

The modal amplitudes defining each wet mode j are selected based on the indices of each wet natural frequency ω_j: $\boldsymbol{\xi}_j = \boldsymbol{\xi}\left(\omega_j\right)$. The eigenvalues and eigenvectors satisfy the following equation of motion:

$$\left(\lambda_j^2 \left(\mathbf{M} + \mathbf{A}\left(\mathrm{Im}(\lambda_j)\right)\right) + \lambda_j \left(\mathbf{B}\left(\mathrm{Im}(\lambda_j)\right) + \mathbf{D}\right) + \mathbf{C} + \mathbf{G} + \mathbf{K}\right) \boldsymbol{\xi}_j = \mathbf{0} \tag{6.36}$$

The wet modal basis thus consists of real and imaginary parts, but the vibratory response of stiff ships due to impulse loads is characterized by high frequencies, where radiation damping pressures tend to zero. Pressure due to added mass scales with ω^2, meaning it dominates hydroelastic loading at higher frequencies and the imaginary part of the wet modal basis can be neglected without significantly affecting the response estimates. For this reason, the first and second wet modes, which correspond most closely with rigid body

heave and pitch motions, are discarded. Estimating the rigid body loading and response using wet modes requires complex (the sum of real and imaginary) amplitude estimates.

The structural response of each wet mode $\mathbf{h}_{\mathrm{w}j}$ is solved by substituting the frequency ω_j associated with the vector of modal amplitudes $\boldsymbol{\xi}$ into the structural frequency domain equation of motion. Each vector of generalized displacements $\mathbf{h}_{\mathbf{w}j}$ forms one column of the wet modal basis matrix $\mathbf{H}_{\mathrm{w}} = \begin{bmatrix} \mathrm{h}_{\mathrm{w}1} & \mathrm{h}_{\mathrm{w}2} & \dots & \mathrm{h}_{\mathrm{w}N} \end{bmatrix}$. The generalized nodal displacements are obtained by summing the modal contributions: $\mathbf{u}_{\mathrm{w}} = \mathbf{H}_{\mathrm{w}}\boldsymbol{\xi}_{\mathrm{w}}$

$$\mathbf{h}_{\mathrm{w}j} = \mathbf{K}^{\mathbf{s}+}\ \mathrm{Re}\Bigg(\underbrace{\left(\omega_j^2\mathbf{M}^{\mathbf{s}} - i\omega_j\mathbf{D}^{\mathbf{s}}\right)\mathbf{H}\boldsymbol{\xi}_j}_{\text{Internal}} + \underbrace{\left(\mathbf{f}_R^{\mathbf{s}}(\omega_j) + \mathbf{f}_C^{\mathbf{s}} + \mathbf{f}_G^{\mathbf{s}}\right)\boldsymbol{\xi}_j}_{\text{External}} \Bigg) \tag{6.37}$$

The wet modal basis is truncated to three modes. Each wet mode consists of structural response and external loading (pressure) information; the structural response is used for estimating the wet modal amplitudes $\boldsymbol{\xi}_{\mathrm{w}}$ and strains $\boldsymbol{\epsilon}_{\mathrm{w}}^{\mathbf{e}}$ at time step t^n.

$$\boldsymbol{\epsilon}_{\mathrm{w}}^{\mathbf{m}} = \mathbf{B}_{\boldsymbol{\epsilon}}^{\mathbf{m}}\mathbf{H}_{\mathrm{w}}\boldsymbol{\xi}_{\mathrm{w}} \quad \text{such that} \quad \boldsymbol{\xi}_{\mathrm{w}}^{\mathbf{e}}(t^n) = \left(\mathbf{B}_{\boldsymbol{\epsilon}}^{\mathbf{m}}\mathbf{H}_{\mathrm{w}}\right)^{+}\boldsymbol{\epsilon}_{\mathrm{w}}^{\mathbf{m}}(t^n) \quad \text{and} \quad \boldsymbol{\epsilon}_{\mathrm{w}}^{\mathbf{e}}(t^n) = \mathbf{B}_{\boldsymbol{\epsilon}}^{\mathbf{e}}\mathbf{H}_{\mathrm{w}}\left(\mathbf{B}_{\boldsymbol{\epsilon}}^{\mathbf{m}}\mathbf{H}_{\mathrm{w}}\right)^{+}\boldsymbol{\epsilon}_{\mathrm{w}}^{\mathbf{m}}(t^n) \tag{6.38}$$

The pressure $p_{\mathrm{w}_k}(\mathbf{x}_m)$ associated with each wet mode shape $\boldsymbol{\xi}_{\mathrm{w}_j}$ is calculated by summing the hydrostatic and radiation pressure contributions. Index j of $\boldsymbol{\xi}_{\mathrm{w}_{jk}}$ corresponds to the vector of wet modal amplitudes; k is the index within that vector corresponding to a generalized mode. Pressures at each collocation point $\mathbf{x}_m$ and time step t^n are estimated using the modal amplitudes $\boldsymbol{\xi}_{\mathrm{w}}^{\mathbf{e}}$.

$$p_{\mathrm{w}_j}(\mathbf{x}_m) = \mathrm{Re}\left[\sum_k \left(p_{C_k}(\mathbf{x}_m)\boldsymbol{\xi}_{\mathrm{w}_{jk}} + p_{R_k}(\mathbf{x}_m,\omega)\boldsymbol{\xi}_{\mathrm{w}_{jk}}\right)\right] \qquad p_{\mathrm{w}}^{\mathbf{e}}(\mathbf{x}_m,t^n) = \sum_j \left(p_{\mathrm{w}_j}(\mathbf{x}_m)\boldsymbol{\xi}_{\mathrm{w}_j}^{\mathbf{e}}(t^n)\right) \tag{6.39}$$

The frequencies associated with the first five wet mode shapes using the stiff backbone configuration (15 mm thickness) are shown in Table 6.2. Only the vertical bending modes (VBM) are used for the wet modal basis.

Mode:	Heave	Pitch	1st VBM	2nd VBM	3rd VBM
Frequency [rad/s]	5.5	5.6	21.2	54.8	101.0

Table 6.2: The wet natural frequencies of the first five wet mode shapes.

Distortion Modes

To arrive at the vector of generalized nodal displacements for the first distortion mode, the hydroelastic incident-diffraction problem is solved for modal amplitudes as a function of incident wave frequency ω and phase ϵ. This first step is required to determine the radiation pressures acting on the structure at a certain frequency and phase.

$$\boldsymbol{\xi}(\omega,\epsilon) = \left(-\omega^2\left(\mathbf{M}+\mathbf{A}(\omega)\right) + i\omega\left(\mathbf{D}+\mathbf{B}(\omega)\right) + \left(\mathbf{C}+\mathbf{G}+\mathbf{K}\right)\right)^{-1}\left(\mathbf{f}_I(\omega,\epsilon) + \mathbf{f}_D(\omega,\epsilon)\right) \tag{6.40}$$

The generalized nodal displacements as a function of frequency and phase are obtained by multiplying the sum of internal and external nodal force vectors by the inverted nodal structural stiffness matrix. The internal nodal forces consist of inertial (mass) and damping (Rayleigh) components, while the external nodal forces include incident, diffraction, radiation, hydrostatic, and gravity components.

$$\mathbf{h}(\omega,\epsilon) = \mathbf{K}^{\mathbf{s}+}\ \mathrm{Re}\Bigg(\underbrace{\left(\omega^2\mathbf{M}^{\mathbf{s}} - i\omega\mathbf{D}^{\mathbf{s}}\right)\mathbf{H}\boldsymbol{\xi}(\omega,\epsilon)}_{\text{Internal}} + \underbrace{\mathbf{f}_I^{\mathbf{s}} + \mathbf{f}_D^{\mathbf{s}} - \left(\mathbf{f}_R^{\mathbf{s}} - \mathbf{f}_C^{\mathbf{s}} - \mathbf{f}_G^{\mathbf{s}}\right)\boldsymbol{\xi}(\omega,\epsilon)}_{\text{External}} \Bigg) \tag{6.41}$$

The solution setup can be verified by evaluating whether the model is balanced: if the sum of vertical internal and external forces is equivalent, the equation above is valid. The first distortion mode $\mathbf{h}_1$ is equivalent to the

vector of nodal displacements which corresponds to a maximal vertical bending moment amidships ($x = 0$). The second mode is selected as the vector of nodal displacements which is most orthogonal to the first, where the dot product is used as a measure of orthogonality:

$$\mathbf{h}_{j+1} = \mathbf{h}_j(\omega, \epsilon) \quad \text{such that} \quad (\omega, \epsilon) \quad \text{minimize} \quad \|\mathbf{h}_i \cdot \mathbf{u}(\omega, \epsilon)\| \tag{6.42}$$

The distortion mode vectors form the column space of the truncated modal basis $\mathbf{H}_\mathrm{d} = \begin{bmatrix}\mathbf{h}_{\mathrm{d}_1} & \mathbf{h}_{\mathrm{d}_2} & \dots & \mathbf{h}_{\mathrm{d}_N}\end{bmatrix}$, where N is the dimension (number of modes). The generalized nodal displacement vector.

Mode	Frequency [rad/s]	Phase [rad]
Mode 1	4.3	3.1
Mode 2	7.7	4.5
Mode 3	8.8	1.7

Table 6.3: The frequencies and phases which define each distortion mode.

Each distortion mode consists of structural response and external loading (pressure) information; the structural response is used for estimating the distortion modal amplitudes $\boldsymbol{\xi}_\mathrm{d}$ and strains $\boldsymbol{\epsilon}^{\mathbf{e}}_\mathrm{d}$ at time step t^n.

$$\boldsymbol{\epsilon}^{\mathbf{m}}_\mathrm{d} = \mathbf{B}^{\mathbf{m}}_{\boldsymbol{\epsilon}}\mathbf{H}_\mathrm{d}\boldsymbol{\xi}_\mathrm{d} \quad \text{such that} \quad \boldsymbol{\xi}^{\mathbf{e}}_\mathrm{d}(t^n) = \left(\mathbf{B}^{\mathbf{m}}_{\boldsymbol{\epsilon}}\mathbf{H}_\mathrm{d}\right)^{+}\boldsymbol{\epsilon}^{\mathbf{m}}_\mathrm{d}(t^n) \quad \text{and} \quad \boldsymbol{\epsilon}^{\mathbf{e}}_\mathrm{d}(t^n) = \mathbf{B}^{\mathbf{e}}_{\boldsymbol{\epsilon}}\mathbf{H}_\mathrm{d}\left(\mathbf{B}^{\mathbf{m}}_{\boldsymbol{\epsilon}}\mathbf{H}_\mathrm{d}\right)^{+}\boldsymbol{\epsilon}^{\mathbf{m}}_\mathrm{w}(t^n) \tag{6.43}$$

The distortion modal basis is truncated to three modes. The pressure p_{d_j} associated with each distortion mode shape $\boldsymbol{\xi}_{\mathrm{d}_j}$ is calculated by summing the hydrostatic, radiation, incident, and diffraction pressure contributions. Index j of $\boldsymbol{\xi}_{\mathrm{d}_{jk}}$ corresponds to the vector of distortion modal amplitudes; k is the index within that vector corresponding to a generalized mode.

$$p_{\mathrm{d}_j}(\mathbf{x}_m) = \mathrm{Re}\left[\sum_k \left(p_{C_k}(\mathbf{x}_m)\boldsymbol{\xi}_{\mathrm{d}_{jk}} + p_{R_k}(\mathbf{x}_m, \omega_j, \epsilon_j)\boldsymbol{\xi}_{\mathrm{d}_{jk}} + p_I(\mathbf{x}_m, \omega_j, \epsilon_j) + p_D(\mathbf{x}_m, \omega_j, \epsilon_j)\right)\right] \tag{6.44}$$

Pressures at each collocation point $\mathbf{x}_m$ and time step t^n are estimated using the distortion modal amplitudes $\boldsymbol{\xi}^{\mathbf{e}}_\mathrm{d}$.

$$p^{\mathbf{e}}_\mathrm{d}(\mathbf{x}_m, t^n) = \sum_j \left(p_{\mathrm{d}_j}(\mathbf{x}_m)\boldsymbol{\xi}^{\mathbf{e}}_{\mathrm{d}_j}(t^n)\right) \tag{6.45}$$

6.2.2 Number and Position of Strain Gauges

To limit the amount of variables introduced in this thesis, the number of strain gauges is set to four. Their positions affect the conditioning of matrix $\mathbf{B}^{\mathbf{m}}_{\boldsymbol{\epsilon}}\mathbf{H}$, which directly impacts the modal amplitude estimate $\boldsymbol{\xi}^{\mathbf{e}}$, regardless of the selected modal basis. If a strain gauge lies directly on the node of a mode shape, for example, the measured strain can be close to zero and contaminated by noise. Modes which are not included in the modal basis can also contribute to the vector of measured strains, which introduces additional error. The condition number is one measure of assessing the sensitivity of an estimate to modeling and measurement errors [147]. Two papers about sensor placement were reviewed: Kammer [148] contends that maximizing the trace and determinant of the Fisher Information Matrix leads to improved estimates and a minimized condition number; however, the algorithm produced in Kammer [148] was reviewed independently by Friswell and Castro-Triguero [149] and found to result in clusters of strain gauges. The condition number was used as the primary metric for assessing the sensor placement algorithm's quality.

Based on the review of these papers, two separate methods were considered for optimally placing strain gauges: the first method minimizes the condition number directly. The second method minimizes the sum of squared off-diagonal terms of the Gram matrix $\mathbf{G}_{ij} = \boldsymbol{\epsilon}^{\mathbf{m}T}_i\boldsymbol{\epsilon}^{\mathbf{m}}_j$, as opposed to maximizing the diagonal terms as suggested by Kammer [148]. Doing so enforces orthogonality within the column space of $\mathbf{B}^{\mathbf{m}}_{\boldsymbol{\epsilon}}\mathbf{H}$, which

is a more important measure than the orthogonality of modal basis $\mathbf{H}$ for assessing the impact of sensor placement on modal amplitude estimates.

$$\epsilon_i^{\mathbf{m}}(x) = \mathbf{B}_{\boldsymbol{\epsilon}}\left(\xi(x)\right)\mathbf{d}_{\mathbf{e}i} \qquad \epsilon_j^{\mathbf{m}}(x) = \mathbf{B}_{\boldsymbol{\epsilon}}\left(\xi(x)\right)\mathbf{d}_{\mathbf{e}j} \qquad \mathbf{x} = \min\left[\sum_{i=1}^{n}\sum_{\substack{j=1\\ j\neq i}}^{n}\left(\boldsymbol{\epsilon}_i^{\mathbf{m}T}\boldsymbol{\epsilon}_j^{\mathbf{m}}\right)^2\right] \tag{6.46}$$

Both methods use the Sequential Least Squares Programming (SLSQP) algorithm (as implemented in `scipy.optimize.minimize`) [150, 151, 152, 153]. A comparison of the two methods showed that using the condition number in the objective function did in fact yield a slightly better-conditioned matrix $\mathbf{B}_{\boldsymbol{\epsilon}}^{\mathbf{m}}\mathbf{H}$ than the method of minimizing the squared off-diagonal terms of the Gram matrix. However, both methods produced similar strain gauge positions for both the distortion and wet modes; the optimal x-coordinates are rounded to the nearest centimeter.

6.2.3 Filtering

Digital filters can be used to suppress noise that would otherwise negatively impact the accuracy of modal amplitude estimates made using strain measurements. Many classes of filters exist, each with varying pass band ripple and cutoff decay. In this thesis, a Butterworth filter is used to minimize the effect of pass band ripple and slow cutoff on the amplitude estimates [154]; the filter itself is implemented using `scipy.signal.butter` [153]. A Butterworth filter is defined by a transfer function $H(s)$ with cutoff frequency ω_c, amplitude H_0, and number of poles equal to n. The gain $G(s)$ is defined as the absolute value, or magnitude, of the transfer function. The gain has a maximum magnitude of G_0. The cutoff frequency ω_c affects the point at which the magnitude $G(s)$ begins to decay, or the extent to which noise above the cutoff frequency is suppressed. The number of poles n controls the sharpness of this cutoff; a higher number of poles yields a steeper slope.

$$\text{Low pass}: \quad G(\omega) = |H(i\omega)| = \frac{G_0}{\sqrt{1+\left(\dfrac{\omega}{\omega_c}\right)^{2n}}} \qquad \text{High pass}: \quad G(\omega) = |H(i\omega)| = \frac{G_0}{\sqrt{1+\left(\dfrac{\omega_c}{\omega}\right)^{2n}}} \tag{6.47}$$

The frequencies at which a stiff ship vibrates during a slam-induced whipping event are significantly higher than the incoming wave frequencies. The measured strains are thus filtered using a low-pass filter to obtain the measured distortion mode strain vector $\boldsymbol{\epsilon}_{\mathrm{d}}^{\mathbf{m}}$, as shown in Figure 6.14, and a high-pass filter to obtain the measured wet mode strain vector $\boldsymbol{\epsilon}_{\mathrm{w}}^{\mathbf{m}}$, as shown in Figure 6.15.

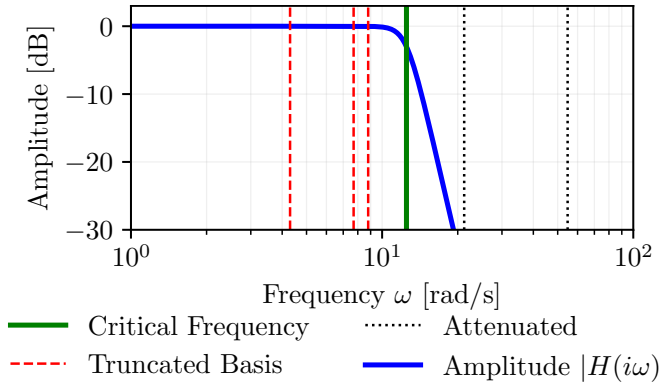


Figure 6.14: Low-pass Butterworth filter Bode plot.

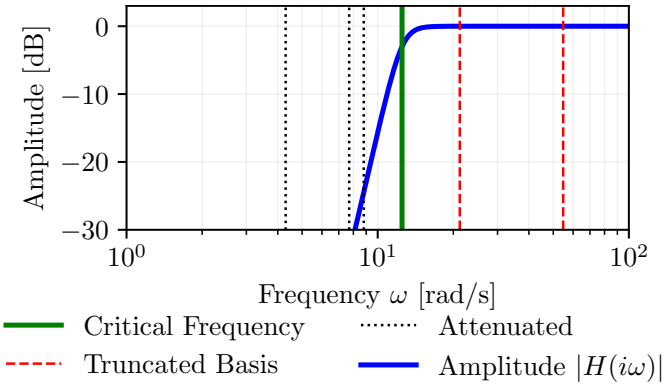


Figure 6.15: High-pass Butterworth filter Bode plot.

6.2.4 Error Metrics

Error is assessed using three normalized error metrics: the Normalized Root Mean Squared Error (NRMSE), Normalized Mean Amplitude Error (NMAE), and Normalized Standard Deviation (NSTD). In all three metrics, the error metric is normalized by the observed signal. A NRMSE or NMAE of 0% indicates that the estimated and observed signals are, within machine precision, the same at all points in the sampled

time range. Comparing an array of zeros with the array of observed strains would yield a 100% NRMSE or NMAE. Inversely, a NSTD of 1 indicates that the standard deviations of the estimated and observed signals are identical, while a NSTD of 0 is obtained by comparing an array of zeros with the array of observed strains. All three metrics can exceed 1 (NSTD), or 100% (NRMSE, NMAE). The three error metrics are calculated for two time windows: $t = [58.5, 62]$ seconds and $t = [10, 180]$ seconds. The wave cut-in period from $t = [0, 10]$ seconds and Hann window from $t = [180, 200]$ seconds are excluded. The NRMSE is obtained by dividing the RMSE by the root mean squared amplitude of the observed signal.

$$\text{NRMSE} = \left(\frac{1}{N} \sum_n \left(\boldsymbol{\epsilon}^{\mathbf{e}}[n] - \boldsymbol{\epsilon}^{\mathbf{o}}[n] \right)^2 \right)^{1/2} \left(\frac{1}{N} \sum_n \left(\boldsymbol{\epsilon}^{\mathbf{o}}[n] \right)^2 \right)^{-1/2} \tag{6.48}$$

The normalized mean average error (NMAE) is also used, since the NRMSE penalizes large errors more heavily.

$$\text{NMAE} = \left(\frac{1}{N} \sum_n \| \boldsymbol{\epsilon}^{\mathbf{e}}[n] - \boldsymbol{\epsilon}^{\mathbf{o}}[n] \| \right) \left(\frac{1}{N} \sum_n \| \boldsymbol{\epsilon}^{\mathbf{o}}[n] \| \right)^{-1} \tag{6.49}$$

The third metric is the normalized standard deviation (NSTD), defined as the ratio of the standard deviation of the estimates $\boldsymbol{\epsilon}^{\mathbf{e}}$ and the observations $\boldsymbol{\epsilon}^{\mathbf{o}}$. Bessel's correction $(N-1)$ is applied to remove estimate variance bias. A ratio of 1 indicates the standard deviations are identical; comparing an array of zeros with the array of observed strains would yield a ratio of 0.

$$\text{NSTD} = \frac{\boldsymbol{\sigma}^{\mathbf{e}}}{\boldsymbol{\sigma}^{\mathbf{o}}} \quad \text{where} \quad \boldsymbol{\sigma} = \left(\frac{1}{N-1} \sum_{n=1}^{N} \left(\boldsymbol{\epsilon}[n] - \boldsymbol{\mu} \right)^2 \right)^{1/2} \quad \text{and} \quad \boldsymbol{\mu} = \frac{1}{N} \sum_{n=1}^{N} \boldsymbol{\epsilon}[n] \tag{6.50}$$

Chapter 7

Local Model: Stiffened Panel

The second aim of this thesis is to assess the feasibility of estimating the far-field stress state in an orthotropically stiffened panel subjected to local, transient slamming pressures using the method of least squares and a dry modal basis. To facilitate an efficient comparative study, an idealized, one-dimensional Euler-Bernoulli beam is modeled using dimensions, structural properties, and boundary conditions which approximately represent a section of one orthotropically stiffened panel bounded by transversal stiffeners and longitudinal girders. Section 7.1 outlines the modeling steps used to evaluate the plate-strip loading and response. Section 7.2 outlines the method used for estimating the stresses based on sparse strain gauge measurements.

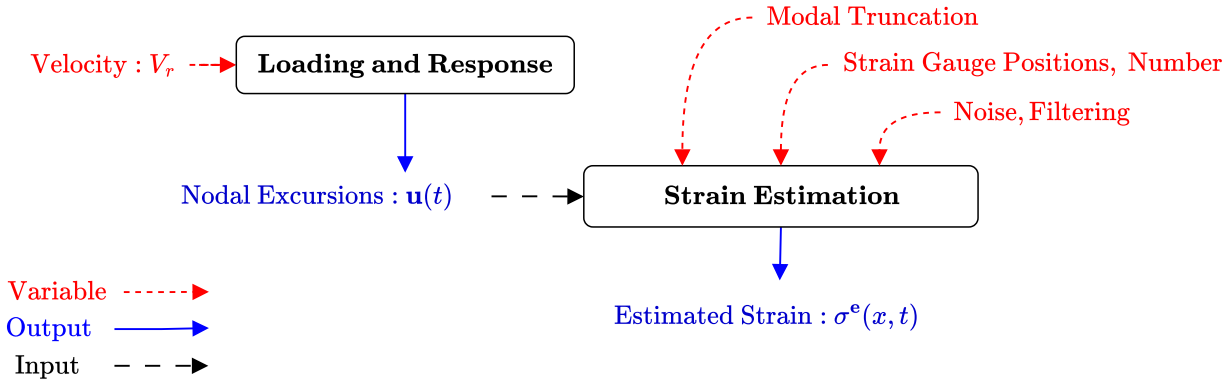


Figure 7.1: Outline of the local modeling workflow, including variables, inputs, and outputs.

7.1 Loading and Response

7.1.1 Model Parameters

A section (strip) of one orthotropically stiffened panel is defined with a thickness of 15 mm, density equal to 7850 kg/m^3, elastic modulus of 210 GPa, plate length of 0.5 m, and width of 1.25 m. The coordinate system is defined as shown in Figure 2.2. The wedge configuration consists of two strips with a total length of 1 m and is symmetric about the $y-z$ plane, while the plate only consists of one strip with a total length of 0.5 m which is also symmetric about the $y-z$ plane. Both strips of the wedge configuration are fixed with Dirichlet boundary conditions (at $x = -0.5$, 0, and 0.5 m), while the plate is fixed at $x = -0.25$, 0.25 m. Fixed boundary conditions are prescribed because the transversal and rotational stiffness of the stiffeners at each end of the panel is large relative to the bending stiffness of the panel itself.

7.1.2 Slamming Model

A Wagner slamming model is used to generate pressures that resemble those exerted on the stiffened panels of a ship's hull during a slamming model. The complex velocity potential $\Phi(s)$ which satisfies the free-surface and far-field boundary conditions is a function of the wetted length $c(t)$, position x, and impact velocity V

is given by: $\Phi(x)|_{z=0} = \phi + i\psi = -V\sqrt{c(t)^2 - x^2} + iVx$. Pressure is evaluated by substituting the real potential into Bernoulli's equation:

$$p(x,t)|_{z=0} = -\rho\phi_t = \rho V \frac{c(t)}{\sqrt{c(t)^2 - x^2}} c_t(t) \tag{7.1}$$

The wetted length $c(t)$ for a wave impacting a plate is given by $c(t) = 2\sqrt{Vt/\zeta k^2}$; the wetted length for a wedge impacting a still water surface is given by $c(t) = \pi Vt/2 \tan\beta_d$, where β_d is the deadrise angle, $V = 1$ [m/s] is the impact velocity, $\zeta = 2$ [m] is the wave elevation, $k = 2\pi/\lambda$ is the wave number (with $\lambda = 50$ [m] being the wavelength), and t is time.

7.1.3 Analytical Euler-Bernoulli Beam Model

An analytical Euler-Bernoulli beam with strong form given by the equation $\rho A w_{tt}(x,t) + EI w_{xxxx}(x,t) = 0$ is used to validate the finite element formulation. Separating the displacement function $w(x,t)$ into time- and space-dependent terms $a(t)$, $\Psi(x)$ allows for the separation of variables.

$$\Psi(x) = C_1\cos(\beta x) + C_2\sin(\beta x) + C_3\cosh(\beta x) + C_4\sinh(\beta x) \quad \text{with} \quad \beta^4 = \frac{\rho A\omega^2}{EI} \tag{7.2}$$

Fixed-fixed kinematic boundary conditions (displacements and rotations are zero) are applied to both ends. The coefficient β is solved by finding roots of the characteristic free vibration equation numerically.

7.1.4 Quasi-Static Response

The quasi-static response of the plate-strip is evaluated using the pressure formulation and the plate width b to obtain the force per unit length $q(x,t)$. The analytical displacement $w(x,t)$ is found by integrating four times and setting the integration constants such that the fixed-fixed boundary conditions are satisfied.

$$q(x,t) = p(x,t)\cdot b = \frac{\rho V c c_t}{\sqrt{c^2 - x^2}} \qquad EI\frac{\partial^4 w}{\partial x^4} = q(x,t)|_{t=t_0} \tag{7.3}$$

The vector of generalized finite element displacements $\mathbf{u}$ is found by integrating the force per unit length $q(x,t)$ along each isoparametric element $_{\mathbf{e}}$, assembling the elemental force vectors into $\mathbf{f}$, and solving the static problem using the inverted structural stiffness matrix $\mathbf{K^{s}}^{-1}$:

$$\mathbf{f} = \sum_e \left[\int_{\Omega_e} \mathbf{N_e}^T \mathbf{n}\cdot q(x,t)\cdot J_e\, d\Omega\right] \qquad \mathbf{u} = \mathbf{K^{s}}^{-1}\mathbf{f} \tag{7.4}$$

Results for the analytical and finite element formulations are shown in Figures 7.2 and 7.3 for the plate and wedge configurations, respectively.

7.1.5 Hydroelastic Response

Pressure Distribution The time- and space-dependent pressure distribution $p(x,t)$ is dependent on the fluid density ρ, relative velocity V, wetted length-averaged velocity $\overline{w}_t$ and acceleration $\overline{w}_{tt}$, and wetted velocity $c(t)$, $c_t(t)$:

$$p(x,t) = \rho\left(\frac{(V - \overline{w}_t)\, c}{\sqrt{c^2 - x^2}} c_t - \overline{w}_{tt}\sqrt{c^2 - x^2}\right) \tag{7.5}$$

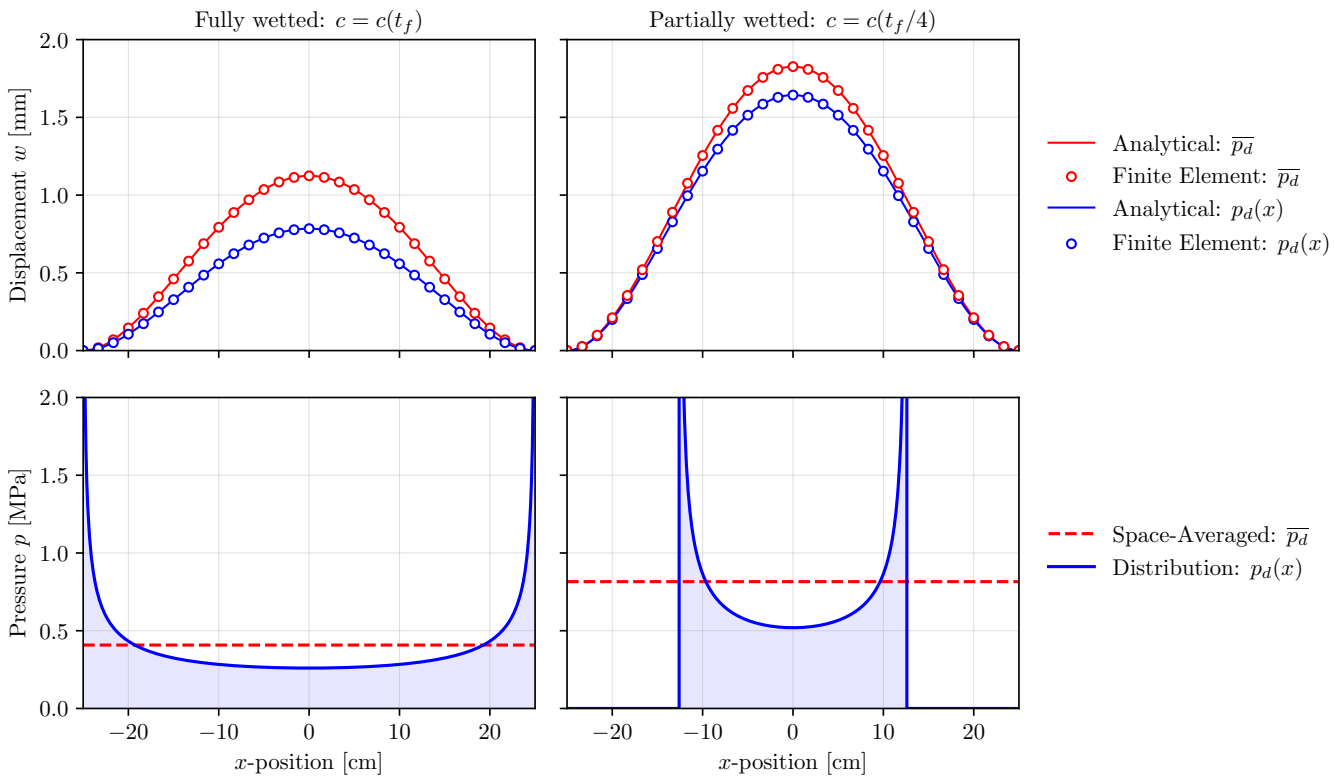


Figure 7.2: Quasi-static displacement of a plate (modeled as an Euler-Bernoulli beam) subjected to uniform (space-averaged) and distributed pressure, as derived using the Wagner model. Analytical and finite element solutions are compared in the top row; the applied pressure distribution is shown in the bottom row.

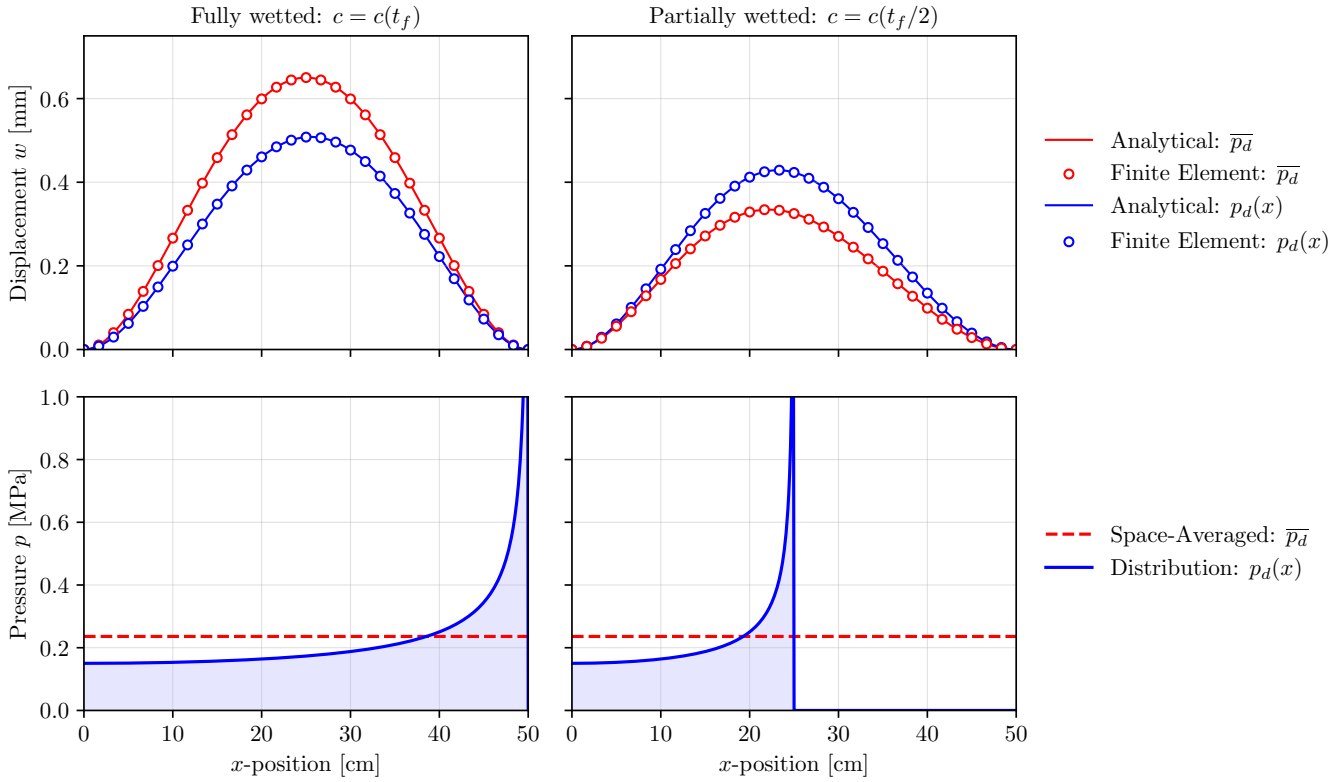


Figure 7.3: Quasi-static displacement of a wedge (modeled as an Euler-Bernoulli beam) subjected to uniform (space-averaged) and distributed pressure, as derived using the Wagner model. Analytical and finite element solutions are compared in the top row; the applied pressure distribution is shown in the bottom row.

Analytical Formulation The modal impact velocity formulation is determined by first evaluating the governing equation for the Euler-Bernoulli beam in modal space for free vibrations (the homogeneous case).

$$\rho A \sum a_{n,tt}(t)\Psi_n(x) + EI \sum a_n(t)\Psi_{n,xxxx}(x) = 0 \tag{7.6}$$

Multiplying by a shape function $\Psi_m(x)$ and integrating over the domain provides Galerkin's weak formulation. Taking advantage of orthogonality, the homogeneous governing equation can be expressed in modal space:

$$\rho A \int_\Omega \Psi_m^2(x)\, d\Omega \cdot a_{m,tt}(t) + EI \int_\Omega \Psi_m(x)\Psi_{m,xxxx}(x)\, d\Omega \cdot a_m(t) = 0 \tag{7.7}$$

Since the fourth spatial derivative of $\Psi_m(x)$ is $\beta^4\Psi_m(x)$, the equation can be rewritten.

$$\rho A \int_\Omega \Psi_m^2(x)\, d\Omega \cdot a_{m,tt}(t) + EI\beta^4 \int_\Omega \Psi_m(x)^2\, d\Omega \cdot a_m(t) = 0 \tag{7.8}$$

In the analytical formulation, the space-averaged modal displacement is found using the following expression:

$$\overline{w}_j = \frac{1}{c}\int_0^c \psi_j\, dx\xi_j \qquad (\overline{w}_j)_t = \frac{1}{c}\int_0^c \psi_j\, dx\, (\xi_j)_t \qquad (\overline{w}_j)_{tt} = \frac{1}{c}\int_0^c \psi_j\, dx\, (\xi_j)_{tt} \tag{7.9}$$

The pressure equation can be separated into components proportional to modal velocity and acceleration, which correspond to damping $\mathbf{B}_{ij}(t)$ and added mass $\mathbf{A}_{ij}(t)$, respectively. Integration is performed using adaptive Gauss quadrature.

$$\mathbf{A}_{ij}(t) = \rho \int_0^c \Psi_i \sqrt{c^2 - x^2}\, dx \frac{1}{c}\int_0^c \Psi_j\, dx \qquad \mathbf{B}_{ij}(t) = \rho c c_t \int_0^c \frac{\Psi_i}{\sqrt{c^2 - x^2}}\, dx \frac{1}{c}\int_0^c \Psi_j\, dx \tag{7.10}$$

The last term corresponds to the modal force $\mathbf{f}_j(t)$:

$$\mathbf{f}_j(t) = \rho V c_t \int_0^c \frac{\Psi_i}{\sqrt{c^2 - x^2}}\, dx \tag{7.11}$$

Finite Element Formulation Two finite element configurations are considered: plate-wave impact and a free-falling wedge. Only the wetted length formulation $c(t)$ and the domain Ω change when switching between the two configurations. To illustrate the hydrostructural effects of the two configurations, the structural properties of a plate strip are used. A plate-strip is considered with width b such that a force per unit length $q(x,t) = p(x,t) \cdot b$. The isoparametric Euler-Bernoulli beam elements used for the global model are adapted to the local model by changing the linear density $(\rho A)_e$ and stiffness $(EI)_e$. Fixed displacement and rotation boundary conditions are applied at the left and right ends of the finite element model.

$$\mathbf{f} = \sum_e \left[\int_{\Omega_e} \mathbf{N_e}^T \mathbf{n} \cdot q(x,t) \cdot J_e\, d\Omega \right] \tag{7.12}$$

The space-averaged velocities and accelerations are dependent on the mode shape $\mathbf{h}_j$ and modal amplitudes $\boldsymbol{\xi}_j$:

$$(\overline{w}_j)_t = \frac{1}{c}\sum_e \left[\int_{\Omega_e} \mathbf{N_e}^T \mathbf{d_e} j J_e\, d\Omega \right] \cdot (\boldsymbol{\xi}_j)_t \qquad \overline{w_{j,tt}} = \frac{1}{c}\sum_e \left[\int_{\Omega_e} \mathbf{N_e}^T \mathbf{d_e} j J_e\, d\Omega \right] \cdot (\boldsymbol{\xi}_j)_{tt} \tag{7.13}$$

Alternatively, the vector of generalized displacements $\mathbf{h}_j$ for each mode j can be moved outside of the assembly term $\sum_e$:

$$(\overline{w}_j)_t = \frac{1}{c}\sum_e \left[\int_{\Omega_e} \mathbf{N_e}^T J_e \, d\Omega\right] \mathbf{h}_j \left(\boldsymbol{\xi}_j\right)_t \qquad \overline{w_{j,tt}} = \frac{1}{c}\sum_e \left[\int_{\Omega_e} \mathbf{N_e}^T J_e \, d\Omega\right] \mathbf{h}_j \left(\boldsymbol{\xi}_j\right)_{tt} \tag{7.14}$$

The force can be separated into three components: external, added mass, and damping:

$$\mathbf{A}_{ij}(t) = \mathbf{h}_i^T \sum_e \left[\rho b \, \overline{w_{j,tt}} \int_{\Omega_e} \mathbf{N_e}^T \mathbf{n} \sqrt{c^2 - x^2} \, d\Omega\right] \quad \text{such that} \quad \mathbf{f} = \mathbf{A}\, \boldsymbol{\xi}_{tt} \tag{7.15}$$

$$\mathbf{B}_{ij}(t) = \mathbf{h}_i^T \sum_e \left[\rho c c_t \, \overline{w_{j,t}} \int_{\Omega_e} \mathbf{N_e}^T \frac{J_e}{\sqrt{c^2 - x^2}} \, d\Omega\right] \quad \text{such that} \quad \mathbf{f} = \mathbf{B}\, \boldsymbol{\xi}_t \tag{7.16}$$

$$\mathbf{f}_j(t) = \mathbf{h}_i^T \sum_e \left[-\rho V c c_t \int_{\Omega_e} \mathbf{N_e}^T \frac{J_e}{\sqrt{c^2 - x^2}} \, d\Omega\right] \tag{7.17}$$

Recognizing that the formulations above make use of three unique integrals, and that the weak form of an Euler-Bernoulli beam can be evaluated exactly using a cubic Hermite polynomial, alternative formulations are found which exploit this advantage. The first integral can be expressed using a change of variable: $x = c\sin\theta$ such that $\sqrt{c^2 - x^2} = c\cos\theta$ and $dx = c\cos\theta\, d\theta$. Note that these terms cancel. Doing so changes the limits of integration over an entire isoparametric element from $\xi = [-1, 1]$ to $\theta = [-\pi/2, \pi/2]$, which has a closed form solution. The matrix of shape functions $\mathbf{N_e}(\xi) = \mathbf{A_e}^{-1}\mathbf{Z}(\xi)$ can be evaluated as $\mathbf{N_e}(\xi(\theta)) = \mathbf{A_e}^{-1}\mathbf{Z}(\xi(\theta))$, where $\xi(\theta) = (x(\theta) - x_e)/J_e$. x_e is the physical coordinate at the center of element e. The change of variable means the Jacobian is no longer a part of the expression.

$$\textbf{Integral 1}: \quad \int_{\Omega_e} \mathbf{N_e}^T \frac{J_e}{\sqrt{c^2 - x^2}} \, d\xi = \int_{\Omega_e} \mathbf{N_e}^T \, d\theta = \mathbf{A_e}^{-T} \int_{\Omega_e} \mathbf{Z}^T(\xi(\theta)) \, d\theta \tag{7.18}$$

The second integral also uses a change of variables, but the radical does not cancel.

$$\textbf{Integral 2}: \quad \int_{\Omega_e} \mathbf{N_e}^T \sqrt{c^2 - x^2} \, d\Omega = \int_{\Omega_e} \mathbf{N_e}^T \; c^2 \cos^2\theta \, d\theta = \mathbf{A_e}^{-T} \int_{\Omega_e} \mathbf{Z}^T(\xi(\theta)) \; c^2 \cos^2\theta \, d\theta \tag{7.19}$$

The third integral is similar to the first, but a change of variables is not needed. Quasi-static forces are also evaluated using the third integral.

$$\textbf{Integral 3}: \quad \int_{\Omega_e} \mathbf{N_e}^T J_e \, d\Omega = \mathbf{A_e}^{-T} \int_{\Omega_e} \mathbf{Z}^T(\xi) J_e \, d\xi \tag{7.20}$$

The domain of integration Ω_e depends on the wetted length c and the center of each element x_e. All wetted elements, except one, use a full domain of integration: $\theta = [-\pi/2, \pi/2]$ or $\xi = [-1, 1]$. The limits of integration at the jet's leading edge are found by splitting the element: $\xi = [-1, (c - x_e)/J_e]$.

Speed is the primary motivator for this approach. The added mass, damping, and force expressions must be evaluated for every combination of modes i and j at each time step, and integration over an analytical Euler-Bernoulli beam using quadrature can become quite computationally expensive due to the singularity at $x = c$, especially when the simulation must be repeated for every slamming event from the global model. Evaluating the three integrals as shown above leads to considerable acceleration, allowing for the estimation of local hydroelastic or quasi-static far-field stresses using the global model solution. Both analytical and numerical (finite element) approaches are implemented in Python for a plate-wave impact and a falling wedge. The numerical model is verified against the analytical solution for both space-averaged and distributed Wagner slamming pressures at two time steps.

The time domain response is estimated using modal amplitudes $\boldsymbol{\xi}$, mass matrix $\mathbf{M} = \mathbf{H}^T\mathbf{M^s}\mathbf{H}$, and stiffness matrix $\mathbf{K} = \mathbf{H}^T\mathbf{K^s}\mathbf{H}$. A fourth-order Runge-Kutta method is used with state-space representation:

$$\begin{bmatrix} \mathbf{0} & \mathbf{I} \\ -\left(\mathbf{M}+\mathbf{A}(t)\right)^{-1}\mathbf{K} & -\left(\mathbf{M}+\mathbf{A}(t)\right)^{-1}\left(\mathbf{B}(t)+\mathbf{D}\right) \end{bmatrix} \begin{bmatrix} \boldsymbol{\xi}(t) \\ \boldsymbol{\xi}_t(t) \end{bmatrix} = \begin{bmatrix} \mathbf{0} \\ -\left(\mathbf{M}+\mathbf{A}(t)\right)^{-1}\mathbf{f}(t) \end{bmatrix} \tag{7.21}$$

The damping and external force depend on the time derivative of the wetted length. When $c(t) = L/2$, the added mass and damping matrices are retained for the subsequent time steps, simulating the free decay response. Vibration following bow emergence is modeled without added mass or damping.

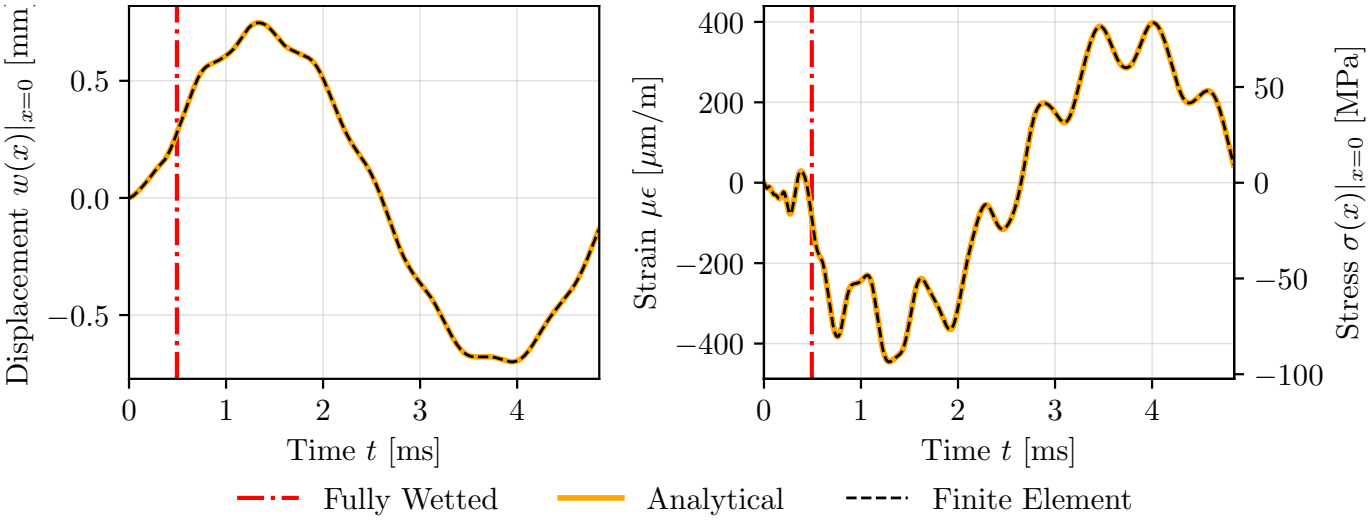


Figure 7.4: The hydroelastic response of a plate to symmetric Wagner wave loading, plotted over the first wet natural period. The analytical solution, integrated using Gauss quadrature, is superimposed on the finite element solution.

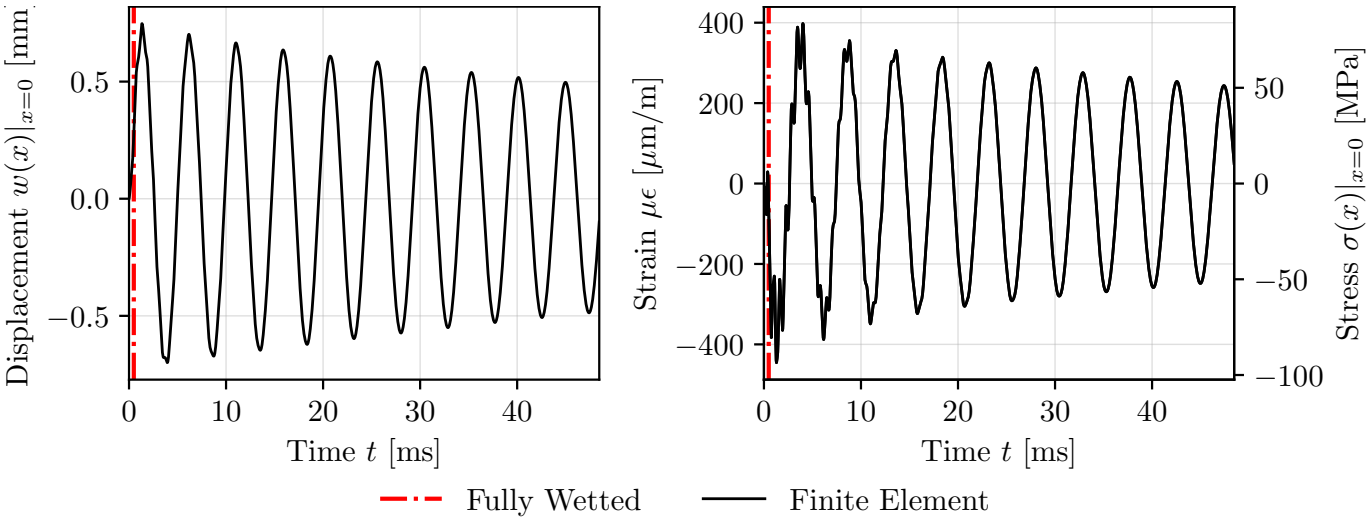


Figure 7.5: The hydroelastic response of a plate to symmetric Wagner wave loading, plotted over the first ten wet natural periods. Only the finite element solution is shown; analytical integration of the Euler Bernoulli beam is computationally prohibitive.

7.2 Stress Estimation

The hydroelastic analysis results in nodal displacements and rotations of the finite element model. These results are used along with the dry modal basis for estimating structural stresses in the time domain. Strain gauges are positioned based on the structural response associated with each mode shape; the condition number is minimized to find the optimal gauge placement. Gaussian noise is introduced to simulate measurement noise. A low-pass Butterworth filter is used to separate the simulated noise from the measured hydroelastic strain response.

7.2.1 Modal Basis

The equation of motion for the finite element Euler-Bernoulli beam is $\mathbf{M^s u}_{tt} + \mathbf{K^s u} = 0$. Eigenvalues and eigenvectors are solved using the following equation: $\mathbf{M^{s-1} K^s u} = \omega^2 \mathbf{I u}$. The eigenvectors span the column space of $\mathbf{H}$, which is truncated to three modes. The stiffness matrix is modified to enforce the Dirichlet boundary conditions at each end of the beam. The number of modes equals the number of sensors in this application; the matrix $\mathbf{B^m_\epsilon H}$ is square and invertible.

$$\boldsymbol{\epsilon}^{\mathbf{m}} = \mathbf{B}^{\mathbf{m}}_{\boldsymbol{\epsilon}} \mathbf{H} \boldsymbol{\xi} \quad \text{such that} \quad \boldsymbol{\xi}^{\mathbf{e}}(t^n) = \left(\mathbf{B}^{\mathbf{m}}_{\boldsymbol{\epsilon}} \mathbf{H}\right)^{+} \boldsymbol{\epsilon}^{\mathbf{m}}(t^n) \quad \text{and} \quad \boldsymbol{\epsilon}^{\mathbf{e}}(t^n) = \mathbf{B}^{\mathbf{e}}_{\boldsymbol{\epsilon}} \mathbf{H} \left(\mathbf{B}^{\mathbf{m}}_{\boldsymbol{\epsilon}} \mathbf{H}\right)^{+} \boldsymbol{\epsilon}^{\mathbf{m}}_{\mathrm{w}}(t^n) \tag{7.22}$$

7.2.2 Number and Position of Strain Gauges

The number of strain gauges is set to three. Estimates are made at the ends and center of the beam. The positions are set by minimizing the condition number of the matrix $\mathbf{B^m_\epsilon H}$.

7.2.3 Noise

To simulate the measurement noise present in a ship structure, noise is introduced with a probability density function equal to that of a normal distribution. The noise is added to the vector of observed strains $\boldsymbol{\epsilon}^{\mathbf{o}}(t)$ with mean $\mu = 0$ and standard deviation σ: $\boldsymbol{\epsilon}^{\mathbf{m}}(t) = \boldsymbol{\epsilon}^{\mathbf{o}}(t) + \boldsymbol{\epsilon}^{\mathbf{n}}(t)$. The parameters used to generate noise $\boldsymbol{\epsilon}^{\mathbf{n}}(t)$ are not intended to be representative of physical processes on a ship such as engines or pumps, which would normally introduce noise with dominant frequencies. This kind of noise is not within scope, but can present a challenge for estimation when the dominant frequencies fall within the filter pass bands.

7.2.4 Filtering

A low-pass Butterworth filter is applied to suppress high-frequency noise. Gaussian noise has a uniform spectrum; low-frequency noise is not suppressed with a low-pass filter.

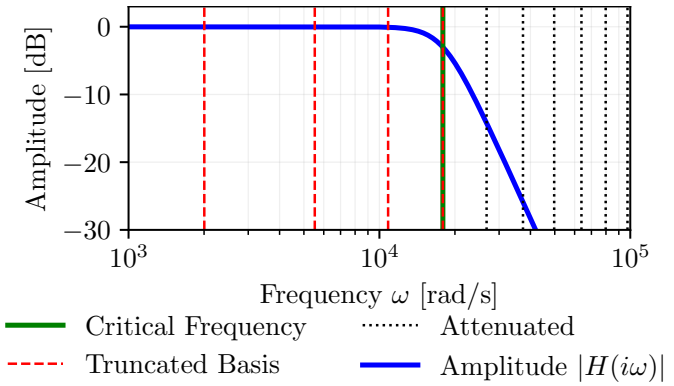


Figure 7.6: Bode plot of the discrete Butterworth filter. The critical frequency and natural frequencies of the finite element Euler-Bernoulli beam are superimposed to show the relative contribution of higher order modes to the estimated response.

7.2.5 Error Metrics

The same three error metrics as presented in Section 6.2.4 (Normalized Root Mean Squared Error (NRMSE), Normalized Mean Amplitude Error (NMAE), and Normalized Standard Deviation (NSTD)) are used for evaluating the quality of the estimates for the local model. The metrics are evaluated on two intervals: the first wet natural period, and the first 10 wet natural periods.

Part III

Results

Chapter 8

Global Results: Segmented Barge

Five loading and response conditions are considered in this chapter: a single regular wave (Section 8.1), irregular waves (Section 8.2), impulse loading (Section 8.3), a regular wave with impulse loading (Section 8.4), and irregular waves with impulse loading (Section 8.5). The strain response is evaluated at twelve equally spaced points along the finite element model and compared with the estimated strains at those points. Strains are measured at the finite element nodes using the averaged result from adjacent isoparametric elements, as shown in Figure 8.1. Pressures are estimated along the base and the side of the hydrodynamic mesh at equally spaced points (twelve for each side of the model), as shown in Figure 8.2. The x coordinate corresponds to that of each finite element node. Each section begins with an overview of the results and an interpretation of the estimate accuracy. The three figures (estimated versus observed strains, side pressures, and keel pressures) follow the summary. The error metrics NRMSE, NMAE, and NSTD are defined in Section 6.2.4 as Normalized Root Mean Squared Error, Normalized Mean Amplitude Error, and Normalized Standard Deviation, respectively.

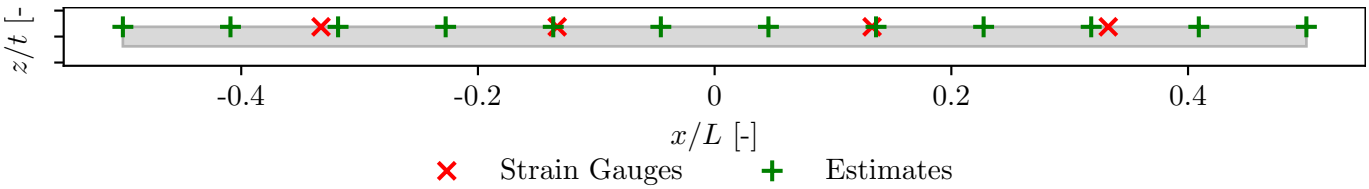


Figure 8.1: Relative positions of the virtual strain gauges and locations where strains are estimated.

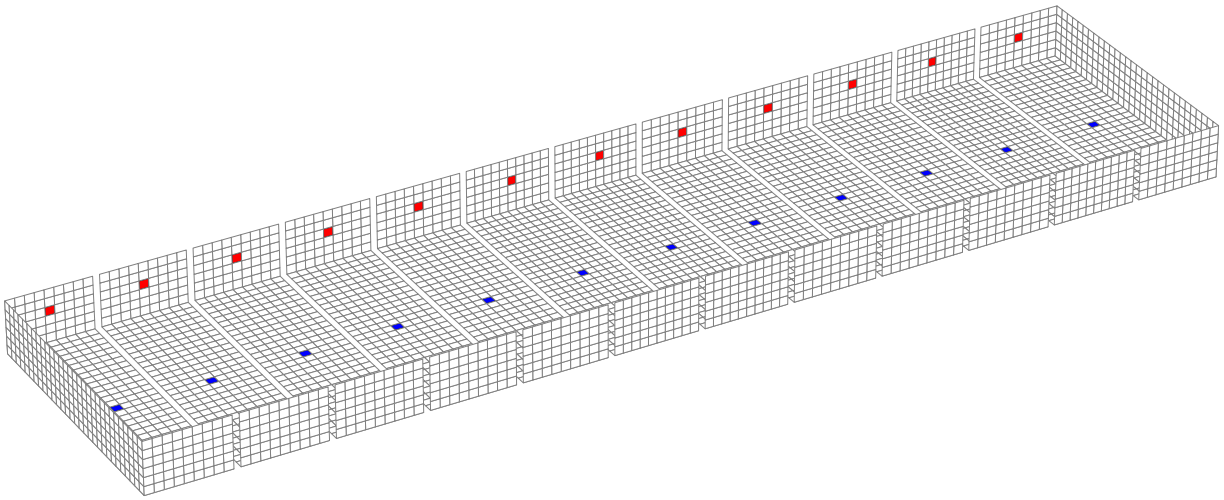


Figure 8.2: Locations where external (hydrostatic, hydrodynamic) pressures are estimated. Blue panels are on the base, or keel, of the barge, while red panels are on the starboard side.

8.1 Regular Wave

The regular wave simulation is intended to verify the method of estimating modal amplitudes and associated loading and response information using distortion modes, since no high frequency content is present and the high-pass filter separates low frequency content from the wet mode amplitude estimates. The regular wave has an amplitude of $\zeta = 48$ millimeters ($H_s = 96$ mm) and a period of 1.6 seconds ($T_p = 1.6$ s), which corresponds to a frequency of 3.93 radians per second. The frequency of the first distortion mode (4.3 radians per second, see Table 6.3) is close to that of the incoming wave. This similarity in frequency does not necessarily imply accurate loading and response estimates because each distortion mode corresponds to a certain phase: a standing wave is assumed. The time window from $t = 10$ to $t = 180$ seconds is used for the error metrics because no transient load is applied.

Strain Estimates The effects of the standing wave assumption are immediately apparent in the strain estimate metrics and plots. The estimated strains at locations close to the strain gauges (ϵ_6 and ϵ_7) are very close to the observed values in both phase and amplitude: NRMSE and NMAE are both below 2% and the NSTD is exactly 1. Such a result is expected when using the method of least squares because the objective function minimizes the length of the error vector at the positions where strain is measured. Strain estimates near and at the ends of the segmented barge have both phase and amplitude errors, which are especially pronounced at ϵ_{12}, the bow node. NRMSE and NMAE values of over 200% are calculated because incident and diffraction pressures are partially discarded when taking the real part of the distortion mode at a specific phase. Simply correcting for the phase error would not reduce the estimated fatigue damage error because the NSTD is also 1.83, meaning phase-corrected values would still overestimate the observed values by a factor of nearly 2.

Table 8.1: Normalized error metrics for the strain estimates (regular wave) over $t \in [10.0, 180.0]$ s

Metric	ϵ_1	ϵ_2	ϵ_3	ϵ_4	ϵ_5	ϵ_6	ϵ_7	ϵ_8	ϵ_9	ϵ_{10}	ϵ_{11}	ϵ_{12}	Mean
NRMSE [%]	118	59.9	23.2	19.3	4.7	1.4	1.0	6.9	18.5	12.8	90.1	212	47.3
NMAE [%]	118	59.9	23.2	19.3	4.7	1.4	1.0	6.9	18.5	12.8	90.0	212	47.3
NSTD [–]	0.81	1.51	0.98	0.96	0.99	1.00	1.00	1.00	1.01	1.01	1.47	1.83	1.13

Pressure Estimates The estimated strains may appear relatively accurate for the purposes of a fatigue assessment since the mean NSTD is 1.13, but the estimated pressures acting on the barge suggest otherwise. The mean NRMSE and NMAE values for both the starboard side and keel panels exceed 330% and the mean NSTD is at least 2.7. A wide range of error values are noted for all panels, which is expected because each distortion mode discards the imaginary pressures at each specified frequency and phase. In this case, the imaginary pressures at an incoming wave frequency of $\omega = 4.3$ radians per second are not included in the estimate, leading to high NRMSE and NMAE values. The high mean NSTD value indicates that phase-corrected pressures would still lead to an overestimate of the accumulated fatigue damage.

Table 8.2: Normalized error metrics for the side-panel pressure estimates (regular wave) over $t \in [10.0, 180.0]$ s

Metric	p_1	p_2	p_3	p_4	p_5	p_6	p_7	p_8	p_9	p_{10}	p_{11}	p_{12}	Mean
NRMSE [%]	92.0	69.9	726	726	457	409	360	312	292	254	185	170	338
NMAE [%]	92.0	69.9	726	726	457	409	360	312	292	254	185	170	338
NSTD [–]	0.43	1.68	8.14	6.52	3.65	3.09	2.63	2.12	1.94	2.58	0.85	0.92	2.88

Table 8.3: Normalized error metrics for the keel pressure estimates (regular wave) over $t \in [10.0, 180.0]$ s

Metric	p_{13}	p_{14}	p_{15}	p_{16}	p_{17}	p_{18}	p_{19}	p_{20}	p_{21}	p_{22}	p_{23}	p_{24}	Mean
NRMSE [%]	82.8	48.8	283	1258	480	378	333	310	393	145	164	153	336
NMAE [%]	82.8	48.8	283	1258	480	378	333	310	393	145	164	153	336
NSTD [–]	0.22	0.94	3.75	11.67	3.82	2.78	2.33	2.11	2.96	0.48	0.73	0.68	2.71

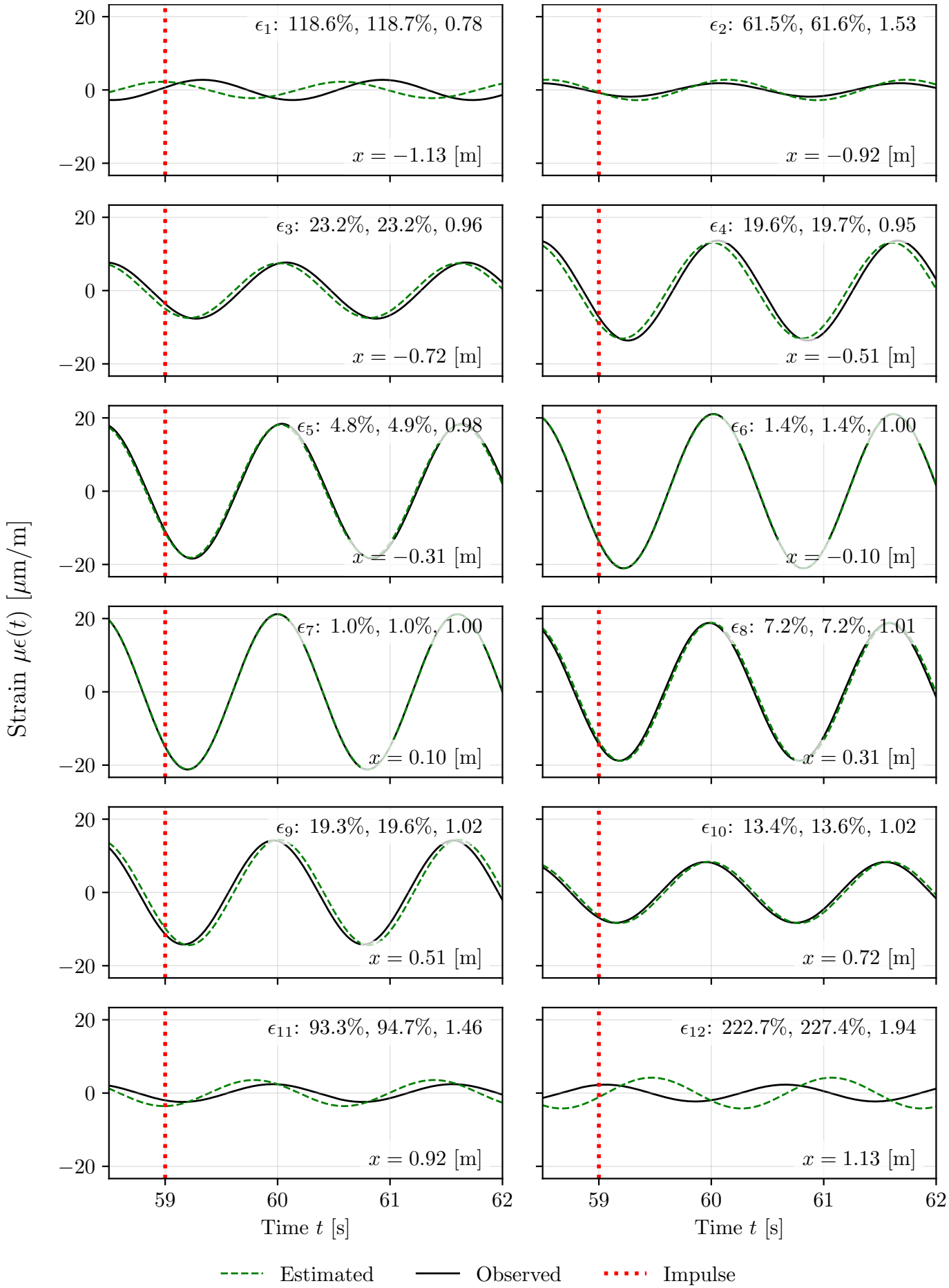


Figure 8.3: **Regular wave** strain response of the segmented barge, plotted at twelve points equally spaced along the backbone. Locations correspond to those shown in Figure 8.1. Error metrics (ϵ_i: NRMSE, NMAE, NSTD) are shown for $t \in [58.5, 62.0]$ [s].

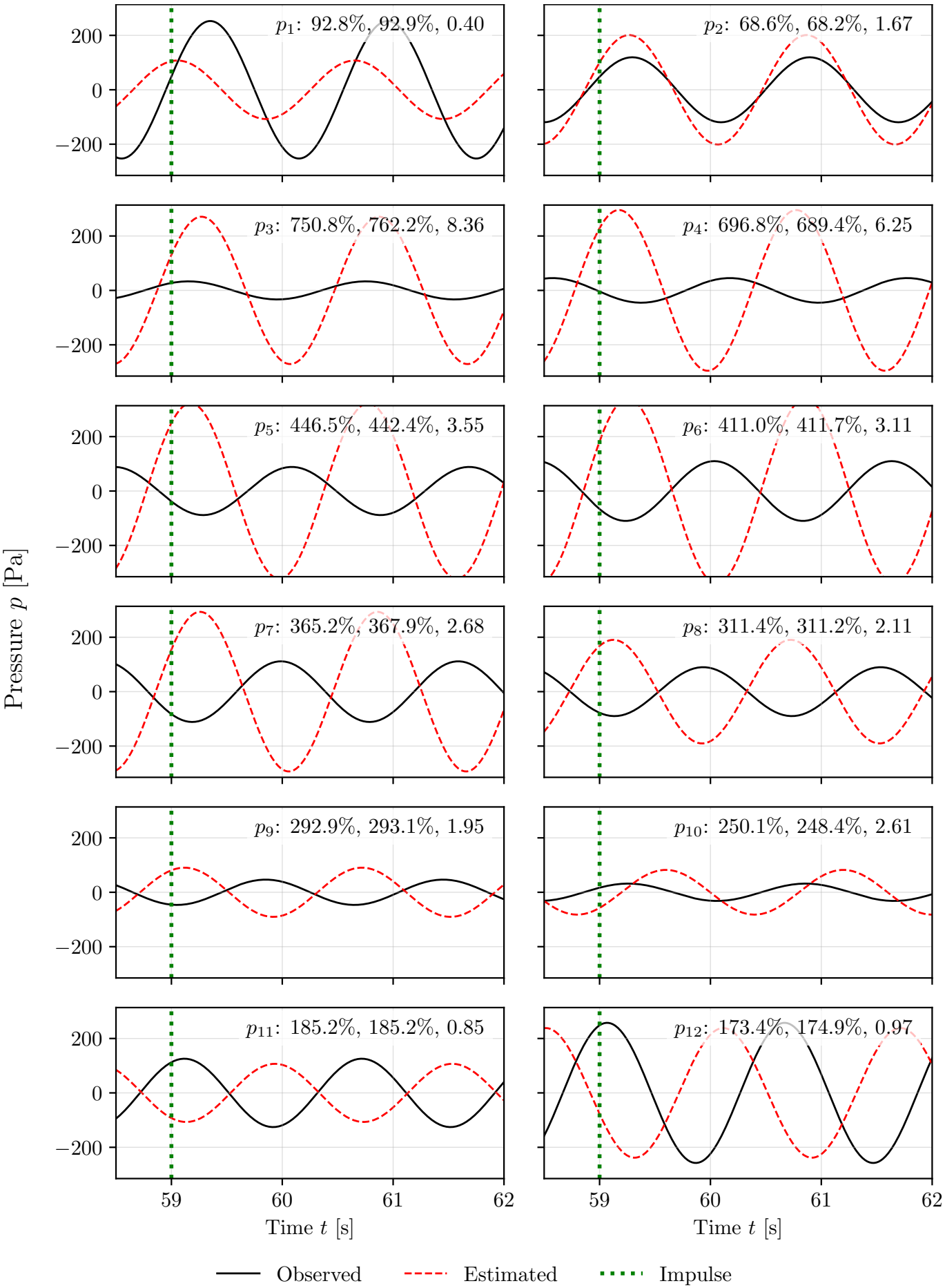


Figure 8.4: **Regular wave:** pressure loading of the segmented barge, plotted at twelve points equally spaced along the starboard side, mid-draft. Locations correspond to those shown in Figure 8.2. Error metrics (p_i: NRMSE, NMAE, NSTD) are shown for $t \in [58.5, 62.0]$ $[s]$.

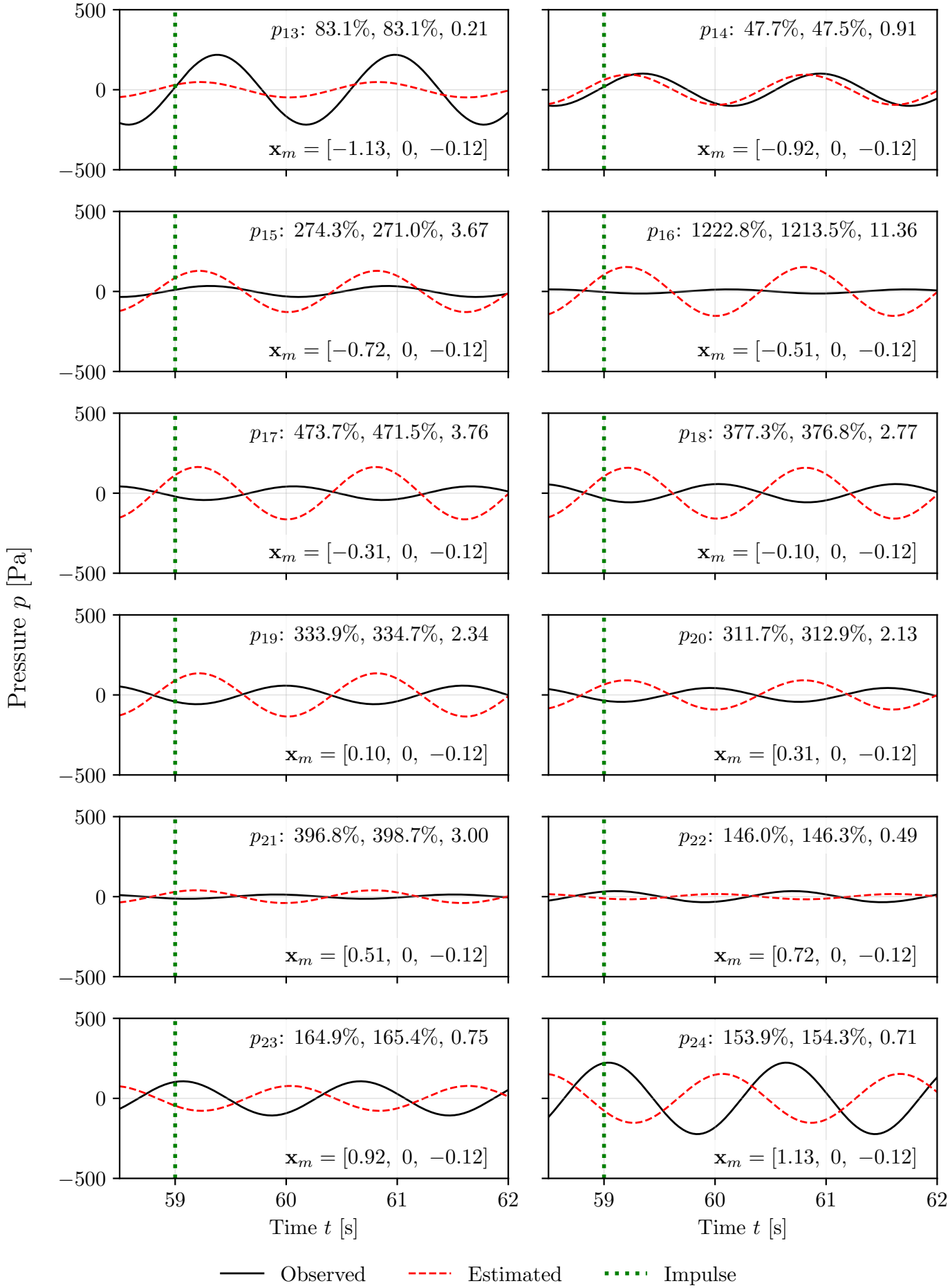


Figure 8.5: **Regular wave:** pressure loading of the segmented barge, plotted at twelve points equally spaced along the base, or keel. Locations correspond to those shown in Figure 8.2. Error metrics (p_i: NRMSE, NMAE, NSTD) are shown for $t \in [58.5, 62.0]$ $[s]$.

8.2 Irregular Waves

The irregular waves simulation introduces additional wave components such that the equivalent significant wave height is $H_s = 96$ mm and the mean zero-crossing period is $T_p = 1.6$ s. This test case is intended to verify the method of estimating modal amplitudes and the associated loading and response information using the full distortion mode basis. The time window from $t = 10$ to $t = 180$ seconds is used for the error metrics because no significant high-frequency transient response is excited by the waves. As in the regular wave simulation, the estimated strains are accurate near measured locations, but error increases near the bow and stern. The limitations of using a basis of distortion modes are especially apparent in the pressure estimates.

Strain Estimates The effects of the standing mode assumption as noted in Section 8.1 apply to the irregular waves simulation as well: NRMSE and NMAE values are lowest at locations ϵ_6 and ϵ_7, yet higher than those calculated during the regular wave simulation. The additional errors are introduced by the other incoming wave frequencies, which are not reflected in the truncated basis of distortion modes. The NRMSE, NMAE, and NSTD values are highest at the bow (ϵ_{12}) and stern (ϵ_1) because of the incident and diffraction loading that is partially discarded by taking the real part of each distortion mode at a specific frequency and phase.

Table 8.4: Normalized error metrics for the strain estimates (irregular waves) over $t \in [10.0, 180.0]$ s

Metric	ϵ_1	ϵ_2	ϵ_3	ϵ_4	ϵ_5	ϵ_6	ϵ_7	ϵ_8	ϵ_9	ϵ_{10}	ϵ_{11}	ϵ_{12}	Mean
NRMSE [%]	130	72.2	32.9	22.7	5.1	4.5	3.0	6.3	19.0	16.5	70.8	128	42.5
NMAE [%]	129	72.4	32.8	22.9	5.2	4.5	3.0	6.4	19.4	16.7	71.0	128	42.6
NSTD [–]	0.78	0.86	0.94	0.97	1.00	1.00	1.00	1.00	0.99	0.98	1.09	1.01	0.97

Pressure Estimates While the estimated strains induced by the irregular wave loading have a mean NSTD of 1.13, the estimated pressures are largely inaccurate. The mean NRMSE and NMAE values are over 200% on both the side and keel panels, with a mean NSTD above 1.6. Significant variation in all error metrics is noted along the length of the segmented barge, which is attributable to the basis of distortion modes. Only a limited number of modes are allowed, meaning the distribution of estimated incident, diffraction, radiation, and hydrostatic pressures cannot fully represent the observed external pressures induced by the irregular incoming waves and the rigid body motions. Adding more modes would not necessarily improve the error metrics because of the discarded imaginary part of each distortion mode.

Table 8.5: Normalized error metrics for the side-panel pressure estimates (irregular waves) over $t \in [10.0, 180.0]$ s

Metric	p_1	p_2	p_3	p_4	p_5	p_6	p_7	p_8	p_9	p_{10}	p_{11}	p_{12}	Mean
NRMSE [%]	109	76.4	285	346	318	294	258	243	207	171	166	143	218
NMAE [%]	109	75.1	282	346	318	296	259	242	203	170	166	143	218
NSTD [–]	0.52	1.41	3.13	3.15	2.50	2.12	1.77	1.52	1.30	1.36	0.72	0.75	1.69

Table 8.6: Normalized error metrics for the keel pressure estimates (irregular waves) over $t \in [10.0, 180.0]$ s

Metric	p_{13}	p_{14}	p_{15}	p_{16}	p_{17}	p_{18}	p_{19}	p_{20}	p_{21}	p_{22}	p_{23}	p_{24}	Mean
NRMSE [%]	85.5	57.1	228	618	438	358	310	275	220	137	158	144	252
NMAE [%]	85.2	56.5	231	627	440	358	310	275	220	137	157	143	253
NSTD [–]	0.23	0.94	3.11	5.94	3.56	2.65	2.15	1.83	1.57	0.41	0.67	0.61	1.97

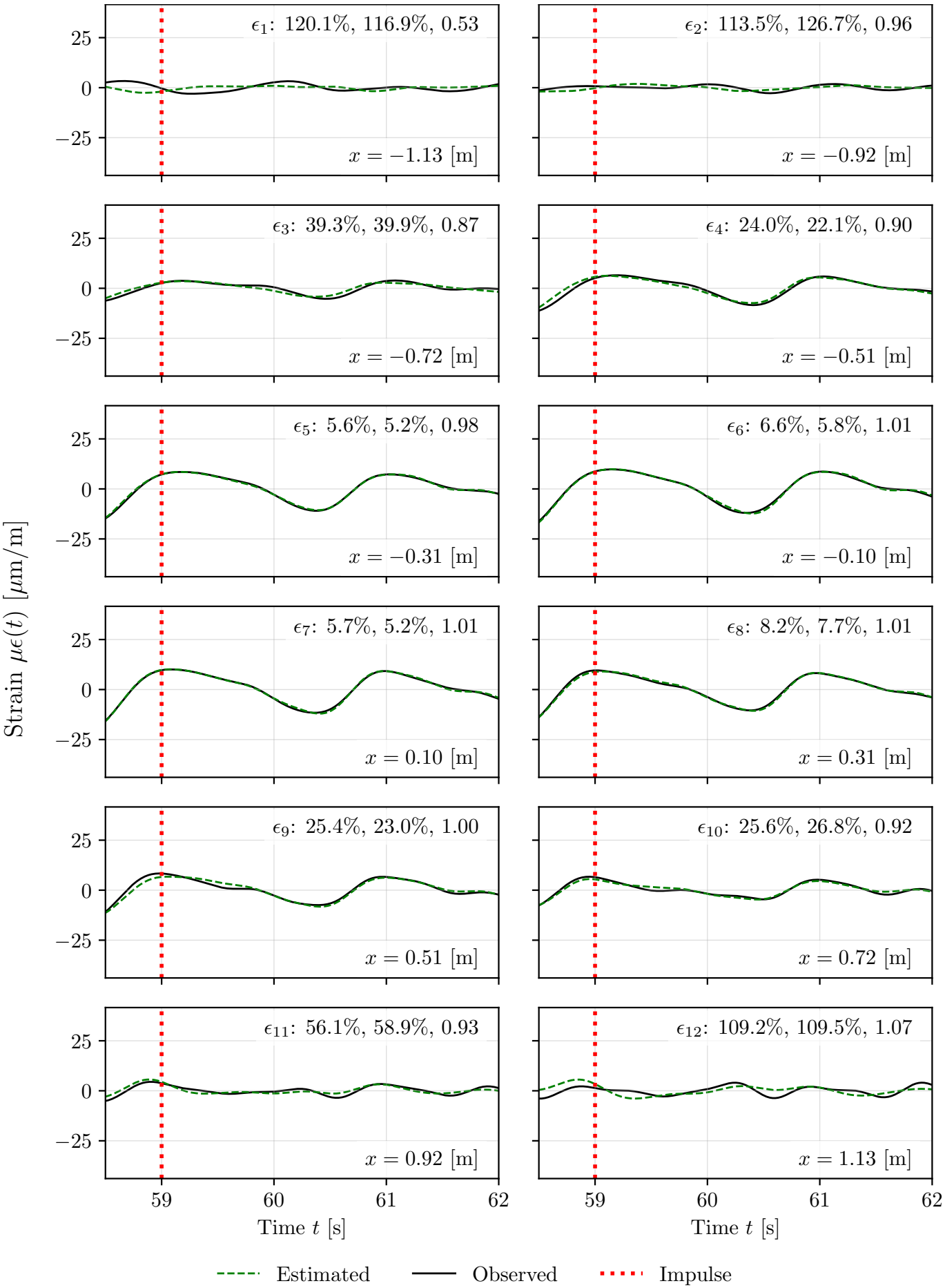


Figure 8.6: **Irregular wave:** strain response of the segmented barge, plotted at twelve points equally spaced along the backbone. Locations correspond to those shown in Figure 8.1. Error metrics (ϵ_i: NRMSE, NMAE, NSTD) are shown for $t \in [58.5, 62.0]$ [s].

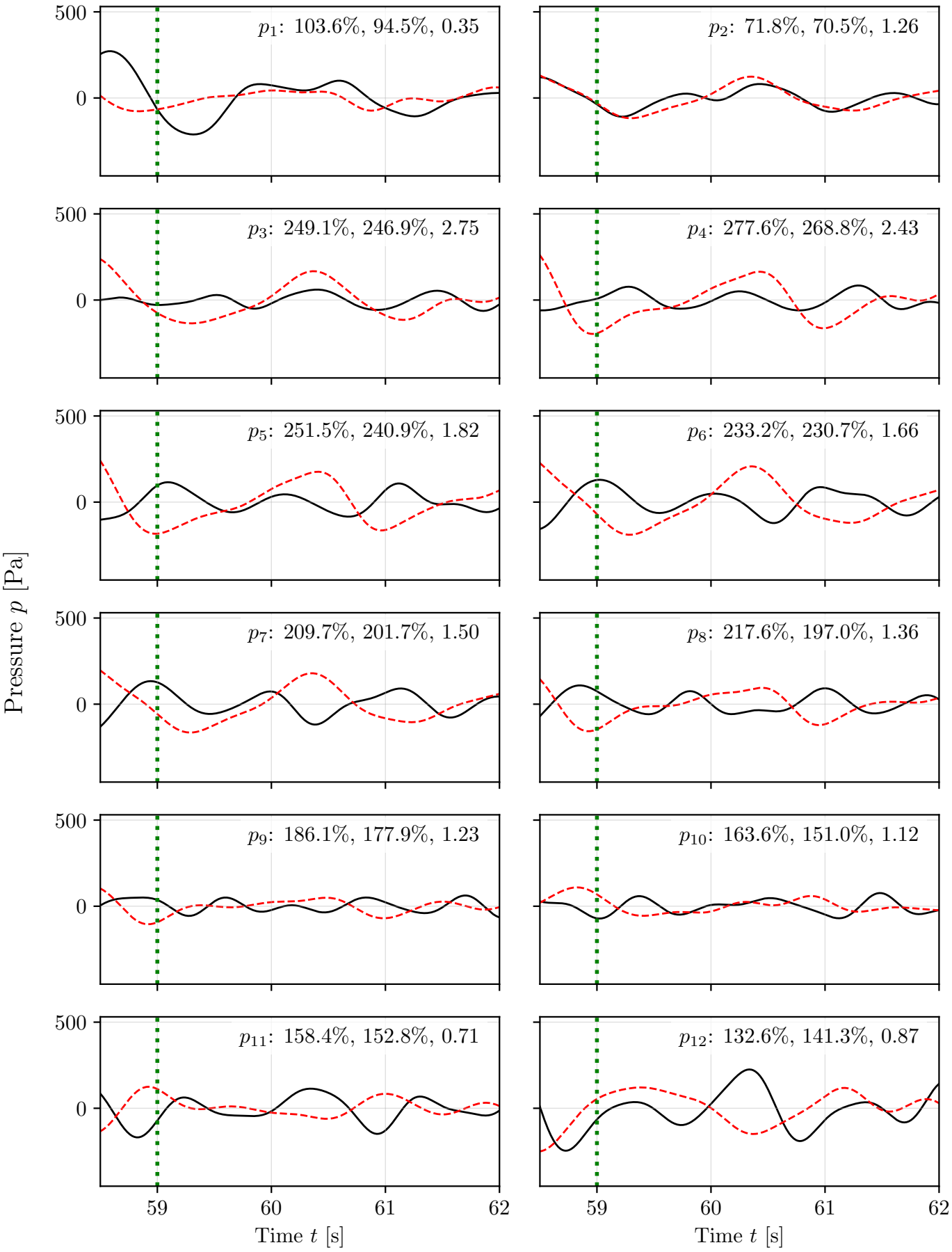


Figure 8.7: **Regular wave:** pressure loading of the segmented barge, plotted at twelve points equally spaced along the starboard side, mid-draft. Locations correspond to those shown in Figure 8.2. Error metrics (p_i: NRMSE, NMAE, NSTD) are shown for $t \in [58.5, 62.0]$ $[s]$.

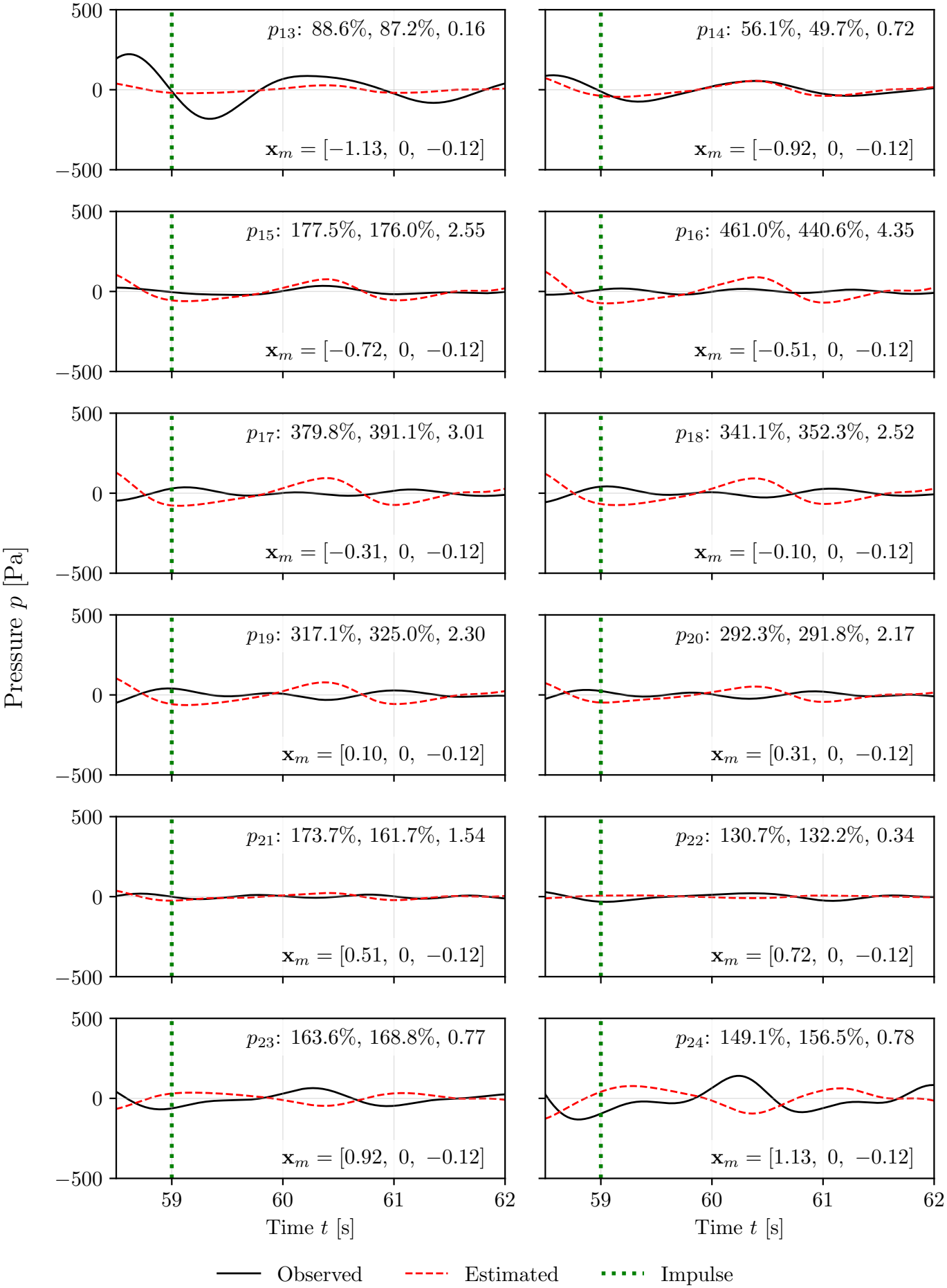


Figure 8.8: **Irregular wave:** pressure loading of the segmented barge, plotted at twelve points equally spaced along the base, or keel. Locations correspond to those shown in Figure 8.2. Error metrics (p_i: NRMSE, NMAE, NSTD) are shown for $t \in [58.5, 62.0]$ $[s]$.

8.3 Impulse Load

The impulse load simulation only uses the wet modal basis for estimating strain response and pressure loading. The wet modal basis itself is truncated to exclude the rigid body modes because adding such modes to the basis of distortion modes could lead to an ill-posed matrix $\mathbf{B}_{\boldsymbol{\epsilon}}^{\mathbf{m}}\mathbf{H}$. A single impulse load is applied to the bow node at $t = 59$ seconds, exactly at the ϵ_{12} location; the time $t = 59$ seconds is arbitrarily selected. The impulse load simulation is intended to isolate and verify the method of estimating modal amplitudes and loading and response information using only the wet modal basis. Low-frequency content is allowed in the vector of measured strains, but suppressed by the high-pass Butterworth filter. In general, high strain and keel pressure estimate accuracy is observed along the length of the beam, but low-frequency rigid body motions induce damping pressures on the sides of each segment. The initial high-order vibrations introduce a discrepancy between NRMSE and NMAE values within the $t \in [58.5, 62.0]$ window, presumably because of the high initial peak in all strain and pressure estimate errors directly after the applied impulse load.

Strain Estimates Strains are accurately estimated across the length of the beam, with the exception of some error prior to the slamming event: mean NRMSE is limited to less than 17%, and mean NMAE is limited to less than 8% for the time period $t \in [10, 180]$ seconds. Higher error is noted in the time window $t \in [58.5, 62.0]$ seconds because of the initial higher order transient effects of the impulse itself, which is not a radiation force. Inspection of the estimated and observed strain plots (Figure 8.9) shows that these metrics are not affected by phase errors, unlike in the regular and irregular wave simulations, where significant phase errors dominate both NRMSE and NMAE metrics. The error before $t = 59$ seconds is introduced by the high-pass Butterworth filter itself, an expected outcome given the relatively high number of poles required to cleanly separate low and high frequency signals. The mean NSTD values across both time windows (1.00 and 1.00) indicate that the strain estimates obtained from the wet modal basis would provide reasonably good inputs for a fatigue damage assessment. The NRMSE is consistently higher than NMAE because of the initial impulse at $t = 59.0$ seconds. NRMSE and NMAE is lowest at ϵ_6 and ϵ_7 for the same reason as mentioned in Sections 8.1 and 8.2. Errors at the bow (ϵ_{12}) and stern (ϵ_1) are still higher than at the center of the beam, but the amplitude is significantly lower. These errors are attributed to the radiation damping at the bow and the stern, which introduces a moment. Recall that the imaginary part of each wet mode is discarded because of the assumption that high-frequency radiation pressures are dominated by added mass, not damping. This assumption leads to the higher, yet marginal, errors at the bow and the stern.

Table 8.7: Normalized error metrics for the strain estimates (impulse load) over $t \in [10.0, 180.0]$ s

Metric	ϵ_1	ϵ_2	ϵ_3	ϵ_4	ϵ_5	ϵ_6	ϵ_7	ϵ_8	ϵ_9	ϵ_{10}	ϵ_{11}	ϵ_{12}	Mean
NRMSE [%]	22.5	7.1	6.1	6.5	7.6	8.7	10.1	12.0	14.6	18.8	27.5	57.7	16.6
NMAE [%]	15.0	3.5	2.6	2.5	2.6	2.9	3.5	4.4	5.6	7.3	10.5	30.1	7.5
NSTD [–]	1.00	1.00	1.00	1.00	1.00	1.00	0.99	0.99	0.99	0.98	0.93	1.18	1.00

Table 8.8: Normalized error metrics for the strain estimates (impulse load) over $t \in [58.5, 62.0]$ s

Metric	ϵ_1	ϵ_2	ϵ_3	ϵ_4	ϵ_5	ϵ_6	ϵ_7	ϵ_8	ϵ_9	ϵ_{10}	ϵ_{11}	ϵ_{12}	Mean
NRMSE [%]	23.4	7.9	6.8	7.5	8.8	10.2	11.8	13.9	16.7	21.1	30.0	60.6	18.2
NMAE [%]	20.4	6.1	4.6	4.6	4.9	5.5	6.7	8.3	10.4	13.4	18.4	44.8	12.4
NSTD [–]	1.00	1.00	1.00	1.00	1.00	0.99	0.99	0.99	0.98	0.97	0.92	1.19	1.00

Pressure Estimates The side panel pressure estimate errors are rather large, with NRMSE and NMAE values exceeding 100% for both time windows; simply setting all estimated strains to zero would yield lower NRMSE and NMAE. Furthermore, the NSTD is quite low: across both time windows, the NSTD is less than 0.5, indicating that the standard deviation is underestimated by more than a factor of two. Figure 8.10 shows two regimes: a high-frequency regime with relatively low amplitude and a high-amplitude, low-frequency regime with an approximate mean period of 1 second, or 6.3 radians per second. This frequency corresponds with rigid body pitch motion (see Table 6.2). The pressure estimates on the side of the barge show that the rigid body damping response is not captured by the wet modal basis, which is expected because the modal basis is truncated to only include the higher-order wet modes. The distribution of error confirms the rigid body pitch behavior, because NSTD values near the center of the barge (at panels p_4 and p_5, for

example) are closer to 1, as shown in Tables 8.9 and 8.10. The NSTD decreases near the bow and stern since the rigid body motions are severely underestimated when only higher-order modes are included in the basis.

Table 8.9: Normalized error metrics for the side-panel pressure estimates (impulse load) over $t \in [10.0, 180.0]$ s

Metric	p_1	p_2	p_3	p_4	p_5	p_6	p_7	p_8	p_9	p_{10}	p_{11}	p_{12}	Mean
NRMSE [%]	112	110	98.7	93.3	140	136	115	104	100.0	99.8	102	103	109
NMAE [%]	125	123	105	112	191	190	146	119	105	102	110	113	128
NSTD [–]	0.28	0.29	0.31	0.76	1.20	0.88	0.51	0.31	0.21	0.12	0.13	0.15	0.43

Table 8.10: Normalized error metrics for the side-panel pressure estimates (impulse load) over $t \in [58.5, 62.0]$ s

Metric	p_1	p_2	p_3	p_4	p_5	p_6	p_7	p_8	p_9	p_{10}	p_{11}	p_{12}	Mean
NRMSE [%]	109	107	98.2	90.0	128	127	111	102	99.7	99.8	101	103	106
NMAE [%]	107	104	100	94.4	137	127	107	101	99.9	100	101	103	107
NSTD [–]	0.25	0.26	0.31	0.77	1.15	0.77	0.45	0.29	0.21	0.12	0.11	0.14	0.40

Pressure estimates on the keel are less affected by rigid body motion because rigid body damping pressures at the frequency of the wet pitch mode are concentrated near the water surface. Mean NRMSE and NMAE values are limited to below 25% for both time windows, and the mean NSTD is slightly higher than 1, indicating relatively good agreement. The pressure estimates are most accurate near the center of the barge, where the pressure amplitude is highest, as shown in Figure 8.11. The first peak and trough after the slamming event and the pressure amplitude closest to the impulse loading location (the bow) introduce error that is readily apparent when comparing the NRMSE and NMAE at ϵ_{12}: for the time window $t \in [58.5, 62.0]$ seconds, NRMSE is 64.1%, while the NMAE is 38.8%. These values drop to 58.1% and 28.9% for the full time window. The initial peak and trough contribute significantly to the mean error because the impulse load itself is not represented in the wet modal basis.

Table 8.11: Normalized error metrics for the keel pressure estimates (impulse load) over $t \in [10.0, 180.0]$ s

Metric	p_{13}	p_{14}	p_{15}	p_{16}	p_{17}	p_{18}	p_{19}	p_{20}	p_{21}	p_{22}	p_{23}	p_{24}	Mean
NRMSE [%]	21.6	16.7	17.2	8.1	10.8	12.7	12.5	16.1	22.0	36.6	50.7	58.1	23.6
NMAE [%]	20.5	14.4	12.4	9.3	10.4	10.9	11.7	13.6	17.2	23.6	19.7	28.9	16.0
NSTD [–]	1.14	1.11	1.03	1.03	1.08	1.10	1.09	1.07	1.05	0.88	0.94	1.05	1.05

Table 8.12: Normalized error metrics for the keel pressure estimates (impulse load) over $t \in [58.5, 62.0]$ s

Metric	p_{13}	p_{14}	p_{15}	p_{16}	p_{17}	p_{18}	p_{19}	p_{20}	p_{21}	p_{22}	p_{23}	p_{24}	Mean
NRMSE [%]	22.5	18.0	17.5	7.9	11.0	13.5	13.3	17.1	22.5	37.3	56.3	64.1	25.1
NMAE [%]	22.7	16.5	13.0	8.6	10.6	11.7	13.2	16.1	19.9	29.7	26.9	38.8	19.0
NSTD [–]	1.13	1.11	1.02	1.03	1.07	1.10	1.09	1.07	1.04	0.87	0.90	1.03	1.04

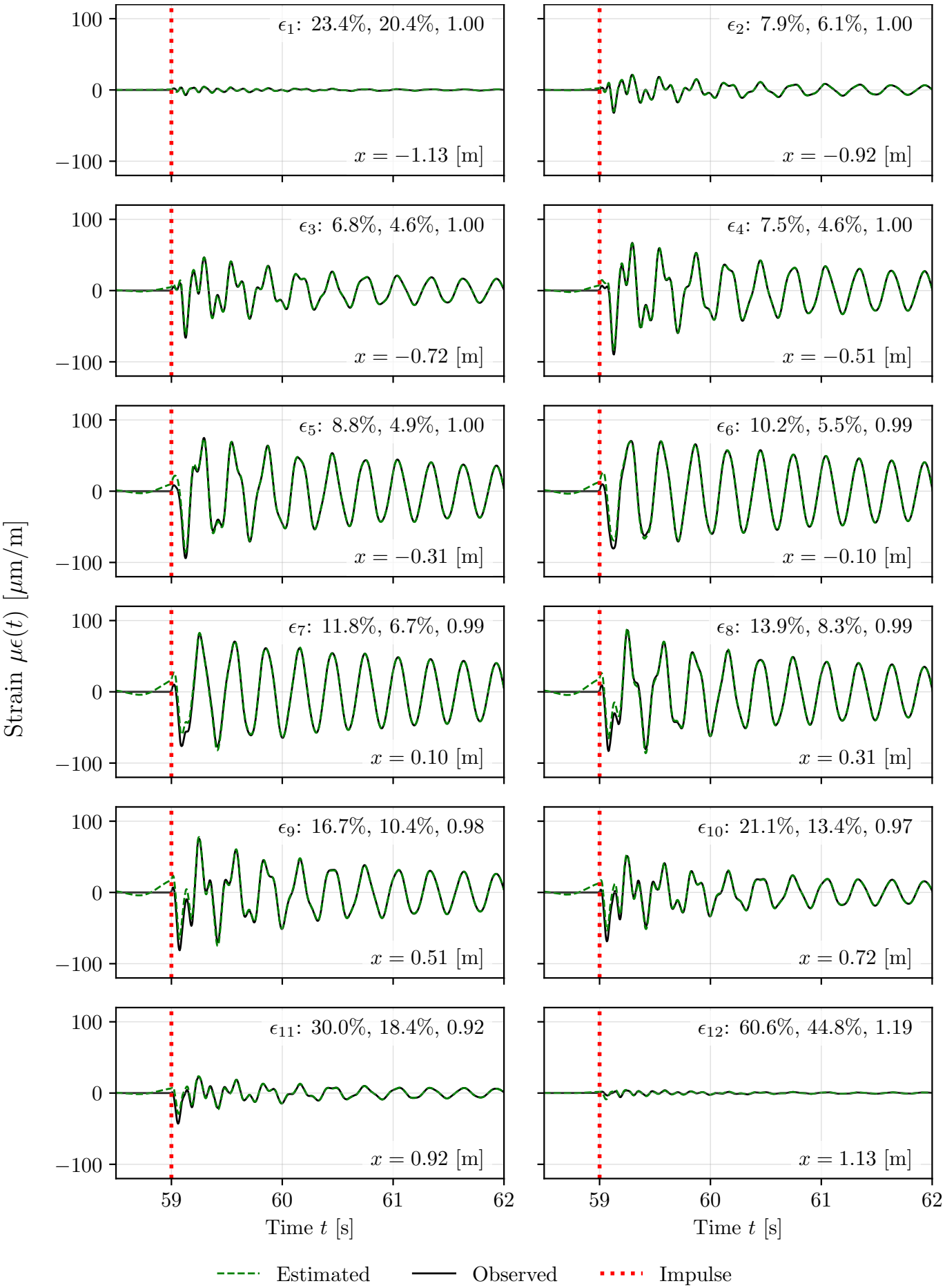


Figure 8.9: **Impulse load:** strain response of the segmented barge, plotted at twelve points equally spaced along the backbone. Locations correspond to those shown in Figure 8.1. Error metrics (ϵ_i: NRMSE, NMAE, NSTD) are shown for $t \in [58.5, 62.0]$ [s].

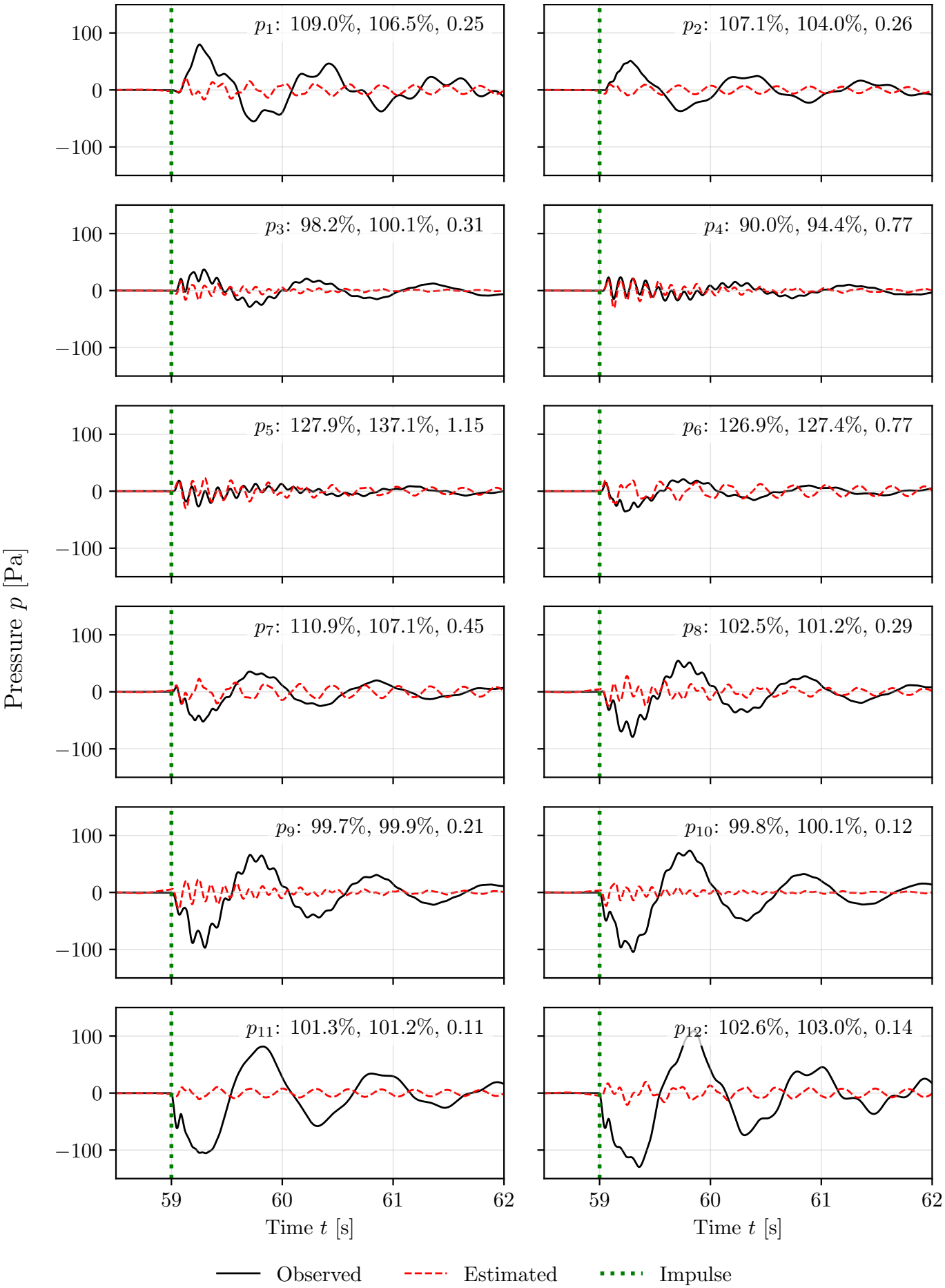


Figure 8.10: **Impulse load:** pressure loading of the segmented barge, plotted at twelve points equally spaced along the starboard side, mid-draft. Locations correspond to those shown in Figure 8.2. Error metrics (p_i: NRMSE, NMAE, NSTD) are shown for $t \in [58.5, 62.0]$ $[s]$.

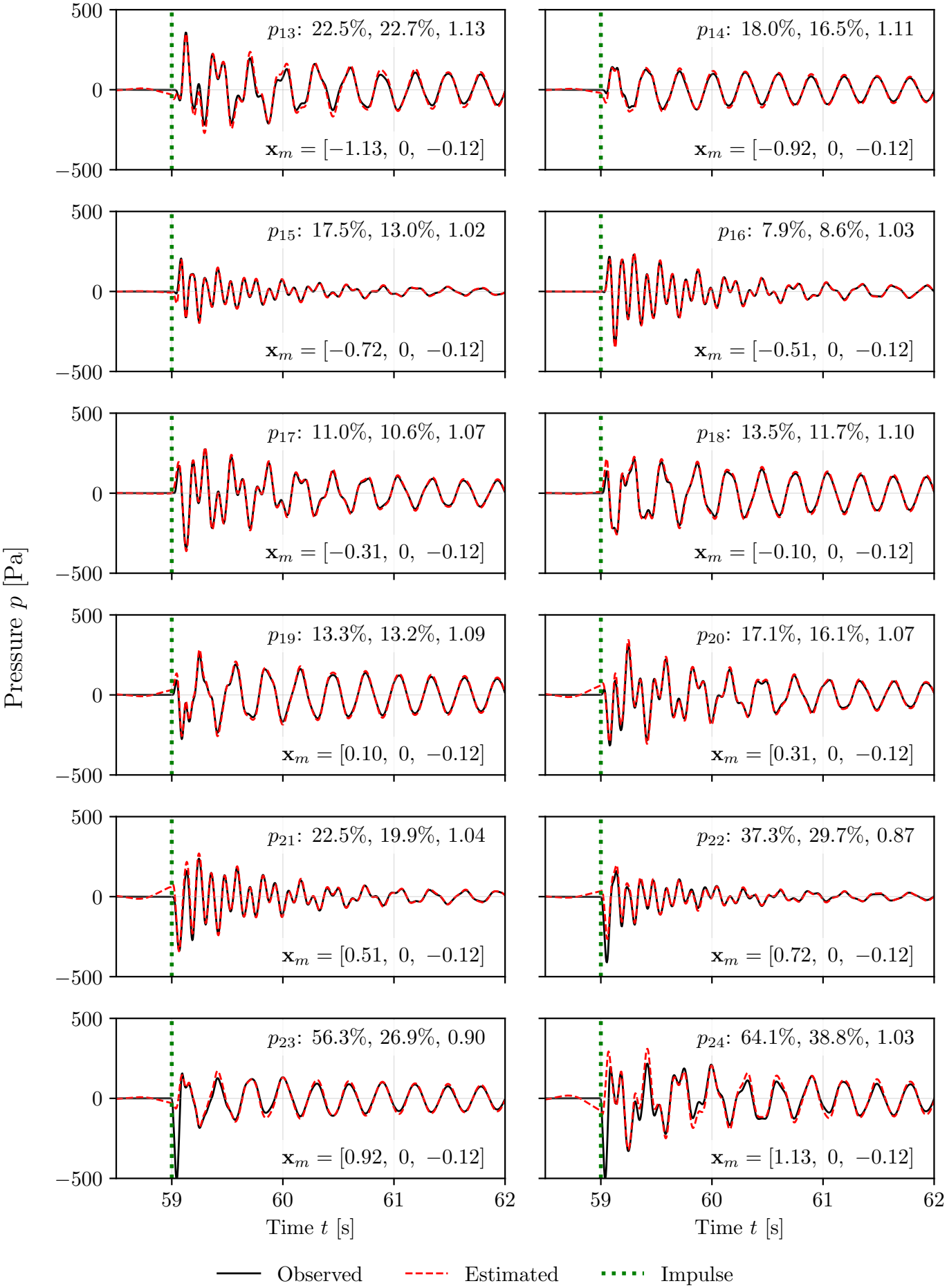


Figure 8.11: **Impulse load:** pressure loading of the segmented barge, plotted at twelve points equally spaced along the base, or keel. Locations correspond to those shown in Figure 8.2. Error metrics (p_i: NRMSE, NMAE, NSTD) are shown for $t \in [58.5, 62.0]$ $[s]$.

8.4 Regular Wave with Impulse Load

The regular wave with impulse load simulation illustrates the effects of using wet and distortion modes during combined regular wave and transient loading. The low- and high-pass filters used for separating the responses is also tested. The assumption of linearity means that the estimated strains and pressures should consist of the superposition of both regular wave and impulse load components. This effect is illustrated in the strain response, where some error at the incoming wave frequency is observed near the bow and stern, while strain estimates in the middle of the barge are quite accurate. A similar effect is observed in the estimated pressure loading: pressures at the base have some low-frequency error which can be attributed to the distortion mode estimates, while pressures on the side of the barge are poorly estimated due to the rigid body damping. Error metrics are calculated for both time windows: $t \in [58.5, 62.0]$ and $t \in [10, 180]$ seconds.

Strain Estimates In general, the same conclusions about the strain response can be drawn from Sections 8.1 and 8.3. The strain estimate errors are low near the locations where strains are measured: NRMSE and NMAE values at ϵ_5, ϵ_6, and ϵ_7 are all at or below 3% for both time windows, which is lower than the combined NRMSE and NMAE values at the same positions for independent regular wave and impulse loading. NRMSE and NMAE values jump to above 200% at the bow (ϵ_{12}) and above 120% at the stern (ϵ_1). Furthermore, the mean NSTD is slightly higher than 1 (1.12 and 1.10 for the long and short time windows, respectively), which is also reflected in the results from the regular wave simulation. These results are consistent with those from Sections 8.1 and 8.3, meaning the use of low- and high-pass Butterworth filters to separate high- and low-frequency measured strain signals does not introduce measurable error. An exception is the first peak and trough after $t = 59.0$ seconds, where the impulse load is applied. As explained earlier, this load is not included in the modal basis and therefore a source of error after the initial load is applied. Additionally, the Butterworth filter introduces negligible error prior to the impulse event: this error persists for approximately one wet period and does not appreciably affect the error metrics.

Table 8.13: Normalized error metrics for the strain estimates (regular wave with impulse load) over $t \in$ [10.0, 180.0] s

Metric	ϵ_1	ϵ_2	ϵ_3	ϵ_4	ϵ_5	ϵ_6	ϵ_7	ϵ_8	ϵ_9	ϵ_{10}	ϵ_{11}	ϵ_{12}	Mean
NRMSE [%]	131	52.0	22.9	18.6	2.9	2.4	0.4	5.1	17.6	13.8	72.3	215	46.2
NMAE [%]	131	62.1	24.4	19.5	3.0	2.5	0.2	5.3	18.4	14.5	83.3	215	48.3
NSTD [–]	0.93	1.35	0.98	0.97	0.99	1.00	1.00	1.00	1.01	1.01	1.32	1.86	1.12

Table 8.14: Normalized error metrics for the strain estimates (regular wave with impulse load) over $t \in$ [58.5, 62.0] s

Metric	ϵ_1	ϵ_2	ϵ_3	ϵ_4	ϵ_5	ϵ_6	ϵ_7	ϵ_8	ϵ_9	ϵ_{10}	ϵ_{11}	ϵ_{12}	Mean
NRMSE [%]	126	16.3	8.4	8.0	2.2	1.6	1.0	2.7	8.7	7.4	21.5	220	35.3
NMAE [%]	135	18.2	9.5	8.9	1.8	1.4	0.6	2.7	9.2	7.5	26.3	216	36.4
NSTD [–]	1.14	1.02	1.00	1.00	1.00	1.00	1.00	1.00	1.00	0.99	1.01	2.03	1.10

Pressure Estimates The conclusions for pressure estimates on the side panels are similar to those drawn in Sections 8.1 and 8.3 as well. In this combined case, discarding imaginary parts of the distortion modes introduces the most error: mean NRMSE and NMAE of over 340% is noted, and the mean NSTD is nearly 3. The high-frequency response is negligible in comparison, which supports the conclusions made earlier about discarding the complex part of each wet mode shape: added mass dominates the high-frequency hydroelastic loading at this stiffness. Disregarding the high-frequency response in the estimates is justified through the error metrics: there is minimal difference in the mean NRMSE, NMAE, and NSTD values between the two time windows. No discernible pattern is observed in the distribution of error on the side panels along the length of the beam, which reflects the fact that distortion modes can only represent a limited number of standing modes, while the incoming waves are traveling.

Table 8.15: Normalized error metrics for the side-panel pressure estimates (regular wave with impulse load) over $t \in [10.0, 180.0]$ s

Metric	p_1	p_2	p_3	p_4	p_5	p_6	p_7	p_8	p_9	p_{10}	p_{11}	p_{12}	Mean
NRMSE [%]	99.9	70.2	745	730	459	410	360	314	286	293	184	171	344
NMAE [%]	100.0	70.2	747	730	459	410	361	314	287	293	184	171	344
NSTD [–]	0.48	1.69	8.30	6.56	3.67	3.10	2.63	2.15	1.91	3.00	0.85	1.00	2.94

Table 8.16: Normalized error metrics for the side-panel pressure estimates (regular wave with impulse load) over $t \in [58.5, 62.0]$ s

Metric	p_1	p_2	p_3	p_4	p_5	p_6	p_7	p_8	p_9	p_{10}	p_{11}	p_{12}	Mean
NRMSE [%]	101	70.9	680	800	496	409	352	325	254	220	217	186	343
NMAE [%]	102	70.8	746	758	477	414	361	314	257	200	215	188	342
NSTD [–]	0.53	1.65	7.53	7.41	4.12	3.10	2.57	2.36	1.77	2.25	1.32	1.17	2.98

The influence of added mass on the keel is more apparent in the pressures shown in Figure 8.14 because the high-frequency oscillations (wet mode estimates) appear to match the observed pressures. Error metrics are more difficult to interpret due to the error imparted by the basis of distortion modes, which is consistent with the conclusions from Sections 8.1 and 8.3. The mean NRMSE and NMAE values remain above 270% for $t \in [10, 180]$ seconds and above 115% for $t \in [58.5, 62.0]$ seconds, while the results from Table 8.11 show mean NRMSE and NMAE values of 23.6% and 16.0% (respectively) for $t \in [10.0, 180.0]$ seconds. Table 8.12 shows mean NRMSE and NMAE values of 25.1% and 19.0% (respectively) for $t \in [58.5, 62.0]$ seconds. The drop in mean NRMSE and NMAE reflects the accuracy of the wet mode-based pressure estimates in the time window $t \in [58.5, 62.0]$ seconds, which primarily consists of high-frequency content dominated by added mass. The highest error is concentrated near the stern, specifically panels p_{15}, p_{16}, and p_{17}. The error at these panels comes primarily from the basis of distortion modes and the standing wave assumption, since high error at these keel panels is not observed in the impulse load results from Section 8.3.

Table 8.17: Normalized error metrics for the keel pressure estimates (regular wave with impulse load) over $t \in [10.0, 180.0]$ s

Metric	p_{13}	p_{14}	p_{15}	p_{16}	p_{17}	p_{18}	p_{19}	p_{20}	p_{21}	p_{22}	p_{23}	p_{24}	Mean
NRMSE [%]	82.2	48.2	275	843	436	353	311	282	262	138	161	152	279
NMAE [%]	82.4	48.4	280	1132	461	366	322	298	353	143	162	152	317
NSTD [–]	0.25	0.94	3.65	7.86	3.50	2.63	2.21	1.97	2.11	0.54	0.75	0.70	2.26

Table 8.18: Normalized error metrics for the keel pressure estimates (regular wave with impulse load) over $t \in [58.5, 62.0]$ s

Metric	p_{13}	p_{14}	p_{15}	p_{16}	p_{17}	p_{18}	p_{19}	p_{20}	p_{21}	p_{22}	p_{23}	p_{24}	Mean
NRMSE [%]	71.8	39.6	152	184	168	160	144	116	72.0	55.2	119	138	118
NMAE [%]	77.0	42.8	178	247	197	176	158	132	87.6	72.1	132	146	137
NSTD [–]	0.60	1.04	2.18	2.01	1.70	1.56	1.41	1.26	1.12	0.88	0.94	0.92	1.30

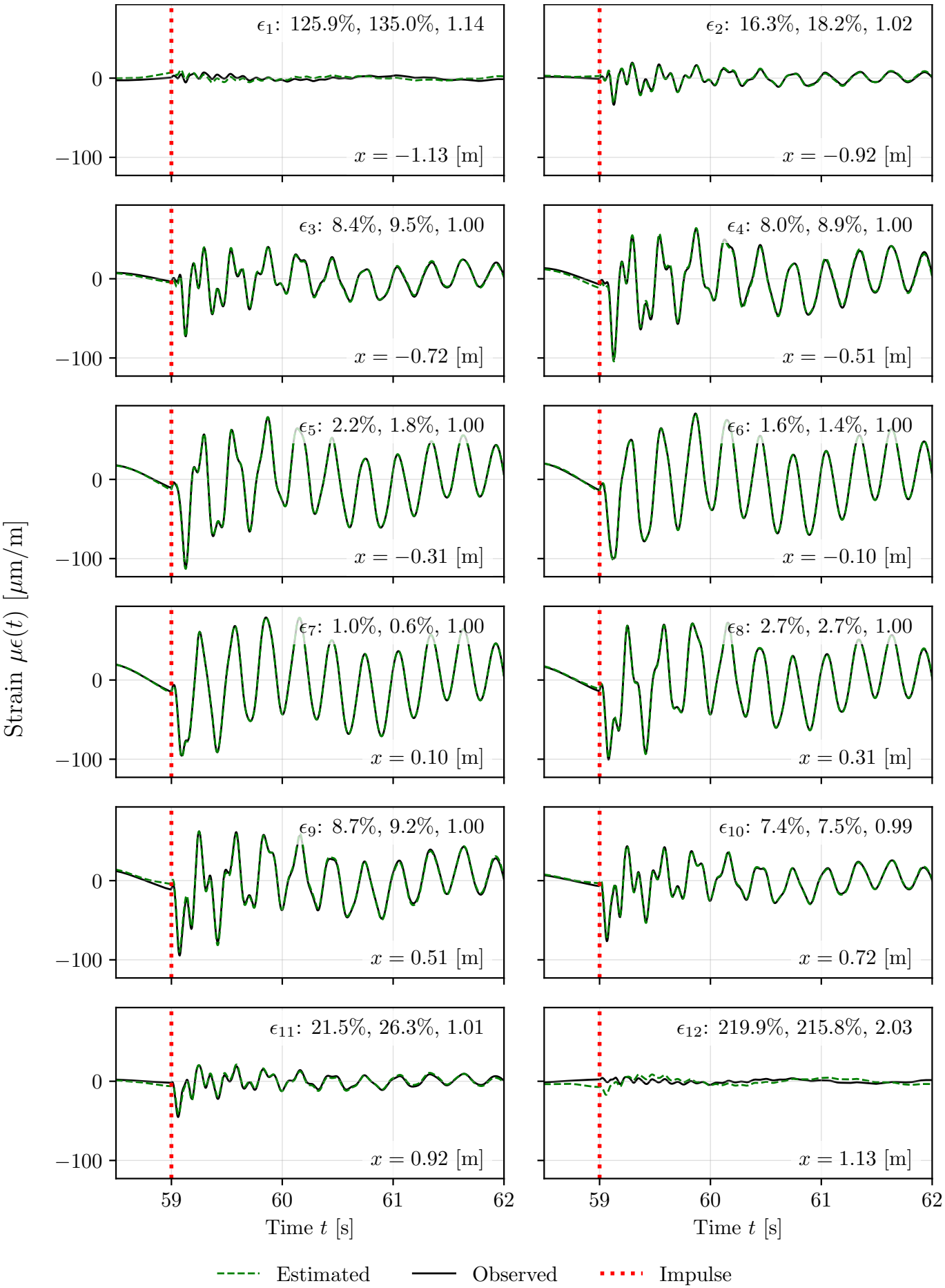


Figure 8.12: **Regular wave with impulse load:** strain response of the segmented barge, plotted at twelve points equally spaced along the backbone. Locations correspond to those shown in Figure 8.1 Error metrics (ϵ_i: NRMSE, NMAE, NSTD) are shown for $t \in [58.5, 62.0]$ [s].

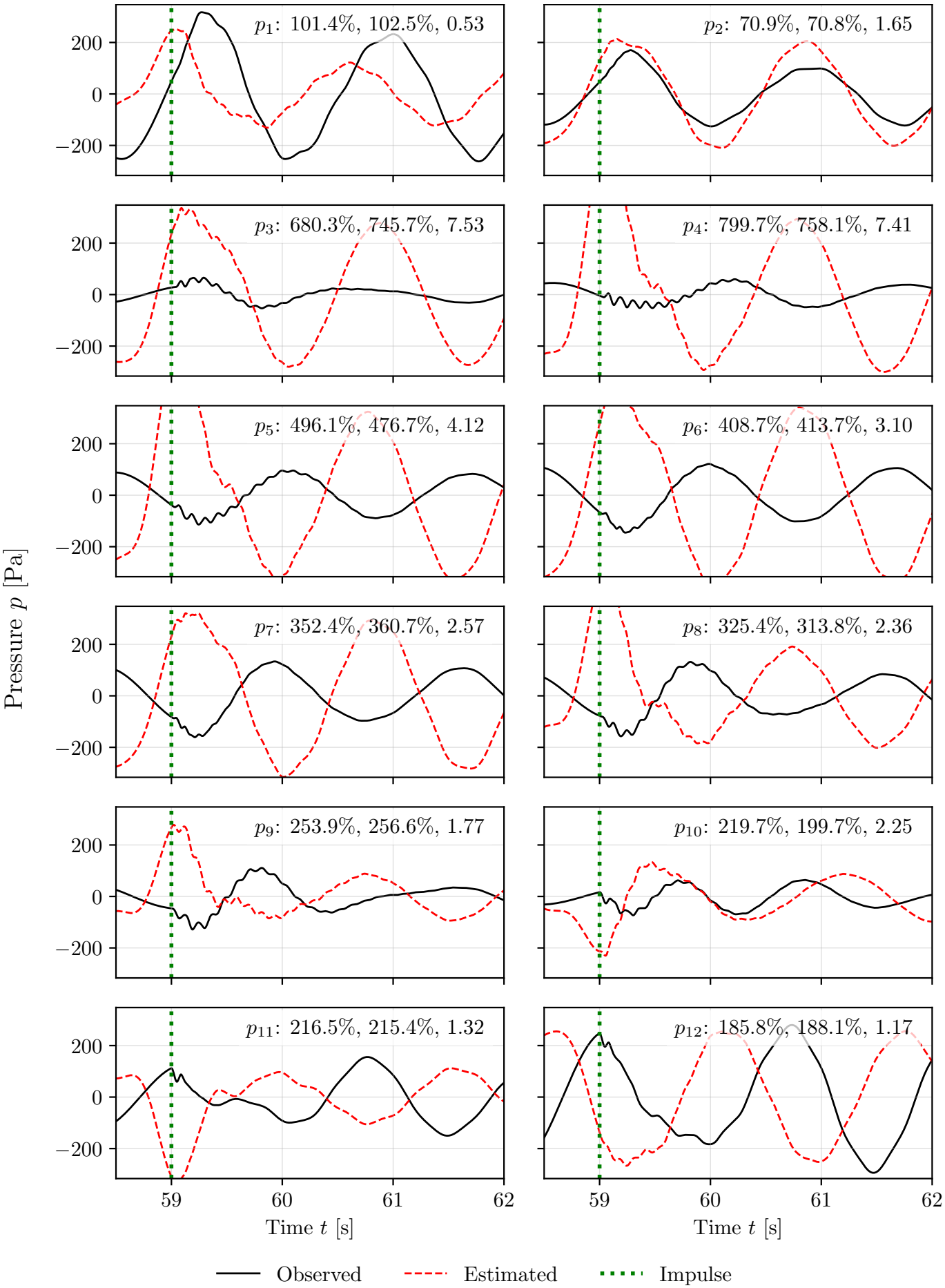


Figure 8.13: **Regular wave with impulse load:** pressure loading of the segmented barge, plotted at twelve points equally spaced along the starboard side, mid-draft. Locations correspond to those shown in Figure 8.2. Error metrics (p_i: NRMSE, NMAE, NSTD) are shown for $t \in [58.5, 62.0]$ $[s]$.

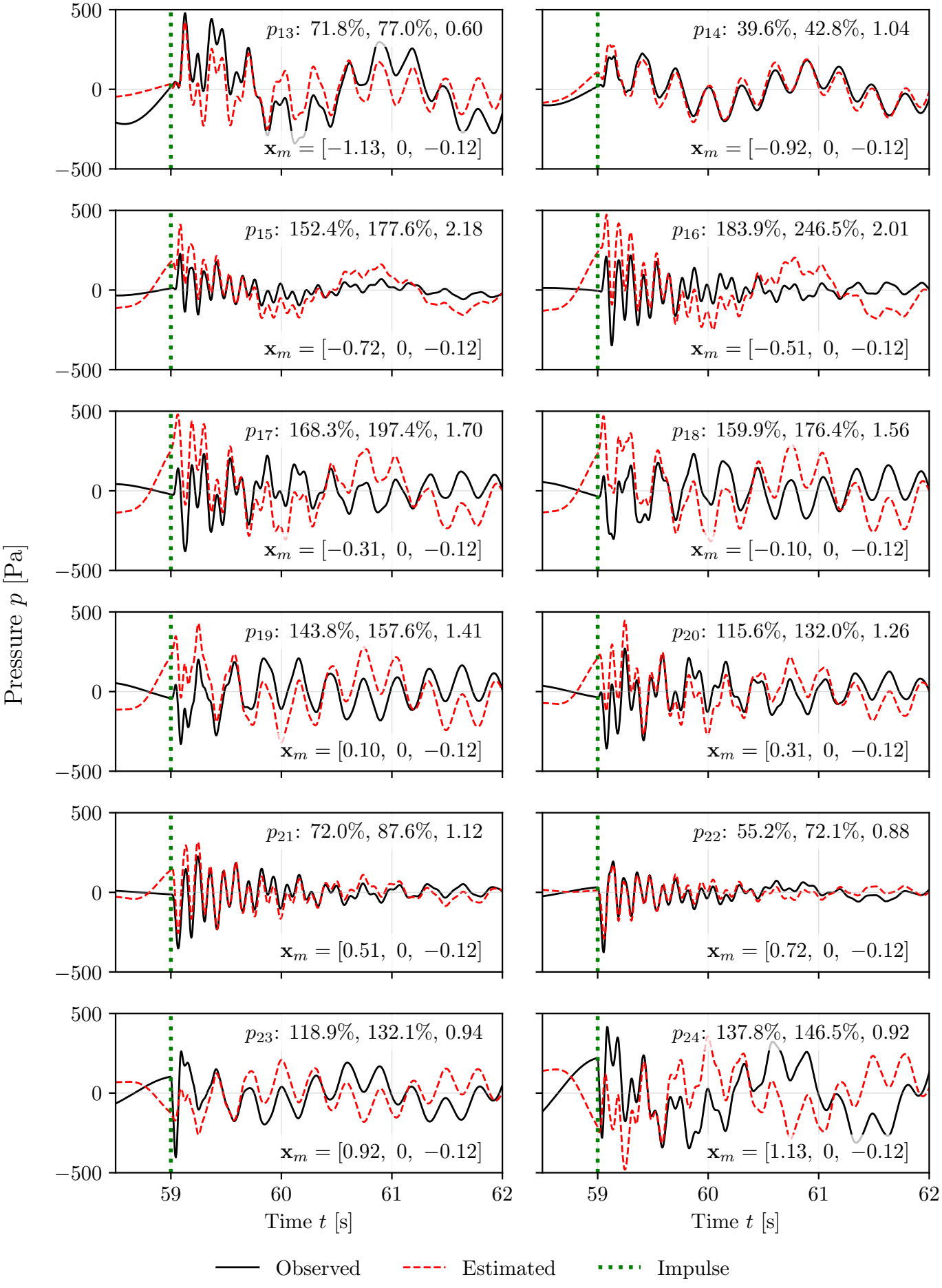


Figure 8.14: **Regular wave with impulse load:** pressure loading of the segmented barge, plotted at twelve points equally spaced along the base, or keel. Locations correspond to those shown in Figure 8.2. Error metrics (p_i: NRMSE, NMAE, NSTD) are shown for $t \in [58.5, 62.0]$ $[s]$.

8.5 Irregular Waves with Impulse Load

The irregular waves with impulse load simulation illustrates the effects of using wet and distortion modes for estimating the strain response and pressure loading during combined irregular wave and transient loading. The low- and high-pass filters used for separating the responses is tested more rigorously than in Section 8.4 because the structure is excited by higher frequency wave components; the high-pass Butterworth filter does not roll off fast enough to attenuate signals above 8 radians per second to an amplitude below -30 dB. The conclusions from Section 8.4 apply to this simulation as well, with some minor differences in error metrics. For example, the mean NRMSE, NMAE, and NSTD values for strain and pressure estimates in both time windows are consistently and significantly lower than those calculated in Section 8.4. The noted reduction in error shows that the low- and high-pass filters effectively separate the two regimes despite the theoretically insufficient roll-off rate. However, the reduced error does not necessarily imply that the basis of distortion modes performs better in the irregular wave case. The distribution of error along the length of the beam still indicates that the standing wave assumption does not accurately represent the traveling wave pressure distribution.

Strain Estimates As noted in Section 8.4, the NRMSE and NMAE values are below 5% in the center of the beam, with a NSTD of 1.00. The accurate estimates at ϵ_5, ϵ_6, and ϵ_7 are expected because the method of least squares enforces high accuracy at the measured locations. Estimated strains at the bow (ϵ_{12}) and stern (ϵ_1) are less accurate because the incident and diffraction pressures are partially discarded when creating the basis of distortion modes. The strain amplitudes at these locations are low relative to the center of the barge because the response associated with heave motion most resembles the two-node bending mode. Despite the inaccuracies at the bow and stern nodes, mean NRMSE and NMAE values of around 40% and 25% are noted in time windows $t \in [10, 180]$ and $t \in [58.5, 62.0]$ seconds, respectively. The reduction in error in the narrow time window is attributable to the accurate transient strains estimated using the wet modal basis and the high-pass filter.

Table 8.19: Normalized error metrics for the strain estimates (irregular waves with impulse load) over $t \in$ [10.0, 180.0] s

Metric	ϵ_1	ϵ_2	ϵ_3	ϵ_4	ϵ_5	ϵ_6	ϵ_7	ϵ_8	ϵ_9	ϵ_{10}	ϵ_{11}	ϵ_{12}	Mean
NRMSE [%]	129	59.3	27.4	19.3	4.5	3.9	2.7	5.5	16.5	14.1	61.5	128	39.3
NMAE [%]	128	65.5	29.7	20.9	4.8	4.2	2.8	5.9	17.8	15.2	66.0	129	40.8
NSTD [–]	0.78	0.91	0.96	0.98	1.00	1.00	1.00	1.00	0.99	0.98	1.06	1.02	0.97

Table 8.20: Normalized error metrics for the strain estimates (irregular waves with impulse load) over $t \in$ [58.5, 62.0] s

Metric	ϵ_1	ϵ_2	ϵ_3	ϵ_4	ϵ_5	ϵ_6	ϵ_7	ϵ_8	ϵ_9	ϵ_{10}	ϵ_{11}	ϵ_{12}	Mean
NRMSE [%]	103	19.6	7.6	5.3	2.1	2.0	1.5	2.2	5.5	5.5	18.7	130	25.2
NMAE [%]	104	22.6	8.0	5.0	1.7	1.7	1.4	1.9	5.0	5.1	19.9	119	24.6
NSTD [–]	0.75	0.99	0.99	1.00	1.00	1.00	1.00	1.00	1.00	0.99	0.96	1.28	1.00

Pressure Estimates The conclusions about pressure estimates on the side panels are similar to those drawn in Sections 8.2 and 8.3. As in the combined regular wave and impulse load simulation, the basis of distortion modes contributes to significant mean NRMSE and NMAE: at least 217% over the full time window and 162% over the limited time window. Correcting for the phase shift could improve these metrics, but only marginally because the mean NSTD is 1.69 and 1.32 for the two time windows, a considerable overestimate. Figure 8.16 shows that the high-frequency pressures estimated using the wet modal basis are negligible relative to the low-frequency pressures, supporting the conclusion that the basis of distortion modes dominates the estimate error metrics. Furthermore, the NRMSE, NMAE, and NSTD values are highest at panels p_4, p_5, and p_6, which indicates that the spatial distribution of pressure associated with the distortion modes does not represent the actual distribution of the wave (incident and diffraction) and radiation pressure.

Table 8.21: Normalized error metrics for the side-panel pressure estimates (irregular waves with impulse load) over $t \in [10.0, 180.0]$ s

Metric	p_1	p_2	p_3	p_4	p_5	p_6	p_7	p_8	p_9	p_{10}	p_{11}	p_{12}	Mean
NRMSE [%]	109	76.5	284	346	318	294	258	242	205	171	166	143	218
NMAE [%]	109	75.2	281	344	317	296	259	241	202	169	166	143	217
NSTD [–]	0.52	1.41	3.12	3.14	2.50	2.12	1.77	1.51	1.29	1.37	0.73	0.75	1.69

Table 8.22: Normalized error metrics for the side-panel pressure estimates (irregular waves with impulse load) over $t \in [58.5, 62.0]$ s

Metric	p_1	p_2	p_3	p_4	p_5	p_6	p_7	p_8	p_9	p_{10}	p_{11}	p_{12}	Mean
NRMSE [%]	113	75.7	214	238	211	222	190	167	145	120	161	135	166
NMAE [%]	103	76.7	208	231	201	221	178	153	147	120	163	139	162
NSTD [–]	0.40	1.27	2.22	2.18	1.80	1.61	1.35	1.10	0.82	1.25	0.93	0.96	1.32

The estimated and observed keel pressures shown in Figure 8.17 tend to have the same high-frequency content and variable low-frequency error. This tendency is also reflected in the error metrics: panel-wise and mean NRMSE, NMAE, and NSTD values in the time window $t \in [58.5, 62.0]$ seconds are comparatively lower than those in the longer time window. The improved accuracy is primarily associated with the wet mode shapes, which correctly estimate the radiation pressures at high frequencies. The low-frequency error is, as noted in Sections 8.1, 8.2, and 8.4, attributable to the basis of distortion modes which discard imaginary pressures at specific frequencies and phases.

Table 8.23: Normalized error metrics for the keel pressure estimates (irregular waves with impulse load) over $t \in [10.0, 180.0]$ s

Metric	p_{13}	p_{14}	p_{15}	p_{16}	p_{17}	p_{18}	p_{19}	p_{20}	p_{21}	p_{22}	p_{23}	p_{24}	Mean
NRMSE [%]	84.7	56.0	218	487	375	318	278	241	174	127	154	143	221
NMAE [%]	84.5	55.5	226	574	404	331	287	255	203	133	154	142	237
NSTD [–]	0.27	0.95	2.99	4.73	3.10	2.41	1.99	1.69	1.39	0.50	0.68	0.62	1.78

Table 8.24: Normalized error metrics for the keel pressure estimates (irregular waves with impulse load) over $t \in [58.5, 62.0]$ s

Metric	p_{13}	p_{14}	p_{15}	p_{16}	p_{17}	p_{18}	p_{19}	p_{20}	p_{21}	p_{22}	p_{23}	p_{24}	Mean
NRMSE [%]	65.5	33.5	62.6	72.7	70.4	68.9	60.7	48.2	38.7	54.2	79.6	97.3	62.7
NMAE [%]	66.4	29.5	77.6	89.1	73.4	64.8	57.2	49.4	43.6	64.2	76.1	96.4	65.6
NSTD [–]	0.80	1.02	1.32	1.24	1.21	1.21	1.17	1.11	1.04	0.81	0.85	0.94	1.06

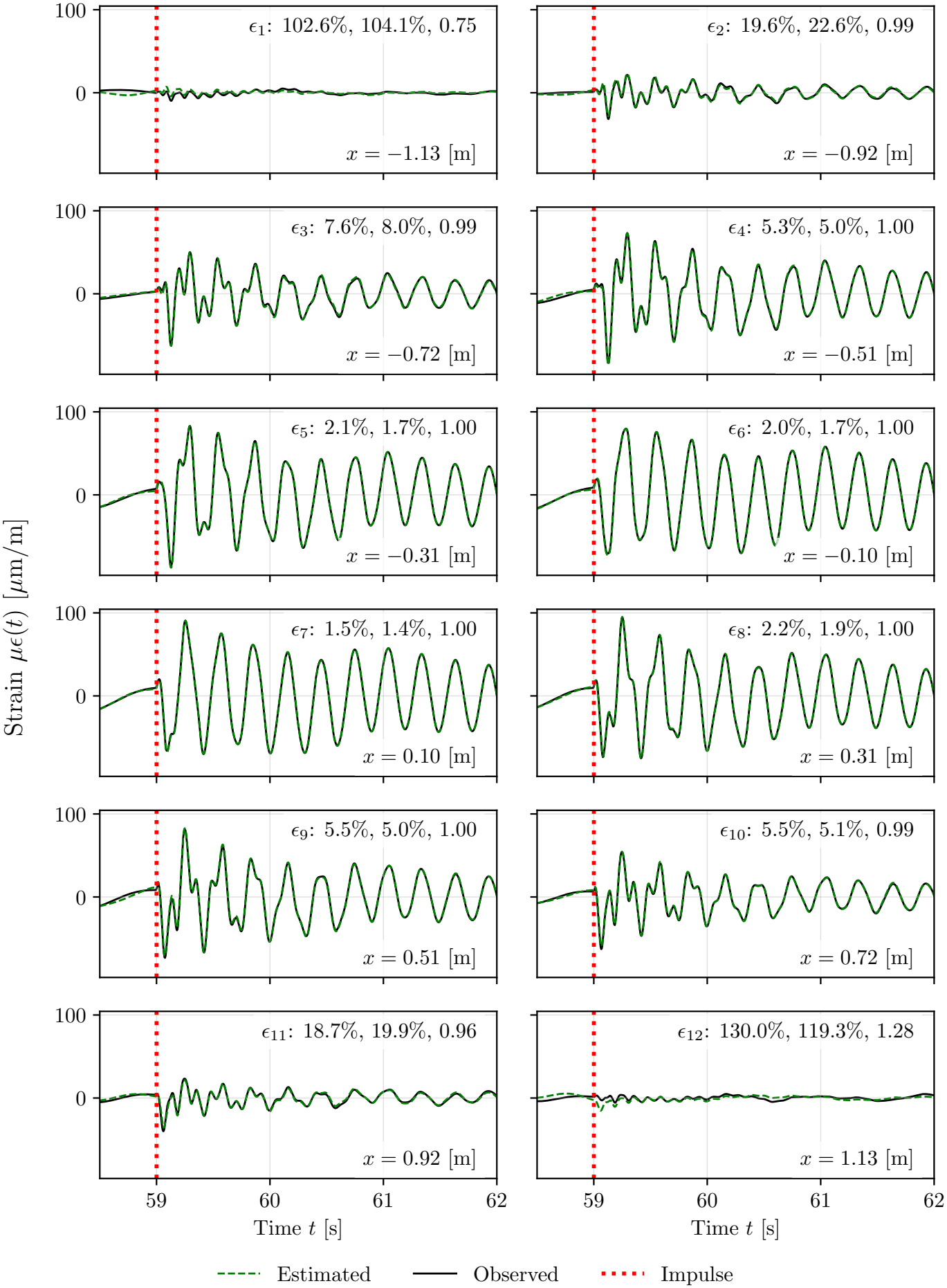


Figure 8.15: **Irregular waves with impulse load:** strain response of the segmented barge, plotted at twelve points equally spaced along the backbone. Locations correspond to those shown in Figure 8.1. Error metrics (ϵ_i: NRMSE, NMAE, NSTD) are shown for $t \in [58.5, 62.0]$ [s].

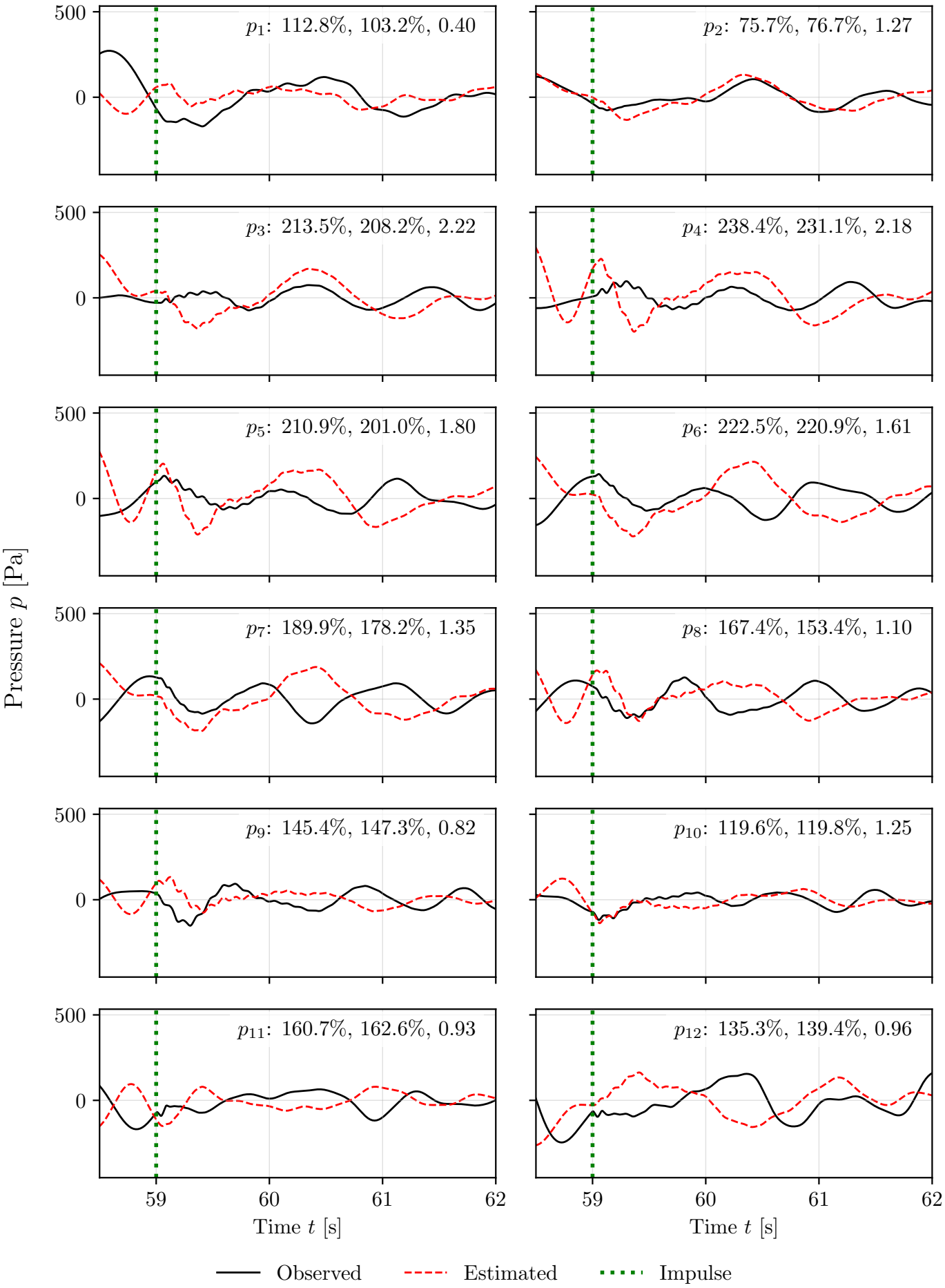


Figure 8.16: **Irregular waves with impulse load:** pressure loading of the segmented barge, plotted at twelve points equally spaced along the starboard side, mid-draft. Locations correspond to those shown in Figure 8.2. Error metrics (p_i: NRMSE, NMAE, NSTD) are shown for $t \in [58.5, 62.0]$ $[s]$.

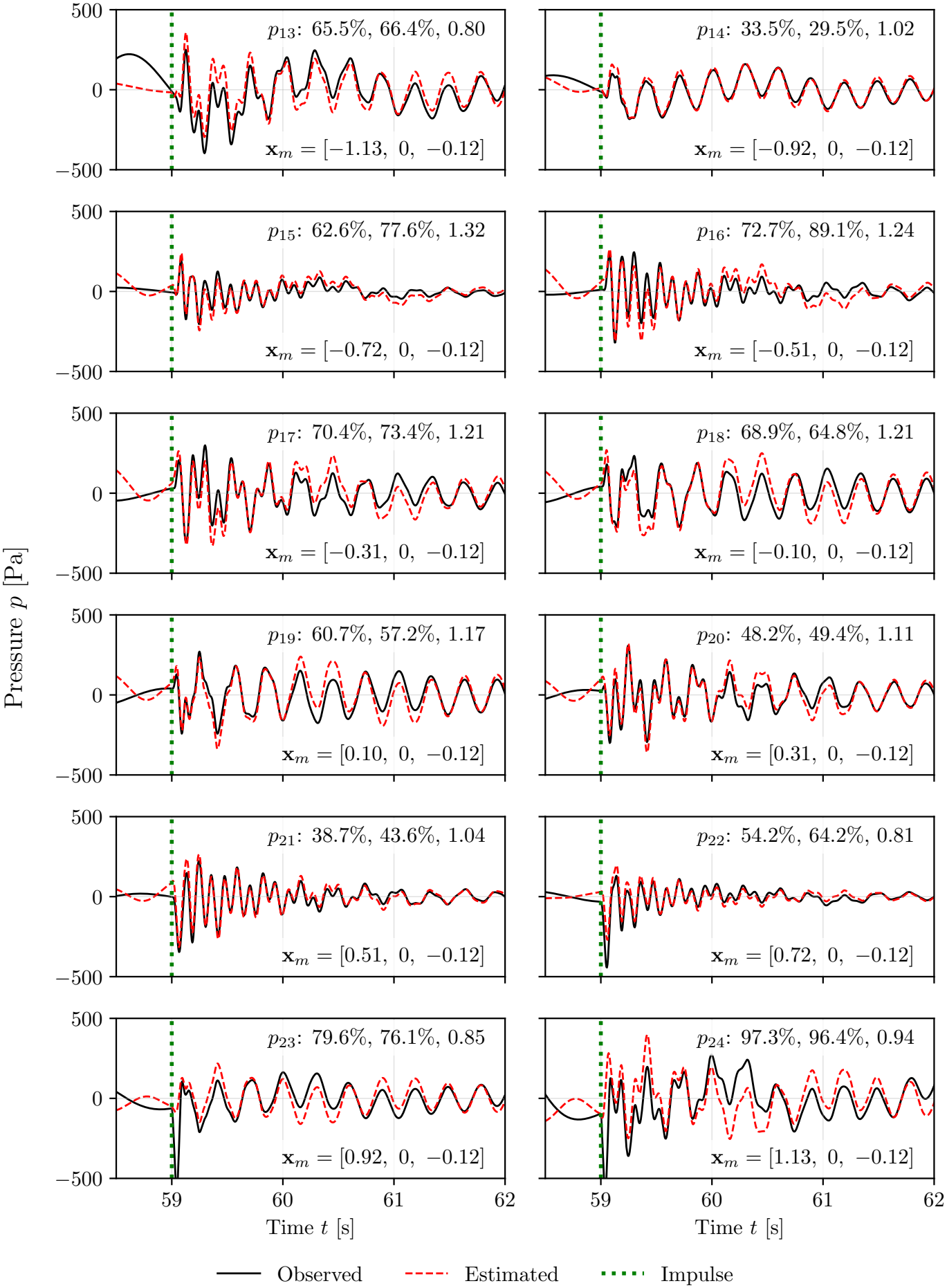


Figure 8.17: **Irregular waves with impulse load:** pressure loading of the segmented barge, plotted at twelve points equally spaced along the base, or keel. Locations correspond to those shown in Figure 8.2. Error metrics (p_i: NRMSE, NMAE, NSTD) are shown for $t \in [58.5, 62.0]$ $[s]$.

Chapter 9

Local Results: Stiffened Panel

Two loading and response conditions are considered for the local model in this chapter: a plate which is impacted by a wave, and a wedge which impacts still water. The strain response is evaluated at the middle and ends of the finite element model, with the estimates at the ends being most relevant for fatigue damage estimates. Both cases illustrate the accuracy of the proposed method: while some high-frequency vibrations from modes outside of the modal basis are noted, especially in the first period of the falling wedge response, the subsequent response estimate amplitudes and phases match the observed response very well.

9.1 Plate Impact with Wave

The strain gauge and estimate locations are shown in Figure 9.1. Strain gauges are placed using the method outlined in Section 6.2.2. Based on the positions, accuracy at the center of the beam is expected to be highest because the method of least squares minimizes the geometric distance between estimated and measured strain vectors at the locations of measured strains.

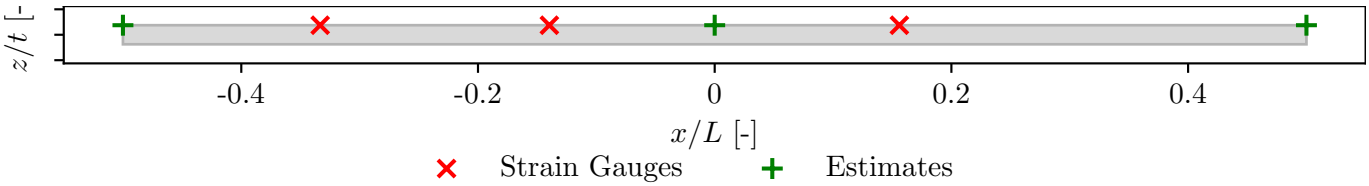


Figure 9.1: A schematic of the plate-strip, showing the positions of strain gauges and the locations where strains and stresses are estimated for the wave-plate impact.

During the first wet natural period (Figure 9.2), low NRMSE and NMAE values are noted at all three estimate locations. The maximum value is 6.5%, which is dominated primarily by high-order vibrations within the first millisecond. The NSTD indicates the amplitudes are uniformly equivalent, with a mean of 0.99.

As the simulation continues, the high-frequency response due to the initial impact decays, leaving a response which is dominated by structural stiffness and added mass. The first dry mode shape approximates this response well, as indicated by the error metrics in Figure 9.3: NRMSE values vary between 2.5% and 2.9%, while NMAE values lie between 1.7% and 1.9%. The mean NSTD is 0.99. Figures 9.2 and 9.3 show that the estimated and observed signals are, visually, nearly indistinguishable.

The results from both time windows provide strong evidence that only the first three modes are necessary for estimating the structural response due to slamming loads. The added mass which persists after the plate is fully wetted does not contribute significantly to response estimate errors. Comparatively, the error metrics from the local model are better than those from the global model in terms of mean strain NRMSE, NMAE, and NSTD during a transient event: 2.7%, 1.8%, and 0.99% (local) versus 16.6%, 7.5%, and 1 (global).

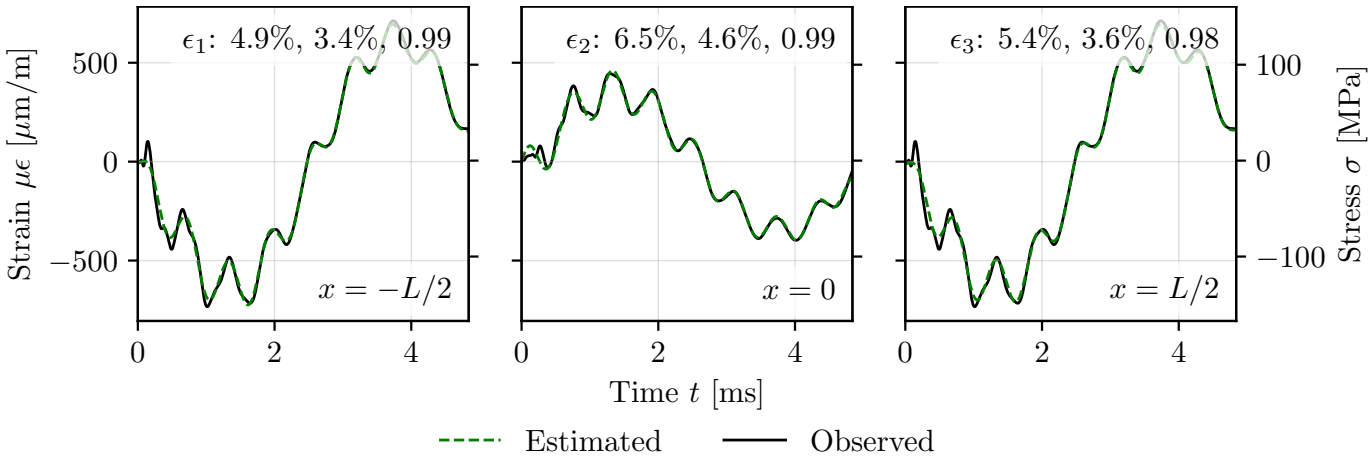


Figure 9.2: **Plate impact with wave:** Stress and strain responses at three locations on a plate strip subjected to hydroelastic wave impact loading. Only the first period of oscillation is shown to highlight the transient higher-order response. Error metrics are shown from left to right: ϵ_i : NRMSE, NMAE, NSTD.

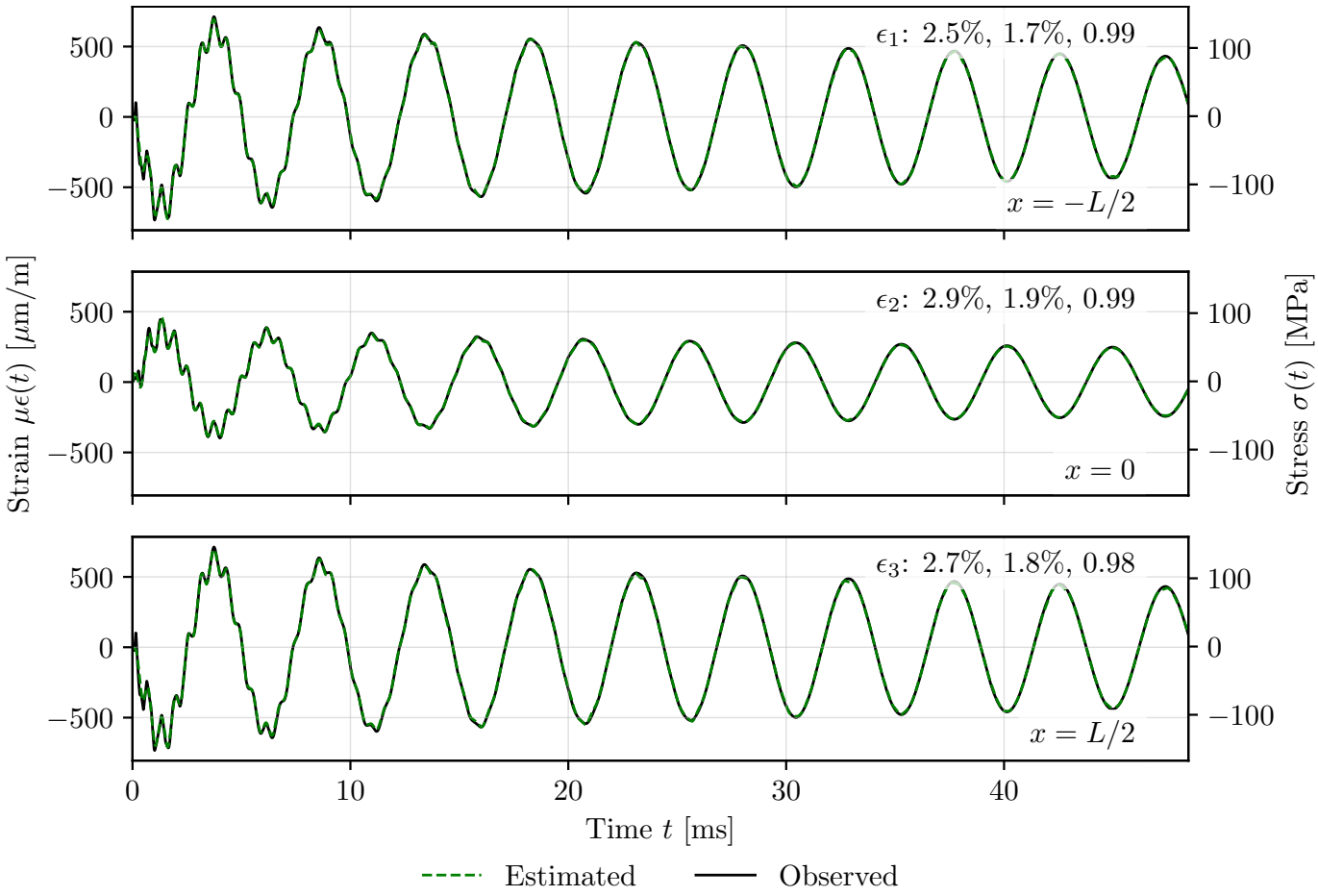


Figure 9.3: **Plate impact with wave:** Stress and strain responses at three locations on a plate strip subjected to hydroelastic wave impact loading. Error metrics are shown from left to right: ϵ_i : NRMSE, NMAE, NSTD.

9.2 Falling Wedge Impact

The strain gauge and estimate locations are shown in Figure 9.4. Strain gauges are placed using the method outlined in Section 6.2.2. Based on the positions, accuracy at the center of the beam is expected to be highest, for the same reason as mentioned in Section 9.1.

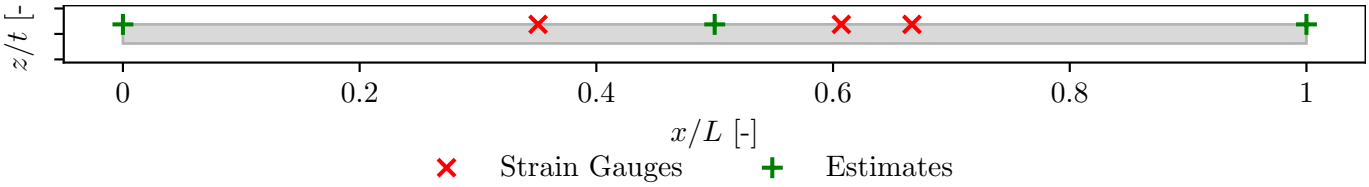


Figure 9.4: A schematic of the wedge, showing the positions of strain gauges and the locations where strains and stresses are estimated.

During the first wet natural period (Figure 9.5), relatively low NRMSE and NMAE values are noted, although the estimates at the left end of the beam are poorer than that at the right end: (NRMSE and NMAE of 8.1% and 7.9% versus NRMSE of 6.3% and NMAE of 5.1%). The variation in error is likely attributable to the asymmetry of the Wagner pressure loading and the asymmetry of the strain gauge locations themselves. Peak pressure is highest at the left end of the beam after $t = 0$; the singularity progresses from left to right until the plate is fully wetted. This moving peak pressure introduces higher-order mode shapes which are not included in the truncated modal basis. However, these mode shapes have low energy. The signals shown in Figure 9.5 are largely sinusoidal with one dominant frequency, which corresponds to the the first dry mode shape in the modal basis. The initial transient asymmetric effects are not included in the plate-wave impact, which is symmetric by definition (peak pressures are symmetric about $x = 0$). The mean NRMSE, NMAE, and NSTD values are 5.9%, 5.3%, and 0.97%, respectively, indicating slightly more error than calculated in the plate-wave impact simulation (5.6%, 3.9%, and 0.99, respectively).

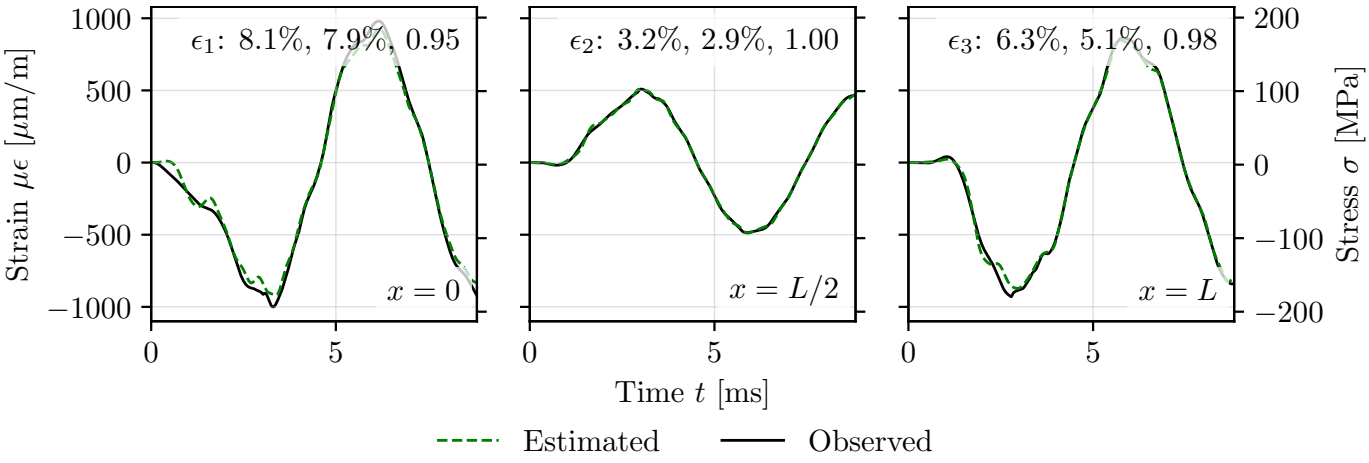


Figure 9.5: **Falling wedge impact:** Stress and strain responses at three locations on a plate strip subjected to hydroelastic wedge impact loading. Only the first period of oscillation is shown to highlight the transient higher-order response. Error metrics are shown from left to right: ϵ_i : NRMSE, NMAE, NSTD.

As the simulation continues, the high-frequency response due to the initial asymmetric impact decays, leaving a response which is also dominated by structural stiffness and added mass. An amplitude discrepancy is observed at the left end: NRMSE and NMAE values drop from 8.1% and 7.9% (first period) to 6.6% and 6.3% (decay), which are higher than those from the plate-wave impact simulation (Figure 9.2). These errors are also visually discernible in Figure 9.6 as a consistent amplitude underestimate. Like the error metrics calculated in the first period window, the estimate at the right end is more accurate than that at the left end. This asymmetry in the decay is an artifact from the simulation itself: once $c(t) = L$, the Wagner slamming force and damping terms drop to zero, and the added mass is frozen in time for the remainder of the simulation. The added mass term is asymmetric at time $t = t_0$ such that $c(t_0) = L$, meaning the asymmetric added mass is used for all subsequent time steps. This behavior is not physically realistic, as the point of peak pressure will continue to shift away from the center of the wedge, leaving a relatively smooth and flat (yet oscillating) pressure distribution near the center of the wedge. Despite this artifact, the error is still relatively low, with mean NRMSE, NMAE, and NSTD values of 5.9%, 5.3%, and 0.97. These relatively accurate estimates indicate that a dry, truncated modal basis captures both symmetric and asymmetric load-induced responses after the plate is fully wetted, even though the response is dominated by structural stiffness and added mass that is not represented in the dry modal basis.

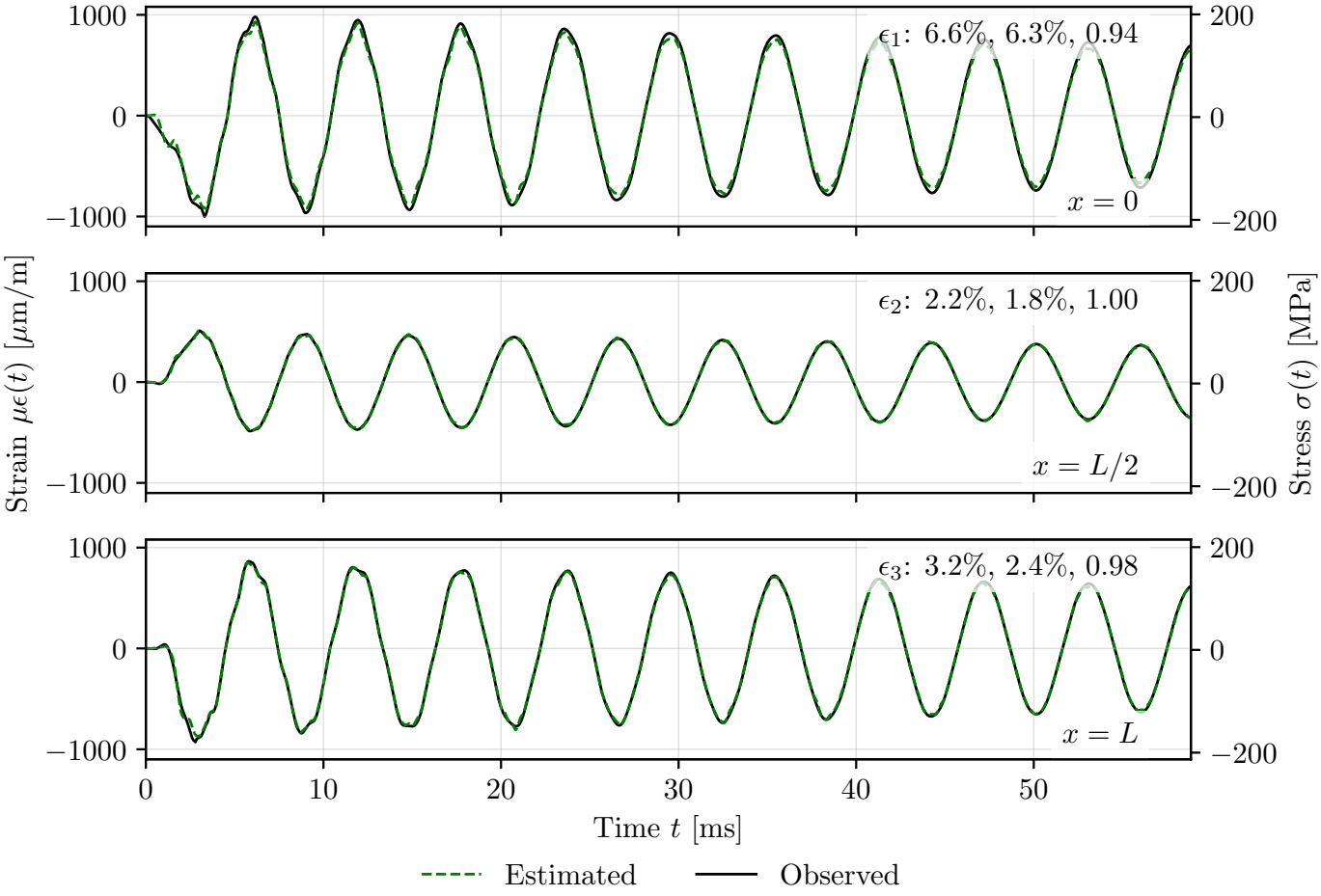


Figure 9.6: **Falling wedge impact:** Stress and strain responses at three locations on a plate strip subjected to hydroelastic wedge impact loading. Error metrics are shown from left to right: ϵ_i : NRMSE, NMAE, NSTD.

Part IV

Judgment and Future Work

Conclusions

HYPOTHESIS 1 The quasi-static and elastic wet mode shapes of a ship structure, obtained from linear radiation and hydrostatic restoring forces in a generalized modes framework, form a suitable modal basis for estimating global steady-state (springing) and transient (slamming, whipping) far-field stresses with the method of least squares.

To test the first hypothesis, a segmented barge is modeled numerically. Steady state (springing) and transient (slamming, whipping) loading and response is simulated in the time domain. Four strain gauges and a modal basis consisting of three distortion modes and three wet modes are used to estimate strains and pressures under five loading conditions. A digital filter separates the frequency content of each strain measurement signal such that the distortion and wet modal bases estimate low- and high-frequency strains and pressures, respectively. Each estimate is quantified using three normalized error metrics.

For an isolated transient response (Section 8.3), the first hypothesis holds: within a truncated time window ($t \in [58.5, 62.0]$ seconds), the twelve high-frequency strain responses are estimated with a mean normalized standard deviation (NSTD) of 1.00, a mean normalized root mean squared error (NRMSE) of 18.2%, and a mean normalized amplitude error (NMAE) of 12.4%. The associated high-frequency radiation pressures on the keel are recovered with similar accuracy: the mean NRMSE, NMAE, and NSTD are 25.1%, 19.0%, and 1.04 within the truncated time window. The accurate estimation of such pressures is important because they are difficult to measure directly on a ship in service, whereas the installation of strain gauges is relatively cheap and robust. The quasi-static part of the pressure loading on the side panels is not accurately captured, however: the high-pass filter that isolates the transient (whipping) response also removes the low-frequency components driven by rigid-body motion, so the radiation damping pressures are lost in the estimate. Within the short time window, the mean NRMSE, NMAE, and NSTD values are 106%, 107%, and 0.40; expanding the time window to the full simulation increases these values to 109%, 128%, and 0.43%. For these reasons, the first hypothesis is partially accepted: only the high-frequency transient (whipping) loading and response is estimated well in this framework.

Additional loading and response conditions are considered to evaluate the effects of combining waves and impulse loads on the low- and high-frequency estimates. By beginning with a single, regular wave (Section 8.1), the validity of using distortion modes for estimating low-frequency loading and response is tested. For example, the first distortion mode is defined by a wave frequency of 4.3 radians per second and a phase of 3.1 radians, yet NRMSE and NMAE values of over 200% are noted at the bow segment in the regular wave case ($T_p = 1.6$ s ≈ 3.93 rad/s) over the full simulation time window. A mean NSTD of 1.13 would normally indicate accurate loading and response estimates, but pressures on the keel and side panels are overestimated by an average of over 2.7 (NSTD). Mean NRMSE and NMAE values also indicate inaccuracy: mean values of 338% and 336% are calculated for the side and keel panels, respectively. The regular wave results show that discarding the imaginary part of each distortion mode also discards important loading and response information. Similar conclusions are drawn when the segmented barge is loaded by irregular waves (Section 8.2), a regular wave combined with an impulse load (Section 8.4), and irregular waves combined with an impulse load (Section 8.5). The most important conclusion from these results is that the mean NSTD for strain indicates accuracy, while the pressure loading suffers from significant error that would affect a fatigue assessment. The combined load cases (Sections 8.4 and 8.5) serve two purposes: to validate the use of low- and high-pass filters to separate loading and response estimates, and to evaluate the effects of using such filtered measurements with distortion and wet modes. Both combined load cases show that the digital filter itself does not introduce significant strain or pressure estimate error.

HYPOTHESIS 2 The dry mode shapes of an orthotropically stiffened panel, obtained from a undamped finite element model, form a suitable modal basis for estimating local quasi-static and hydroelastic transient (slamming) far-field stresses with the method of least squares.

To test the second hypothesis, a strip of an orthotropically stiffened panel is modeled numerically. The hydroelastic slamming response is simulated in the time domain. Three strain gauges and a modal basis consisting of three dry mode shapes are used to estimate strains in two configurations: a plate-strip subjected to a wave impact, and a wedge impacting still water. A digital filter suppresses noise. Each strain estimate is quantified using three normalized error metrics.

For a wave impact, the second hypothesis holds: the three strain responses are estimated with NRMSE, NMAE and NSTD values of 5.6%, 3.9%, and 0.99 for $t \in [0, 5]$ ms (the first wet natural period) and 2.7%, 1.8%, and 0.99 for $t \in [0, 50]$ ms. Higher-order responses within the wetting time are not included in the modal basis, which contributes the most to the error in the time window $t \in [0, 5]$ ms. The second hypothesis also holds for the falling wedge impact, although the asymmetric Wagner slamming pressure introduces higher error at the estimate location closest to the center of the wedge: mean NRMSE, NMAE, and NSTD values of 5.9%, 5.3%, and 0.97 for $t \in [0, 5]$ ms and 4.0%, 3.5%, and 0.97 for $t \in [0, 50]$ ms are noted.

These local results indicate that the dry mode shapes of an undamped finite element model accurately capture hydroelastic transient stresses induced by symmetric and asymmetric Wagner slamming pressures, provided that measurement noise is separated using a high-pass filter. Based on these observations, the second hypothesis is accepted. For the considered panel geometry and impact velocity, the first three mode shapes are required to accurately estimate strains at the ends of the panel. At least three sensors are required to estimate the modal amplitude of each dry mode shape and the associated structural response.

RESEARCH QUESTION How can steady-state and transient wave loading-induced fatigue damage accumulation be accurately estimated in a linear elastic ship structure using sparse strain measurements?

Transient For isolated transient (slamming) loading and response, wet mode shapes accurately estimate high frequency strain responses and pressure loads. However, the damping pressures associated with rigid-body motion are not captured when a discrete filter is used to separate the measured responses, leading to low-frequency pressure errors on the sides of the ship structure. The local hydroelastic slamming response is accurately estimated using a basis of dry modes. The number of strain gauges must be strictly equal to or greater than the number of modes, but high-frequency hydroelastic loading is dominated by less than three modes at both the local and global levels, meaning a minimum of three strain gauges is required. At least four are recommended for redundancy. The use of wet modes for estimating global transient loading and response and dry modes for estimating local slamming-induced responses represents an advancement beyond current methods that only take into account steady-state linear wave loading and response.

Steady-State The strain estimates induced by steady-state (regular and irregular wave) loading are reasonably accurate when using a basis of distortion modes, particularly at locations close to and between strain gauges. This accuracy is misleading: moderate strain errors and exceedingly high pressure errors are shown to persist. The method of constructing distortion modes introduces several assumptions that lead to these errors. For example, the imaginary part of each mode should be part of the time domain solution, but is discarded. In addition, the structural response (strain) of each mode is conflated with pressure loading such that incident and diffraction pressures at frequencies outside of the wave spectrum can be included in the estimate. The condition of orthogonality, an essential step when creating distortion modes, limits possible solutions to these sources of error. Including additional sensors and modes such that the entire spectrum is reasonably represented could yield an ill-conditioned matrix $\mathbf{B}_{\boldsymbol{\epsilon}}^{\mathbf{m}}\mathbf{H}$ because the quasi-static structural response at many low frequencies is similar. The imaginary structural response also resembles real mode shapes. For these reasons, the steady-state part of the research question cannot be conclusively addressed.

Discussion

A number of assumptions and linearization steps are made to arrive at tractable problems, which affect the applicability of the global and local models. Most notably, the assumptions of linearity and small motions inherent to the global and local models limit the extent to which conclusions can be drawn for ship structures undergoing large amplitude motions, a necessary precedent for most slamming events. These assumptions must be critically examined in future research, ideally by adapting a simple model such as the one presented in this thesis for large amplitude motions. The side panel estimates are most affected by this assumption, but bow emergence renders pressure estimates made using the assumption of linearity inaccurate.

Global results show that estimated strain and pressure errors exist even when the assumptions of linearity and small motions are applied, particularly when distortion modes are used for the low-frequency modal basis. These errors are expected because distortion modes conflate incident, diffraction, and radiation pressure loading with structural responses, and implicitly assert that waves are standing. Simply increasing the number of modes does not necessarily remedy this shortcoming because of the condition of orthogonality imposed when selecting additional modes. Wet mode shapes benefit from the standing wave assumption because high-frequency vibrations are dominated by added mass. Additional investigation into the pressures estimated using distortion modes is warranted.

As shown in the global results, reasonably accurate strain estimates do not necessarily imply correct loading estimates. Justifying the use of a particular modal basis by only comparing estimated and observed strains introduces confirmation bias, because estimated strains close to the measured locations will tend to be accurate regardless of the chosen modal basis. Furthermore, orthogonality of a modal basis does not guarantee orthogonality of the column space of the matrix used in the method of least squares. The number and position of strain gauges affects the condition number and orthogonality of the column space of this matrix. Future research should emphasize these metrics.

Another assumption is that the structure is stiff, which allows for the separation of low and high frequency strain measurements. However, the number of filter poles cannot be increased excessively due to the limitations of discrete filtering theory, and the first non-rigid body wet natural frequency must be high enough such that the attenuated low-frequency strain measurements do not contaminate the wet mode inputs. Flexible structures such as ultra-large container ships introduce hydroelastic effects at the frequency of the incoming waves, which complicates the use of wet modes when estimating the transient response. In particular, the radiation damping is assumed to be negligible during high-frequency transient (slamming and whipping) events, but this assumption does not hold within the frequency range of the incoming wave spectrum, as shown by the error metrics calculated for the pressures estimated using distortion modes.

A long list of additional assumptions, such as the absence of cargo, ballast, temperature effects, propeller and rotating machinery noise, green water loading, vehicles, and ice loads, all serve to limit the sources of error to only the variables specified in this thesis. Additional load cases are not part of the modal basis, and are thus sources of additional error. One particularly relevant effect is that of changing draft, which is relevant for (among others) the icebreaker hull form considered in the introduction. Draft affects the added mass and damping coefficients of the ship, as well as the position of the center of gravity relative to the waterline: the wet modes calculated for an unloaded ship will necessarily be different from those calculated for a loaded ship.

The segmented barge model itself has a significant weakness that requires a simplifying assumption: the gap panels used to suppress fluid oscillation between each segment have no physical analogy. It could be worthwhile to stiffen the backbone such that the segmented barge is rigid enough to assume rigid body

motion, and then rerun analyses using a more advanced time domain solver, such as the volume of fluid method. Doing so would at least allow for the quantification of errors introduced by the open gaps in between each segment. Another way to address this weakness is by actually constructing gap panels on the physical model, a common practice when constructing scale ship models. In general, the use of physical models for the verification of future numerical models is highly recommended. The results in this thesis are primarily comparative, which means modeling errors are in some ways canceled, but errors between the numerical and physical models still exist. These errors are difficult to quantify without a physical model. Another consideration is scaling; Grammatikopoulos [57] provides a thorough summary of the possible scaling methods and their limitations for fluid-structure interaction problems.

Some avenues towards improved loading and response estimates are identified based on the results of this thesis. Local results show that high structural response estimate accuracy is achieved with a limited number of sensors when the local panel is subjected to a complex hydroelastic load case, while the global results show that incident and diffraction wave pressures estimated using distortion modes are often over- or underestimated. These two observations lead to a possible area of future research: the use of locally installed strain gauges at specific points on the hull to estimate the total external water pressure at that panel and thus complement the global response estimates. A constant, uniform pressure-based mode combined with at least two strain gauges is recommended for each considered local panel such that both pressure-strain and girder bending-strain relationships are captured.

Locally installed strain gauges could also address the loading effects of rigid body motions, which must be acknowledged when estimating ship structural response and loading: zero and first order hydrostatic and radiation pressures can dominate the rigid body pressure loading, as shown in the side pressures induced by the isolated transient impulse load. Additional sensor types such as accelerometers and inclinometers could assist in the accurate assessment of these motions and the corresponding loading and response, but the physical values of acceleration are not directly applicable for the method of least squares used in this thesis. In particular, accelerations must be integrated twice to arrive at displacement, forcing the use of the frequency domain as an intermediate estimation step. Additional information about error quantification in this framework can be found in Van Zijl et al. [83].

A fatigue assessment is not performed in this thesis, but the resulting accuracy of the estimated damage is the most important metric for repairing fatigue cracks in a ship structure. Simple models are strongly encouraged for future research, such as estimating fatigue damage in an orthotropically stiffened panel subjected to high-frequency oscillations when the external surface of the panel is submerged. The error metrics presented in this thesis also have important ramifications for a fatigue assessment: the estimated variable amplitude (VA) loading could strongly affect the estimated remaining life (the number of cycles N in the SN curve). This effect could be especially pronounced if the VA loading yields an effective constant amplitude (CA) stress S which lies close to or within a shallow SN slope (i.e. for a bilinear relationship).

Wet modes can be implemented using commercial finite element software and a suitable boundary element solver using the methods outlined in this thesis, with two caveats: finite element displacements must be projected onto the hydrodynamic mesh, and pressures must be integrated using Gauss points after solving the potentials at those locations on the finite element mesh. An implementation of these steps can be found in Malenica et al. [155] and Malenica et al. [39].

Finally, a number of modeling step are introduced in this thesis to address practical implementation gaps found in literature, but their novelty is not expressly guaranteed. Some examples include the enforcement of numerical linearity using a small perturbation of each mode shape, which avoids lengthy equations for calculating hydrostatic restoring coefficients and the gradients of each mode shape; the implementation of the method of generalized modes in a finite element framework, as opposed to strictly using the boundary element method for calculating modal values; the interpolation and extrapolation of damping and added mass coefficients by means of an exponential decay law and the Kramers-Kronig relations; the use of isoparametric finite elements for calculating the hydroelastic response of a plate subjected to Wagner slamming pressures; the derivation and calculation of structural response of a free-floating structure using the pseudoinverse of the structural stiffness matrix; and the exclusive use of open-source (Python) software for all modeling and visualization steps in this thesis. Essential libraries used include NumPy [156], SciPy [153], Matplotlib [157], and Capytaine [142]; LaTeX [158] is used for the compiling of this document.

Bibliography

[1] J. T. Tuitman, "Hydro-elastic response of ship structures to slamming induced whipping," Ph.D. dissertation, Delft University of Technology, S.l., 2010.

[2] K. Pferdekamper and A. Bekker, *Full-Scale Fatigue Damage Investigation of a Slamming-Prone Vessel with Unique Section Modulus Characteristics*, 1st ed. London: CRC Press, Nov. 2021, pp. 334–341.

[3] K.-H. Pferdekämper and A. Bekker, "Investigation of vessel slamming and fatigue using a full-scale test sequence," *Appl. Ocean Res.*, vol. 144, Mar. 2024.

[4] R. Hascoët and N. Jacques, "On the risk of fatigue failure of structural elements exposed to bottom wave slamming – Impulse response regime," *Appl. Ocean Res.*, vol. 154, Jan. 2025.

[5] I. Drummen, M. Schiere, R. Dallinga, and K. Stambaugh, "Full and model scale testing of a new class of US coast guard cutter," in *Ship Struct. Symp. Linthicum Heights MD*, 2014.

[6] R. E. D. Bishop and W. G. Price, *Hydroelasticity of Ships*. Cambridge University Press, 1979.

[7] J. N. Newman, "Wave effects on deformable bodies," *Appl. Ocean Res.*, vol. 16, no. 1, pp. 47–59, Jan. 1994.

[8] O. M. Faltinsen, "Hydroelastic slamming," *J. Mar. Sci. Technol.*, vol. 5, no. 2, pp. 49–65, Dec. 2000.

[9] J. J. Stoker, *Water Waves: The Mathematical Theory with Applications*, ser. Pure and Applied Mathematics. New York, NY etc.: Interscience, 1957, no. vol. 4.

[10] M. Witvoet, "Mean Stress Effects in Temporal and Spectral Fatigue Analysis," MSc Thesis, Delft University of Technology, Delft, The Netherlands, 2022.

[11] T. von Karman, "The Impact on Seaplane Floats During Landing," National Advisory Committee for Aeronautics, Washington, Tech. Rep. NACA-TN 321, 1929.

[12] H. Wagner, "über Stoß- und Gleitvorgänge an der Oberfläche von Flüssigkeiten," *ZAMM - J. Appl. Math. Mech. Z. Angew. Math. Mech.*, vol. 12, no. 4, pp. 193–215, 1932.

[13] J. N. Newman, *Marine Hydrodynamics*. Cambridge, MA: The MIT Press, 1977.

[14] R. Cointe and J.-L. Armand, "Hydrodynamic Impact Analysis of a Cylinder," *J. Offshore Mech. Arct. Eng.*, vol. 109, no. 3, pp. 237–243, Aug. 1987.

[15] A. A. Korobkin and V. V. Pukhnachov, "Initial Stage of Water Impact," in *Annu. Rev. Fluid Mech.*, 1988.

[16] R. Zhao and O. Faltinsen, "Water entry of two-dimensional bodies," *J. Fluid Mech.*, vol. 246, pp. 593–612, Jan. 1993.

[17] R. Zhao, "Water entry of arbitrary two-dimensional sections with and without flow separation," in *Proc. 21st Symp. Nav. Hysdrodynamics Trondheim*. National Academy Press, 1996, pp. 408–423.

[18] O. M. Faltinsen, "The effect of hydroelasticity on ship slamming," *Philos. Trans. R. Soc. Lond. Ser. Math. Phys. Eng. Sci.*, vol. 355, no. 1724, pp. 575–591, Mar. 1997.

[19] O. M. Faltinsen, J. Kvålsvold, and J. V. Aarsnes, "Wave impact on a horizontal elastic plate," *J. Mar. Sci. Technol.*, vol. 2, no. 2, pp. 87–100, Jun. 1997.

[20] O. M. Faltinsen, "Water Entry of a Wedge by Hydroelastic Orthotropic Plate Theory," *J. Ship Res.*, vol. 43, no. 03, pp. 180–193, Sep. 1999.

[21] A. Bereznitski, "Local hydroelastic response of ship structures under impact loads from water (slamming)," Ph.D. dissertation, Delft University of Technology, 2003.

[22] W. E. Cummins, "The Impulse Response Function and Ship Motions," Department of the Navy - David Taylor Model Basin, Arlington Hall Station, Tech. Rep. 1661, 1962.

[23] F. Ogilvie T., "Second Order Hydrodynamic Effects on Ocean Platforms," in *Int Workshop Ship Platf. Motions 1983*. University of California, 1983.

[24] J. N. Newman, "Algorithms for the free-surface Green function," *J. Eng. Math.*, vol. 19, no. 1, pp. 57–67, 1985.

[25] H. Wu, C. Zhang, Y. Zhu, W. Li, D. Wan, and F. Noblesse, "A global approximation to the Green function for diffraction radiation of water waves," *Eur. J. Mech. - BFluids*, vol. 65, pp. 54–64, Sep. 2017.

[26] J. Newman, "An expansion of the oscillatory source potential," *Appl. Ocean Res.*, vol. 6, no. 2, pp. 116–117, Apr. 1984.

[27] K. Sim and K. Lee, "A Comparative Study on the Structural Response of Multi-Linked Floating Offshore Structure between Digital Model and Physical Model Test for Digital Twin Implementation," *J. Mar. Sci. Eng.*, vol. 12, no. 2, p. 262, Feb. 2024.

[28] J. Newman, "Double-precision evaluation of the oscillatory source potential," *J. Ship Res.*, vol. 28, no. 03, pp. 151–154, 1984.

[29] J. G. Telste and F. Noblesse, "Numerical Evaluation of the Green Function of Water-Wave Radiation and Diffraction," *J. Ship Res.*, vol. 30, no. 02, pp. 69–84, Jun. 1986.

[30] G. Delhommeau, "Amélioration des performances des codes de calcul de diffraction-radiation au premier ordre," in *Proc. 2èmes Journ. L'Hydrodynamique Nantes Fr.*, 1989, pp. 13–15.

[31] C. Xie, Y. Choi, F. Rongère, A. H. Clément, G. Delhommeau, and A. Babarit, "Comparison of existing methods for the calculation of the infinite water depth free-surface Green function for the wave–structure interaction problem," *Appl. Ocean Res.*, vol. 81, pp. 150–163, Dec. 2018.

[32] J. V. Wehausen and E. V. Laitone, "Surface Waves," in *Fluid Dynamics / Strömungsmechanik*, S. Flügge and C. Truesdell, Eds. Berlin, Heidelberg: Springer Berlin Heidelberg, 1960, vol. 3 / 9, pp. 446–778.

[33] J. M. J. Journée and W. W. Massie, *Offshore Hydromechanics*. Delft University of Technology, 2015.

[34] S. Malenica and X. B. Chen, "On the irregular frequencies appearing in wave diffraction-radiation solutions," *Int. J. Offshore Polar Eng.*, vol. 8, no. 02, 1998.

[35] R. D. Cook, D. S. Malkus, and M. E. Plesha, *Concepts and Applications of Finite Element Analysis*, 3rd ed. New York: Wiley, 1989.

[36] K.-J. Bathe, *Finite Element Procedures*. Klaus-Jürgen Bathe, 2006.

[37] B. Fabien, *Analytical System Dynamics: Modeling and Simulation*. Springer Science & Business Media, 2008.

[38] S. Malenica, B. Molin, and F. Remy, "Hydroelastic response of a barge to impulsive and non-impulsive wave loads," in *Proc. Third Int. Conf. Hydroelasticity Mar. Technol.* Oxford, United Kingdom: University of Oxford, 2003.

[39] S. Malenica, J. Tuitman, F. Bigot, and F. Sireta, "Some Aspects of 3D Linear Hydroelastic Models of Springing," *Int. J. Nav. Archit. Ocean Eng.*, 2008.

[40] T. H. Farstad, "Transient Seakeeping Analysis Using Generalized Modes," Master's thesis, Massachusetts Institute of Technology, 1995.

[41] R. E. D. Bishop, W. G. Price, and Y. Wu, "A General Linear Hydroelasticity Theory of Floating Structures Moving in a Seaway," *Philos. Trans. R. Soc. Lond. Ser. Math. Phys. Sci.*, vol. 316, no. 1538, pp. 375–426, 1986.

[42] J. N. Newman, "Deformable floating bodies," in *8th Int. Workshop Water Waves Float. Bodies.* St. John's, Newfoundland, 1993, pp. 109–112.

[43] P. Léger and E. Wilson, "Generation of load dependent Ritz transformation vectors in structural dynamics," *Eng. Comput.*, vol. 4, no. 4, pp. 309–318, Apr. 1987.

[44] P. Léger, "Load dependent subspace reduction methods for structural dynamic computations," *Comput. Struct.*, vol. 29, no. 6, pp. 993–999, Jan. 1988.

[45] P. Leger, "Microcomputer Solution of Large Structural Dynamic Problems," *Comput.-Aided Civ. Infrastruct. Eng.*, vol. 4, no. 2, pp. 127–132, Jun. 1989.

[46] J. M. Ricles and P. Léger, "Use of load-dependent vectors for dynamic analysis of large space structures," *Commun. Numer. Methods Eng.*, vol. 9, no. 11, pp. 897–908, Nov. 1993.

[47] Y.-C. Yiu, "Reduced Vector Basis for Dynamic Analysis of Large Damped Structures," Ph.D. dissertation, University of California, Berkeley, May 1990.

[48] M. Tarpø, T. Friis, C. Georgakis, and R. Brincker, "Full-field strain estimation of subsystems within time-varying and nonlinear systems using modal expansion," *Mech. Syst. Signal Process.*, vol. 153, May 2021.

[49] J. T. Tuitman and S. Malenica, "Fully coupled seakeeping, slamming, and whipping calculations," in *Proc. Inst. Mech. Eng. Part M J. Eng. Marit. Environ.*, vol. 223. SAGE Publications, Sep. 2009, pp. 439–456.

[50] F. van Walree, A. Serani, M. Diez, and F. Stern, "Prediction of Heavy Weather Seakeeping of a Destroyer Hull Form by Means of Time Domain Panel and CFD Codes," in *Proc. 33nd Symp. Nav. Hydrodyn. Osaka Jpn.*, 2020.

[51] S. Malenica, Q. Derbanne, F. Sireta, E. Tiphine, F. Bigot, G. De-Hauteçlocque, and X. B. Chen, "HOMER Integrated Hydro-Structure Interactions Tool for Naval and Off-Shore Applications," in *Proc. Int. Conf. Comput. Appl. Shipbuild.* Busan, Korea: Royal Institute of Naval Architects, 2013, pp. 209–221.

[52] F. Van Walree, D. Sgarioto, and P. Graham, "Validation of a Time Domain Panel Code for Prediction of Impulsive Wave Loads on Naval Ships," in *Vol. 2 Struct. Saf. Reliab.* Melbourne, Australia: American Society of Mechanical Engineers, Jun. 2023.

[53] T. F. Ogilvie, "Recent progress toward the understanding and prediction of ship motions," in *Fifth Symp. Nav. Hydrodyn.* Bergen, Norway, 1964, pp. 3–79.

[54] F.-X. Sireta, Q. Derbanne, F. Bigot, Š. Malenica, and E. Baudin, "Hydroelastic Response of a Ship Structural Detail to Seakeeping Loads Using a Top-Down Scheme," in *Vol. 2 Struct. Saf. Reliab.* Rio de Janeiro, Brazil: American Society of Mechanical Engineers, Jul. 2012, pp. 289–297.

[55] W. M. Lin and D. Yue, "Numerical Solutions for Large-Amplitude Ship Motions in the Time Domain," in *Eighteenth Symp. Oñ Nav. Hydrodyn. Ship Motions Ship Hydrodyn. Exp.* Ann Arbor, MI, USA: National Academy Press, 1991, p. 41.

[56] D. Lisi, "A Beam Finite Element Model Including Warping," Ph.D. dissertation, Politecnico Milano, 2012.

[57] A. Grammatikopoulos, "A review of physical flexible ship models used for hydroelastic experiments," *Mar. Struct.*, vol. 90, Jul. 2023.

[58] J. Schijve, *Fatigue of Structures and Materials*, 2nd ed. Dordrecht: Springer, 2010.

[59] H. den Besten, "Fatigue damage criteria classification, modelling developments and trends for welded joints in marine structures," *Ships Offshore Struct.*, vol. 13, no. 8, pp. 787–808, Nov. 2018.

[60] J. H. den Besten, "Fatigue Resistance of Welded Joints in Aluminium High-Speed Craft: A Total Stress Concept," Ph.D. dissertation, Technische Universiteit Delft, Delft, The Netherlands, 2015.

[61] NEN, "Eurocode 3: Ontwerp en berekening van staalconstructies - Deel 1-9: Vermoeing," NEN, Technical Report, Sep. 2012.

[62] A. F. Hobbacher, "The new IIW recommendations for fatigue assessment of welded joints and components – A comprehensive code recently updated," *Int. J. Fatigue*, vol. 31, no. 1, pp. 50–58, Jan. 2009.

[63] P. Dong, J. K. Hong, and Z. Cao, "Stresses and stress intensities at notches:'anomalous crack growth'revisited," *Int. J. Fatigue*, vol. 25, no. 9-11, pp. 811–825, 2003.

[64] E. Niemi, W. Fricke, and S. J. Maddox, *Structural Hot-Spot Stress Approach to Fatigue Analysis of Welded Components: Designer's Guide*, 2nd ed., ser. IIW Collection. Singapore: Springer Singapore, 2018.

[65] J. Den Besten and M. Kaminski, "Fatigue in aluminium high-speed craft: A large scale specimen design life parameter estimate," in *FAST - Int. Conf. Fast Sea Transp.* FAST 2013 Secretariat, 2013.

[66] C. M. Sonsino, W. Fricke, F. de Bruyne, A. Hoppe, A. Ahmadi, and G. Zhang, "Notch stress concepts for the fatigue assessment of welded joints – Background and applications," *Int. J. Fatigue*, vol. 34, no. 1, pp. 2–16, Jan. 2012.

[67] H. Neuber, *Theory of Notch Stresses: Principles for Exact Stress Calculation (Kerbspannungslehre: Grundlagen Für Genaue Spannungsrechnung) Berlin, Julius Springer, 1937.* Navy Department David Taylor model basin, 1937.

[68] Y. Qin, H. den Besten, S. Palkar, and M. L. Kaminski, "Fatigue design of welded double-sided T-joints and double-sided cruciform joints in steel marine structures: A total stress concept," *Fatigue Fract. Eng. Mater. Struct.*, vol. 42, no. 12, pp. 2674–2693, 2019.

[69] Det Norske Veritas Classification AS, "Classification note 30.7: Fatigue assessment of ship structures," Det Norske Veritas, 1322 Høvik, Norway, Technical Report, 2014.

[70] A. Wöhler, *Über die Festigkeitsversuche mit Eisen und Stahl.* Ernst & Korn, 1870.

[71] P. Dong, X. Pei, S. Xing, and M. H. Kim, "A structural strain method for low-cycle fatigue evaluation of welded components," *Int. J. Press. Vessels Pip.*, vol. 119, pp. 39–51, Jul. 2014.

[72] Y. Qin, H. den Besten, S. Palkar, and M. L. Kaminski, "Mid- and High-Cycle Fatigue of Welded Joints in Steel Marine Structures: Effective Notch Stress and Total Stress Concept Evaluations," *Int. J. Fatigue*, vol. 142, Jan. 2021.

[73] A. F. Hobbacher and J. Baumgartner, *Recommendations for Fatigue Design of Welded Joints and Components*, ser. IIW Collection. Cham: Springer Nature Switzerland, 2024.

[74] M. L. Deul, "Fatigue damage accumulation in steel welded joints, subject to (random) variable amplitude loading conditions," Master's thesis, Delft University of Technology, 2021.

[75] M. A. Miner, "Cumulative Damage in Fatigue," *J. Appl. Mech.*, vol. 12, no. 3, pp. A159–A164, 1945.

[76] I. Rychlik, "A new definition of the rainflow cycle counting method," *Int. J. Fatigue*, vol. 9, no. 2, pp. 119–121, Apr. 1987.

[77] T. Lassen and N. Récho, *Fatigue Life Analyses of Welded Structures*, 1st ed. Wiley, Jan. 2006.

[78] K. Walker, "The Effect of Stress Ratio During Crack Propagation and Fatigue for 2024-T3 and 7075-T6 Aluminum," in *Effects of Environment and Complex Load History on Fatigue Life*, MS. Rosenfeld, Ed. ASTM International, Jan. 1970, vol. STP462-EB.

[79] I. Drummen, L. Rogers, A. Benhamou, R. Hageman, and K. Stambaugh, "Hull structure monitoring of a new class of US coast guard cutters," in *Proc. ASNE Technol. Syst. Ships Wash. DC USA*, 2019, pp. 18–20.

[80] S. Kong, H. Cui, Y. Tian, and S. Ji, "Identification of ice loads on shell structure of ice-going vessel with Green kernel and regularization method," *Mar. Struct.*, vol. 74, Nov. 2020.

[81] P. C. Hansen, "The L-curve and its use in the numerical treatment of inverse problems," *Comput. Inverse Probl. Electrocardiol.*, pp. 119–142, 1999.

[82] ——, "Analysis of Discrete Ill-Posed Problems by Means of the L-Curve," *SIAM Rev.*, vol. 34, no. 4, pp. 561–580, Dec. 1992.

[83] C. Van Zijl, J. Jovanova, and A. Grammatikopoulos, "On the limitations of inverse force estimation with strain-based sensing and reduced modal models in hydroelastic systems," *J. Sound Vib.*, 2026.

[84] F. Bigot, Q. Derbanne, and E. Baudin, "A Review of Strains to Internal Loads Conversion Methods in Full Scale Measurements," in *Proc. 12th Int. Symp. Pract. Des. Ships Float. Struct.*, 2013.

[85] F. Bigot, F.-X. Sireta, E. Baudin, Q. Derbanne, E. Tiphine, and Š. Malenica, "A Novel Solution to Compute Stress Time Series in Nonlinear Hydro-Structure Simulations," in *Vol. 3 Struct. Saf. Reliab.* St. John's, Newfoundland, Canada: American Society of Mechanical Engineers, May 2015.

[86] A. Andoniu, J. De Lauzon, and K. Pidery, "Hybrid Structural Health Monitoring of an FPSO: Measuring Stress at Un-Instrumented Structural Details," in *Offshore Technol. Conf.* Houston, Texas, USA: OTC, Apr. 2024.

[87] D. Augustyn, R. R. Pedersen, U. T. Tygesen, M. D. Ulriksen, and J. D. Sørensen, "Feasibility of modal expansion for virtual sensing in offshore wind jacket substructures," *Mar. Struct.*, vol. 79, Sep. 2021.

[88] M. Henkel, W. Weijtjens, and C. Devriendt, "Fatigue Stress Estimation for Submerged and Sub-Soil Welds of Offshore Wind Turbines on Monopiles Using Modal Expansion," *Energies*, vol. 14, no. 22, p. 7576, Jan. 2021.

[89] A. Skafte, J. Kristoffersen, J. Vestermark, U. T. Tygesen, and R. Brincker, "Experimental study of strain prediction on wave induced structures using modal decomposition and quasi static Ritz vectors," *Eng. Struct.*, vol. 136, pp. 261–276, Apr. 2017.

[90] A. Tessler, "A Variational Principle for Reconstruction of Elastic Deformations in Shear Deformable Plates and Shells," *Plates Shells*, 2003.

[91] A. Kefal and E. Oterkus, "Shape Sensing of Aerospace Structures by Coupling Isogeometric Analysis and Inverse Finite Element Method," in *58th AIAA Struct. Struct. Dyn. Mater. Conf.* Grapevine, Texas: American Institute of Aeronautics and Astronautics, Jan. 2017.

[92] A. Tessler, "Structural Analysis Methods for Structural Health Management of Future Aerospace Vehicles," *Key Eng. Mater.*, vol. 347, pp. 57–66, Sep. 2007.

[93] M. Gherlone, P. Cerracchio, M. Mattone, M. D. Sciuva, and A. Tessler, "Dynamic Shape Reconstruction of Three-Dimensional Frame Structures Using the Inverse Finite Element Method," in *Proc. 3rd Int. Conf. Comput. Methods Struct. Dyn. Earthq. Eng.*, 2011.

[94] M. Gherlone, P. Cerracchio, M. Mattone, M. Di Sciuva, and A. Tessler, "Shape sensing of 3D frame structures using an inverse Finite Element Method," *Int. J. Solids Struct.*, vol. 49, no. 22, pp. 3100–3112, Nov. 2012.

[95] ——, "An inverse finite element method for beam shape sensing: Theoretical framework and experimental validation," *Smart Mater. Struct.*, vol. 23, no. 4, Apr. 2014.

[96] A. Kefal and E. Oterkus, "Structural Health Monitoring of marine structures by using inverse Finite Element Method," in *Analysis and Design of Marine Structures V*, 0th ed. CRC Press, Mar. 2015, pp. 355–364.

[97] ——, "Displacement and stress monitoring of a Panamax containership using inverse finite element method," *Ocean Eng.*, vol. 119, pp. 16–29, Jun. 2016.

[98] ——, "Displacement and stress monitoring of a chemical tanker based on inverse finite element method," *Ocean Eng.*, vol. 112, pp. 33–46, Jan. 2016.

[99] A. Kefal, J. B. Mayang, E. Oterkus, and M. Yildiz, "Three dimensional shape and stress monitoring of bulk carriers based on iFEM methodology," *Ocean Eng.*, vol. 147, pp. 256–267, Jan. 2018.

[100] M. Li, A. Kefal, E. Oterkus, and S. Oterkus, "Structural health monitoring of an offshore wind turbine tower using iFEM methodology," *Ocean Eng.*, vol. 204, May 2020.

[101] R. Roy, A. Tessler, C. Surace, and M. Gherlone, "Efficient shape sensing of plate structures using the inverse Finite Element Method aided by strain pre-extrapolation," *Thin-Walled Struct.*, vol. 180, Nov. 2022.

[102] R. E. Kalman, "A New Approach to Linear Filtering and Prediction Problems," *J. Basic Eng.*, vol. 82, no. 1, pp. 35–45, Mar. 1960.

[103] K. Maes, W. Weijtjens, E. J. de Ridder, and G. Lombaert, "Inverse estimation of breaking wave loads on monopile wind turbines," *Ocean Eng.*, vol. 163, pp. 544–554, Sep. 2018.

[104] E. Lourens, E. Reynders, G. De Roeck, G. Degrande, and G. Lombaert, "An augmented Kalman filter for force identification in structural dynamics," *Mech. Syst. Signal Process.*, vol. 27, pp. 446–460, Feb. 2012.

[105] K. Maes, A. Iliopoulos, W. Weijtjens, C. Devriendt, and G. Lombaert, "Dynamic strain estimation for fatigue assessment of an offshore monopile wind turbine using filtering and modal expansion algorithms," *Mech. Syst. Signal Process.*, vol. 76–77, pp. 592–611, Aug. 2016.

[106] E. Lourens, C. Papadimitriou, S. Gillijns, E. Reynders, G. De Roeck, and G. Lombaert, "Joint input-response estimation for structural systems based on reduced-order models and vibration data from a limited number of sensors," *Mech. Syst. Signal Process.*, vol. 29, pp. 310–327, May 2012.

[107] L. Caglio, A. Sadeqi, H. Stang, and E. Katsanos, "Joint input-state estimation of structures subjected to complex loads via augmented Kalman Filter with physics informed latent force models," *Mech. Syst. Signal Process.*, vol. 223, Jan. 2025.

[108] E. Lourens and D. Fallais, "Full-field response monitoring in structural systems driven by a set of identified equivalent forces," *Mech. Syst. Signal Process.*, vol. 114, pp. 106–119, Jan. 2019.

[109] M. Vigsø, "Indirect Wave Load Estimates Using Operational Modal Analysis," Ph.D. dissertation, Aarhus University, 2020.

[110] N. M. M. Maia, J. M. M. Silva, and A. M. R. Ribeiro, "The Transmissibility Concept in Multi-Degree-of-Freedom Systems," *Mech. Syst. Signal Process.*, vol. 15, no. 1, pp. 129–137, Jan. 2001.

[111] A. M. R. Ribeiro, J. M. M. Silva, and N. M. M. Maia, "On the Generalisation of the Transmissibility Concept," *Mech. Syst. Signal Process.*, vol. 14, no. 1, pp. 29–35, Jan. 2000.

[112] D. De Klerk and A. Ossipov, "Operational transfer path analysis: Theory, guidelines and tire noise application," *Mech. Syst. Signal Process.*, vol. 24, no. 7, pp. 1950–1962, Oct. 2010.

[113] D. de Klerk, "Dynamic response characterization of complex systems through operational identification and dynamic substructuring: An application to gear noise propagation in the automotive industry," Ph.D. dissertation, Delft University of Technology, S.l., 2009.

[114] T. Moi, A. Cibicik, and T. Rølvåg, "Digital twin based condition monitoring of a knuckle boom crane: An experimental study," *Eng. Fail. Anal.*, vol. 112, May 2020.

[115] S. Gebrezgabir, D. S. Holloway, and J. Ali-Lavroff, "Slam and wave load response reconstruction in high speed catamarans using transmissibility on full scale sea trials," *Ocean Eng.*, vol. 271, Mar. 2023.

[116] A. Alsalah, "Exploiting non-stationary structural wave characteristics of ship-wave impulse responses for temporal and spatial slam detection," Thesis, University of Tasmania, May 2025.

[117] G. Durandt and A. Bekker, "The prediction of hull strain for a polar vessel from structural vibration with transmissibility-based transfer function models," in *Proc. 44th Int. Conf. Ocean Offshore Arct. Eng.* Vancouver, British Columbia: ASME, 2025.

[118] ——, "Utilizing an Acceleration-Strain Transmissibility Relationship for the Prediction of Midship Strain on a Polar Vessel," in *Proc. Int. Conf. Offshore Mech. Arct. Eng.*, 2025.

[119] G. Jagite, S. Malenica, J. de Lauzon, and Q. Derbanne, "Advances in Hybrid Structural Health Monitoring for Ships and Offshore Structures," in *Proc. 16th Int. Symp. Pract. Des. Ships Float. Struct.*, Ann Arbor, MI, USA, 2025.

[120] F.-X. Sireta, J. Van der Cammen, and G. Storhaug, "Aoka Mizu FPSO Hybrid Twin Pilot-A Spectral Approach for Holistic Hull Structure Monitoring from Strain Gauges Measurements and Structural Analysis," in *Proc. Annu. Offshore Technol. Conf.* Offshore Technology Conference, 2022.

[121] B. Peeters and G. De roeck, "Reference-Based Stochastic Subspace Identification for Output-Only Modal Analysis," *Mech. Syst. Signal Process.*, vol. 13, no. 6, pp. 855–878, Nov. 1999.

[122] R. Brincker, L. Zhang, and P. Andersen, "Modal identification of output-only systems using frequency domain decomposition," *Smart Mater. Struct.*, vol. 10, no. 3, p. 441, Jun. 2001.

[123] R. Brincker and P. Andersen, "Understanding Stochastic Subspace Identification," in *Proc. Soc. Exp. Mech. Ser.*, 2006.

[124] C. Van Zijl, K. Soal, R. Volkmar, Y. Govers, M. Böswald, and A. Bekker, "The use of operational modal analysis and mode tracking for insight into polar vessel operations," *Mar. Struct.*, vol. 79, Sep. 2021.

[125] K. Soal, Y. Govers, J. Bienert, and A. Bekker, "System identification and tracking using a statistical model and a Kalman filter," *Mech. Syst. Signal Process.*, vol. 133, Nov. 2019.

[126] R. B. Hageman and I. Drummen, "Modal analysis for the global flexural response of ships," *Mar. Struct.*, vol. 63, pp. 318–332, Jan. 2019.

[127] A. Alsalah, D. Holloway, M. Mousavi, and J. Lavroff, "Identification of wave impacts and separation of responses using EMD," *Mech. Syst. Signal Process.*, vol. 151, Apr. 2021.

[128] W. Amin, M. Davis, G. Thomas, and D. Holloway, "Analysis of wave slam induced hull vibrations using continuous wavelet transforms," *Ocean Eng.*, vol. 58, pp. 154–166, Jan. 2013.

[129] D. Dessi, "Whipping-based criterion for the identification of slamming events," *Int. J. Nav. Archit. Ocean Eng.*, vol. 6, no. 4, pp. 1082–1095, Dec. 2014.

[130] Y. Kim, J.-H. Kim, and Y. Kim, "Whipping identification of a flexible ship using wavelet cross-correlation," *Ocean Eng.*, vol. 74, pp. 90–100, Dec. 2013.

[131] A. Bekker, C. M. Van Zijl, and C. F. W. Saunders, "The detection of wave slamming from vibration measurements on a polar supply and research vessel," in *14th Int. Conf. Vib. Eng. Technol. Mach. VETOMAC XIV*, N. Maia and Z. Dimitrovová, Eds., vol. 211, 2018, p. 11002.

[132] S. Du, D. A. Hudson, W. G. Price, P. Temarel, R. Chen, and Y. Wu, "Wavelet Analysis of Loads on a Flexible Ship Model Traveling in Large-Amplitude Waves," *J. Ship Res.*, vol. 52, no. 04, pp. 249–262, Dec. 2008.

[133] D. Gabor, "Theory of communication. Part 1: The analysis of information," *J. Inst. Electr. Eng. - Part III Radio Commun. Eng.*, vol. 93, no. 26, pp. 429–441, Nov. 1946.

[134] J. C. Bossau and A. Bekker, "Line detection techniques to pinpoint slamming impulses in time-frequency images of hull acceleration measurements," *Ocean Eng.*, vol. 249, Apr. 2022.

[135] D. Dessi, "Reconstruction of the Experimental Slamming Force Distribution Based on POD," in *Vol. 9 Odd M Faltinsen Honor. Symp. Mar. Hydrodyn.* Nantes, France: American Society of Mechanical Engineers, Jun. 2013.

[136] M. K. Ochi and L. E. Motter, "Prediction of Slamming Characteristics and Hull Responses for Ship Design," in *Annu. Meet. SNAME*, no. 4. Society of Naval Architects and Marine Engineers, Sep. 1973.

[137] D. Dessi and E. Ciappi, "Slamming clustering on fast ships: From impact dynamics to global response analysis," *Ocean Eng.*, vol. 62, pp. 110–122, Apr. 2013.

[138] D. Dessi, "Experimental Reconstruction of the Hull Sectional Forces Under Slamming Events," in *Vol. 11 Prof Robert F Beck Honor. Symp. Mar. Hydrodyn.* St. John's, Newfoundland, Canada: American Society of Mechanical Engineers, May 2015.

[139] D. Dessi and R. Mariani, "Analysis and Prediction of Slamming-Induced Loads of a High-Speed Monohull in Regular Waves," *J. Ship Res.*, vol. 52, no. 01, pp. 71–86, Mar. 2008.

[140] G. Thomas, S. Winkler, M. Davis, D. Holloway, S. Matsubara, J. Lavroff, and B. French, "Slam events of high-speed catamarans in irregular waves," *J. Mar. Sci. Technol.*, vol. 16, no. 1, pp. 8–21, Mar. 2011.

[141] J. T. Tuitman, Š. Malenica, and R. Van 'T Veer, "Generalized Modes in Time-Domain Seakeeping Calculations," *J. Ship Res.*, vol. 56, no. 4, pp. 215–233, Dec. 2012.

[142] M. Ancellin and F. Dias, "Capytaine: A Python-based linear potential flow solver," *J. Open Source Softw.*, vol. 4, no. 36, Apr. 2019.

[143] M. Ancellin and N. Nguyen, "Case studies of BEM solver accuracy with the open-source code Capytaine," in *Int. Conf. Offshore Mech. Arct. Eng.* American Society of Mechanical Engineers, 2024.

[144] E. M. Lewandowski, *Dynamics Of Marine Craft, The: Maneuvering And Seakeeping.* World scientific, 2004, vol. 22.

[145] A. Hulme, "The wave forces acting on a floating hemisphere undergoing forced periodic oscillations," *J. Fluid Mech.*, vol. 121, pp. 443–463, 1982.

[146] M. B. Kramer, J. Andersen, S. Thomas, F. B. Bendixen, H. Bingham, R. Read, N. Holk, E. Ransley, S. Brown, and Y.-H. Yu, "Highly accurate experimental heave decay tests with a floating sphere: A public benchmark dataset for model validation of fluid–structure interaction," *Energies*, vol. 14, no. 2, p. 269, 2021.

[147] G. Strang, *Introduction to Linear Algebra.* SIAM, 2022.

[148] D. C. Kammer, "Sensor placement for on-orbit modal identification and correlation of large space structures," *J. Guid. Control Dyn.*, vol. 14, no. 2, pp. 251–259, Mar. 1991.

[149] M. I. Friswell and R. Castro-Triguero, "Clustering of Sensor Locations Using the Effective Independence Method," *AIAA J.*, vol. 53, no. 5, pp. 1388–1391, May 2015.

[150] J. Nocedal and S. J. Wright, *Quadratic Programming.* New York, NY: Springer New York, 2006, pp. 448–496.

[151] D. Kraft, "A software package for sequential quadratic programming," *Forschungsbericht- Dtsch. Forsch.- Vers. Luft- Raumfahrt*, 1988.

[152] C. L. Lawson and R. J. Hanson, *Solving Least Squares Problems.* Society for Industrial and Applied Mathematics, Jan. 1995.

[153] P. Virtanen, R. Gommers, T. E. Oliphant, M. Haberland, T. Reddy, D. Cournapeau, E. Burovski, P. Peterson, W. Weckesser, J. Bright, S. J. van der Walt, M. Brett, J. Wilson, K. J. Millman, N. Mayorov, A. R. J. Nelson, E. Jones, R. Kern, E. Larson, C. J. Carey, İ. Polat, Y. Feng, E. W. Moore, J. VanderPlas, D. Laxalde, J. Perktold, R. Cimrman, I. Henriksen, E. A. Quintero, C. R. Harris, A. M. Archibald, A. H. Ribeiro, F. Pedregosa, and P. van Mulbregt, "SciPy 1.0: Fundamental algorithms for scientific computing in Python," *Nat. Methods*, vol. 17, no. 3, pp. 261–272, Mar. 2020.

[154] S. Butterworth, "On the theory of filter amplifiers," *Wirel. Eng.*, vol. 7, no. 6, pp. 536–541, 1930.

[155] S. Malenica, E. Stumpf, F.-X. Sireta, and X.-B. Chen, "Consistent Hydro-Structure Interface for Evaluation of Global Structural Responses in Linear Seakeeping," in *Vol. 6 Nick Newman Symp. Mar. Hydrodyn. Yoshida Maeda Spec. Symp. Ocean Space Util. Spec. Symp. Offshore Renew. Energy.* Estoril, Portugal: ASMEDC, Jan. 2008, pp. 61–68.

[156] C. R. Harris, K. J. Millman, S. J. van der Walt, R. Gommers, P. Virtanen, D. Cournapeau, E. Wieser, J. Taylor, S. Berg, N. J. Smith, R. Kern, M. Picus, S. Hoyer, M. H. van Kerkwijk, M. Brett, A. Haldane, J. F. del Río, M. Wiebe, P. Peterson, P. Gérard-Marchant, K. Sheppard, T. Reddy, W. Weckesser, H. Abbasi, C. Gohlke, and T. E. Oliphant, "Array programming with NumPy," *Nature*, vol. 585, no. 7825, pp. 357–362, Sep. 2020.

[157] J. D. Hunter, "Matplotlib: A 2D Graphics Environment," *Comput. Sci. Eng.*, vol. 9, no. 3, pp. 90–95, May 2007.

[158] L. Lamport, "LaTeX: A document preparation system. User's Guide and Reference Manual," Jan. 1986.

